

Title	Optical comb injection for optical demultiplexing and harmonic frequency locking
Authors	Shortiss, Kevin
Publication date	2020-04-17
Original Citation	Shortiss, K. 2020. Optical comb injection for optical demultiplexing and harmonic frequency locking. PhD Thesis, University College Cork.
Type of publication	Doctoral thesis
Rights	© 2020, Kevin Shortiss. - https://creativecommons.org/licenses/by-nc-nd/4.0/
Download date	2023-05-07 22:02:51
Item downloaded from	http://hdl.handle.net/10468/9995

Optical Comb Injection for Optical Demultiplexing and Harmonic Frequency Locking

Thesis

Kevin Shortiss

**Thesis submitted for the degree of
Doctor of Philosophy**



NATIONAL UNIVERSITY OF IRELAND, CORK

SCHOOL OF SCIENCE
DEPARTMENT OF PHYSICS

17 April 2020

Head of Department: Prof John McNerney

Supervisors: Prof Frank Peters
Prof Eoin O'Reilly

Research supported by SFI

I, Kevin Shortiss, certify that this thesis is my own work and has not been submitted for another degree at University College Cork or elsewhere.

Kevin Shortiss

Contents

Abstract	iv
Acknowledgements	v
List of Publications	vii
List of Acronyms	ix
List of Figures	x
List of Tables	xvi
1 Introduction	1
1.1 Fibre-optic Communications	2
1.1.1 Wavelength Division Multiplexing	2
1.1.2 Optical Transmission Windows	3
1.1.3 Optical Superchannels based on Frequency Combs	4
1.2 The Fundamentals of a Laser	7
1.2.1 Energy Levels in Solids and Semiconductors	7
1.3 Radiative Recombination and Stimulated Generation	9
1.3.1 Spontaneous Recombination	9
1.3.2 Stimulated Emission	10
1.3.3 Stimulated Generation	10
1.4 Non-radiative Recombination	10
1.4.1 Auger Recombination	11
1.4.2 Surface and Defect Recombination	11
1.5 Semiconductor Lasers and Photonic Integration	12
1.5.1 An Overview of Photonic Integration	13
1.5.2 Hybrid and Heterogeneous Integration	14
1.5.3 Monolithic Integration	16
1.5.4 Regrowth Free Monolithically Integrable Semiconductor Lasers	17
1.6 Optical Combs	18
1.7 Optical Injection Locking	20
1.8 Integrated Optical Demultiplexers	23
1.9 Thesis Motivation and Outline	25
2 Fabry-Pérot Model and Cavity Q	27
2.1 Experimental Set-up	27
2.2 Fabry-Pérot Model Description	28
2.3 Gain and the Thermal Tuning of Gain	32
2.4 Scattering Matrices and the Transmission Matrix Method	34
2.4.1 Modelled Reflection Spectra	37
2.5 Model Results	39
2.5.1 Free Running Model Results	40
2.5.2 Simulated Mode Suppression and Optical Demultiplexing	41
2.6 Cavity Quality Factor and Optical Comb Demultiplexing	44
2.7 Conclusions	46
3 Rate Equation Model and the Side Mode Suppression Ratio versus Comb Spacing	48
3.1 Rate Equation Model Description	49
3.1.1 Free-Running Steady State Solutions	50
3.2 Model Results, Optimal Device Current and Predictions	51
3.2.1 Phasor Plots in Optical Comb Injection	55
3.3 Probe Signal Method of Measuring Narrowly Spaced Demultiplexed Optical Combs	59
3.4 SMSR Versus Optical Comb Spacing	62
3.5 SMSR Versus Detuning	66
3.5.1 Comb Spacings close to ω_r	69
3.5.2 Comb Spacings close to $2\omega_r$	69

3.5.3	Comb Spacings close to $3\omega_r$	71
3.6	Chapter Conclusion	73
4	Harmonic Locking and the Frequency Locking of Relaxation Oscillations	74
4.1	Experimental Set-up	75
4.2	Detuning Sweeps	76
4.2.1	Single Frequency Detuning Sweep	76
4.2.2	Frequency comb detuning sweep	78
4.2.3	Sweeping Direction and Hysteresis	80
4.2.4	Modelling Detuning Sweeps	81
4.2.5	Model Comparison with High Resolution Detuning Sweep	83
4.3	Arnol'd Tongues, Harmonic Locking, and the appearance of a Devil's Staircase	85
4.3.1	The Circle Map	85
4.3.2	The Devil's Staircase in the Frequency and Amplitude Locking of Non-linear Oscillators with Continuous Modulated Forcing	87
4.4	Relative Locking Stability and the Role of Linewidth Enhancement Factor . . .	91
4.4.1	Relationship Between the Relaxation Oscillations and the Size of Arnol'd Tongues	93
4.5	Asymmetry of Relaxation Oscillation Locking around the Centre Comb Line . .	94
4.6	Large Comb Spacings and the Limits of the Harmonic Locking Mechanism . .	95
4.7	Chapter Conclusion	97
5	Conclusion	98
5.1	Overview of the Results Presented	98
5.2	Future Work	100
A	The Inverse Scattering Method for Single Mode Devices	102
A.1	Derivation of First Order Perturbation to Gain	103
A.2	Solving the Inverse Problem	109
A.3	Method for Computing Perturbation Positions	111
A.4	Designing Etched Facet Devices	112
A.5	Device Results	114
A.6	Conclusions	117
B	Scanning Electron Microscope Images of Device Sections	118
C	Growth of Arnol'd Tongues with Pump Current for $\alpha = 0$ and $\alpha = 3$	121
D	Material and Substrate Information	123
E	Runge-Kutta Formula	125
E.1	Varying the Time Steps used in Rate Equation Models	126

Abstract

With the continued growth of internet traffic, new optical communication infrastructures capable of dramatically increasing network bandwidth are being considered. Optical superchannels consisting of densely packed channels will be required for future networks, which could potentially be implemented using optical frequency combs – optical sources which consists of a series of discrete, equally spaced frequency lines. Optical combs can increase the spectral efficiency of these superchannels by allowing the channels to be more densely packed, while simultaneously reducing the number of components required (decreasing the energy consumption), and simplifying the digital signal processing required.

Despite these advantages, the trade-off between cost and performance must be favourable in order for optical combs to become feasible for use in future communication networks. Photonic integrated circuits integrate several components together on a single semiconductor chip. These photonic circuits reduce both the cost and power consumption of devices, and hence recent research has been focused on creating suitable on-chip coherent optical comb transmitters.

This thesis investigates an approach which is being used to demultiplex narrowly spaced optical combs on a photonic integrated circuit. By injection locking a laser to one of the lines in the optical comb (i.e, forcing a laser to lase with the frequency of that comb line), the comb line can be amplified and demultiplexed. This work investigates the physics of these active demultiplexers, both experimentally and numerically. It is found that the optimal side mode suppression ratio is obtained when the ratio of the comb's power to the injected laser's power is small, which also indicates optimal performance occurs when the locking range of the injected laser is at its smallest. The relaxation oscillations of the injected laser affect how well the comb can be demultiplexed, and as a result better side mode suppression ratios can be achieved at larger comb spacings. Further, it is shown that the relaxation oscillations within the injected laser can become undamped due to the comb injection, and frequency lock to fractions of the optical comb spacing. The injected laser can even become locked at detunings between the comb lines, creating a new output optical comb through nonlinear processes. The above phenomena are investigated numerically using two dimensional maps, and it is found that Arnol'd tongues appear in the injected laser's locking map.

Acknowledgements

First and foremost, I would like to thank my supervisor Prof. Frank Peters for giving me the opportunity to study photonics over the last 4 years. I have learned so much more than just how to perform experimental and theoretical research in my short time in the integrated photonics group in Tyndall. Frank's mentoring allowed me the academic freedom to investigate and pursue what I believed was interesting, while ensuring my PhD project remained coherent and focused. Thank you Frank for all the support you have given me during this project, I thoroughly enjoyed working with you throughout my PhD.

To my family, thank you for always supporting me. Mom and Dad, I recognise that you regularly give all of your energy and time to ensure Ciara, Eimear, Eoin and myself have nothing to worry about. You have always gone above and beyond to make sure we are healthy and happy, you have enabled us to become the best versions of ourselves. Thank you for helping me solve the (thankfully few) problems I have had to face over the last few years, I am grateful every day.

To my partner Anna, thank you for standing beside me throughout this journey. Thank you for putting up with late nights, and continuing to believe in the week where "I should be less busy". You keep my life structured and put everything in perspective. You are a constant source of joy and silliness, I am very lucky to have you in my life. I look forward to all of our future adventures together!

To Fabien, Kieran, Tommy, and everyone else who has worked with me in Kane 1.16; I immensely enjoyed your company over the last few years. Firstly, thank you Fabien for being a friend and providing moral support for the majority of my project. Your enthusiasm and optimism helped me when I felt all my batteries were drained. Working with you as you finished your PhD helped me prepare for writing my own thesis; you were my go to for all types of questions, and I greatly appreciate your support. Thanks Kieran for helping to make the first year of my PhD the most stress free; although some bad habits may have stuck with us from undergraduate, your work ethic, natural interest in physics, and patented whiteboard groove, will never be forgotten. Thank you for answering all the questions I should have known the answer to, maybe someday I will read "Visual Complex Analysis". Thank you Tommy for being there over the last year – I always enjoyed catching up with you, chatting about different types of curved waveguides, and speculating during the early days of the COVID-19 virus outbreak. Finally, to Sean and Aisling, you are some of the friendliest and most bubbly people I have met, I'm glad you briefly spent some time with us in Frank's postgrad lab.

To all the other members of IPG: Alison, Mohamad, Ludovic, Shane, Maryam, Masoud, Hui, Jack, John, Zhengkai, Moises, Xing, Justin, Niall and Hua – thank you all for your help and guidance. Travelling together to conferences and exploring new cities together was a lot of fun and very memorable. I was lucky to be part of such a strong team, and watching others go through the PhD process prepared me for my own viva. To past members Rob, Eddie and Padraic, thank you for giving me a strong starting point.

To Bryan, Benjamin and Michael – thank you for fully adopting me into the laser dynamics group. All of the group meetings I attended were friendly, enjoyable, interesting and informative. Thanks for answering all my questions; without your help, it would have taken me much longer to understand some aspects of my project. I am very glad our collaboration went so well.

I want to thank all the friends I am fortunate enough to have made over the last decade. To my housemates Shane, Amy and Tom, each of us has gone through the highs and lows of our PhDs together, and I'm proud that all of us have come out the other end still very close friends. We have seen a quarantine, a hurricane and a snow storm in the last 4 years, and have so

many memories together, from yearly Christmas dinners to the intensely competitive annual Pokemon speed run. To Sebastian and Fred, thank you both for unwinding with me everyday at lunch. Someday soon, our kickstarter project will be funded, and the main rest will finally have some spices. It's a pity we couldn't have one last Joe's and Bros together. To everyone I worked with in Tyndall and UCC's student chapter; I am very fortunate to have taken part in such an amazing group! I will always remember the enthusiasm, energy and ingenuity that I experienced as part of the group. To Anna, Eoin, Eon, and all the other members of Cork Action League, thank you for helping me unwind while playing board games every Monday! You introduced me to so many new games, and I have enjoyed countless hours calculating, strategising and hiding my hidden role.

Finally, I would like to thank all my other colleagues and friends in the UCC physics department and in Tyndall who helped me during my time studying. I am also grateful to Science Foundation Ireland, for funding this research (under grant number 13/IA/1960).

List of Publications

First Author Publications

K. J. Shortiss, M. Shayesteh, F. H. Peters, "Modelling the effect of slave laser gain and frequency comb spacing on the selective amplification of injection locked semiconductor lasers", *Optical and Quantum Electronics*, 50: 49 (2018).

K. Shortiss, M. Dernaika, L. Caro, M. Seifikar, F. H. Peters, "Inverse Scattering Method Design of Regrowth-Free Single-Mode Semiconductor Lasers Using Pit Perturbations for Monolithic Integration", *IEEE Photonics Journal*, 10:5 (2018).

K. Shortiss, M. Shayesteh, W. Cotter, A. Perrott, M. Dernaika, F. H. Peters, "Mode Suppression in Injection Locked Multi-Mode and Single-Mode Lasers for Optical Demultiplexing", *Photonics*, 6(1), 27 (2019).

K. Shortiss, B. Lingnau, F. Dubois, B. Kelleher, F. H. Peters, "Harmonic Frequency Locking and Tuning of Comb Frequency Spacing through Optical Injection", *Optics Express*, *Optics Express* 27(25), 36976-36989 (2019).

K. Shortiss, M. Dernaika, M. Shayesteh, F. H. Peters, "The Effect of Relaxation Oscillations in Integrated Optical Comb Demultiplexers based on Injection Locking", *IEEE Journal of Quantum Electronics*, 55(6), 1-6, (2019).

Conference Talks

K. Shortiss, M. Shayesteh, F. H. Peters, "Injection locked semiconductor lasers as optical comb filters", presented at Photonics Ireland, Galway, Ireland, session 10, 13th - 15th September 2017.

K. Shortiss, M. Dernaika, L. Caro, M. Seifikar, F. H. Peters, "Inverse Scattering Method Design of Regrowth-free Single-mode Semiconductor Lasers for Monolithic Integration", presented at Advanced Photonics, Zurich, Switzerland, ITu4B.4, 2nd - 5th July 2018.

K. Shortiss, M. Dernaika, M. Shayesteh, F. H. Peters, "Integrated optical demultiplexing by injection locking", presented at Photonics Ireland, Cork, Ireland, session B1, 3rd - 5th September 2018.

K. Shortiss, M. Dernaika, M. Shayesteh, F. H. Peters, "The Effect of Optical Comb Spacing, Detuning and Injected Power on Optical Demultiplexing through Injection Locking", presented at the European Conference of Integrated Optics, Ghent, Belgium, Parallel session T.A2, 24th - 26th April 2019.

K. Shortiss, B. Lingnau, F. Dubois, F. H. Peters, B. Kelleher, "Tailored Optical Frequency Combs by Harmonic Frequency and Amplitude Locking in an Optically Injected Laser", presented at The European Conference on Lasers and Electro-Optics, Munich, Germany, CB-9.2, 23rd - 27th June 2019.

K. Shortiss, B. Lingnau, F. Dubois, B. Kelleher, F. H. Peters, “Frequency Locking Mechanisms enabled by Optical Frequency Comb Injection” presented at the European Semiconductor Laser Workshop, Cork, Ireland, session 4, 27th - 28th September 2019.

Conference Posters

K. Shortiss, W. Cotter, M. Shayesteh, A. H. Perrott, F. H. Peters, “Modelling injection locked semiconductor lasers”, presented at Photon 16, Leeds, United Kingdom, P:89, 5th - 8th September 2016.

K. Shortiss, M. Dernaika, L. Caro, N. P. Kelly, F. H. Peters, “Minimising Waveguide Loss on Photonic Integrated Circuits”, Institute of Physics Spring Meet, Dublin, Ireland, 11th March 2017.

K. Shortiss, M. Shayesteh, F. H. Peters, “Modeling the Effect of Slave Laser Gain and Frequency Comb Spacing on the Selective Amplification of Injection Locked Semiconductor Lasers”, presented at NUSOD 2017, Copenhagen, Denmark, 24th - 28th July 2017.

M. Shayesteh, **K. Shortiss**, W. Cotter, P. E. Morrissey, A. H. Perrott, N. P. Kelly, F. H. Peters, “De-multiplexing coherent optical combs within Photonic Integrated Circuits”, at The European Conference on Lasers and Electro-Optics 2017, Eindhoven, Netherlands, **M3.2**, 3rd - 5th April 2017.

Other Publications

M. Dernaika, N. Kelly, L. Caro, **K. Shortiss**, F. Peters, “Regrowth-free single mode semiconductor laser suitable for monolithic integration based on pits mirror”, *Optical Engineering*, 56(8), (2017).

B. Lingnau, **K. Shortiss**, F. Dubois, F. H. Peters, B. Kelleher, “The Devil’s Staircase in the Frequency and Amplitude Locking of Nonlinear Oscillators with Continuous Modulated Forcing”, arxiv:1905.01122 (2019).

List of Acronyms

AWG	Arrayed Waveguide Grating
CMOS	Complementary metaloxidesemiconductor
DBR	Distributed Bragg Grating
DFB	Distributed Feedback Laser
DUT	Device Under Test
EDFA	Erbium Doped Fiber Amplifier
ESA	Electrical Spectrum Analyzer
FFT	Fast Fourier Transform
FP	Fabry-Pérot
FSR	Free Spectral Range
FWM	Four Wave Mixing
HR	High Reflectance
Iso	Isolator
IQE	International Quantum Epitaxy
LHS	Left Hand Side
LI	Light Current
MMI	MultiMode Interferometer
MZM	Mach-Zehnder Modulator
ODE	Ordinary Differential Equation
OFC	Optical Frequency Comb
OSA	Optical Spectrum Analyzer
P1	Period 1
P2	Period 2
PC	Polarisation Controller
PD	Photo-Diode
PECVD ...	Plasma-Enhanced Chemical Vapor Deposition
PIC	Photonic Integrated Circuit
PR	Photo Resist
Q-factor ...	Quality Factor
QW	Quantum Well
QWI	Quantum Well Intermixing
RF	Radio Frequency
RHS	Right Hand Side
RK4	4th order Runge Kutta method
RO	Relaxation Oscillation
SFP	Slotted Fabry-Pérot
SEM	Scanning Electron Microscope
SIL	Stable Injection
SMSR	Side Mode Suppression Ratio
SOA	Semiconductor Optical Amplifier
TLS	Tunable Laser Source
TMM	Transfer Matrix Method
VCSEL ...	Vertical Cavity Surface Emitting Laser
VOA	Variable Optical Attenuator
WDM	Wavelength Division Multiplexing

List of Figures

1.1	Plot of internet traffic and high end consumer internet speeds.	2
1.2	Illustration of a wavelength division multiplexing (WDM) system.	3
1.3	Optical loss versus wavelength of commercially available fibre from the early 1970s to the early 1990s.	4
1.4	Illustration of WDM channels in frequency space.	5
1.5	Illustration of a wavelength division multiplexing (WDM) system, which uses an optical comb source instead of individual lasers.	6
1.6	(a) Illustration of laser cavity and (b) energy levels of atom splitting due to covalent bonding to form a solid.	7
1.7	Illustration of the radiative recombination and stimulated generation processes between the conduction band and the valence band.	9
1.8	Illustration of (a) one of the Auger nonradiative recombination processes, and (b) an example of phonon assisted nonradiative recombination.	10
1.9	Illustrations of (a) a simple transverse laser cavity, (b) a vertical laser cavity, (c) edge emitting laser diode and (d) vertical cavity laser diode.	12
1.10	Different techniques for monolithic photonic integration.	15
1.11	Large scale photonic integrated circuit from Ref. [60].	16
1.12	Scanning electron microscope images of (a) a shallow etched slot and a deep etched slot and (b) a pit perturbation etched into the waveguide of a ridge laser.	18
1.13	Illustration of an optical frequency comb.	19
1.14	Illustration of the RF bias, carrier density and photon density in a gain switched laser.	20
1.15	Comparison between optically injected and free running laser spectra.	22
1.16	Size comparison of an 8 channel arrayed waveguide grating (AWG) demultiplexer and a 1×3 optical injection demultiplexer.	23
1.17	(a) Microscope image of a 1×4 demultiplexer. (b) Illustration of an input comb, with 4 slave lasers locking to different lines in the comb.	24
2.1	Experimental setup used to measure the intensity plots of the optical injection locking experiments.	28
2.2	(a) Image of a device under test. (b) Typical 10 GHz optical comb injected into the device under test.	28
2.3	Illustrations of the fields inside a Fabry-Pérot laser cavity, including two mirrors with reflection coefficients r_1 and r_2	29
2.4	Comparison between measured device gain from a FP laser calculated using the Cassidy gain method [176], and the gain g_m implemented in the model.	30
2.5	Plot of the gain of the AlInGaAs material measured at 20°C, using both the Hakki-Paoli and the Cassidy gain methods.	34
2.6	Illustration of different inputs and outputs of a 3 port scattering junction.	35
2.7	Interface between two dielectric material.	35
2.8	Two scattering junctions, T and T', side by side.	36

2.9	(a) Reflection calculated using transmission matrices, of a 700 μm long passive FP cavity. (b) Optical spectrum from a 1050 μm long FP laser at 3.0 times threshold.	37
2.10	(a) A 3D illustration of a waveguide slot. Inset: A scanning electron microscope image of a slot in a fabricated device. (b) Illustration of how the mode overlaps with the slot interface both within and outside of the slotted region.	38
2.11	(a) Illustration of the SFP design. (b) Calculated reflection spectrum of an 8 slot mirror. (c) Calculated resonance of the full SFP laser, from the end of the mirror section to the facet. (d) Measured lasing spectrum of a SFP device, for comparison.	39
2.12	(a) Calculated LI curve from a 700 μm long FP device. (b) Calculated lasing spectrum of the same device at 2.5 times threshold current. (c) Measured lasing spectrum of a 700 μm long real FP device at 2.5 times threshold, for comparison.	40
2.13	(a) Calculated LI curve from the SFP device depicted in Fig. 2.11(a). (b) Calculated lasing spectrum of the same device at 2.0 times threshold current. (c) Measured lasing spectrum of a real SFP laser.	41
2.14	Experimental and calculated injected wavelength sweeps of a 700 μm FP device.	42
2.15	Experimental and calculated temperature sweeps of an optically injected 600 μm long two section slotted FP device, with a single etched slot in the center of the device separating the sections.	43
2.16	(a) Comb demultiplexer, featuring a 1×2 multimode interferometer (MMI) and 2 SFP lasers [168]. (b) Optical comb injected into the demultiplexer.	43
2.17	(a) Experimental and (b) calculated injected comb sweeps of an optical demultiplexer, as shown in Fig. 2.16(a), with an injected optical comb as shown in Fig. 2.16(b).	44
2.18	(a) Plot showing how the SMSR of the output spectrum varies as the Q of the laser cavity increases. (b) Intensity plot of how SMSR varies versus detuning and Q factor. (c) Plot the locking range of the FP laser versus Q, for the same injection ratios and parameters as in (a).	45
2.19	An example of four wave mixing occurring in a detuning sweep, where a single frequency is injected into a multi-mode FP device.	46
3.1	A comparison between the measured RO frequency and the calculated RO frequency (using Eq. (3.10)) of a single mode laser, for the parameter values presented in Table 3.1.	50
3.2	(a) Plot of the electric field and (b) carrier density as a function of time in a slave laser under optical injection, calculated using a single mode rate equation.	52
3.3	(a) The experimental setup used to measure the SMSR from the 1×2 device under test. (b) Experimental and theoretical results showing the change in SMSR as the slave laser's current increased.	53
3.4	(a) Plot of how the calculated SMSR varied as the frequency spacing between the injected comb lines changed, when locked to the higher frequency, lower frequency and center frequency lines in a three line comb. (b) Plot of how the calculated SMSR varied as a function of comb spacing for different carrier lifetime values.	54

3.5	(i) Phasor diagrams and (ii) computed optical spectra for single frequency optical injection at different detunings.	56
3.6	(i) Phasor diagrams and (ii) computed optical spectra for comb injection at different detunings.	57
3.7	Comparison between the bounded phase limit cycles presented in Fig. 3.5(b) and Fig. 3.6(b).	58
3.8	Comparison showing how the comb spacing effects the undamping of the relaxation oscillations.	59
3.9	Optical spectra from a standard 2 GHz resolution optical spectrum analyser, showing the limitations of measuring SMSR of narrowly spaced combs with low frequency resolution.	60
3.10	(a) The experimental setup used to perform the comb experiments. (b) Illustration showing where the probe wavelength from the second TLS was located relative to the demultiplexed comb.	61
3.11	Example ESA traces measured while performing the SMSR versus comb spacing experiment.	61
3.12	Experimental results (and calculated results on the right hand side axis) showing the average beat note of the unlocked comb line with the probe TLS versus comb spacing obtained over five experimental runs.	62
3.13	(a) Comparison of 5 GHz optical comb spectra, measured on a 2 GHz resolution OSA and a 5 MHz high resolution OSA. (b) Experimental setup used to investigate the SMSR obtainable.	63
3.14	Free-running spectra measured of (a) a single mode laser and (b) a FP laser, using a high resolution optical spectrum analyser.	63
3.15	Measured SMSR as the frequency spacing of the injected optical comb was varied, for four different optical injection strengths.	64
3.16	Demultiplexed optical spectra, measured using an optical spectrum analyser with 5 MHz resolution. The spectra presented highlight four operating conditions with distinct behaviour.	65
3.17	(a) Calculated SMSR versus frequency spacing, simulating the experimental results presented in Fig. 3.15. (b) Calculated SMSR versus injected comb frequency spacing for pump currents of 1.6, 2.0 and 3.0 times the free running laser threshold.	66
3.18	Calculated intensity plot showing the slave laser output SMSR, as a function of detuning and optical injection power, for a three line 10 GHz comb.	67
3.19	Four calculated intensity plots, which show how the SMSR varies around the Adler locking tongue for comb spacings Δ around the relaxation oscillation frequency. Below the four intensity plots, optical spectra from the slave laser at different points are shown.	68
3.20	Four calculated intensity plots, which show how the SMSR varies around the Adler locking tongue for comb spacings Δ around twice the relaxation oscillation frequency. Below the four intensity plots, optical spectra from the slave laser at different points are shown.	70

3.21	Four calculated intensity plots, which show how the SMSR varies around the Adler locking tongue for comb spacings Δ around three times the relaxation oscillation frequency. Below the four intensity plots, optical spectra from the slave laser at different points are shown.	72
4.1	Experimental setup for performing optical comb injection.	76
4.2	Experimental results from a detuning sweep, as a single mode slave laser's frequency was tuned across a single frequency injected signal.	77
4.3	Experimental results of a detuning sweep, as a single mode slave laser's frequency was tuned across a three line 10 GHz optical comb.	79
4.4	Individual ESA traces from a detuning sweep obtained when injecting a three line 10 GHz comb with optical injection strength -1.8 dBm into a single mode laser.	80
4.5	Experimental results from two separate detuning sweeps, where a slave laser's frequency was tuned (a) , (b) from negative to positive detuning and (c) , (d) from positive to negative detuning.	81
4.6	Measured and calculated ROs offset vertically to show different applied bias.	82
4.7	Experimental and theoretical results from a frequency detuning sweep, where the slave laser was tuned across a 10 GHz comb.	84
4.8	(a) Winding number as a function of the driving phase and injection strength for the circle map, for $0 \leq K \leq 2\pi$. (b) Single slice from (a), which shows the complete devil's staircase found in the winding number as the driving phase is swept from 0 to 2π , evaluated at $K = 1$	85
4.9	Two dimensional map spanning the injection strength K and driving phase ν , showing the Arnol'd tongues which appear, for $0 \leq K \leq 2\pi$. In each Arnol'd tongue, the map is mode locked to a different harmonic. For clarity, only the first 8 resonances are shown.	86
4.10	(a) Experimental and (b) simulated optical spectra, and the corresponding (c) measured and (d) simulated power spectra of the laser output for a sweep of the relative frequency detuning ν of the slave laser.	89
4.11	Two-dimensional resonance diagrams, showing (a) the period T_{per} of the intensity oscillations, and (b) average optical frequency $\langle \nu_{\text{opt}} \rangle$, in dependence on the injection strength K and the laser detuning ν from the center comb line with respect to the free-running slave laser frequency.	90
4.12	Comparison of the locking behaviour of different driven systems, showing the average phase velocity for the circle map, the Hopf normal form, and the laser equations.	91
4.13	Two dimensional maps of the parameter space spanned by detuning and injected power, showing (a) a map of the output comb frequency spacing and (b) the RF linewidth of the dominant harmonic's beat note, over the same parameter space as in (a).	92
4.14	Plots showing the relative size of the Arnol'd resonances as a function of slave laser pump current, for (a) $\alpha = 3$, and (b) $\alpha = 0$	93

4.15	(a) Intensity plot showing the electrical spectra measured as the frequency of a single mode slave laser was swept across the injected 6.5 GHz optical comb. (b) Corresponding simulated experiment for the parameters in (a). (c) Two dimensional map of the parameter space spanned by detuning and injected power, showing the output comb frequency spacing.	95
4.16	Two dimensional maps of the parameter space spanned by detuning and injected power, which show the output frequency spacing of the slave laser, for (a) 10 GHz, (b) 15 GHz, (c) 20 GHz, (d) 25 GHz, (e) 30 GHz, and (f) 35 GHz. . .	96
5.1	Schematic of a photonic integrated circuit (PIC) for the generation of an integrated coherent optical comb transmitter, taken from Ref. [221].	101
A.1	(a) Illustration of N perturbations introduced to the cavity, creating $2N + 1$ sections. (b) Illustration of a single perturbation, where ϵ_j gives the centre of the perturbation.	104
A.2	(a) Ideal threshold modulation function, as given by Eq. (A.47) for $a = 20$ and $\tau = 0.036$. (b) Fourier transform of the ideal threshold modulation function shown in (a).	110
A.3	Plot of the perturbation positions required to make a single moded device with lasing wavelength at $1.55 \mu\text{m}$	112
A.4	Plot of the threshold gain from the grating in Fig. A.3.	112
A.5	(a) Feature density function for the etched facet side of the device only, for a 1 mm long laser cavity. (b) Illustration of the perturbation positions found using the inverse scattering method when 6, 10, 15 and 20 perturbations are used. . .	113
A.6	Calculated threshold gain versus wavelength for the gratings shown in Fig. A.5(b). The solid horizontal line in each plot is the calculated unperturbed threshold gain of the laser cavity, i.e. $\gamma_m^{(0)} = 10.46 \text{ cm}^{-1}$	114
A.7	(a) Scanning electron microscope image of one of the pits used as perturbations in the waveguide. (b) View of the sidewall of a test device after the second etch step in the process.	115
A.8	Comparison between the spectra of a FP cavity and a 15 pit device at 140 mA, at 20°C	116
A.9	(a) A plot of voltage versus current for 1 mm long devices with 6, 10, 15 and 20 pits. (b) LI curves for the devices plotted in (b).	116
A.10	Optical spectra from the fabricated devices, for the gratings shown in Fig. A.5(b), at injected currents of 1.5 times threshold at 20°C	116
A.11	(a) Comparison between the lasing SMSR and the lasing wavelength of devices as the number of pits was altered, at 20°C . (b) Lasing wavelengths with over 30 dB SMSR from a set of devices designed to lase at 1545 nm, 1550 nm, 1555 nm, and 1565 nm.	117
B.1	Scanning electron microscope images of (a) an etched facet and (b) a metal covered etched facet used in device designs.	118
B.2	(a) Scanning electron microscope image of a 1×3 multimode interferometer (MMI). (b) A close up of the output waveguides from the MMI in (a).	119
B.3	Scanning electron microscope images of pit perturbations.	120

C.1	Two dimensional maps of the slave laser behaviour while under injection of a 10 GHz optical comb, for the case of $\alpha = 0$	121
C.2	Two dimensional maps of the slave laser behaviour while under injection of a 10 GHz optical comb, for the case of $\alpha = 3$	122
E.1	Illustrations of how (a) the Euler method and (b) the fourth order Runge-Kutta integrate an ordinary differential equation (ODE).	126
E.2	(a) Illustration showing how the simulation time steps were compared. (b) Time traces which indicate the magnitude of the difference between simulations which used different time steps (as highlighted in red in (a)), over the first 10 ns. (c) Total magnitude difference summed over all comparison times for 50 ns simulations, with no noise in the rate equations.	126
E.3	(a) Time traces which indicate the magnitude of the difference between simulations which used different time steps (as highlighted in red in Fig. E.2(a)), over the first 10 ns. The data shows how that for very course time steps, the Runge-Kutta method does not accurately predict the behaviour of the slave laser. (b) Total magnitude difference summed over all comparison times for 50 ns simulations.	127

List of Tables

2.1	Parameterised values used in the Fabry-Pérot laser model.	32
2.2	Table containing common scattering matrices and their corresponding transmission matrices; namely, the matrix for a dielectric interface, and the matrix for propagation through a distance L . It is assumed here that $r_{12} = -r_{21}$, $t_{12} = t_{21}$, with $r_{12}^2 + t_{12}^2 = 1$	37
2.3	Parameters used to model the SFP mirrors.	39
3.1	Parameter values used in the rate equation model.	51
4.1	Simulation parameters used to model the detuning sweeps, unless noted otherwise.	83
D.1	Epitaxial structure of the material. A right arrow (\rightarrow) indicates a gradient in composition, from lower layer numbers to higher layer numbers.	123
D.2	Doping information for the layers contained in Table D.1.	124
D.3	Epitaxial structure of the substrate on which the material in Table D.1 was grown on.	124

Chapter 1

Introduction

The goal of this chapter is to superficially introduce the broad background and motivation behind semiconductor lasers, fibre based optical communication systems, and methods of photonic integration.

As will be outlined below, there is a need for smaller and more cost effective methods of filtering separate wavelengths of light on a photonic integrated circuit (PIC). PICs allow the integration of multiple photonic components onto a single chip, and can reduce production costs, energy consumption and total device size, while making packaging devices simpler. The traditional on-chip optical filters (such as arrayed grating waveguides, discussed in Section 1.8) grow in size and require more accurate fabrication processes as the frequency bandwidth of the filter shrinks. This thesis instead focuses on an active method of optical filtering, which involves injecting light into a semiconductor laser. When injecting an optical frequency comb (an optical source which consists of a series of discrete, equally spaced frequency lines (see Section 1.6)) into a laser, the laser can lock to a particular line in the frequency comb, amplifying and filtering out that comb line. Optical comb injection is the central focus of this work, and the following chapters present experimental and theoretical work detailing how effective this type of optical filtering is, as well as some of the different types of dynamics which can occur with comb injection.

This introductory chapter is split into 9 parts, starting with a very broad introduction, and becoming more specific as the sections go on. Firstly, fibre based optical communication networks are discussed, and the reasons why more spectrally efficient networks are required are introduced. Semiconductor lasers make up the backbone of optical communication networks, and hence are introduced in Section 1.2. The main recombination processes in lasers are described in Sections 1.3 and 1.4. Following this, different types of photonic integration are compared, and the integration platform used in this work is presented. Optical frequency combs and optical injection locking are then introduced, which completes the groundwork required to discuss integrated demultiplexers, and how optical injection could be used as an active demultiplexer. Finally, in Section 1.9 the motivation and contents of the rest of the thesis are laid out.

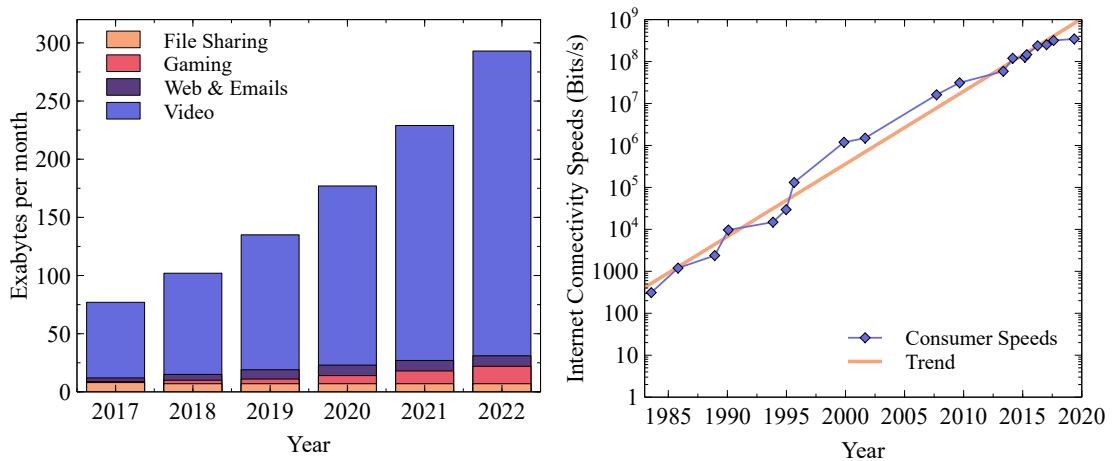


Figure 1.1: (a) Measured (2017-2019) and predicted (2020-2022) monthly data traffic, with breakdowns given for the 4 main categories, measured in exabytes [2]. With recent support for 8K video streaming on platforms such as Youtube and Vimeo, in the future larger portions of the total internet traffic will likely be taken up by video. (b) Data which indicates how consumer internet speeds have exponentially increased over the last 35 years [3].

1.1 Fibre-optic Communications

The internet has become ubiquitous in modern day life. When the first data packet was transmitted long distance in 1969, it could not have been predicted that access to the internet would be considered essential – in 2016 the UN condemned intentional internet access disruption as a “human rights violation” [1]. This ruling relays how dependent we have become on the internet, and hence as result, shows how humanity is becoming increasingly reliant on optical communications. Every month, over 100 exabytes (10^{20} bytes) of data is transmitted over optical networks. Figure 1.1(a) shows the average monthly data transmitted over optical fibre from 2017 to the present day, with estimated data traffic from 2020 onward. In the next 4 years global internet traffic is expected to double, as a large portion of humanity still does not have internet access. With more of the earth’s population becoming connected, an increasing amount of bandwidth will used up by video streaming services.

Simultaneously, consumer internet connectivity speeds have exponentially increased over the last 35 years, as shown in Fig. 1.1(b). These trends (greater internet speeds with steadily increasing internet traffic) have been made possible due to decades of preceding research into semiconductor lasers and all other components in optical communication networks.

The following few sections will describe how optical communication networks operate, and will reveal that network bandwidth is in fact finite.

1.1.1 Wavelength Division Multiplexing

Conventional optical communication networks operate using wavelength division multiplexing. A simplified schematic of what is involved in these networks is illustrated in Fig. 1.2. On the left hand side of Fig. 1.2, a bank of individual laser sources emit light at slightly different wavelengths. The light from each laser can then be modulated (using it’s amplitude [4], phase [5], or a combination of the two [6]) to impart data on the light. The separate wavelengths are then combined (multiplexed) into a single fibre, before being amplified and transmitted. As

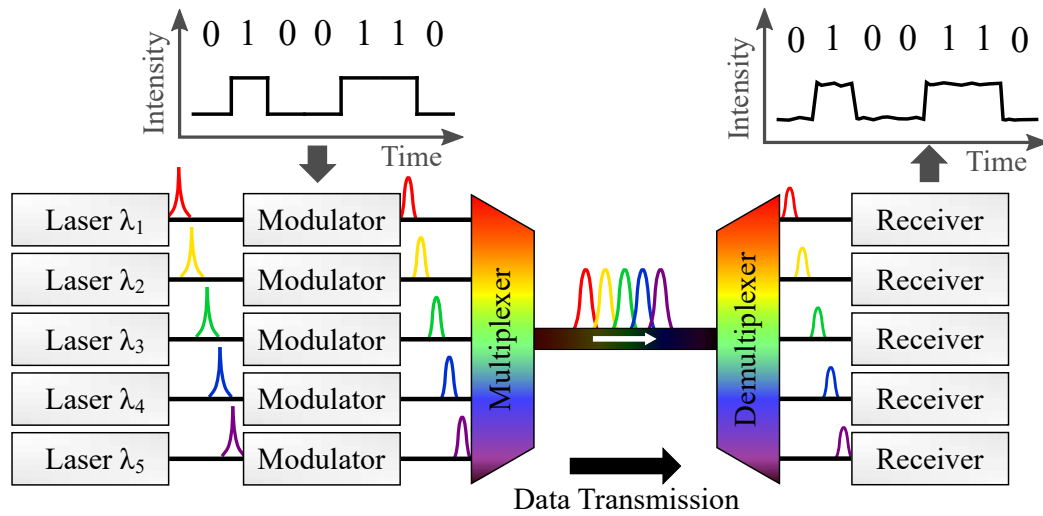


Figure 1.2: Illustration of a wavelength division multiplexing (WDM) system. From left to right, information is transmitted using a bank of lasers with slightly different wavelengths. Unique data (in the form of electrical 1's and 0's) is imparted on each separate wavelength. The signals are then combined using a multiplexer and transmitted. On the receiver side, the transmitted wavelengths are then demultiplexed, to enable the detection of each channel individually.

each wavelength can carry different information, a single fibre can carry multiple data channels. This transmitted signal can travel up to several thousand kilometres before reaching a receiver, and possibly require multiple amplification steps along the way.

On the receiver side, the transmitted optical signal must be converted back to an electronic signal. As all wavelength channels are propagated together, the light must be split up into the individual channels in order to process each stream of data, in a process called demultiplexing. Once demultiplexed, the data on each individual channel can be detected without unwanted crosstalk from neighbouring channels, using a photoreceiver.

As the wavelengths of light are multiplexed together to transmit information, this approach is called wavelength division multiplexing (WDM). The growth of data speeds in standard WDM systems has significantly slowed in recent years. Dense wavelength division multiplexing (DWDM) systems use narrower channel spacings [7], to include more carriers and improve data speeds. Further efforts have improved data speeds by moving to coherent WDM systems [8] (which use both light and phase modulation, as well as two separate polarisations), yet current optical communication systems are still approaching what has been termed a “capacity crunch” [9]. There is a fundamental limit to the amount of information that can be transmitted over a finite bandwidth, called the nonlinear Shannon limit [10]. In the following Subsections, the usable bandwidth for optical communications, and the advantages that coherent optical combs can bring to such a network are discussed.

1.1.2 Optical Transmission Windows

Low loss optical fibres are a key component in optical communication systems. Typically, silica fibres featuring a high refractive index core and low index cladding are used in communication systems¹, and successfully guide light through total internal reflection. Although glass

¹Plastic optical fibres are often used in short distance communication systems, like within an airplane or a car.

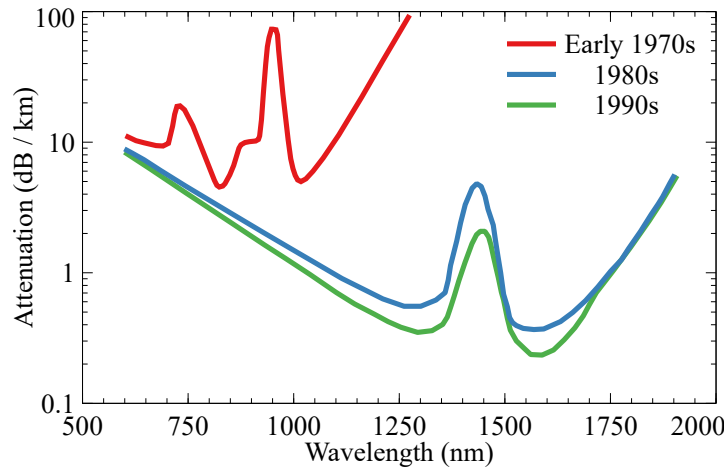


Figure 1.3: Optical loss versus wavelength of commercially available fibre from the early 1970s to the early 1990s [11]. Vast improvements in optical loss have enabled long haul optical communication. The large absorption peak at approximately 1400nm is due to hydroxyl ions present within the glass core structure, and more modern manufacturers are able to dramatically reduce these losses [12].

fibres were initially produced 100 years ago, they originally had extremely high optical losses (≈ 1000 dB/km) [13]. It wasn't until the 1970s that the optical loss in fibres was reduced enough to be considered for long haul communication. Fig. 1.3 shows the improvements made in fibre manufacturing from the early 1970s to the 1990s. Different windows of low loss were considered for transmission, and when choosing these windows, fibre dispersion, fibre loss, cost, and the availability of transmitters, receivers and optical amplifiers was taken into account.

Ultimately, largely due to the invention of the erbium doped fibre amplifier [14] (EDFA) and the availability of low cost semiconductor lasers, the low loss window at 1550 nm was chosen for long haul communication. In optical fibres, below 1550 nm the loss is dominated by rayleigh scattering, and above 1650 nm the loss is dominated by infrared absorption. The bandwidth of this low loss region (and also the bandwidth of the EDFAs) limits the total bandwidth of the system at 1550 nm.

Recently, optical communication systems have been considered at 2 μm [15]–[18], as optical losses of lower than 0.1 dB/km have been predicted using hollow-core optical fibre [19]. These optical fibres also offer lower non-linearities, raising the nonlinear Shannon limit and allowing for higher maximum data transfer. Thulium doped fibre amplifiers have been developed and have similar operating properties as EDFAs, as they also provide inline amplification² at 2 μm [20], [21]. However, as the cost of components is still very high, and the low loss predicted in hollow core optical fibres has yet to be realised, full 2 μm optical communication systems cannot yet be achieved in practice.

1.1.3 Optical Superchannels based on Frequency Combs

As described in the previous sections, due to restrictions imposed by optical loss, non-linearities and finite amplifier bandwidths, there is a finite frequency bandwidth available for use in optical communication systems. Modern networks employ hundreds of lasers, each

²Inline amplification refers to how the optical signal can be amplified as it propagates through fibre (i.e, it can be amplified without the need for detection and re-transmission).

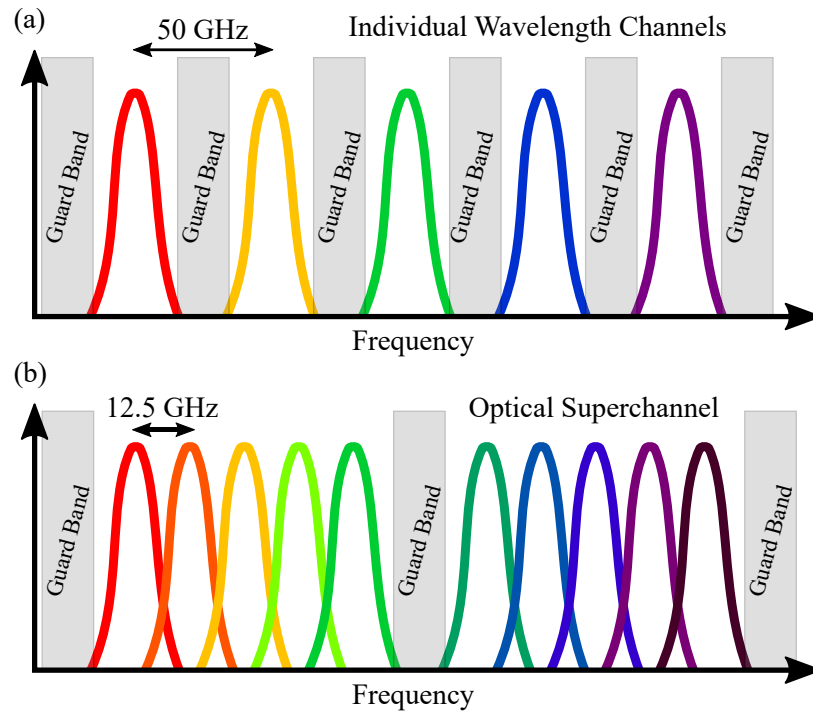


Figure 1.4: Illustration of WDM channels in frequency space. **(a)** Frequency channels generated using a bank of individual lasers. Large guard bands between the channels in frequency space are required to protect against crosstalk due to laser frequency jitter or otherwise. **(b)** Two separate optical superchannels generated with optical comb sources. As the subchannels within each superchannel all come from the same source, there are no longer guard bands required between the individual subchannels. Good comb sources can generate far more than 5 subchannels within each superchannel, further improving the spectral efficiency. Coherent transmission of comb superchannels with inter-channel spacings as low as 6.25 GHz have been demonstrated [22].

with its own fixed lasing frequency. Each channel in the network must have a distinct frequency, as otherwise crosstalk can cause the receivers to struggle to decipher the information imparted on the channels used. Further, due to instabilities in the lasing frequencies (often called frequency jitter), large guard bands³ are used to avoid catastrophic channel overlap. Figure 1.4(a) shows an illustration of WDM channels separated by a 50 GHz optical spacing, with guard bands between the individual channels. These guard bands occupy a significant portion of the available bandwidth, reducing the efficiency of the network.

Optical frequency combs can overcome the frequency jitter introduced by using separate lasers. An optical frequency comb features many different frequencies of light, each separated by some fixed spacing (different frequency comb sources are discussed later in Section 1.6). As the frequencies in a comb are all produced from the same source, the frequency jitter due to slight instabilities is common to all lines in the comb. Hence, the guard bands in between the frequencies generated by a comb can be removed, allowing the channels to be more closely spaced [8], [22]–[25] (see Fig. 1.4(b)). This greatly improves the spectral efficiency of the WDM system.

These tightly spaced channels are often grouped together and called an optical superchannel [26] – all subchannels within the superchannel must be transmitted and received together. The other main advantages to using optical combs in WDM networks are as follows:

³A guard band is an unused part of the frequency spectrum for the purpose of preventing interference.

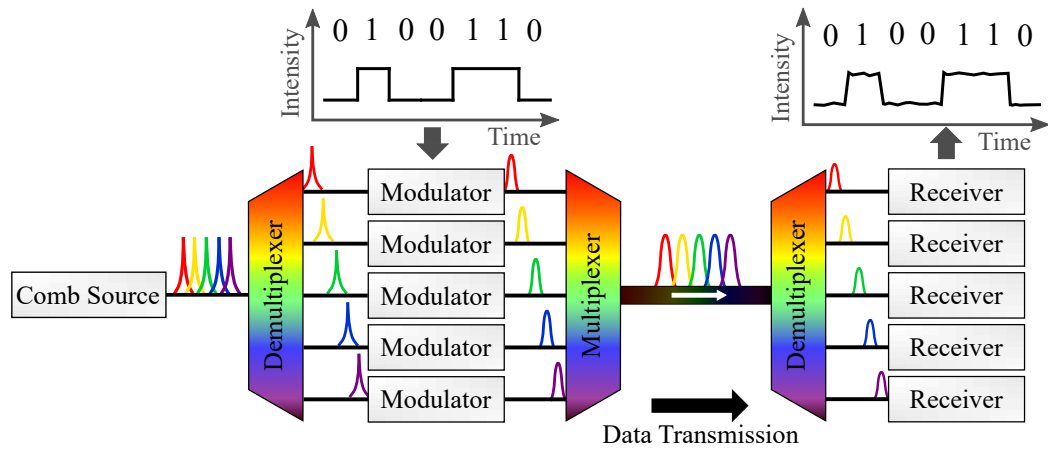


Figure 1.5: Illustration of a wavelength division multiplexing (WDM) system, which uses an optical comb source instead of individual lasers. The lines in the optical comb must first be demultiplexed in order to put data on each line in the comb. The rest of the WDM system can then operate as in Fig. 1.2.

- An optical frequency comb source provides many optical channels, reducing the number of components required in the WDM system. This in turn can reduce the energy consumption of the system [27].
- The digital signal processing on the receiver side can either be significantly simplified, or implemented with an increased phase-noise tolerance, as the phase from one transmitted comb line can be reused for the other lines in the network [28], [29].
- Pilot tones⁴ can be co-transmitted with the data, which can generate the local oscillators required for coherent WDM systems. Only two pilot tones are required to regenerate a local comb based phase locked oscillator [24], simplifying the data detection (phase locking will be described in more detail in Section 1.7).

Recent proposals have suggested changing the WDM network architecture from the standard configurations which use equally spaced channels to something more flexible. Flexible (or elastic) optical networks differ from the preceding rigid WDM networks, as they allow the optical bandwidth and modulation formats used throughout the network to be dynamically adjusted to meet changing network traffic [30], [31]. As a result, the power consumption of such networks can be efficiently managed, reducing the overall energy consumption. These flexible optical networks can be implemented using optical superchannels generated by coherent optical combs⁵ [23], [25], [32]. The channel spacing [33] and modulation formats can be varied from superchannel to superchannel, to optimise the baud rates used between different nodes in the network [34], [35]. The centre frequency of each superchannel could also be controlled using a similar method as discussed in Ref. [33].

Hence, optical comb based superchannels are good candidates for future communication networks. Network speeds to date have shown over 10 Tb/s transmission speeds [24], which shows promise that these networks will be able to deliver the transmission speeds required in the future.

⁴In telecommunications, a pilot tone is a signal, transmitted over a communications system for supervisory, control, equalization, continuity, synchronization, or reference purposes.

⁵Coherent optical combs have a fixed phase relation between their comb lines. More detail on optical combs is discussed in Section 1.6.

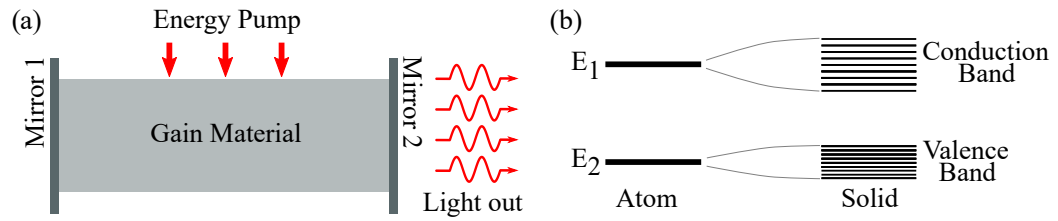


Figure 1.6: (a) Illustration of the components of a laser cavity. (b) Energy levels of atom splitting due to covalent bonding to form a solid. Electrical energy is plotted vertically.

Figure 1.5 shows how a WDM system with an optical comb source could be implemented. The key difference between Figs. 1.2 and 1.5 is the extra demultiplexing step which must take place before transmission. The demultiplexing methods used on the transmitter and receiver sides in Fig. 1.5 can be significantly different, and this thesis will focus on the demultiplexing which occurs on the transmitter side of the WDM network. Comb sources will be discussed in more detail in Section 1.6, and optical demultiplexing is then discussed in Section 1.8.

1.2 The Fundamentals of a Laser

Lasers are devices that create coherent radiation at infra-red, visible, or ultraviolet frequencies, due to the stimulated emission of electromagnetic radiation. The word laser is an acronym for “Light Amplification by Stimulated Emission of Radiation”. Lasers typically emit a very narrow spectrum of light, and have a very long list of applications, from the welding and cutting of materials, to barcode scanners and optical disk drives.

A simplified schematic of a laser is shown in Fig. 1.6(a). There are three main components in any laser:

- A gain medium.
- An energy pump (either electrical or optical).
- An optical cavity or resonator to provide feedback.

The gain medium is some material which usually absorbs specific frequencies of radiation. In particular, it requires specific energy transitions to be possible in the atoms of the material (more detail on the characteristics of the material is given in the following Subsection 1.2.1). Since their first demonstration in a ruby laser [36], lasers have been made using gases, solids, liquids, and plasmas as the gain material. If the material used as the gain medium is pumped (either optically or electrically), electrons within the material can be excited to higher non-equilibrium energy levels. There are several processes in which these electrons can return to their equilibrium state, but the processes are in general classified as radiative and non-radiative emission. Radiative and non-radiative recombination in semiconductors is described in Sections 1.3 and 1.4.

1.2.1 Energy Levels in Solids and Semiconductors

In a single atom, there are discrete allowed energy states which electrons can occupy. However, when more than one atom is brought together, the energy levels available to energetic electrons can split and broaden. In gas and solid state lasers, the energy levels of the active atoms which

are used to emit light are only slightly perturbed by the surrounding gas or solid host atoms. In a covalently bonded solid like a semiconductor however, the energy states broaden into bands.

To picture this, consider what happens to two identical atoms as they create a covalent bond together. When the bond is formed, the outer valence electron of one of the atoms can arrange itself to form a low-energy bonding (symmetric) charge distribution or a high-energy anti-bonding (antisymmetric) distribution. Hence, the discrete energy level that the electrons occupied has been split into two energy levels, corresponding to the bonding and antibonding states, due to the two ways the electron can arrange itself around the atom. If a third atom is brought close to the first two, a new charge distribution that is neither completely bonding or anti-bonding is possible, creating a third energy level. Hence, as N atoms are brought close together, N energy levels distributed between the lowest energy bonding state and the highest energy level antibonding state are created. The transition from a single atom to a solid is shown in Fig. 1.6(b), and as can be seen in the case of the solid, bands of energy levels are created. The valence band is defined to be the collection of bands which are filled at absolute zero temperature. The conduction band is defined as the bands which are completely empty at zero temperature. At temperatures greater than zero, the electrons inside in the material have sufficient energy to occupy some of the energy levels inside the conduction band, due to Fermi statistics. When an electron leaves the valence band to occupy a higher energy level, it leaves behind a hole in the valence band. The term hole simply implies 'the absence of an electron', however it will be useful to refer to holes as if they are themselves particles.

A material is said to have a direct band gap if the minimal energy state in the conduction band and the maximal energy state of the valence band occur at the same value of electron momentum. Direct band gap materials are very good at generating electromagnetic radiation, as the electron does not require a large change in its momentum in order to relax to the lower level energy state in the valence band. Examples of direct band gap materials include gallium arsenide (GaAs) or indium phosphide (InP). An indirect band occurs when the minimal energy state in the conduction band and the maximal energy state of the valence band occur at different values of electron momentum. In an indirect band gap material, electrons in the lower energy states of the conduction band (i.e, the highly populated states) require a large change in momentum in order to recombine and emit a photon (this is possible, but is much more unlikely to occur than in the direct band gap case). Examples of indirect band gap materials are crystalline silicon and germanium.

The number of free electrons and holes available can be altered by intentionally introducing impurities to the semiconductor material. p-type semiconductors are semiconductors with a larger hole concentration than electron concentration, and likewise n-type semiconductors are semiconductors with a larger electron concentration than hole concentration.

In the case of semiconductor lasers, the primary region of interest is the area where the electrons in the conduction band and the holes in valence band interact with one another. Semiconductor lasers are formed by putting an undoped (or intrinsic) semiconductor in between p-type and n-type semiconductors, creating a p-i-n junction. These junctions are semiconductor diodes, and allow the free holes in the p-type and the free electrons in the n-type to flow toward one another and meet in the intrinsic region, when a bias is applied in the correct

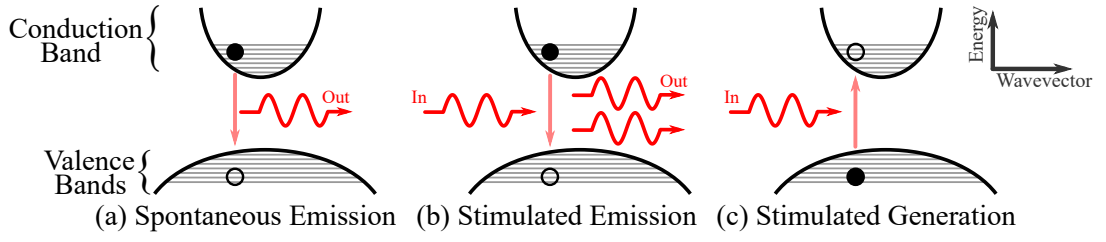


Figure 1.7: Illustration of the (a) spontaneous emission, (b) stimulated emission and (c) stimulated generation processes between the conduction band and the valence band. Electrons and holes are represented by filled circles and empty circles respectively, and photons are depicted in red. The horizontal lines indicate the different allowed energy states. Although it appears in the illustration that many different transitions are possible, each transition must conserve momentum (which is related to the wavevector k by momentum $= \hbar k$).

direction across the junction.

Hence, semiconductor diodes can be electrically pumped in order to provide light. Other lasers (such as gas lasers or some solid state lasers) can instead be optically pumped. In these cases, an electromagnetic radiation at a different frequency than the lasing frequency can be used to excite the electrons within the atoms to higher energy states, and as those atoms relax, they release photons. Sometimes, electrons can relax through 2 or 3 different energy states before returning to the ground state, only emitting a photon in one of those transitions [37].

1.3 Radiative Recombination and Stimulated Generation

In this section, the interactions involving photons that can occur between the electrons in the conduction band and the holes in the valence band are discussed. Recombination is the term used to describe when an electron of energy E_2 drops down from the conduction band, and fills a hole of energy E_1 in the valence band. Similarly, the term generation is given to the processes that cause electrons to leave the valence band for the conduction band, leaving a hole in the valence band. Recombination processes that involve photons are called radiative recombination processes, whereas processes that don't involve photons are called non-radiative processes. There are three optical processes that occur, each briefly described below. Non-radiative recombination processes are described in Section 1.4.

1.3.1 Spontaneous Recombination

Spontaneous recombination occurs when an electron of energy E_2 spontaneously drops from the higher energy conduction band to the lower energy valence band, recombining with a hole of energy E_1 . The change in energy due to this recombination creates a photon of energy:

$$E_{21} = E_2 - E_1 = \frac{hc}{\lambda}, \quad (1.1)$$

where h is Planck's constant, c is the speed of light, and λ is the wavelength at which the photon was created. This process is illustrated in Fig. 1.7(a). This photon has random orientation and phase, and hence spontaneous emission does not contribute significantly to the coherent emission of the laser once lasing has begun. The above equation also illustrates why lasers

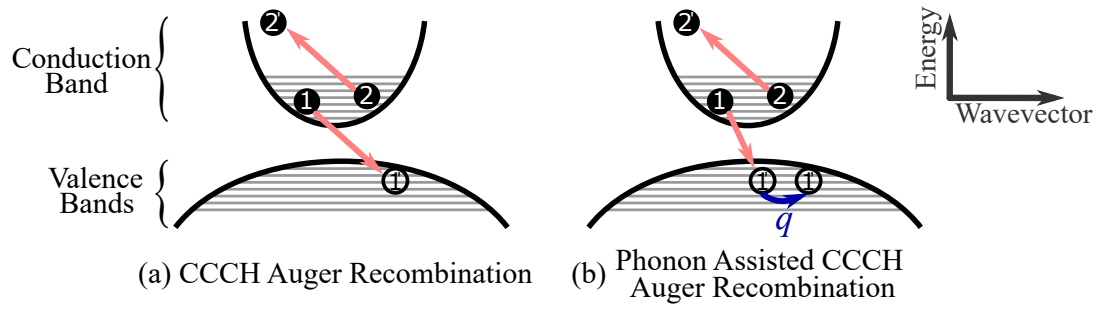


Figure 1.8: (a) Illustration of one of the Auger nonradiative recombination processes (in particular, the process illustrated is often called the CCCH recombination process). The naming convention of Auger recombination process uses letters to denote the carriers involved – in this case, C stands for conduction band, and H stands for heavy-hole. (b) An example of phonon assisted nonradiative recombination. The phonon q (in blue) interacts with a hole, conserving the total momentum of the transition.

and LEDs only emit over a small range of wavelengths; only certain energy transitions are possible between the conduction band and valence band, and additionally, some are much more probable than others.

1.3.2 Stimulated Emission

Stimulated emission occurs when a photon perturbs an electron in the conduction band, causing it to recombine with a hole in the valence band. Displayed in Fig. 1.7(b), this results in another photon being emitted with the same phase and direction as the incident photon. Hence, stimulated emission is the all important phenomenon which causes optical amplification (i.e, optical gain) in semiconductor lasers. As long as there is a sufficient number of electrons (or carriers) in the higher energy levels, an incoming photon can result in the creation of multiple new photons as it passes through the material.

1.3.3 Stimulated Generation

In the case of stimulated generation, an incident photon is absorbed by an electron in the valence band. The energy of the photon is used to promote the electron from the valence band to a higher energy level in the conduction band, leaving a hole in the valence band, as shown in Fig. 1.7(c).

1.4 Non-radiative Recombination

There are many recombination processes possible which do not involve the absorption or emission of photons, and these transitions are called non-radiative recombination processes. Non-radiative recombination ultimately decreases the efficiency of a laser, and hence minimizing non-radiative recombination is key to making efficient devices.

Three such examples of non-radiative recombination are surface recombination, defect recombination and Auger recombination, and each will be discussed briefly in this section. For a more in-depth discussion and a mathematical approach to non-radiative recombination, the topic is presented well in Ref. [38].

1.4.1 Auger Recombination

The basis of the Auger recombination effect is the Coulomb interaction between two carriers. Auger recombination occurs when one carrier perturbs another, and initiates recombination. There are two classifications of Auger recombination, band-to-band and phonon-assisted Auger recombination [39].

1. **Band-to-Band Auger Recombination.** Band-to-band Auger recombination occurs when one carrier perturbs another, causing an electron to drop from the conduction band to the valence band. The excess energy produced by the change in energy of the electron is transmitted to other carriers in the material. Many possible Auger processes exist; only two such examples are given here. A band-to-band Auger recombination process (referred to as CHCC) is illustrated in Fig. 1.8(a). In this example, electron 1 perturbs electron 2, causing electron 2 to recombine with a hole in the valence band. The energy released due to the recombination of electron 2 is then transferred to electron 1, causing electron 1 to be excited to a higher energy level. Over time, electron 1 can dissipate its energy in the form of lattice vibrations, and lower its energy level back to its initial state. Note that the total wavevector of the process must be conserved. Other examples of band-to-band Auger recombination can be found in Refs. [38], [39].
2. **Phonon-Assisted Auger Recombination.** A phonon is the quantization of lattice vibrations inside of a solid. Phonon-assisted Auger recombination involves a phonon interacting with one of the carriers (either an electron or a hole) in order to allow the recombination process occur. As displayed in Fig. 1.8(b), the phonon contributes to the total momentum of the transition, which in turn relaxes some of the energy and momentum conservation requirements for the process. Phonon-assisted Auger recombination is less likely to occur than band-to-band Auger recombination, as it involves an extra particle. As temperature increases, so do lattice vibrations, and hence the chance of phonon-assisted Auger recombination increases as the temperature of the material increases.

Auger-recombination processes are characterised by their strong temperature and band-gap dependence; these dependencies arise from the laws of energy and momentum conservation that the electrons and holes involved must obey.

1.4.2 Surface and Defect Recombination

Non-radiative recombination can also occur on surfaces and at defects in semiconductor materials. A defect in a semiconductor laser can occur during the growth of the material, or during the fabrication of the device. Further defects occur if the atomic distances between the atoms in the different materials used in the device are not carefully matched. Defects produce a continuum of states in a localized region, and electrons or holes within a diffusion length from the edge of a defect can recombine non-radiatively [38].

Surface recombination occurs in devices as some of the surfaces of the semiconductor are exposed to the surrounding materials of the device. The atoms of the semiconductor material on the surface of the device can have dangling bonds, which allow further non-radiative recombination.

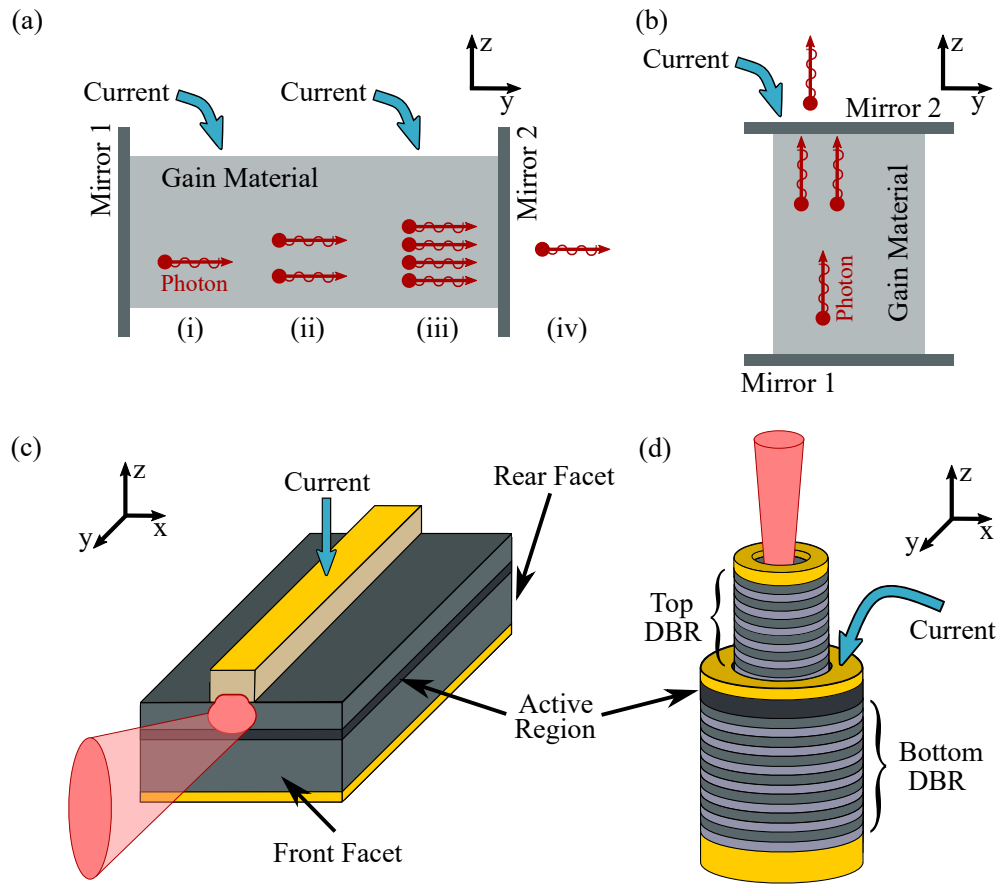


Figure 1.9: (a) Simplified illustration of a transverse Fabry-Pérot laser cavity. As the laser is electrically pumped, photons within the cavity can undergo stimulated emission, (shown as time progresses from point (i) to point (iii)). The laser's emission then is transmitted through one of the cavity's mirrors (point (iv)). (b) Simplified illustration of a vertical Fabry-Pérot laser cavity. (c) Illustration of an edge emitting laser diode. Current is pumped through the waveguide on top, which flows through the active region in the laser, generating light. Feedback is provided by the two device facets. (d) Illustration of a vertical cavity laser diode. Current is pumped through the active region of the device to generate light. Feedback within the cavity is provided by distributed Bragg gratings (DBRs) above and below the active region. Light is emitted from the surface of the laser.

1.5 Semiconductor Lasers and Photonic Integration

Semiconductor diode lasers have become common place in everyday life - in particular, they make up the backbone of telecommunication networks, as they provide the light used to transmit data. Lasers typically emit a very narrow spectrum of light in comparison to other light sources. As well as having better efficiencies than other solid state and gas lasers, the high reliability, small size and relatively low cost of semiconductor lasers make them ideal for use in optical communications.

As discussed in Section 1.2, semiconductor lasers are formed by joining p-type, intrinsic, and n-type semiconductors together, creating a junction which produces light if electrically pumped. If these semiconductor junctions are placed between two reflective mirrors with sufficient feedback, a photon created within the material can pass through the laser cavity multiple times, and create more photons through stimulated emission (see Fig. 1.9(a)). The simplest type of optical cavity is a Fabry-Pérot cavity, which consists of two broadband reflec-

tive surfaces on either side of the semiconductor material. As the optical gain within modern semiconductor substrates is high, a simple cleave of the material can suffice as a mirror.

There are two main types of semiconductor lasers; edge emitting and vertical cavity lasers. Edge emitting laser diodes were created first, and as shown in Fig. 1.9(c), light propagates horizontally as the gain medium is pumped with electrons. The laser's emission comes from a facet of the device. The light is guided within a waveguide⁶, which is typically defined by removing semiconductor material⁷, leaving behind a narrow ridge of material. The narrow ridge on top of the semiconductor material in Fig. 1.9(c) is what a ridge waveguide looks like in an edge emitting device. Waveguides can be "active" or "passive"; an active waveguide needs to be electrically pumped in order to generate light (or, needs to be pumped in order to have low optical loss). Passive waveguides cannot generate light and hence do not need to be electrically pumped, but have very low loss.

In contrast to edge emitting lasers, vertical cavity lasers emit from the surface of the material from which they are made (Fig. 1.9(d)). Typically in vertical cavity lasers, many layers with slightly different refractive indices are grown around the active layer in the device, creating strong optical feedback. Although edge emitting devices produce higher optical power, vertical cavity devices are much more energy efficient.

Edge emitting lasers naturally lend themselves to photonic circuit design, as each component in the photonic circuit can be connected via horizontal waveguides. Hence, light can flow without interruption or any discontinuity, remaining within a waveguide on the entire photonic circuit. On the other hand, vertical cavity lasers are very difficult to incorporate in a large photonic circuit, as they emit the light vertically into the air. The light would need to be re-coupled (either back into a waveguide on the same substrate, or possibly into a different photonic element), which adds significant complexity. Vertical cavity lasers can however be integrated into 2 dimensional arrays for high power output [40], or other applications (such as facial recognition [41]). As this thesis focuses on technologies which can be easily integrated onto a photonic circuit, all further discussion in this thesis is focused on edge emitting devices.

1.5.1 An Overview of Photonic Integration

Electronic integrated circuits were first demonstrated in 1958 [42], and their importance was quickly realised. Jack Kilby was awarded the nobel prize in physics for "for his part in the invention of the integrated circuit" in the year 2000. Since 1958, engineers and physicists have jointly focused on understanding the science of the materials involved, in order to integrate more and more components onto the same substrate. This focus on integration prompted the size of electronic components to shrink, so much so that the length of modern CPU and GPU transistors⁸ can be measured by their number of atoms (around 70 silicon atoms or so). The drive behind this integration has been to increase speed, and to reduce cost, size and packaging⁹.

⁶A waveguide is a structure that guides electromagnetic waves, restricting the propagation of the electromagnetic signal to one dimension.

⁷The controlled removal of semiconductor material is called an etch.

⁸A transistor is a basic electrical component that alters the flow of electrical current. Transistors are the building blocks of electrical integrated circuits, such as computer processors.

⁹Electronic packaging refers to enclosures for integrated circuits, passive devices and circuit cards. Photonics packaging involves a similar same process in concept.

The same motivation applies in most photonics platforms – photonic integrated circuits (PICs) allow the integration of multiple photonic components onto a single chip, and can reduce production costs, energy consumption and total device size, while making packaging devices simpler. As packaging is often the most expensive part of producing photonic circuits and devices, simplifying the packaging process is sufficient cause alone. WDM systems require many different functional components, from tunable laser sources to modulators and optical filters, and hence integrating these components on a single circuit is challenging. In general, photonic devices use a larger range of materials than standard complementary metal oxide semiconductor (CMOS) processing, and as a result it has taken many years for the industry to begin to become standardised. In recent years, companies such as SMART Photonics [43] have started to offer multi-project wafer runs, allowing multiple projects to all be apart of the same fabrication run, which will hopefully begin the standardisation that electronics saw decades ago. For the moment, different research groups and companies each have their own methods of integrating several devices on a single chip (and sometimes these methods are unique to the fabricators creating the devices). The following sections give an insight into the different types of photonic integration that have been considered over the years.

1.5.2 Hybrid and Heterogeneous Integration

Hybrid and heterogeneous integration techniques refer to processes which involve integrating devices made on different types of material substrates together onto a final common substrate [44]. Typically, each component of the PIC is fabricated and processed separately, before being combined to make the final circuit. The natural advantage this method has in comparison with others is the ability to choose the best materials possible for each component in the circuit. This often still requires a compromise of device operation to be able to integrate each piece successfully, as losses occur at the transitions between components.

Silicon photonics is one such example of hybrid integration, and has become a recent hot topic which “is a disruptive technology that is poised to revolutionize a number of application areas” [45]. As silicon has been extensively researched over the last century and CMOS fabrication tools have reached such a high standard, high resolution photonic circuits can be fabricated at low cost [46], [47]. Silicon waveguides are passive (i.e, the waveguides do not need to be electrically pumped) and have very low loss [48], and due to the refractive index difference between silicon waveguides and the SiO₂ cladding used, waveguides which guide 1.55 μm light are smaller in silicon than in other active materials, which shrinks device size. Further, electronic circuits can almost seamlessly be integrated with silicon photonic circuits, which adds to the functionality of devices. The biggest and most fundamental drawback to using silicon is that silicon cannot produce light due to it’s indirect bandgap. As a result, light generation must happen in separate material, and then be coupled to the silicon photonic circuit. One such technique to integrate a photonic device within a silicon electronic circuit is to flip a pre-processed photonic device over, and bond it upside down to the silicon circuit [49], [50]. This process is slightly complicated, and requires good alignment in order to avoid large optical losses. Moreover, heat sinking of the active device must be accounted for and considered in all designs, as thermal effects degradate the operation of common semiconductor lasers.

A more recent innovation for integrating active material on passive circuits is a process called

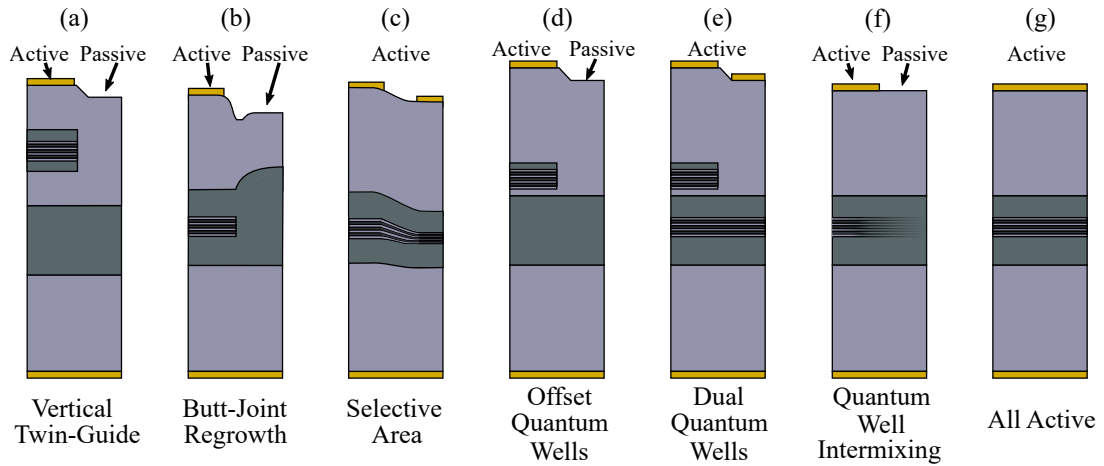


Figure 1.10: A cross section view of semiconductor wafers used in different photonic integration techniques. Active regions have high optical loss, and need to be pumped electrically in order to be transparent or provide optical amplification. These sections are required to make a laser. Passive material has relatively low optical loss, and among other things, can be used for transporting light across large distances on a PIC. As the photonic integration industry has not been standardised, there are still many different approaches to try and complete full photonic circuits on a single substrate.

micro transfer printing [51]–[53]. This involves fabricating the active devices on their native substrates, and including steps to etch away a release layer below the undersides of the devices, leaving narrow tethers which hold the devices in place. The devices can then be picked up and “printed” on the target passive wafer. An advantage with this technique is that large arrays of devices can be printed simultaneously with relative ease. However, devices can still suffer from poor thermal performance among other challenges.

There are many more hybrid integration examples; wafer bonding removes issues with device misalignment [54], as a silicon wafer is bonded to a wafer of active material prior to processing, creating a hybrid wafer. The hybrid wafer can then be processed in the same fabrication run, allowing the active and passive waveguides to be aligned. Other groups are trying to grow active material on silicon [55], to circumnavigate the natural indirect band gap of silicon. Many quantum dot devices have been successfully grown on silicon [56], [57], however due to the relatively large defect densities, conventional ridge quantum well devices have not yet been realised.

Finally, there is another class of hybrid devices which rely on gratings to couple light to and from the passive silicon waveguides. By using sub-wavelength gratings, reasonable coupling efficiencies can be achieved between standard single mode fibres and passive silicon waveguides [58]. These gratings avoid the need for spot size converters¹⁰, which are required in almost all types of hybrid integration to convert the mode supported in the active material to a mode supported in the passive material’s waveguides. This transfers the dependence on alignment during the fabrication process to the packaging process instead.

The examples listed above are not intended to be exhaustive, and the list is instead intended to give an idea of the many different approaches which have tried to find an integration platform that both has high performance and makes economic sense.

¹⁰Spot size converters are intermediate sections used to improve the coupling efficiency between the device’s waveguide and a fibre.

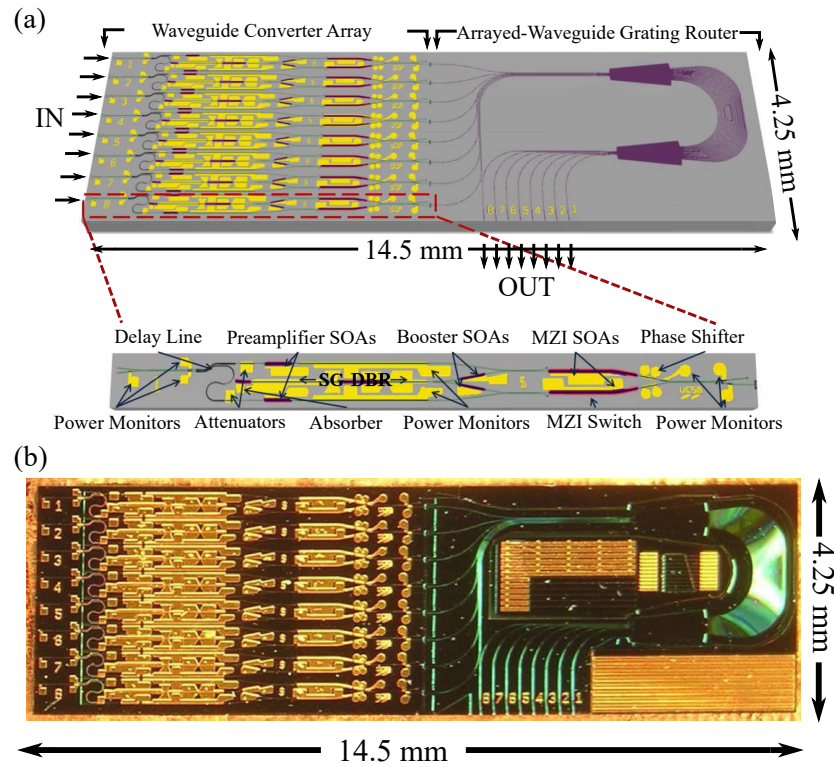


Figure 1.11: Large scale photonic integrated circuit from Ref. [60], which is a demonstration of how active and passive regions can be integrated side-by-side. Active regions have gold contacts, where current can be sourced into the material. The waveguides in the arrayed-waveguide grating router are passive. **(a)** Device design and **(b)** microscope image of the fabricated device, with test structures in the centre of the arrayed-waveguide grating router.

1.5.3 Monolithic Integration

Monolithic integration is the simplest conceptually of the approaches to photonic integration, as all the devices are made on the same substrate during a single fabrication process. As there isn't method of growing a substrate capable of providing all the possible functions that could be required on a circuit, often other materials are grown on top of the substrate during the fabrication process, in order to facilitate specific functions [59]. Different types of monolithic integration are depicted in Fig. 1.10, and examples (a) through (e) involve growing material during the fabrication process. This regrowth process which adds material on top of the substrate is time consuming, and makes carrying out device fabrication costly and complicated. However, excellent device results can be achieved using high resolution fabrication in combination with material regrowth.

Distributed feedback lasers (DFBs) are some of the most successful commercial semiconductor lasers as they have narrow linewidth, strong single wavelength emission, and high output power [61]. DFBs can be easily integrated with other components on a photonic circuit, such as integrated electro-absorption modulators [62], [63]. However the reflectors used in DFBs typically require many regrowth steps (although there are examples in the literature where this is not the case [64], [65]). Distributed Bragg reflector (DBR) based lasers also work well [66], and while simpler, DBRs have many of the same drawbacks. Many more significantly larger monolithic photonic circuits have also been implemented using regrowth, such as the tunable optical router shown in Fig. 1.11 [60], or integrated circuits capable of data transmission [67].

There are alternatives to using expensive and time consuming material regrowth processes. Figure 1.10(f) illustrates a process called quantum well intermixing (QWI) – no material is added or removed from the passive section of the waveguides with QWI [68]. Instead, the quantum wells within the substrate are altered as atoms from the wells and their corresponding barriers interdiffuse, and the centre wavelengths of emission and absorption are shifted far from those of the active areas (through ion bombardment [69], the introduction of impurities [68] or impurity-free vacancy diffusion [70]). In this way, light can be generated in the active regions, and should see very little absorption in the intermixed passive regions. As demonstrated in Ref. [67], QWI can be very effective, and can eliminate any design restrictions required in regrowth integration schemes [71].

In this project, a regrowth-free, QWI-free, approach was considered. As mentioned, this greatly reduces the length of time and cost involved with fabrication, yet it also introduces some design constraints, as in particular passive waveguides are not possible. This regrowth-free monolithic approach is worthwhile investigating however, as often elegant and impressively engineered solutions don't see commercial success, if simpler more cost effective with slightly worse performance methods are available [72]. The following subsection introduces the types of regrowth-free lasers developed to be fabricated using standard contact lithography and be monolithically integrable. These devices are used in parts of this project.

1.5.4 Regrowth Free Monolithically Integrable Semiconductor Lasers

Much research has been carried out to find alternatives to the expensive DFB and DBR based lasers mentioned previously. The goal is to find a semiconductor laser which is free from regrowth steps and that uses standard contact UV lithography.

Slotted Fabry-Pérot lasers (SFPs) [73]–[76] are one such example, which use slots etched into the ridge of the waveguide to provide feedback and mode selectivity (see Fig. 1.12(a) for an example of a slot etched into a waveguide). These slots have good reflectivity and reasonably low loss, and several etched slots with regular (or irregular) spacing can create enough reflectivity to replace cleaved facets¹¹ [77]. Slotted devices with reasonably simple mirror sections have been demonstrated with both high side-mode suppression ratios and low linewidth. Many examples in the literature also discuss how the lasing wavelengths of devices can be controlled using different sections separated by slots [78], or different slot spacings in the mirror sections of the devices [75], [79].

One issue with SFP devices is that the slots which provide the wavelength selectivity of the laser are etch depth dependent [80], [81]. As a result, etch stop layers are required to accurately control the reflectivity of the slots, and the anisotropy of chemical etches [82] can lead to different results across a wafer. Hence, recent alternative reflectors have been developed [81], [83]. In particular, etch depth insensitive pit perturbations [81] etched into the waveguide of a laser were used in place of slots for some of the devices used during this work (see Fig. 1.12(b) for an example of a pit perturbation etched into a waveguide). Devices with high side mode suppression ratio (SMSR) (> 37 dB) and low linewidth have been previously demonstrated using 30 pits in an integrated DBR like mirror [84]. Unlike the slotted lasers, the side wall roughness and etch depth of the pit perturbations used aren't as integral to the device's

¹¹A cleaved facet is a flat face in the material that is made by cutting through the semiconductor material.

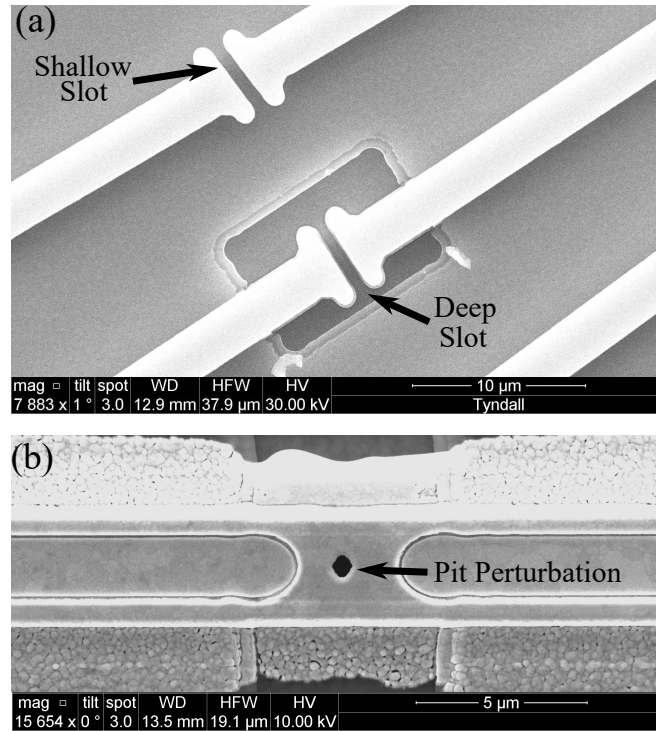


Figure 1.12: Top down scanning electron microscope images of (a) a shallow etched slot (top) and a deep etched slot (bottom) and (b) a pit perturbation etched into the waveguide of different devices. Pit perturbations and slots provide reflection within the laser cavity, and are used to ensure only one longitudinal mode in the cavity resonates, creating a single mode laser.

operation, as the deeply etched pits are used as local perturbations in the laser's waveguide. During this project, devices were designed using an inverse scattering method [85]–[87], and these single mode devices were used in some of the experiments presented in Chapters 3 and 4. A full description of the inverse scattering pit devices is contained in Appendix A.

1.6 Optical Combs

An optical frequency comb source is a laser source which contains multiple discrete frequencies, equally spaced at some set interval (as depicted in Fig. 1.13), and with a strong phase correlation between the frequencies in the comb. In general throughout this thesis, frequency combs will be characterised by the frequency spacing between their comb lines, and their optical power (which indicates the power in the full comb, not just the peak power of the individual lines).

In recent years, optical frequency combs have seen increasing attention. When it was shown that optical frequency combs could enable the most accurate atomic clocks to date¹², optical combs took the scientific spotlight [94], [95]. The applications of optical frequency combs are continuing to grow. Frequency comb spectroscopy uses optical combs to inspect the composi-

¹²Modern optical atomic clocks have incredible accuracy [91]. If such an optical clock was initialised during the big bang, it would have lost less than a second over the 13.77 billion years to this point. These clocks are so accurate, that they can observe general relativistic effects on laboratory tabletops, as demonstrated when one clock was raised a couple of *centimetres* higher than another [92], [93].

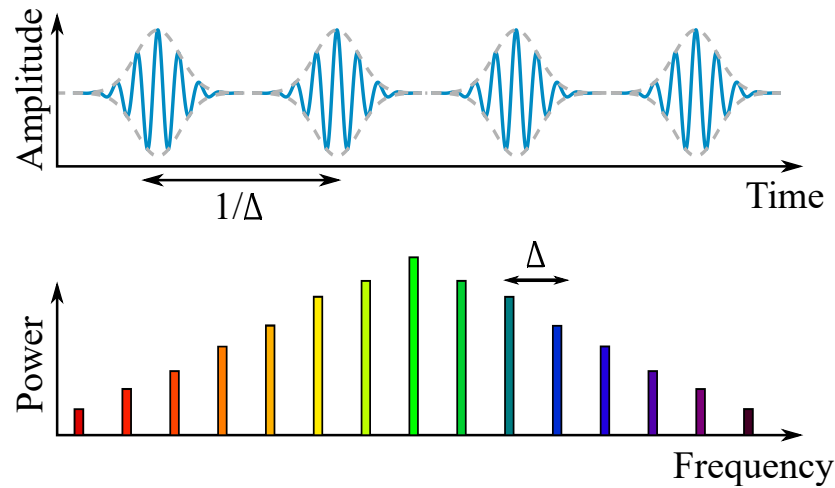


Figure 1.13: Illustration of an optical frequency comb. **(a)** In the time domain, an optical frequency comb looks like a series of optical pulses. If the output comb spacing is Δ , these pulses are separated by $1/\Delta$. For example, a frequency comb with an optical spacing of 10 GHz has a pulse period of 1×10^{-10} s. **(b)** In the frequency domain, the optical comb looks like a set of discrete frequencies, each one equally spaced from its neighbours (in this case, the lines in the comb are separated by the comb spacing Δ). In the recent review article by Fortier and Baumann [88], a detailed comparison of optical combs is presented, where they give examples of optical combs with frequency spacings from 27.56 MHz [89] to 375 GHz [90].

tion of samples [96]. These combs can be used in many radio frequency (RF) applications too, such as RF arbitrary waveform generation [97], [98]. Combs have even been used to create optical arbitrary waveform generators [98], [99]. In this thesis however, we focus on optical combs for communications.

There are multiple ways to generate a frequency comb, some of which have been successfully integrated on a photonic circuit. Mode locking is one such technique, which involves introducing a fixed phase relation between the longitudinal modes in a laser. The fixed phase relation allows constructive interference to occur, producing pulses of light. There are now many examples of integrated mode locked lasers on both InP and heterogeneous platforms (see Ref. [100] for a review). Impressive optical combs have also been generated using the nonlinear Kerr effect [90], [101]–[103]. These combs use the nonlinear coupling of resonant modes in ultra high Q resonators [104] to generate combs spanning large frequency ranges. However, these combs require strong (external) optical pumps and low loss passive materials. While Kerr-effect optical combs have been demonstrated in silicon on insulator platforms, we are particularly interested in optical comb sources which can be monolithically integrated on an InP photonic circuit.

As such, gain switched optical combs are good candidates [105]–[107], as they can be implemented using relatively straightforward device designs and can be integrated onto InP PICs [108]–[110]. Gain switching is a technique in which a section of a semiconductor laser is modulated using a large amplitude RF signal [111], [112]. By applying a sinusoidal voltage, the carrier density in the laser can be forced to oscillate above and below the threshold density¹³, which in effect turns the laser on and off rapidly, creating a series of optical pulses. As shown

¹³A laser's threshold density is the carrier density at which there is sufficient gain in the laser to overcome all cavity losses. In experiment, it is much easier to refer to the threshold current of the device, which has essentially the equivalent meaning.

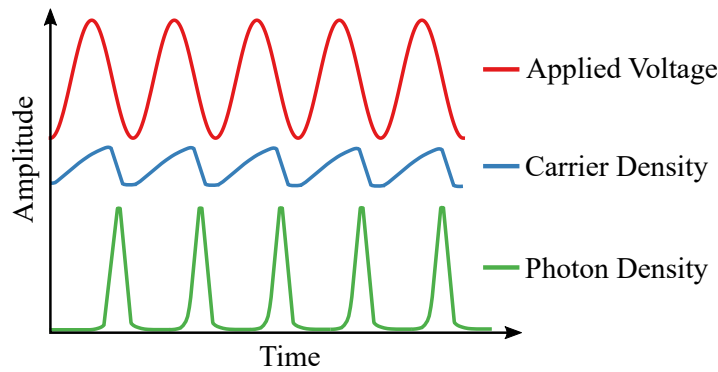


Figure 1.14: Illustration of the RF bias, carriers and optical signal in a gain switched laser.

in Fig. 1.14, the carriers in the laser undergo a delayed response to the sinusoidal bias applied, as the carriers in the semiconductor laser cannot respond instantaneously to the applied current. Hence, the photon population also does not instantaneously materialise, beginning to grow only after the threshold carrier density has been achieved. The delay in the generation of photons is favourable, as it means that the optical pulse widths are typically much shorter than the applied RF-period.

As discussed above in Section 1.1.3, optical combs are very attractive for use in optical communication systems, as all comb frequency lines share common frequency drift. Hence, the guard bands on either side of each channel can be reduced (or removed completely). Additionally, a single comb source can replace an array of lasers, reducing the total cost and energy consumption of a WDM transmitter. However, to use optical combs on an integrated platform for optical communications, each comb line must be demultiplexed, modulated, and then re-combined all on the same photonic circuit before transmission. In Section 1.8, different types of integrated optical demultiplexers are discussed, and the reasons for selecting the type of optical demultiplexer studied in this project are outlined.

1.7 Optical Injection Locking

Before discussing the type of integrated optical demultiplexer studied later in this thesis, optical injection locking must be first introduced.

In general, the injection of a periodic signal into any type of oscillator can lead to interesting types of dynamics. For example, if the injected signal is strong enough and close enough to the oscillator's natural frequency, the oscillator's frequency and phase will transition from its free-running values, to match the frequency and phase of the injected signal. In this case we call the oscillator phase locked to the driving signal. This was originally discovered by Dutch scientist Christiaan Huygens, as he noticed two pendulum clocks in his room synchronised if they were hung close enough to one another [113]. For a while, it was even believed that human sleep patterns were locked to earth's natural 24 hour cycle, as it was claimed that in isolation humans prefer 25 hour wake-sleep cycles (however further studies into these claims has shown this is likely false [114]).

Optical injection locking is just one example of injection locking, which involves injecting a

master laser's signal into a slave laser. In particular, we will deal with the case where light from the slave laser does not interact with the master laser in any way. The terms master and slave now appear slightly outdated in 21st century language, however as these are very common place in current literature, they will also be used throughout this thesis.

Some injection locked systems can be described by using Adler's equation [115]:

$$\frac{d}{dt}\phi(t) = -\nu - K \sin(\phi(t)) \quad (1.2)$$

where ϕ is the relative phase difference between the oscillator and driving force, ν is the frequency detuning between the injected signal and the oscillator's fundamental frequency, and K is the driving strength. To derive some physical meaning from the above, consider an oscillator with signal $A_0 e^{i(\omega_0 + \phi_0(t))}$ that is injected by an external signal $A_{inj} e^{i(\omega_{inj} + \phi_{inj}(t))}$. Here, A_j denotes the amplitude of the signal, ω_j denotes the frequency, and ϕ_j denotes the phase of each signal. Equation 1.2 then gives the rate of change of the phase difference between the two oscillators, as measured from the reference frame of the master oscillator. The first term on the right hand side of Eq. 1.2 describes how the difference between the frequencies ω_{inj} and ω_0 adds to the total phase difference between the oscillators (where $\nu = \omega_{inj} - \omega_0$). The second term describes how the magnitude of the external force effects the phase of oscillator under injection, and in general K is proportional to the ratio A_{inj}/A_0 .

Equation 1.2 assumes that the amplitude of oscillations is constant, and can be used to find the regions where the slave is stably locked to the master. By looking at the steady state solution of Eq. 1.2, the slave is phase locked when $|\nu/K| \leq 1$. While the slave oscillator is phase locked, the phase of the slave oscillator directly matches that of the master oscillator. This can remain true for a bandwidth of frequencies around the slave oscillator's natural frequency (i.e, a range of detunings around the slave's frequency). The locking bandwidth of the slave in this case is given by $2K$. While the slave oscillator is phase locked, it's frequency also perfectly matches that of the master oscillator (hence, the slave is also frequency locked to the master).

Adler's equation describes the low injection limit of optically injected semiconductor lasers very well [116], [117], but as the injection strength increases, additional amplitude dynamics must be introduced. With real master-slave semiconductor laser systems, there is no longer a simple binary transition between phase/frequency locked states and unlocked states. Rather, there exists a third state, where at certain detunings and injection strengths, the slave's frequency can be locked, while the phase difference between the master and slave varies in time. In this case, the slave is frequency locked, and not phase locked [118]. The reverse is never possible – it is impossible for a slave laser to be phase locked and not frequency locked. This is discussed in more detail in Section 3.2.1.

Optical injection locking has been used in many applications, such as increasing laser modulation bandwidths [119], [120], reducing laser linewidth [121]–[123], improving optical comb generation [124], [125], and radio frequency (RF) signal generation [126], [127]. As an example, Fig. 1.15 shows the free-running and injection locked optical spectra of a Fabry-Pérot (FP) slave laser. The free-running laser spectrum (in blue) has many lasing modes, as the device used was a simple FP cavity. The response of the FP laser to an optically injected signal of power +1.7 dBm is plotted in red. All the modes in the slave laser except for the injected mode

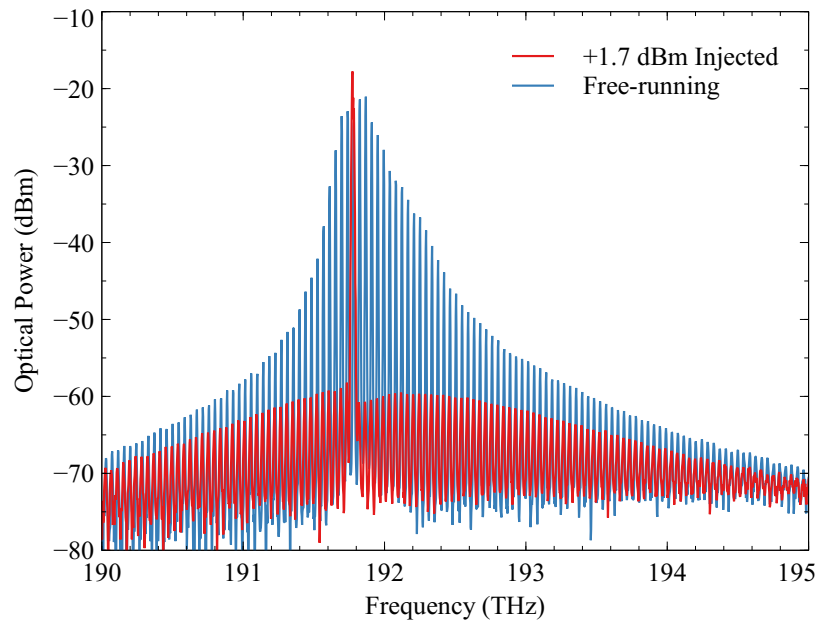


Figure 1.15: Comparison between optically injected and free running laser spectra. The slave laser was a 1050 μm long Fabry-Pérot laser, biased at 60 mA with coupled output power +2.4 dBm. Plotted in red is the output from the slave laser when injected with an optical power of +1.7 dBm. When injected, only a single longitudinal mode lases, with all the other modes in the slave laser suppressed.

are suppressed due to the injected signal, as the carriers used to generate these other modes in the free-running case are now contributing to the injected mode. The injected signal is amplified slightly as it passes through the cavity, and this is the main mechanism which will be used for active optical demultiplexing. If instead the master signal was an optical comb and the slave laser was locked to one of the lines in the comb, the signal could be demultiplexed. This was first demonstrated in Ref. [128], and since then many different studies presenting new devices [129]–[131], key parameters [132], [133] or demonstrating new optical demultiplexing results [134]–[139] have been completed. This thesis follows on from these works, adding to what has already been shown.

Optical injection was initially studied from a physical perspective [140]–[142], however the complicated dynamics which arise from the amplitude-phase coupling within the semiconductor laser's electric field attracted many purely dynamics based studies. In fact, optical injection set-ups are considered good testbeds to study complicated nonlinear delay-coupled systems [143], and there are many studies and reports which thoroughly discuss the dynamics involved with single frequency injection (see Refs. [144]–[146] and citations within). However, very few of these analyses have focused on optical comb injection, and to our knowledge, the most relevant studies have already been mentioned in the paragraph above. Studies such as those performed in Ref. [147] and Ref. [148] deal with multiple frequency injection, however the injected lines are not coherent in these cases, as they are in all cases considered here. Hence, a secondary goal of this thesis was to investigate the dynamical behaviour of the slave laser while under injection from an optical comb. Several other groups have published articles on the dynamics of comb injection [149], [150] in the last few months, which shows there is a growing interest in this topic.

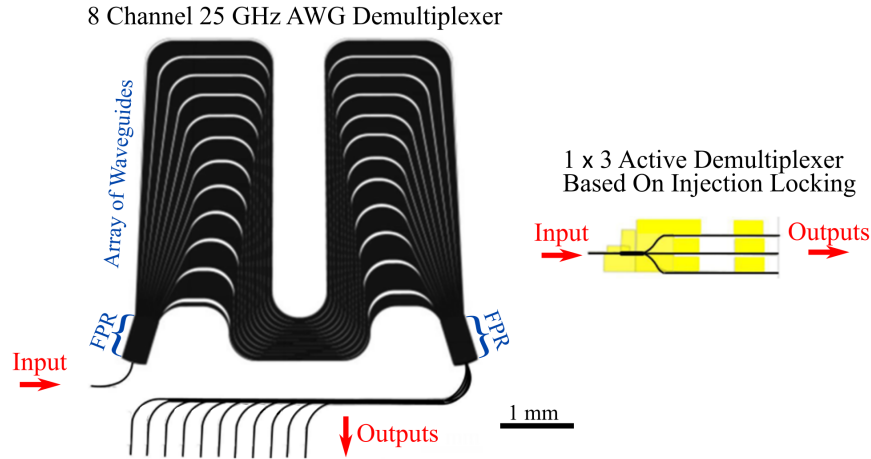


Figure 1.16: Size comparison of an 8 channel arrayed waveguide grating (AWG) demultiplexer (left) and a 1×3 optical injection demultiplexer (right). Only the metal (yellow) and waveguides (black) layers of the device design are shown. The AWG design is very similar to that shown in Fig. 1.11, where the input light first enters a free propagation region (FPR), before entering an array of waveguides. The waveguides in the array have slightly lengths, which means that there is a phase difference between consecutive waveguides at output FPR. Only the metal (yellow) and waveguides (black) are shown. The AWG was designed to have 25 GHz channel spacing, and narrower channel spacings would result in a larger AWG size. The channel spacing of the optical injection demultiplexer is not fixed.

1.8 Integrated Optical Demultiplexers

A key component on a photonic integrated circuit is the ability to split and combine different wavelength signals. Optical multiplexers are required pre-transmission, with de-multiplexers required after transmission. As this thesis is focused on demultiplexers, only viable on-chip demultiplexers are discussed below.

There are several types of integrable optical filters, including asymmetric Mach-Zehnder demultiplexers [151], [152] and echelle gratings [153], [154], with the most successful commercial type being the array waveguide grating (AWG) (also known as a phased array). With the first demonstration of a dispersive phase array in 1988 [155], AWGs became a hot research topic, with designs featuring sub 2 nanometre channel separation quickly following [156], [157]. AWGs feature an array of waveguides which map the input onto multiple output channels. The path lengths of the waveguides in the array are all slightly different, which causes the different wavelengths in the input channel to be mapped to different output channels. A design of a modern 25 GHz AWG is shown in Fig. 1.16.

An AWG features a large array of waveguides, connected on either end with a free propagation region (FPR). Input light is first split up over the many waveguides in the input FPR. Each waveguide in the AWG has a slightly different length, and hence, when the light from these waveguides reaches the output FPR, the output from each waveguide will have a slightly different phase. In order to demultiplex a signal, an AWG uses the phase change in each waveguide to steer different wavelengths of light into the final output waveguides. As the output channel frequency spacing is decreased, the required phase change difference between consecutive waveguides increases. Hence, in order to decrease the output channel frequency spacing in an AWG, the optical path lengths of the waveguides in the device must increase.

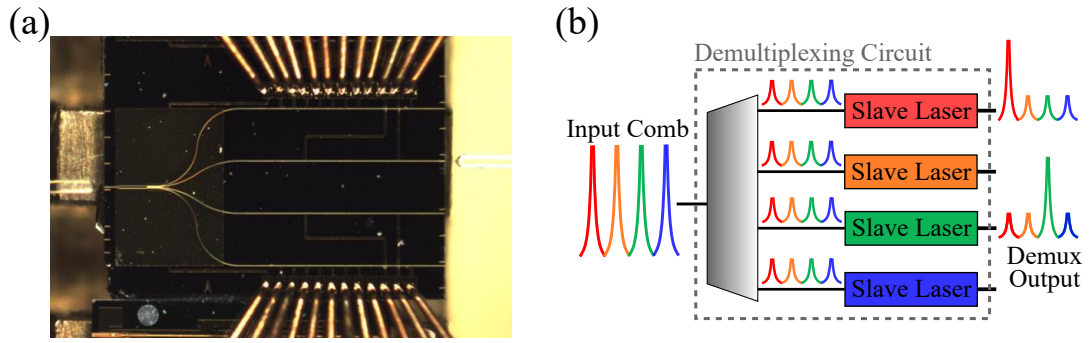


Figure 1.17: (a) Microscope image of a 1×4 demultiplexer. (b) Illustration of an input comb, with 4 slave lasers locking to different lines in the comb.

[158], [159]. This both increases the device footprint and demands more from the device fabrication process. Waveguide imperfections can cause optical phase errors, which significantly adds to the crosstalk in devices [160]. As a result, accurate and high resolution fabrication of large devices adds to the cost of making AWGs with narrow spacing.

As mentioned above, many different materials are being used for photonic integration, and AWG performance varies from platform to platform. The crosstalk between channels is commonly used to determine the performance of an AWG, where crosstalk is a measure how much of a signal transmitted on one channel leaks into other channels in the circuit. Typically, channel frequency spacings between 25 GHz and 100 GHz have been focused on, with many examples in the literature across the different photonic platforms; e.g, on silicon nitride [161], or on InP [162]. Further examples of ultra narrow (with 1 GHz channel spacing) AWGs have been demonstrated in silica on silicon [163], and more recently on pure silicon photonics platforms [164], due to the advantage of the high contrast index on these platforms.

On InP, monolithically integrable 10 GHz AWGs have been demonstrated, with large footsized and reasonably high crosstalks [165]–[167] when compared with other platforms. Hence, cost effective high performance monolithically integrable optical demultiplexers on InP capable of demultiplexing narrow optical combs are still required.

Prior to commencement of this project, research had began on using optical injection locking as an active filter [128]. Optical demultiplexers such as the one shown in Fig. 1.17(a) injection lock individual slave lasers to each line in the optical comb, allowing each comb line to be demultiplexed and amplified [129]–[131], [133], [168]. The illustration in Fig. 1.17(b) shows how these optical demultiplexers operate; first, the optical comb is split equally over the output channels using a multimode interference (MMI) coupler [169], and then each slave laser injection locks to a one of the optical comb lines (each laser's frequency can be tuned slightly to match a different comb line). As shown in Ref. [170], these demultiplexers can be monolithically integrated directly with electro-absorption modulators, in order to create coherent transmitters.

These injection locked optical demultiplexers have several advantages over other types of integrated demultiplexers:

- High resolution fabrication processes or complicated regrowth steps are not required.
- Decreasing the output channel spacing does not require the device size to grow.

- The lasing frequency of the slave lasers can be tuned if integrated tunable lasers are used (e.g. Ref. [75]), and hence these demultiplexers could be used with a flexible optical comb.
- As each slave laser has a locking bandwidth, injection locking demultiplexers have inherent wavelength tracking, protecting against small frequency drifts in the system.

For the above reasons, these active wavelength filters are an attractive type of integrated demultiplexer.

1.9 Thesis Motivation and Outline

The motivation for this thesis was to investigate and further the understanding of the active optical filters discussed in the previous section. To briefly summarise what was discussed in this introductory chapter, the bandwidth of conventional WDM systems is quickly filling up due to increasing demand. By moving to optical comb sources, large amounts of bandwidth reserved to protect from frequency jitter and other types of instabilities can be freed-up, increasing network capacity. Ideally, these comb sources would be integrated with modulators and packaged on a single photonic integrated circuit, as in the proof of principle demonstrated in Ref. [170]. This would make future devices cost effective and mass producible. However, integrating and modulating an optical comb on-chip requires efficient optical demultiplexers.

The reasons for the monolithic integration technology used throughout this thesis were outlined in Section 1.5. Two types of integrable single mode lasers were briefly discussed (slotted Fabry-Pérot lasers and single mode pit lasers). Devices which were designed using an inverse scattering method are discussed in Appendix A, as these laser designs were developed over the course of this project. As discussed in Section 1.8, common types of integrated optical demultiplexers are not currently feasible on photonic integrated circuits for small frequency spacings. Hence, following from research into active optical demultiplexing based on optical injection locking [128], [130], the goal of this thesis was to study and further the understanding of how a slave laser injected with an optical comb demultiplexes the comb lines.

The rest of this thesis is outlined as follows:

- Chapter 2 discuss the initial investigation performed using low optical injection strengths. A steady state numerical Fabry-Pérot laser model is presented and discussed in detail. The model was then compared with results from both single frequency injection and optical comb injection experiments, and good agreement was found in both cases. Based on the agreement seen between theory and experiment, the model was then used to determine how the SMSR achieved through active filtering improved with increasing the Q factor of the slave lasers in the devices.
- As the Fabry-Pérot model was limited by its steady state assumptions, Chapter 3 instead uses a single mode rate equation to investigate how the SMSR achievable varies with optical comb spacing and drive current. As rate equation models have previously been used extensively to model the dynamical behaviour of lasers, further investigation into the output state of the demultiplexed comb is discussed. The model predicts that

the relaxation oscillations within the slave laser limit the side mode suppression ratio (SMSR) at low comb frequency spacings, and this was verified using two separate experimental techniques. Using a high resolution optical spectrum analyser, it was also found that the excited relaxation oscillations within the slave laser can frequency lock to rational spacings of the optical comb spacing. The chapter is concluded with two dimensional parameter maps spanned by detuning and the optical injection power, which lay out the parameter regions with high and low SMSR for different comb spacings.

- Chapter 4 furthers the study of the dynamics present with optical comb injection. The frequency locking of the relaxation oscillations within the slave laser is studied in more detail both experimentally and theoretically, and frequency detuning sweeps are presented. It is found that a Devil's staircase in the slave laser's lasing frequency appears as the slave is tuned in between the optical comb lines. After a brief discussion of the circle map and Arnol'd tongues, this extra locking mechanism is discussed and studied as a function of the slave's natural RO frequency. Two dimensional parameter maps are used to detail wider areas of interest, and it is shown that the optical output comb from an injected slave laser can be tuned using the injection strength and detuning. Further, it is shown that the output combs can have improved stability and lower linewidths.
- Finally, Chapter 5 concludes this thesis. The main results are summarised, and possible future research is discussed.

After the conclusions and the main body of this thesis, several appendices are included to provide supplementary discussion material.

Chapter 2

Fabry-Pérot Model and Cavity Q

To begin the investigation into the active mode filtering provided through optical injection, a simple and intuitive laser model was adopted. The first goal was to use the model to reproduce the different measured lasing spectra from Fabry-Pérot (FP) and slotted Fabry-Pérot (SFP) devices. Then, optical injection was added to the model. With good agreement between the single frequency optical injection experiments and the model results, optical comb injection was then also investigated.

In the following sections, the optical injection experimental setup and FP laser model are introduced. To model the different device structures, a transmission matrix method was used to determine the reflection and transmission of different mirrors and device structures. The transmission matrix method is introduced in Section 2.4, with full model results presented in Section 2.5. The mode suppression due to optical injection is then investigated in Section 2.5, and good qualitative agreement is found between theory and experiment. Finally, the impact of the quality factor (or Q factor) on how much an optical comb could be demultiplexed is investigated, and it is found that the side mode suppression ratio (SMSR) improves with increasing Q. Some of the results presented in this chapter were published in the MDPI journal *Photonics* (see Ref. [171] for the published article).

2.1 Experimental Set-up

To provide context for the theoretical model in the following section, the set-up used to investigate optical injection is presented here first. The full set-up is illustrated in Fig. 2.1, where the device under test (DUT) is mounted on a temperature controlled brass chuck. Figure 2.2(a) shows a device under test, contacted electrically using a tungsten needle. Throughout the experiments, a tunable laser source (TLS) was used as the master laser. Light from the lasers was collected by coupling a lensed fibre to the device's facet. To generate the optical combs used in some of the results presented, the components inside the dashed section in Fig. 2.1 were included in the setup. In these cases, an RF signal generator was used to intensity modulate the master laser signal passing through a LiNbO₃ Mach-Zehnder modulator (MZM) (an example of a typical 10 GHz optical comb is plotted in Fig. 2.2(b)). An erbium doped fiber amplifier

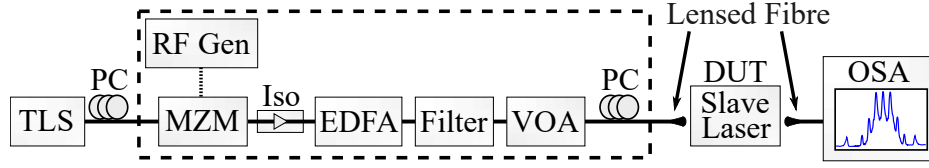


Figure 2.1: Experimental setup used to measure the intensity plots of the optical injection locking experiments. Dashed lines indicate the additional setup used when injecting optical combs. TLS: Tunable laser source, MZM: Mach zehnder modulator, PC: Polarisation controller, EDFA: Erbium doped fibre amplifier, VOA: Variable optical attenuator, OSA: Optical spectrum analyser, DUT: Device under test.

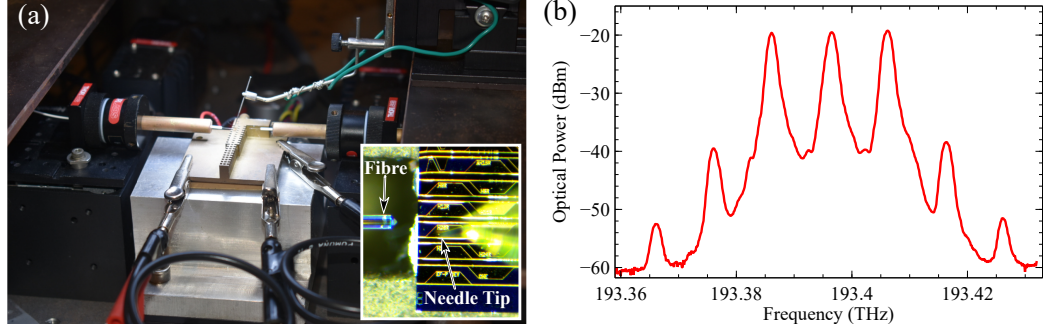


Figure 2.2: (a) Image of a device under test. The tungsten needle is used to supply electrical current to the device – current flows from the needle, through the device and the temperature controlled brass chuck, completing the loop through the crocodile clips on the chuck. The position of the lensed fibre pictured is controlled using micro controllers. Inset: a microscope image of a device being probed. The blurry out of focus object on the right is the needle. The lensed fibre on the left can be aligned with the laser waveguide to coupled light from the laser. (b) Typical 10 GHz optical comb injected into the device's under test.

(EDFA) was used to amplify and control the optical power injected into the device. The output from the slave laser was measured on an optical spectrum analyser (OSA). Polarisation controllers (PC) were used before the MZM and the DUT to maintain polarisation throughout the experiments¹, as both the comb generation and optical injection aspects of the experiment depend strongly on polarisation [172].

2.2 Fabry-Pérot Model Description

The laser model adapted in this work has previously been proven to accurately replicate the characteristics of lasers with multi-mode and single moded lasing [173]–[175]. As discussed in the introduction, Fabry-Pérot lasers are very simple cavities, which have broadband reflectors on either side of a gain material. The Fabry-Pérot laser model was chosen to start modelling experimental results as the model is physically intuitive, and can be scaled to a multimode model with relative ease. In the following section, the model will first be summarized, then how the model was altered to include optical injection will be described.

In order to derive the optical power of each longitudinal mode within a laser cavity, we start by considering the electric fields within a cavity of length L as shown in Fig. 2.3, and let E_{A1} and E_{A2} represent the electric fields propagating into the mirrors at boundaries 1 and 2; similarly,

¹The interaction between light and a crystalline solid can often depend strongly on the polarisation of the light. This is true in most semiconductors, and in this particular case, both the mach-zehnder modulator and the laser itself are polarisation dependent.

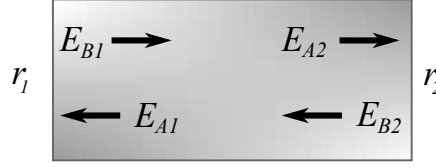


Figure 2.3: Illustrations of the fields inside a Fabry-Pérot laser cavity, including two mirrors with reflection coefficients r_1 and r_2 .

E_{B1} and E_{B2} denote the fields propagating into the mirrors at boundaries 1 and 2. The fields at the interfaces can be related to one another by:

$$\begin{aligned} E_{B1} &= r_1 E_{A1}, & E_{A2} &= E_{B1} e^{(\Gamma - i\theta)L} + \delta_+, \\ E_{A1} &= E_{B2} e^{(\Gamma - i\theta)L} + \delta_-, & E_{B2} &= r_2 E_{A2}, \end{aligned}$$

where Γ is the gain per unit distance of the laser cavity, θ is the propagation constant, and δ_+ and δ_- are contribution of the spontaneous emission to the fields as they travels to the left and right. The intensity of the field at the left facet $|E_{A1}|^2$ can be found using algebra:

$$|E_{A1}|^2 = \frac{|\delta_-|^2 + |\delta_+|^2 g^2 r_2^2 + \delta_-^* \delta_+ g r_2 e^{-i\theta L} + \delta_- \delta_+^* g r_2 e^{i\theta L}}{(1 - r_1 r_2 g^2)^2 + 4g^2 r_1 r_2 \sin^2(\theta L)}, \quad (2.1)$$

where $g = e^{\Gamma L}$ represents the single pass gain seen by the fields in the cavity. To proceed, we assume that the time averaged contributions of the terms $\delta_-^* \delta_+$ and $\delta_- \delta_+^*$ are zero (as δ_- and δ_+ are uncorrelated, and on average don't contribute to the constructive interference which forms the mode), and we also assume the magnitude of the spontaneous emission in both directions is equal, so that $|\delta_-|^2 = |\delta_+|^2 = |\delta|^2$. Defining $\phi = \theta L$ and integrating over one period from $\phi = -\frac{\pi}{2}$ to $\phi = \frac{\pi}{2}$ gives the power from one longitudinal mode in the laser. Hence, the power I in each mode of the laser is given by:

$$I = \int_{\phi=-\frac{\pi}{2}}^{\phi=\frac{\pi}{2}} \frac{|\delta|^2 (1 + g^2 r_2^2)}{(1 - r_1 r_2 g^2)^2 + 4g^2 r_1 r_2 \sin^2(\phi)} d\phi. \quad (2.2)$$

This integral can be evaluated using mathematica (or otherwise) and found to be:

$$I_m = \frac{\pi |\delta_m|^2 (1 + g_m^2 r_{2m}^2)}{1 - r_{1m}^2 r_{2m}^2 g_m^4}, \quad (2.3)$$

where now the subscript m has been added to indicate that values for the gain, reflection and spontaneous emission coupling to each mode can differ across the longitudinal modes in the laser. The reflection coefficients r_{1m} and r_{2m} for the different laser cavities considered in the following section were calculated using a one-dimensional transmission matrix method [159] (see Section 2.4 for further details). The modal gain dependence is modelled as:

$$g_m = \exp \left[\frac{n\sigma_m - \alpha_{int}}{2} L \right], \quad (2.4)$$

where α_{int} is the cavity loss, L is the length of the gain section of the laser, σ_m is the gain shape of the laser material and n is the number of free carriers (i.e, the number of carriers available

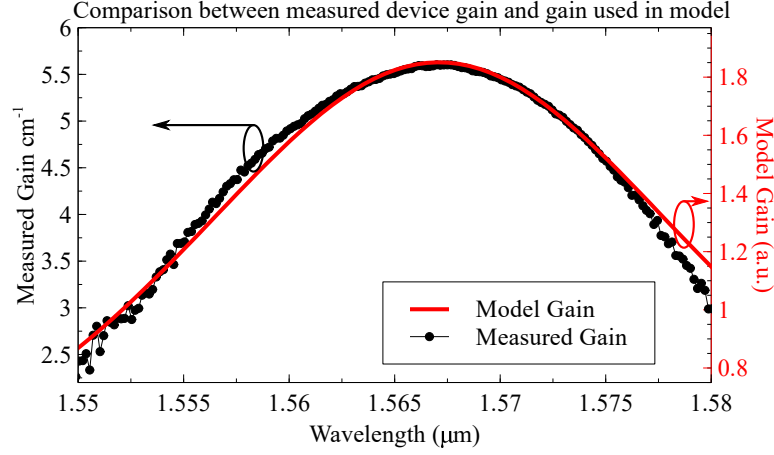


Figure 2.4: Comparison between measured device gain (left vertical axis) from a FP laser calculated using the Cassidy gain method [176], and the gain g_m implemented in the model (right vertical axis). The Cassidy gain method is discussed in more detail in Sec. 2.3.

for recombination). The gain lineshape in the model was chosen to be of the form:

$$\sigma_m(\lambda) = \frac{a}{\mu\sqrt{2\pi}} e^{-\left(\frac{\lambda-\lambda_c}{\sqrt{2}\mu}\right)^2}, \quad (2.5)$$

where here, λ_c gives the center gain wavelength, and a and μ were used as fitting parameters to approximate the measured gain. Figure 2.4 shows the gain g_m compared with the measured gain of the InGaAs semiconductor devices tested, and although the asymmetry of the real device gain is not represented by (2.5), good qualitative agreement is observed around the peak modal gain. Far away from the gain center, the Gaussian expression for the gain lineshape remains positive, implying there are no wavelengths which are absorptive or lossy. Hence, the model's simulation range was restricted to within the range of experimentally measured positive gain. The Gaussian expression for gain lineshape also allowed the overall gain to be transposed and manipulated easily. Further information on how the gain was measured and modelled is given in Section 2.3.

The spontaneous emission in the model is defined as in Ref. [173], by the term B_m :

$$\pi|\delta_m|^2 = B_m = \frac{\beta_{sp}n}{\tau_p} \left(\frac{g_m^2 - 1}{\ln g_m^2} \right), \quad (2.6)$$

where β_{sp} is the spontaneous emission factor and τ_p is the photon lifetime. The number of free carriers n is modelled by:

$$\frac{dn}{dt} = N - \frac{n}{\tau_c} - 2n \sum_m \sigma_m I_m. \quad (2.7)$$

Here, N is the rate of injected carriers and τ_c is the carrier lifetime. The term n/τ_c accounts for the carriers which undergo non-radiative recombination, and the final term $2n \sum_m \sigma_m I_m$ takes into account the number of carriers recombining due to stimulated emission in the laser

material. The steady state value for the carriers is:

$$n = \frac{N}{\frac{1}{\tau_c} + 2 \sum_m \sigma_m I_m}. \quad (2.8)$$

As rate equation models more accurately model the locking range and power in the slave laser under optical injection [177], the optical injection in the model uses results derived from a rate equation approach. To derive the required results, we start with the standard injection locking rate equations as reported in [142], [178]:

$$\frac{dE(t)}{dt} = \frac{\gamma_g - \gamma_c}{2} E(t) + f_d E_{\text{Inj}}(t) \cos[\Delta\omega t - \phi(t)], \quad (2.9)$$

$$\frac{d\phi(t)}{dt} = \frac{\gamma_g - \gamma_c}{2} \alpha_H + f_d \frac{E_{\text{Inj}}(t)}{E(t)} \sin[\Delta\omega t - \phi(t)]. \quad (2.10)$$

Here, $E_{\text{Inj}}(t)$ is the amplitude of the injected field, γ_g and γ_c are the rates of cavity gain and cavity losses, f_d is the longitudinal mode spacing, α_H is the linewidth enhancement factor, and $\Delta\omega = \omega_1 - \omega_0$ is the difference between the natural frequencies of the master and slave laser. In the steady state, equation Eq. (2.9) gives us a relation between the growth and decay rates inside the laser:

$$\gamma_c - \gamma_g = 2f_d \frac{E_{\text{Inj}}(t)}{E(t)} \cos[\Delta\omega t - \phi(t)]. \quad (2.11)$$

To relate the steady state solution for the amplitude in Eq. (2.11) to the optical power in the FP modes, we note that one can write the power E^2 in terms of the saturation power of the gain medium by [178]:

$$E_0^2 = \left(\frac{\gamma_{g0}}{\gamma_c} - 1 \right) E_{\text{sat}}^2 = (g_m - 1) E_{\text{sat}}^2, \quad (2.12)$$

where $g_m = \gamma_{g0}/\gamma_c$ is the amount by which the unsaturated gain in the laser exceeds the cavity losses. By assuming that the laser growth rate inside the cavity saturates under injection in the form [178],

$$\gamma_g = \frac{\gamma_{g0}}{1 + E^2/E_{\text{sat}}^2}, \quad (2.13)$$

we can eliminate the unknown saturation power level E_{sat}^2 using Eq. (2.12) and Eq. (2.13), and find:

$$\gamma_c - \gamma_g = \frac{E^2(g_m - 1) - E_0^2(g_m - 1)}{E^2(g_m - 1) + E_0^2} = 2f_d \frac{E_{\text{Inj}}}{E} \cos[\Delta\omega t - \phi(t)], \quad (2.14)$$

where the last equality follows from Eq. (2.11). A first order approximation assuming that $E_1 \ll E_0$ is given in Ref. [178] as:

$$E^2(\omega_1) \approx E_0^2 \left[1 + \frac{2g_m}{(g_m - 1)} \frac{f_d E_{\text{Inj}}}{g_m c E_0} \cos[\phi_L(\omega_1)] \right]. \quad (2.15)$$

Hence, using Eq. (2.15) we can describe the how the power in an injection locked mode in the

Table 2.1: Parameterised values used in the model, unless otherwise stated. Values for τ_p , τ_c and β were as used in Ref. [168], and for a , μ and α_{int} were obtained via fitting to the measured gain spectra. The value for α_H in semiconductors can be between 1 and 5 [144], and was chosen to be 3.5 as it matched the locking bandwidth of the experimental data well.

Parametrised values used in calculations			
α_H	3.5	a	78.2
τ_p	1	μ	0.01235
τ_c	100	α_{int}	1.27
β	10^{-6}		

FP model varies with detuning, assuming that our injected optical field strength is small.

From Eq. (2.10), we can also determine the range of frequencies for which the slave laser will be frequency locked. Using Eq. (2.11) in Eq. (2.10), we can determine the locked phase ϕ_L of the slave relative to the master:

$$\Delta\omega = -f_d \frac{E_{Inj}(t)}{E(t)} (\sin[\phi_L(\omega_1)] + \alpha_H \cos[\phi_L(\omega_1)]), \quad (2.16)$$

$$\phi_L(\omega_1) = -\arcsin\left(\Delta\omega / \left\{f_d \frac{E_{Inj}(t)}{E(t)} \sqrt{1 + \alpha_H^2}\right\}\right) - \arctan \alpha_H. \quad (2.17)$$

The range of frequencies for which the slave laser is locked to the master laser can then also be shown to be [142], [179]:

$$\omega_0 - \sqrt{1 + \alpha_H^2} \frac{v}{2L} \frac{E_{Inj}}{E_0} \leq \omega_1 \leq \omega_0 + \frac{v}{2L} \frac{E_{Inj}}{E_0}. \quad (2.18)$$

Hence, Eq. (2.15) and Eq. (2.18) were used to describe the effect of the master laser on the output of the slave laser.

As a steady state solution is presumed in equation Eq. (2.8), the dynamical regions of operation of the slave laser which arise at different injection strengths and detunings are omitted by the model. However, it will be shown in the following discussion that under these assumptions, this simple model can still accurately model behaviour of the SMSR of the slave lasers under weak injection, and can even be used to qualitatively predict the suppression obtainable through injection locking a slave laser to a single injection frequency or to one of the lines of an injected optical comb.

2.3 Gain and the Thermal Tuning of Gain

Two methods to estimate laser gain were used, the Hakki-Paoli method [180] and the Cassidy method [176]. Both rely on accurate measurements of the optical spectra of FP devices, to determine the measured power in the peaks and troughs of each mode. The Hakki-Paoli method averages the power of two neighbouring peaks, and divides by the power in the intermediate trough between the two peaks, obtaining a depth of modulation d_i . The corresponding gain G_i is then given as:

$$G_i = \frac{1}{L} \ln \left[\frac{d_i^{0.5} + 1}{d_i^{0.5} - 1} \right] + \frac{1}{L} \ln R, \quad (2.19)$$

where here L is the length of the laser and R is the estimated mirror reflectivity of the laser.

The Cassidy method, published a decade after the Hakki-Paoli method, improves on the Hakki-Paoli method by removing the optical response function of the OSA from the measurements. Cassidy noted that response functions of common optical instruments have the effect of underestimating the peak powers in the spectra, while overestimating the minima in the spectrum [176]. To accurately measure laser gain, the Cassidy method instead integrates over each mode in the FP laser to find the optical power contained in each mode. The power at the troughs of the mode can be written analytically as:

$$I_{min_m} = \frac{B_m (1 + RG_m) (1 - R)}{(1 + RG_m)^2 - 4RG_m} \quad (2.20)$$

and the total power in a single longitudinal mode of a Fabry-Pérot laser is given by:

$$I_{tot_m} = \left(\frac{c}{2l}\right) \frac{B_m (1 + RG_m) (1 - R)}{1 - R^2 G_m^2}, \quad (2.21)$$

where R is the reflection from the cavities mirrors, l is the length of the cavity, B_m is as in (2.6), and G_m is the gain of the mode that we're interested in measuring. The ratio of I_{tot_m} and I_{min_m} is then

$$p = \left(\frac{c}{2l}\right) \frac{1 + RG_m}{1 - RG_m}. \quad (2.22)$$

By measuring the ratio p experimentally, the gain of the mode can be found, as

$$G_m = \frac{1}{R} \left(\frac{p' - 1}{p' + 1} \right) \quad (2.23)$$

where now $p' = p \frac{2l}{c}$. Figure 2.5 shows a comparison of the gain measured using both methods. The Hakki-Paoli method under estimates the actual gain of real devices, and in Fig. 2.5 the Cassidy method's estimate of the gain is significantly larger. The Cassidy method is also less prone to error due to inaccurate determination of the peaks and troughs in an optical trace.

As shown previously in Fig. 2.4, the model gain was fit to match the gain from the Cassidy method. In order to model temperature and current sweeps in the FP model, the gain in the model was allowed to vary with temperature. For these sweeps, the σ_m term in Eq. (2.4) was allowed to vary as a function of temperature:

$$\sigma_m(\lambda, T) = \frac{a}{\mu(T)} e^{-\left(\frac{\lambda - \lambda_c(T)}{\sqrt{2}\mu(T)}\right)^2} \quad (2.24)$$

where here $\lambda_c(T)$ allows the center of the gain to be varied with temperature T , and $\mu(T)$ alters the shape of the gain as temperature changed. Over the temperature ranges used experimentally ($< 10^\circ C$), the change in the gain center wavelength was approximately linear, given by $\lambda_c(T) = 1.5625 + 2.634 \times 10^{-4}T$, for T in Celsius. By making μ a function of temperature, the height and width of the Gaussian gain can be changed as the temperature is varied. Increasing μ decreases the magnitude of the gain, while causing the gain to spread laterally. The

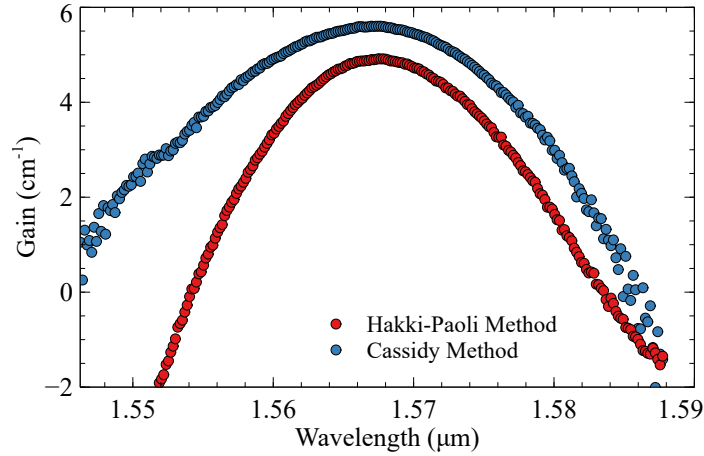


Figure 2.5: Plot of the gain of the AlInGaAs material measured at 20°C, using both the Hakki-Paoli and the Cassidy gain methods. The Hakki-Paoli method typically underestimates the gain of devices.

rate of change of $\mu(T)$ was defined as:

$$\mu(T) = 13.1836e^{0.01235T},$$

for T in Celsius. The constants used in the definitions of $\lambda_C(T)$ and $\mu(T)$ were chosen to match the change in lasing wavelength and the decrease of lasing power seen in experimental work. This empirical method of defining how the gain varied as a function of temperature is not rigorous, however for the purpose of modelling the experimental traces observed, worked well.

2.4 Scattering Matrices and the Transmission Matrix Method

The FP model can be used to model a variety of different cavity types; by varying the effective refractive index along the cavity, different laser structures (both single mode and multimode) can be investigated. In order to do this, we require a description of how the reflection coefficients r_{1m} , r_{2m} vary with wavelength for these structures. To model devices with more complicated mirrors and reflectors, such as the slotted FP devices introduced in Section 1.5.4, techniques such as the thin film method [181] or the transmission matrix method (TMM) [159] can be used. Both of these methods can provide a 1 dimensional description of reflection as a function of wavelength, and hence either could be used to calculate the reflection coefficients r_{1m} , r_{2m} in the FP model. The slotted structures were investigated numerically using both methods, however as the transmission matrix method was simpler to implement numerically, it was predominantly used throughout this project. This section will hence describe the TMM and show some example reflection spectra.

To describe the transmission matrix method, it is first useful to introduce scattering matrices; a scattering matrix linearly relates the inputs and outputs at some scattering junction (e.g, Fig. 2.6). Each entry S_{ij} of a scattering matrix \mathbf{S} relates an output B_i of the junction with a linear

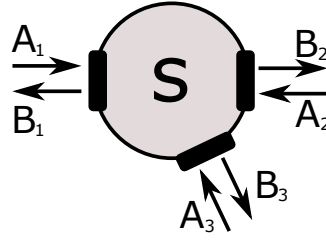


Figure 2.6: Illustration of different inputs and outputs of a 3 port scattering junction. The scattering matrix \mathbf{S} in this example would be a 3×3 matrix, relating each output B_1, B_2 and B_3 with the inputs A_1, A_2 and A_3 .

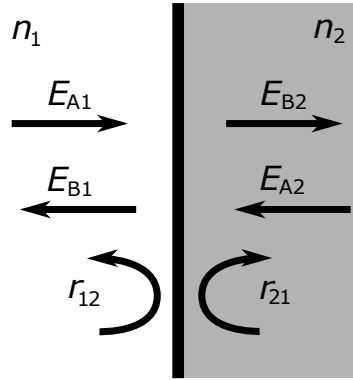


Figure 2.7: Interface between two dielectric material.

combination of inputs A_j . In general,

$$B_i = \sum_j S_{ij} A_j.$$

A dielectric interface between two media can be considered a scattering junction, as the electric field on the left hand and right hand side of the boundary can be linearly related to each other. As in Fig. 2.7, the fields E_{A1} , E_{A2} , E_{B1} and E_{B2} can be related by:

$$\begin{bmatrix} E_{B1} \\ E_{B2} \end{bmatrix} = \begin{bmatrix} S_{11} & S_{12} \\ S_{21} & S_{22} \end{bmatrix} \begin{bmatrix} E_{A1} \\ E_{A2} \end{bmatrix} = \begin{bmatrix} r_{12} & t_{21} \\ t_{12} & r_{21} \end{bmatrix} \begin{bmatrix} E_{A1} \\ E_{A2} \end{bmatrix}, \quad (2.25)$$

where r_{12} is the reflection coefficient seen by an electric field as it passes from medium 1 into medium 2, and t_{12} is the transmission coefficient under the same circumstance. Similarly for r_{21} and t_{21} . As with standard dielectrics,

$$r_{12} = \frac{n_2 - n_1}{n_2 + n_1} = -r_{21},$$

where n_1 and n_2 are the refractive indices of medium 1 and 2. This is approximately true for weakly guided waveguide modes [159], however the refractive indices n_1 and n_2 must be replaced by the effective index of the mode in each waveguide. The transmission coefficients t_{12} and t_{21} are also found trivially for a dielectric interface:

$$t_{12} = \sqrt{1 - r_{12}^2} = t_{21}.$$

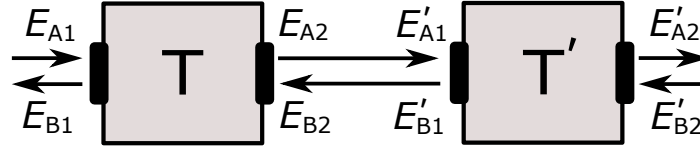


Figure 2.8: Two scattering junctions side by side. T and T' represent the transmission matrices of each junction.

Scattering matrices are useful for relating the inputs and outputs of a single scattering junction. However, to model the effect of a series of scattering junctions, it is simpler to use transmission matrices. Transmission matrices are easier to use in practice, as to model the effect of multiple junctions, you multiply the transmission matrices in the order which they appear. Instead of relating inputs with outputs as with scattering matrices, transmission matrices relate the left hand side of the boundary with the right hand side of the boundary. For example, as in Fig. 2.8, the fields on the left hand side of the boundary in medium 1 can be related to those on the right by

$$\begin{bmatrix} E_{A1} \\ E_{B1} \end{bmatrix} = \begin{bmatrix} T_{11} & T_{12} \\ T_{21} & T_{22} \end{bmatrix} \begin{bmatrix} E_{A2} \\ E_{B2} \end{bmatrix} \quad \text{and} \quad \begin{bmatrix} E'_{A1} \\ E'_{B1} \end{bmatrix} = \begin{bmatrix} T'_{11} & T'_{12} \\ T'_{21} & T'_{22} \end{bmatrix} \begin{bmatrix} E'_{A2} \\ E'_{B2} \end{bmatrix}$$

Putting these together, we find that

$$\begin{bmatrix} E_{A1} \\ E_{B1} \end{bmatrix} = \begin{bmatrix} T_{11} & T_{12} \\ T_{21} & T_{22} \end{bmatrix} \begin{bmatrix} T'_{11} & T'_{12} \\ T'_{21} & T'_{22} \end{bmatrix} \begin{bmatrix} E'_{A2} \\ E'_{B2} \end{bmatrix}.$$

This method is easily scalable, and hence can be used to model a complicated series of dielectric interfaces. In order to get information on the reflection and transmission of the structure, the resulting total transmission matrix must be converted back to a scattering matrix by the following:

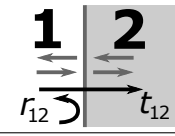
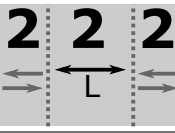
$$\begin{aligned} S_{11} &= \frac{T_{21}}{T_{11}}, & S_{12} &= \frac{T_{11}T_{22} - T_{12}T_{21}}{T_{11}}, \\ S_{21} &= \frac{1}{T_{11}}, & S_{22} &= -\frac{T_{12}}{T_{11}}. \end{aligned} \tag{2.26}$$

The inverse relations are given by:

$$\begin{aligned} T_{11} &= \frac{1}{S_{21}}, & T_{12} &= -\frac{S_{22}}{S_{21}}, \\ T_{21} &= \frac{S_{11}}{S_{21}}, & T_{22} &= -\frac{S_{11}S_{22} - S_{12}S_{21}}{S_{21}}. \end{aligned} \tag{2.27}$$

The entries S_{11} and S_{12} give the reflection and transmission coefficients for the whole system, and hence using the above relations the reflection/transmission can be found from the system's complete T matrix. The two most common S and T matrices are given in Table 2.2. Example reflection spectra calculated using this method are shown in the following section, which prove the effectiveness of using a 1-dimensional method to estimate a mirror's reflection.

Table 2.2: Table containing common scattering matrices and their corresponding transmission matrices; namely, the matrix for a dielectric interface, and the matrix for propagation through a distance L . It is assumed here that $r_{12} = -r_{21}$, $t_{12} = t_{21}$, with $r_{12}^2 + t_{12}^2 = 1$.

Scattering Matrix	Structure	Transmission Matrix
$\begin{bmatrix} r_{12} & t_{12} \\ t_{21} & -r_{12} \end{bmatrix}$		$\frac{1}{t_{12}} \begin{bmatrix} 1 & r_{12} \\ r_{12} & 1 \end{bmatrix}$
$\begin{bmatrix} 0 & e^{-i2\pi n_2 L/\lambda} \\ e^{-i2\pi n_2 L/\lambda} & 0 \end{bmatrix}$		$\begin{bmatrix} e^{i2\pi n_2 L/\lambda} & 0 \\ 0 & e^{-i2\pi n_2 L/\lambda} \end{bmatrix}$

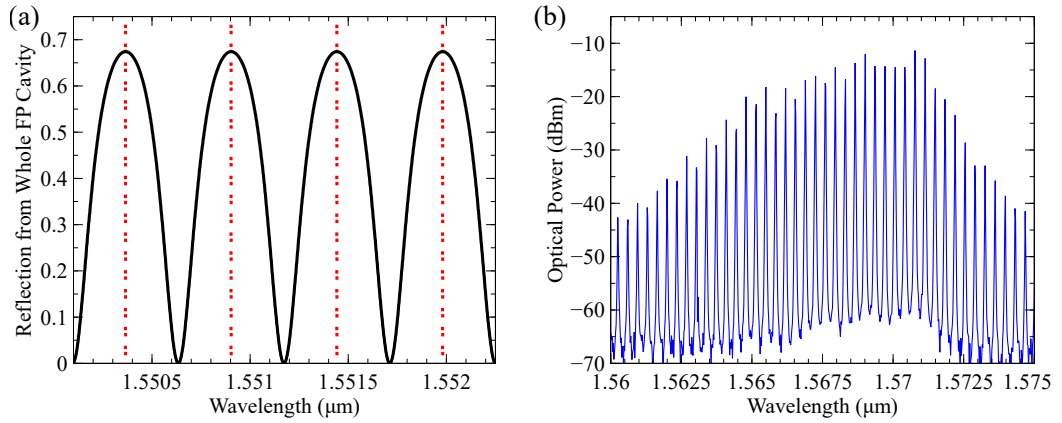


Figure 2.9: (a) Reflection calculated using transmission matrices, of a 700 μm long passive FP cavity, with facet reflections $\approx 0.27\%$. The solutions to equation (2.28) are plotted in vertical red dotted lines, which show that the modes supported in the FP cavity correspond with the peak reflections. (b) Optical spectrum from a 1050 μm long FP laser at 3.0 times threshold. The lasing spectrum features many modes, as the reflection seen by each mode is nominally the same, and the lasing material's gain varies slowly with wavelength.

2.4.1 Modelled Reflection Spectra

We start by first modelling the simplest type of cavity; a FP cavity, as shown in Fig. 2.3. Although the magnitude of the facet reflection seen by all wavelengths around the lasing gain peak in the FP cavity is nominally the same, only certain longitudinal modes with specific wavelengths can exist within the FP cavity. The modes supported within a cavity are those which wavelengths can resonate and allow constructive interference within the cavity; the relationship between the lasing wavelength λ and a cavity of length L and refractive index n is:

$$\lambda = \frac{2nL}{m}, \quad (2.28)$$

where here m can be any integer number. Figure 2.9(a) shows the resonances supported by a 700 μm long FP cavity, around the material gain peak. The spacing between the longitudinal modes (also known as the free spectral range $\Delta\lambda_{\text{FSR}}$) is determined by the optical path length (nL) within the cavity:

$$\Delta\lambda_{\text{FSR}} = \frac{\lambda^2}{nL}. \quad (2.29)$$

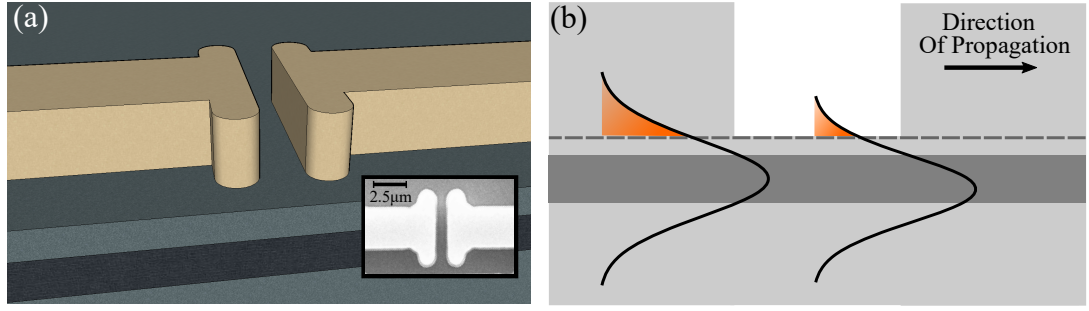


Figure 2.10: (a) A 3D illustration of a waveguide slot. Inset: A scanning electron microscope image of a slot in a fabricated device. (b) Illustration of how the mode overlaps with the slot interface both within and outside of the slotted region.

In Fig. 2.9(b), the lasing spectrum of a FP laser is shown at 3.0 times threshold. As the magnitude of the reflections is nominally the same for all modes, there is strong mode competition within the laser, resulting in low SMSR.

Single mode lasers are required for most telecommunications applications. As described previously in Section 1.5.4, slotted FP lasers are re-growth free cost effective devices which can achieve single mode lasing. As these were used pre-dominantly in the early stages of this work, the transmission and reflection spectra of the slotted FP lasers were also calculated using the transmission matrix method.

Each slot provides some reflection at two separate interfaces; at the transition from the waveguide to the slot, and the transition from the slot to the waveguide (shown in Fig. 2.10(a)). A 1-dimensional approach to modelling the scattering at these transitions cannot precisely predict the reflection due to each slot [80], however the slot reflection can be reasonably approximated by assuming fractions of the optical mode see different reflections [168]. As illustrated in Fig. 2.10(b), the modes supported within the waveguide and the slots differ slightly. In particular the tail of the optical mode which overlaps with the slot interface is different depending on the transition. The reflections between the slot and the waveguide were split into two parts for simplicity, and weighted by the amount the optical mode overlapped with the slot in each region (Γ_s or Γ_{wg}). Hence, the slot reflections were set to be:

$$r_{wg \rightarrow s} = \Gamma_{wg} r_{air} + (1 - \Gamma_{wg}) r_{wg} \quad (2.30)$$

$$r_{s \rightarrow wg} = \Gamma_s r_{air} + (1 - \Gamma_s) r_{wg} \quad (2.31)$$

where r_{air} is the reflection coefficient due to an index change from the material to air, and r_{wg} is the reflection coefficient due to an index change from the material to the slightly lower effective index within the slot. In this way, $r_{wg \rightarrow s} > r_{s \rightarrow wg}$, as predicted in [80].

Figure 2.11(b) shows the reflection spectrum calculated for the 8 slot mirror section of an SFP as illustrated in Fig. 2.11(a), with 1 μm slot width and 108 μm inter-slot spacing. The refractive indices used are contained in Table 2.3. Both the slot width and inter-slot spacing affect the locations of the reflection peaks, which have peak reflection values of approximately 27%. Although a crude approximation was used to model the slots, good agreement is seen between the resonance of the laser cavity and real device spectra. Figure 2.11(c) shows the calculated resonance of an entire 8 slot device from mirror section to facet, and for comparison, a real

Table 2.3: Parameters used to model the SFP mirrors. The values for n_{wg} and n_s were calculated using a two dimensional mode solver, in the material detailed in Appendix D. The values for Γ_{wg} and Γ_s were similar to those used in [168].

Parameter	Description	Value
n_{air}	Refractive index of air	1.0
n_{wg}	Effective refractive index in waveguide	3.19043
n_s	Effective refractive index in slot	3.16919
Γ_{wg}	Mode overlap with slot interface in waveguide	0.250
Γ_s	Mode overlap with slot interface in slot	0.09

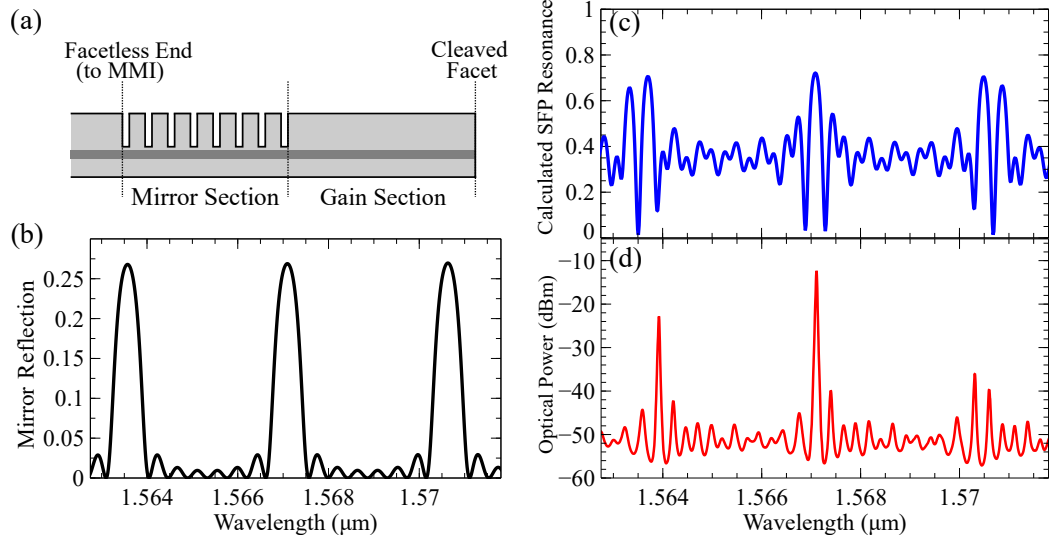


Figure 2.11: (a) Illustration of the SFP design (not to scale). The mirror section featured a total of 8 slots. (b) Calculated reflection spectrum of an 8 slot mirror, with slot width = 1 μm, and inter slot distance = 108 μm. (c) Calculated resonance of the full SFP laser, from the end of the mirror section to the facet. (d) Measured lasing spectrum of a SFP device, for comparison.

SFP lasing spectrum is plotted in Fig. 2.11(d). Good agreement is found between the location of the calculated resonant peaks, and the lasing modes in the device. The smaller resonances have similar shape, however have slightly worse agreement with what was measured. As these lower peaks contribute significantly less to the laser spectrum, it was assumed this has negligible effect.

2.5 Model Results

Using the above FP model in conjunction with the transmission matrix method, a wide variety of lasers can be simulated (such as FP, slotted FP (SFP), pit lasers and even ring lasers). In the following subsections, the model is first used to look at examples of free running laser spectra, along with light intensity (LI) curves. Following this, we then compare optical injection experimental results with simulated results from the model, using several different laser types. As the coupling efficiency between the lensed fibre and the devices tested was unknown in experiment, the calculated results are presented using the ratio of the injection strength to the slave laser power (i.e, I_{inj}/I_{slave}), and assume the coupling efficiency was 1 in all cases.

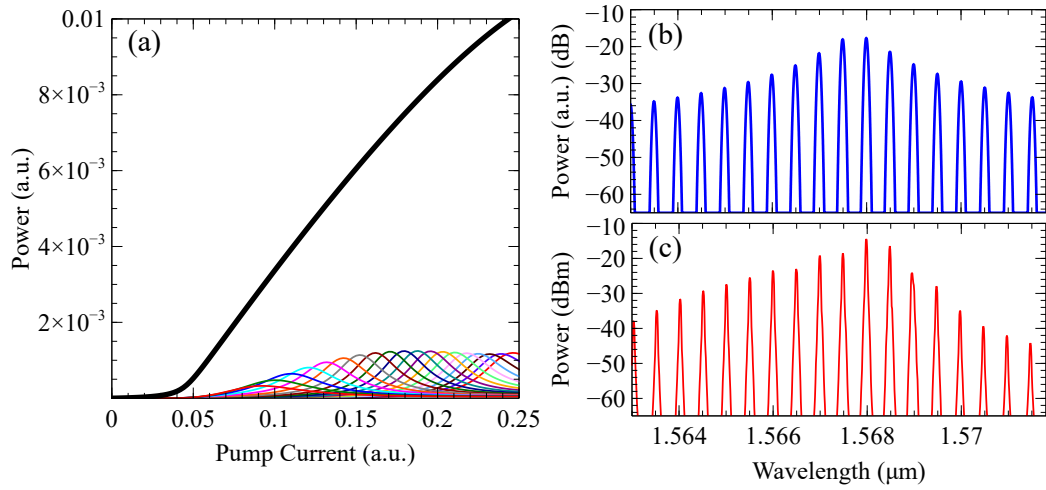


Figure 2.12: (a) Calculated LI curve from a 700 μm long FP device. In black, the total power output from the laser is shown. Below the black curve, the power level in each mode is plotted in separate colours. The strongest mode shifts as the pump current is increased, as higher pump rates contribute more heat to the device, shifting the centre of device gain. Note: a.u. denotes arbitrary units. (b) Calculated lasing spectrum of the same device at 2.5 times threshold current. (c) Measured lasing spectrum of a 700 μm long real FP device at 2.5 times threshold, for comparison.

2.5.1 Free Running Model Results

The simulated free running laser characteristics need to match experimentally measured results before the laser model can be trusted to accurately reproduce what happens when the slave laser is optically injected.

Figure 2.12(a) shows an LI curve from a 700 μm long FP device, which is plotted in black. Below the LI curve, the power of each mode in the FP device is plotted, in many different colours. At any one pump current, the power in the FP laser is split over many different modes, as expected, as FP devices are strongly multimode. By finding the maximum of the first derivative of the LI curve, the threshold current of the device was determined as $N = 0.044$ (recall that N is the number of injected carriers in the model). The total LI is sublinear, due to the effects of heating within the laser caused by the increase in current, which affects both the gain centre and magnitude of the gain (see Equations (2.24) and (2.25)).

The lasing spectrum at 2.5 times threshold from the same simulated FP device is shown in Fig. 2.12(b), with the equivalent real measured FP spectrum shown in Fig. 2.12(c). To compare the output spectrum from the model with the measured spectra on the OSA, the model output was convolved with a Voigt profile². The mode spacing is equivalent in the simulated and measured cases, however the powers in each mode differ slightly. In the simulated case, the gain is symmetric around the peak gain, and as a result the mode powers are also symmetric around the peak gain. However, in the measured spectrum, the modes on the shorter wavelength side of the peak gain have higher lasing powers than those on the higher wavelength side; this is due to some asymmetry in the real lasing gain.

A calculated single facet SFP LI curve is shown in Fig. 2.13(a). The total power from the SFP device is shown in black, with the powers in each of the modes of the device shown in different

²In reality, the shape of each lasers mode is Lorentzian, however the impulse response of the optical spectrum analyser is Gaussian, and hence the measure result is the convolution between the two (i.e, a Voigt function).

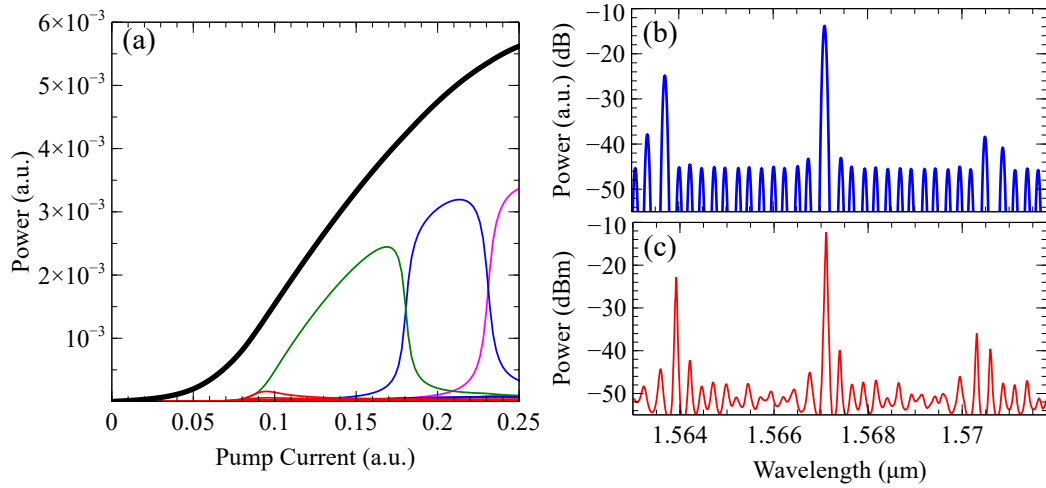


Figure 2.13: (a) Calculated LI curve from the SFP device depicted in Fig. 2.11(a). In black, the total power output from the laser is shown. Below the black curve, the power level in each mode is plotted in separate colours. The strongest mode shifts as the pump current is increased. In comparison with Fig. 2.12(a), a higher percentage of the total lasing power is contained in a single mode. Note: a.u. denotes arbitrary units. (b) Calculated lasing spectrum of the same device at 2.0 times threshold current. (c) Measured lasing spectrum of a real SFP laser as part of a 1×2 optical demultiplexer, as shown in Fig. 2.11(d), at 2.0 times threshold.

colours below. In contrast to the simulated FP LI curve, significantly more of the total power is contained within a single mode. The laser threshold in this case was $N = 0.06$.

A comparison between the lasing spectra of a simulated and real single facet SFP device can be made by comparing Figs. 2.13(b) and 2.13(c). The mirror section parameters match those as in Fig. 2.11. The lasing peak of the simulated trace and the measured trace match well, and although the side modes are located slightly further away in the simulated case than in the real device, good agreement is seen between the heights of the side modes relative to the main mode. The weak modes in the simulated case however do not have the same definition as in experiment; although the number of modes between the side modes match, the spacing and height of the weaker modes varies significantly more in the experimental trace. As these modes only contribute slightly to the overall lasing power, this discrepancy should have little influence on the behaviour of the main modes when injection locked.

2.5.2 Simulated Mode Suppression and Optical Demultiplexing

Having compared free-running simulated devices with real measured results, the model can now be used to investigate how slave lasers are affected by optical injection, with some confidence that the model can accurately reproduce what is seen in experiment.

Throughout this section, experimental results will be compared with the corresponding simulated results; in all cases, the experiments were performed using the setup shown in Fig. 2.1.

Figure 2.14 shows a comparison between the measured and the calculated results of a 700 μm long FP laser under optical injection, as the wavelength of the master laser is swept from 1568.95 nm to 1569.05 nm in each case. Figure 2.14(a) shows the measured spectrum from the FP device, biased at 45 mA (2.5 times threshold). The mirrors of the device were uncoated

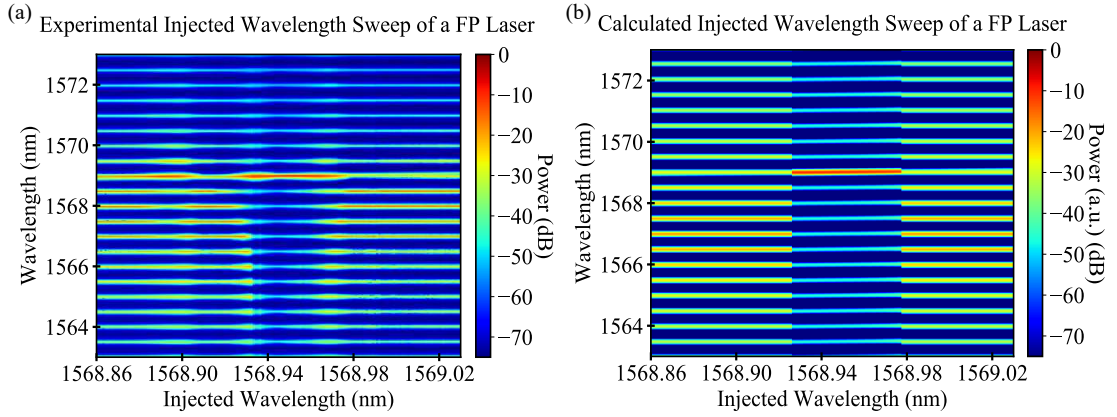


Figure 2.14: Experimental and calculated injected wavelength sweeps of a 700 μm FP device. In both cases, the slave laser was biased at 2.5 times threshold. **(a)** Experimental sweep, for an injected power of -12.5 dBm, and free running slave power of -4 dBm. The injected wavelength was stepped in increments of 0.001 nm. **(b)** Calculated sweep, for an injection ratio of 1.33×10^{-3} .

cleaved facets, each with an estimated reflection of 30%. At an injected wavelength of 1568.938 nm the slave laser locked to the master laser, and remained frequency locked over a span of 0.031 nm (or 3.87 GHz). While locked, the side modes of the slave laser were suppressed, and the SMSR was larger than 20 dB over a span of 3.6 GHz, with a maximum SMSR of 35.77 dB.

The simulated results of the same FP sweep are shown in Fig. 2.14(b). While the slave's lasing wavelengths remain outside of the locking range given by Eq. (2.18), the slave laser is unlocked, and the powers in the slave laser's modes are calculated by solving equations Eq. (2.3) and Eq. (2.8), with the injected light undergoing single pass gain. When a mode is locked, the locked mode's power is given by Eq. (2.15), with the power in the other modes calculated as previously. Equation (2.15) requires the free running mode power, and hence prior knowledge of the free running mode powers is required at each step. The parameters used in all the calculations presented are contained in Table 2.1. To account for the gain/loss seen by the unlocked injected signal, the injected light was amplified by the single pass gain of the laser at the wavelength. The refractive index (≈ 3.5) of the slave laser was used as a fitting parameter to line up the modes of the simulated spectra with the experiment. The simulated slave laser was biased at 2.5 times threshold, and the injected wavelength sweep matched that in the experimental trace. The optical spectrum of the slave laser undergoes sharp transitions at 1568.933 nm and 1568.978 nm unlike in the experimental case, as the model only calculates the locked steady state solutions. The complicated dynamics at the locking boundaries cannot be replicated due to the steady state assumption in the model. The optical suppression reaches a maximum of 35.1 dB, and there was a SMSR of over 20 dB over the whole locking range of 3.74 GHz, both of which are in good agreement with experiment.

Thermal tuning in the model is shown and compared with experiment in Fig. 2.15. The experimental trace presented in Fig. 2.15(a) has been taken from Ref. [128]. The slave laser used in this experiment was a two section, single mode tunable, slotted Fabry-Pérot laser. The temperature of the two section laser was swept over 2°C , with a constant injected wavelength at 1563.35. At 20.9°C , the slave laser frequency locks for approximately 0.24°C of the temperature sweep. The SMSR from the experiment was >20 dB over a frequency span of 1.29 GHz. The matching simulated result in Fig. 2.15(b) shows the slave device lock for 0.4°C , with

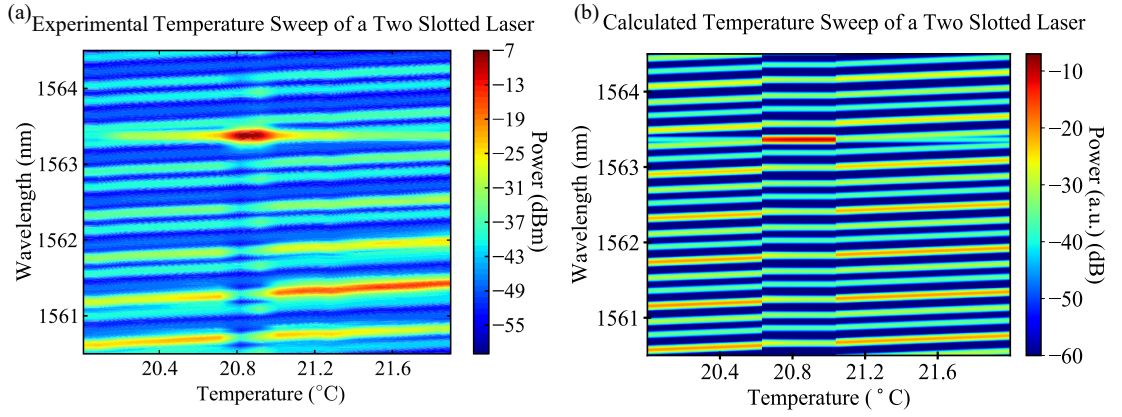


Figure 2.15: Experimental and calculated temperature sweeps of an optically injected 600 μm long two section slotted FP device, with a single etched slot in the center of the device separating the sections. In each case, the slave laser was under optical injection at wavelength 1563.36 nm. **(a)** Experimental sweep from Ref. [128]. The temperature was stepped in increments of 0.01 $^{\circ}\text{C}$. **(b)** Calculated sweep for an injection ratio of 6.13×10^{-4} .

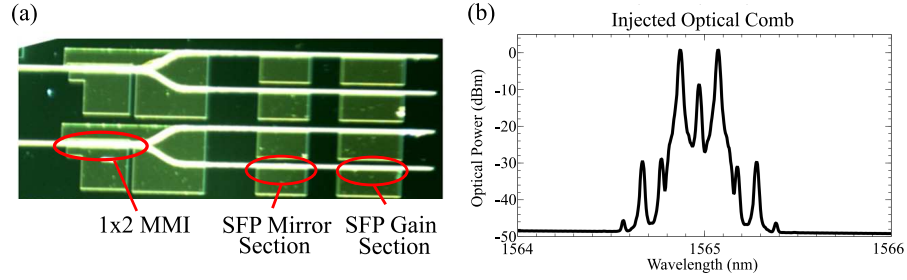


Figure 2.16: **(a)** Comb demultiplexer, featuring a 1×2 multimode interferometer (MMI) and 2 SFP lasers [168]. **(b)** Optical comb injected into the demultiplexer. This two line comb was generated by biasing the MZM at the point where the carrier is suppressed, giving two strong lines.

>18 dB SMSR over a frequency span of 0.95 GHz. Thermal tuning was introduced into the model by varying the optical path length of the laser material to match the 0.1 nm/ $^{\circ}\text{C}$ seen in experiment, as well as allowing the centre of the material gain to red shift with increasing temperature. The SMSR predicted by the model was slightly lower than experiment, likely due to the limitations in using a 1-dimension transmission matrix to describe the slot in the device [80]. The optical power in the mode that undergoes the frequency locking has a strong impact on the amplification the injected signal sees when locked, and the mismatch in the power of that mode could be the cause of the different SMSRs predicted.

As a final example, results from a 1×2 demultiplexer as shown in Fig. 2.16(a) are simulated. A two line optical comb, as shown in Fig. 2.16(b) was injected. Each line of the 2 line optical comb locks to the 2 side modes of the SFP laser, with the center of the comb (8 dB lower) also interacting with the slave laser's side mode as it tunes.

In the experimental trace in Fig. 2.17(a), maximum SMSRs of 18.4 dB and 20.6 dB were achieved as the two strongest comb lines locked to the side mode of the slave laser. The slave laser in the demultiplexer remained locked for spans of 2 GHz and 2.5 GHz respectively. The straight through line (8 dB lower than the 2 comb lines) is amplified slightly as it passes over the side mode, however it doesn't stably lock to the side mode. In the simulated trace in Fig. 2.17(b) the results obtained are quite similar. The SMSRs obtained as the comb locked to the

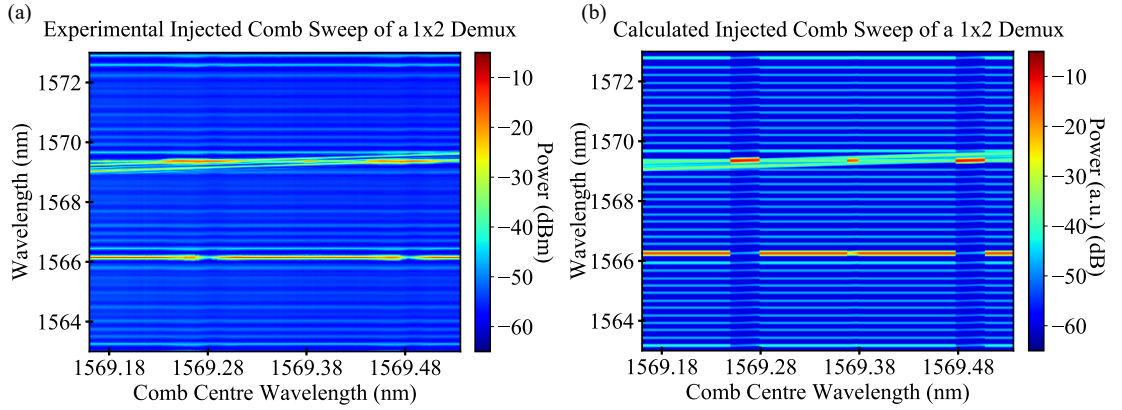


Figure 2.17: (a) Experimental and (b) calculated injected comb sweeps of an optical demultiplexer, as shown in Fig. 2.16(a), with an injected optical comb as shown in Fig. 2.16(b) (with a shifted centre wavelength). The experiment was performed by Dr. Maryam Shayesteh, a postdoctoral researcher in the group. The SFP's main lasing mode is visible at a wavelength close to 1566 nm. The strongest side-mode in the laser's spectrum has a wavelength of approximately 1569 nm. Due to the optical coupling of the lensed fibre, both outputs of the demultiplexer could not be measured simultaneously. The comb's centre wavelength was stepped in increments of 0.001 nm in experiment.

side mode were 22.1 dB and 22.9 dB, and the slave laser was locked over 3.2 GHz in each case. The model did predict that the centre line of the comb locks to the side mode, however at 8 dB less peak power the injected power wasn't sufficient to suppress the main lasing mode. The locking ranges in the simulated case are larger than in experiment again as bi-stable and dynamical locking regions are included in Eq. (2.18), but the suppression seen in the model closely resembles what was measured.

The SMSR obtained when demultiplexing these optical combs does not meet the 30 dB figure required for most telecommunications applications, possibly as comb lines which the slave laser is not locked to only undergo a small amount of optical loss. To try and improve the SMSR obtainable, the following section investigates how the quality factor of devices affects the demultiplexing.

2.6 Cavity Quality Factor and Optical Comb Demultiplexing

We now wish to use our model to identify the parameters of the slave laser which can be optimised in order to increase the slave laser's demultiplexing ability. In the case of passive resonators, the quality factor (or Q factor) is related to the frequency selectivity of the resonator, with higher Q cavities acting as better frequency filters than those with low Q. As a result, we start by investigating how the Q factor of the laser cavity effects the SMSR of the injected optical comb. In the following, we vary the Q of a FP laser by varying the reflection of the facets, and measuring the Q of the equivalent lossless cavity, given by:

$$Q = \frac{2nl\omega}{c} \frac{-1}{\ln[R_1 R_2]}. \quad (2.32)$$

Figure 2.18(a) compares the SMSR achieved as the Q of the laser cavity is improved, when injecting a 3 line 12.5 GHz optical comb into a FP laser for high and low injection ratios. The

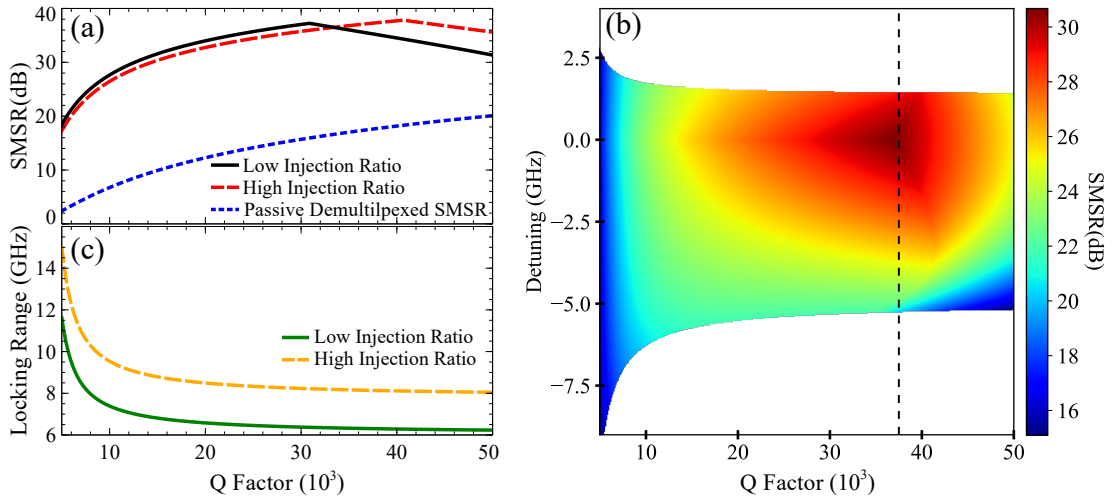


Figure 2.18: Calculated results from optical comb injection simulations, of a 700 μm FP laser. **(a)** Plot showing how the SMSR of the output spectrum varies as the Q of the laser cavity increases, for two different injection ratios, assuming zero detuning and biased at 3.0 times threshold. The higher injection ratio was initialised at 16.9×10^{-3} , and the corresponding lower injection ratio at 10.1×10^{-3} . For qualitative comparison, the SMSR from a passive cavity with equivalent Q is also plotted. **(b)** Intensity plot of how SMSR varies versus detuning and Q factor, for an injection ratio of 6.7×10^{-3} , at a current of 2.5 times threshold. The white regions indicate where the slave laser was unlocked. **(c)** Plot the locking range of the FP laser versus Q, for the same injection ratios and parameters as in (a).

slave laser was biased at 3 times threshold for each Q value used, to avoid influencing the results by increasing the pumping of the slave. As the power of the free running slave laser was not constant as a function of the Q factor, a fixed injection strength was used throughout, and hence the injection ratios are given for the lowest Q factor in each plot in Fig. 2.18. Figure 2.18(a) shows that for the lower injection ratio, the SMSR increases with improved cavity quality factor up until $Q = 31 \times 10^3$, with similar behaviour for the slightly higher ratio. As Q increases past this point, the other longitudinal modes in the laser cavity become less suppressed due to the optical injection, and as a result eventually the unlocked FP modes become stronger than the unlocked comb lines passing through the cavity. As shown in the red dashed line in Fig. 2.18(a), stronger injected optical powers suppress the unlocked FP modes up until a higher Q value. For a qualitative comparison, the SMSR obtainable from a passive FP cavity with equivalent Q is also plotted in Fig. 2.18(a), in a blue dotted line. Notably, the increase in SMSR seen by the injection locked FP laser sees a similar growth rate as the passive case.

The SMSR obtainable also varies with the detuning between the slave laser and the injected optical comb. Figure 2.18(b) shows a colour map of how the SMSR varies as the detuning and Q factor are varied. The importance of the detuning between the slave and master is highlighted, and as the Q factor of the laser increases, the gradient in the SMSR over the detuning increases notably. At $Q = 37.5 \times 10^3$ (marked with the vertical dotted line), we see that the SMSR varies by a maximum of 10 dB as the detuning is varied. As a result, even though the slave laser can account for some frequency drift in either the injected comb or its lasing frequency, this shows that drift can still strongly impact the output SMSR.

An investigation into the behaviour of the locking range of the laser as its quality factor is improved is presented in Fig. 2.18(c), for the two injection ratios used in Fig. 2.18(a). From the comparisons of the model with experiment in Section 2.5.2, we expect the locking range of

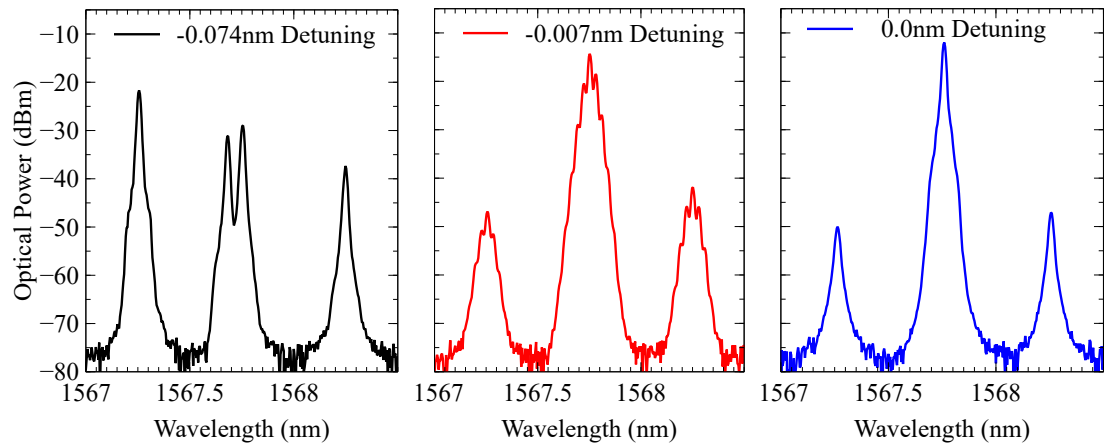


Figure 2.19: An example of four wave mixing occurring in a detuning sweep, where a single frequency is injected into a multi-mode FP device. Three different detunings are presented. At low detuning, there is no interaction between the injected signal and the slave laser. At -0.007 nm detuning, extra frequencies appear on all three laser modes shown, as the slave laser undergoes four wave mixing. Finally, the third panel shows the slave laser locked. The FP model cannot model the transition from no interaction to locked.

real devices to be slightly smaller than what's predicted here. However, the trend shown in Fig. 2.18(c) is encouraging, as for higher Q the locking range tends to a constant value.

We can conclude that higher Q cavities increase the SMSR obtainable. We have found that improving the Q of laser cavities increases the SMSR at a rate comparable to a passive demultiplexer. At higher Q values, the unlocked modes in the FP laser require a higher injected power to be suppressed, and as a result, the side modes become stronger than the comb lines which the slave laser is not locked to. The locking range of the slave laser varies slowly in high Q cavities, however the effect of detuning the slave laser relative to the injected comb increases in sensitivity as Q increases. If it was possible to create active lasers with very high Q factors (such as a high Q semiconductor ring laser), then it would be possible to use optical injection locking to demultiplex optical combs for use in optical communication systems.

2.7 Conclusions

In this chapter, a numerical model for simulating multimode devices was presented. The model was extended to include optical injection, by using an assumption that the injected field was much weaker than the free running field in the slave. By using transmission matrices to describe the reflection/transmission at each interface in a mirror, both single mode and multi-mode devices were investigated. Single frequency optical injection experiments and calculated results were compared, and good agreement was found between experiment and theory. Results for the SMSR obtainable when injecting an optical comb were also presented, and the effect of the Q factor of the slave laser on the demultiplexed comb output was investigated theoretically. It was found that increasing the Q factor of the device does increase the output SMSR, and that for a fixed pump rate relative to threshold, the locking range of the devices tends asymptotically to a fixed value with increasing Q . Hence, for high SMSR devices, high Q is required.

However, many of the interesting dynamical oscillations and quasi-periodic states typically observed in injection locking experiments are ignored due to the steady state assumptions in the model. For example, four wave mixing (a non-linear process in which two or more frequencies interact to create one or two more frequencies (as in Fig. 2.19)) or any oscillatory state in the slave-master system cannot be reproduced with the model as presented here. The following chapter describes work completed using a laser rate equation model, which inherently includes dynamical processes. With the rate equation model, higher injected powers can be used, and the difference between stable and unstable locking states can be discerned.

Chapter 3

Rate Equation Model and the Side Mode Suppression Ratio versus Comb Spacing

In the previous chapter, the Fabry-Pérot model was used to simulate the side mode suppression ratio (SMSR) obtainable when both single wavelength sources and optical combs were injected into a slave laser. While the model does reproduce the optical spectra well, the steady state assumption in the model excludes a lot of dynamics. Additionally, the optical injection was added to the model under the assumption that the master laser's field amplitude was weak in comparison to the free running slave's field.

Rate equation models have been used extensively to model laser dynamics in the literature [144], and models such as the one proposed in Ref. [142] have reliably reproduced the dynamics of optically injected lasers. Hence, to understand and study the dynamics which are omitted by the FP model, a single mode rate equation was formulated and implemented.

This chapter presents the work completed using this rate equation model, and further experimental results which show that the relaxation oscillations within the slave laser have a strong effect on the optical demultiplexing of the optical comb lines. With the insight from the rate equation model, it was found that due to beating between the unlocked comb lines and the slave laser, the slave's field and carriers are modulated slightly. In the following, the rate equation model used to investigate the optical injection is formulated. Early model predictions about how the SMSR varies with optical comb spacing is shown, and two different experimental attempts at measuring the SMSR versus comb spacing are presented. The experimental results show that the ROs can become undamped, and even frequency locked to rational fractions of the optical comb spacing. The chapter concludes by discussing how the SMSR varies over the Adler locking tongue, and investigating how the Adler locking tongue changes as optical combs with spacings close to multiples of the relaxation oscillation frequency are injected. Results from this chapter have been published in two separate journal articles; the first was published in Springer's journal of Optical and Quantum Electronics (see Ref. [87]), with the second published in the IEEE Journal of Quantum Electronics (Ref. [182]).

3.1 Rate Equation Model Description

The single mode rate equation model used was a slightly adapted version of the models in Refs. [135], [142]; the model simplifies the description of the slave laser's field and carriers by spatially lumping them to discrete entities. The rate of change of the slave laser's electric field is given as:

$$\frac{d}{dt}\tilde{E}_s(t) = \left(i\omega(N) + \frac{1}{2} \left[G_N(N - N_{th}) - \frac{1}{\tau_p} \right] \right) \tilde{E}_s(t) + F_{sp} + \eta f_d \tilde{E}_M(t), \quad (3.1)$$

where G_N is the laser's differential gain, N_{th} is the free running threshold carrier density, τ_p is the photon lifetime within the laser cavity, η is the coupling efficiency, f_d is the longitudinal mode spacing of the slave laser, and F_{sp} describes the spontaneous emission in the laser cavity. The change in angular optical frequency with carrier density is given as:

$$\omega(N) = \omega_0 + \frac{1}{2} \alpha G_N \Delta N, \quad (3.2)$$

where ω_0 is the free running angular frequency of the slave, α is the linewidth enhancement factor, and $\Delta N = (N - N_{th})$. Without light injection, the carrier density is clamped at the threshold value N_{th} where $G(N_{th}) = 1/\tau_p$. The field of the master laser $\tilde{E}_M(t)$ which couples to the slave laser's signal was defined as in Ref. [135]:

$$\eta f_d \tilde{E}_M(t) = \sum_j E_j e^{i(\omega_j t + \phi_j(t))}. \quad (3.3)$$

Here, E_j and ω_j are the field amplitude and angular frequency of the j -th comb line. We assume that the three comb lines are in phase, and without loss of generality we can assume $\phi_j(0) = 0$. A dimensionless optical injection strength K was defined as in Ref. [144], with $K = f_d E_j / \omega_r E_{0s}$. Both ω_r (the relaxation oscillation frequency) and E_{0s} (the steady state free running electric field amplitude of the slave laser) are defined analytically in the following subsection. It is important to note that K gives the strength of a single line in the comb, and hence the injection strength of the whole comb would be $3K$.

The field of the slave laser can be written in the most general form as:

$$\tilde{E}_s(t) = E_s(t) e^{i(\omega_s t + \phi_s(t))}. \quad (3.4)$$

Taking the derivative with respect to time of (3.4) gives:

$$\frac{d\tilde{E}_s(t)}{dt} = \frac{dE_s}{dt} e^{i(\omega_s t + \phi_s(t))} + E_s(t) \left(i\omega_s + i \frac{d\phi_s}{dt} \right) e^{i(\omega_s t + \phi_s(t))}, \quad (3.5)$$

and comparing this to (3.1) allows us to write rate equations explicitly for the amplitude E_s and phase ϕ_s of the slave laser's field:

$$\frac{dE_s}{dt} = \frac{1}{2} G_N (N - N_{th}) E_s(t) + \sqrt{\beta} \xi' + f_d \sum_j E_j \cos(\Delta\omega_j t - \phi_s(t)), \quad (3.6)$$

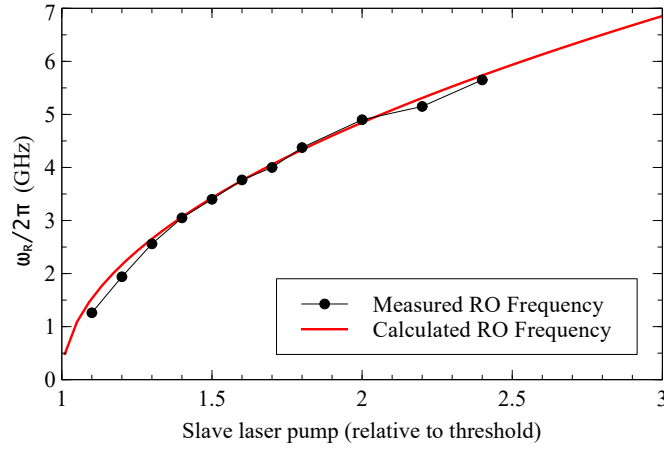


Figure 3.1: A comparison between the measured RO frequency and the calculated RO frequency (using Eq. (3.10)) of a single mode laser, for the parameter values presented in Table 3.1.

$$\frac{d\phi_s}{dt} = \frac{\alpha_H}{2} G_N (N - N_{th}) + \sqrt{\beta} \xi'' + f_d \sum_j \frac{E_j}{E_s} \sin(\Delta\omega_j t - \phi_s(t)), \quad (3.7)$$

where $\Delta\omega_j$ is the difference in the angular frequency of the free running laser and the j -th comb line, β defines the spontaneous emission strength, and ξ' and ξ'' are the Gaussian white noise source terms which contribute to the spontaneous emission term F_{sp} . The real and imaginary parts ξ' and ξ'' of the noise fulfil the conditions $\langle \xi'(t) \xi'(t') \rangle = \langle \xi''(t) \xi''(t') \rangle = \delta(t - t')$, and $\langle \xi'(t) \xi''(t') \rangle = 0$. The rate of change of carriers for a pump rate R_p was given as

$$\frac{dN}{dt} = R_p - \frac{N}{\tau_s} - G_N (N - N_{th}) E_s(t)^2 - \frac{1}{\tau_p} E_s(t)^2. \quad (3.8)$$

3.1.1 Free-Running Steady State Solutions

Disregarding the noise terms and the optical injection terms in the above equations, steady state values for the free-running slave laser can be determined. In steady state, the modal gain of the slave is zero, giving a steady state electric field amplitude E_{0s} of:

$$E_{0s} = \sqrt{\tau_p \left(R_p - \frac{N_{th}}{\tau_s} \right)} \quad (3.9)$$

The threshold pump of the free running slave laser is then $R_p = N_{th}/\tau_s$.

As in Ref. [142], the free running relaxation oscillation frequency ω_r is given by:

$$\omega_r = E_{0s} \sqrt{\frac{G_N}{\tau_p}} = \sqrt{G_N \left(R_p - \frac{N_{th}}{\tau_s} \right)} \quad (3.10)$$

Approximate values for N_{th} , G_N and τ_s were found by fitting measured values of the slave laser's free running relaxation oscillation frequency. Figure 3.1 shows a comparison between the measured and calculated values, where values of the other parameters were determined from examples in the literature [135]. All parameters values used in the model, unless otherwise stated, are presented in Table 3.1.

Table 3.1: Parameter values used in the rate equation model. Approximate values for N_{th} , G_N and τ_s were found by fitting measured values of the slave laser's free running relaxation oscillation frequency. All other values were taken from Ref. [135].

Differential gain	G_N	$8.1 \times 10^{-13} \text{ m}^3/\text{s}$
Slave laser natural frequency	ω_0	$3.798 \times 10^{14} \text{ rad/s}$
Spontaneous Emission Factor	β	1×10^{-5}
Threshold carrier density	N_{th}	$1.7172 \times 10^{24} \text{ m}^{-3}$
Linewidth enhancement factor	α_H	3.5
Carrier lifetime	τ_s	$1.5 \times 10^{-9} \text{ s}$
Photon lifetime	τ_p	$2.0 \times 10^{-12} \text{ s}$
Coupling efficiency	η	1
Longitudinal mode spacing of the slave laser	f_d	$36 \times 10^9 \text{ Hz}$

3.2 Model Results, Optimal Device Current and Predictions

As mentioned above, using a rate equation model gives information on how the slave laser's field, phase, and carriers evolve over time. This provides us with different methods of analysing the slave laser output than are available using the FP model. We no longer assume steady state operation, and can observe how the slave laser's field and phase vary dynamically in time. The slave's optical spectrum can be obtained from the field's time trace, and as the optical comb frequency spacings used here were significantly narrower than the inter-mode spacings in devices ($\approx 40 \text{ GHz}$), it was assumed that a single mode model would sufficiently describe the interaction between the comb and the lasing mode.

In order to solve the rate equations, a fourth order Runge-Kutta method was used (as described in Appendix E). The accuracy of the Runge-Kutta method depends on the time step used during the calculations – too coarse a time step, and the results might not be accurate [183], [184]. In order to choose a sufficiently small time step, free-running and simulations with optical injection were compared at multiple time steps, and the difference in results was computed. It was found that consecutive simulation results only differed by a small amount as the time steps were decreased below 1 picoseconds. More details are contained in Appendix E.1.

As an example of the model output, Fig. 3.2 shows the turn on dynamics over the first 50 ns, as a current of 1.6 times threshold is applied to the slave laser. Figure 3.2(a) shows how the electric field within the slave laser responds, and over the first 10 ns, the field's power spikes quickly, and a ringing can be observed as the field approaches its steady state value. Figure 3.2(b) shows the response of the slave laser's carrier density over the same time. As the electric field rises, the carrier density in the slave laser decreases. Ringing is also present in the carrier density, and reaches steady state as the slave's electric field settles. At $t = 25 \text{ ns}$ (marked with a red dotted vertical line), the slave is optically injected with a single wavelength source, at a detuning of 200 MHz, with an optical injection strength of $K = 0.0011$. Inset in Fig. 3.2(a) and (b) are plots centred around the free running steady state of the slave laser. As is clear in the inset figures, once the slave is optically injected, the slave's field and carrier density respond by oscillating around new steady states values. This ringing eventually settles to a new steady state, with the slave's field slightly stronger than the free running case, and the slave's carrier density slightly lower than in the free-running case.

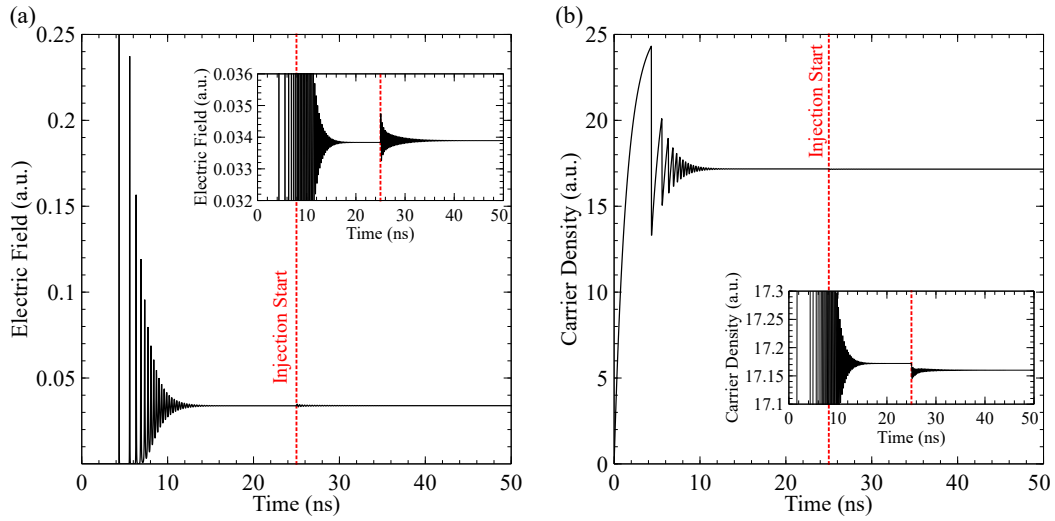


Figure 3.2: (a) Plot of the electric field in the slave laser as a function of time, for a noiseless simulation ($\beta = 0$). At $t = 0$, the pump parameter R_p was set to 1.6 times laser threshold. The field in the slave laser grows exponentially, and a characteristic ringing is seen after the field first spikes. After 15 ns, the laser's field has reached its steady state value. At $t = 25$ ns (indicated with a vertical dashed red line), the laser was optically injected with a single wavelength source, at a detuning of 200 MHz, with an optical injection strength $K = 0.0011$. Inset: the same simulated data, plotted with a smaller range on the y-axis. The effect of the injected light can be seen, as the slave laser's field is initially kicked from its steady state, and decays back to a new steady state. (b) Plot of the laser's carrier density as a function of time, for the same simulation as in (a). In the inset plot, it can be seen the slave's carriers are also affected by the injected electric field. After optical injection, the steady state value of the carrier density is reduced.

Information on the lasing spectrum of the slave laser can be obtained from the model by taking a numerical Fast Fourier transform (FFT) of the slave laser's field. With a time step of 2.56 ps, the resolution in the frequency spectra was 6.66 kHz. Care was taken to ensure the lasing frequency and the frequencies of all injected signals coincided exactly with a frequency on the Fourier transform frequency axis, as the signal strength measured by the FFT is underestimated if the frequency lies between two points on the frequency axis.

The model was used initially to reproduce results measured as the bias of the slave laser within a 1×2 demux was increased (the same demultiplexer shown in Fig. 2.16(a)). Experimental data showing the roll off of the SMSR as the slave bias was increased is shown in Fig. 3.3(b), with the corresponding experimental setup shown in figure 3.3(a) (these experiments were performed by a postdoctoral researcher in the group). The optical comb had a frequency spacing of 12.5 GHz, with optical power of +7 dBm. As the SMSR is affected by the detuning of the comb lines frequency relative to the slave laser's natural frequency [133]. The optical comb's center wavelength was swept slowly across the slave's frequency, and the highest SMSR value was taken from the trace. The slave laser was initially biased at threshold, which was 24 mA in the MMI section of the 1×2 demux, and 40 mA in the SFP gain and mirror sections, and then the current in the gain section was swept from 40 mA to 75 mA. In the experimental results shown, the SMSR increased from 12.5 dB at device threshold to 21.6 dB at 1.62 times threshold. The decrease in the SMSR after 1.62 times threshold was due to the increase in gain seen by the other comb lines. As expected, the locking width measured in the experiment also significantly decreased as the applied current increased, due to the increase in power in the slave laser [140].

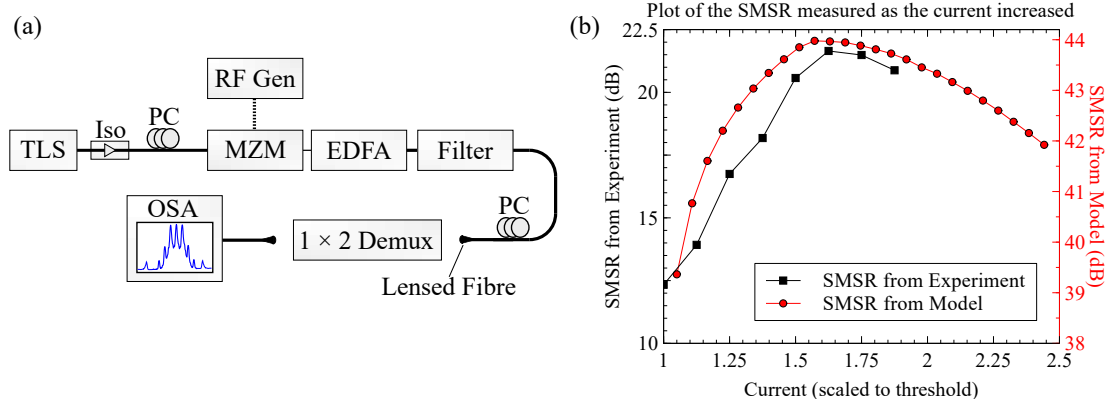


Figure 3.3: (a) The experimental setup used to measure the SMSR from the 1×2 device under test. The experiment was performed by Dr. Maryam Shayesteh, a postdoctoral researcher in the group. (b) Experimental (black) and theoretical (red) results showing the change in SMSR as the slave laser's current increased. The slave laser parameters used here were: $G_N = 7.9 \times 10^{-13} m^3 s^{-1}$, $N_{th} = 2.91924 \times 10^{24} m^{-3}$, $\alpha_H = 5.0$, $\tau_s = 2 \times 10^{-9} s$ and $\beta = 0$. All other parameters were as stated in Table 3.1.

The theoretical results shown in Fig. 3.3(b) match the trend of the experimental results well. Zero detuning was assumed between the center comb line and the slave laser's free running frequency (as will be shown later in Section 3.5, the amplification seen by the centre comb line only varies slightly with detuning for large comb spacings (>10 GHz)). The calculated SMSR increases from 39.36 dB to 44 dB, with a maximum SMSR at 1.57 times threshold. At threshold, the optical injection ratio used was -30 dB, and decreased to -35 dB as the slave's pump current was increased to 2.5 times threshold. The difference in magnitude between the SMSR in theory and in experiment is in part due to the single moded assumption of the model. As the free spectral range of the devices tested in experiment was 36 GHz, it was assumed that the injected 3 line comb with a spacing of 12.5 GHz only interacted with the main lasing mode of the slave laser. However in the test devices, the loss experienced by the unsupported combs lines in the SFP laser is lessened by the wide gain bandwidth of the active material. These simulation results also did not include spontaneous emission (i.e. $\beta = 0$), which means the gain seen by the unlocked comb lines is underestimated by the model, and hence the SMSR is over estimated in the theoretical results in Fig. 3.3(b). The model also does not consider the effect of injected light passing through the cavity (without any amplification associated with this transition). Including this effect would also decrease the SMSR computed in the model.

The dependence of the SMSR obtainable on the slave laser's drive current has an impact on the practical application of this technology – on an integrated device such as the one studied, the slave laser's wavelength can be tuned slightly by varying the temperature and the current pumped through the gain and mirror sections of the slave laser. The devices studied showed a 3dB decrease in the SMSR over a range of 0.25 times the threshold current. Hence, in practice we expect there to be a trade off between choosing the optimal device bias and frequency matching each slave to a line in the optical comb

Following these results, we became interested in numerically investigating if the SMSR changes when locking to the higher, lower, or centre frequency line in the three line optical comb. In particular, it was of interest to see how the slave laser responded as the frequency spacing decreased, as in the experiment only optical combs with spacings of greater than 10 GHz had been investigated at that point. Shown in Fig. 3.4(a), the simulated slave laser was injection

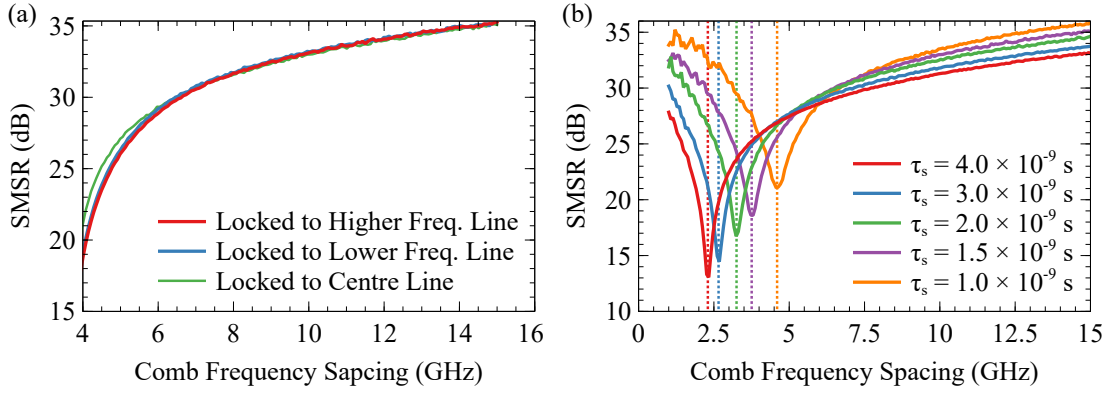


Figure 3.4: (a) Plot of how the calculated SMSR varied as the frequency spacing between the injected comb lines changed, when locked to the higher frequency, lower frequency and center frequency lines in a three line comb, with an injected power of $K = 0.0011$. (b) Plot of how the calculated SMSR varied as a function of comb spacing for different carrier lifetime values, when locked to the center line of a three line comb. The slave laser was driven at 1.6 times threshold for each run. The dotted vertical lines correspond to the analytically calculated relaxation oscillation frequencies for each τ_s .

locked to each line of a three line frequency comb. At large frequency spacings, there is no discrepancy between locking to any of the three comb lines used, which shows that as long as the neighbouring unlocked comb lines are sufficiently far away, they do not affect the demultiplexing. As the frequency spacing of the comb decreased, the performance of the demultiplexer worsens significantly, and a difference becomes noticeable between the case when the slave laser locked to the center line and the two outer comb lines, resulting in a 2 dB difference at a comb spacing of 4 GHz. When this was repeated using 5, 7 and 9 line optical combs, the SMSR obtained was qualitatively similar – the SMSR of the two comb lines on the extremes of the combs deviated slightly, showing that the slightly better SMSR can be obtained if there is some symmetry in the optical power on either side of the slave laser's mode.

The downward trend seen in the SMSR as the comb frequency spacing decreased in Fig. 3.4(a) was then investigated more thoroughly. Figure 3.4(b) shows the calculated results for different slave laser carrier lifetimes, as the comb's frequency spacing was swept from 1 GHz to 15 GHz. Again, zero detuning was assumed between the center comb line and the slave's free-running frequency. A constant injected power of $K = 0.0011$ was used, and the slave laser was pumped at 1.6 times threshold. Above 10 GHz, the suppression of the unlocked comb lines in the slave laser varies smoothly as the frequency is decreased, with little difference between the different carrier lifetimes. As the frequency spacing is decreased further, the SMSR drops sharply to a point, and then begins increasing again. Vertical dotted lines indicate the free-running relaxation oscillation frequency ω_r (as given by equation (3.10)). The minima of the traces in Fig. 3.4(b) match very well with the free-running RO frequency.

The frequency of the slave's ROs does vary slightly when the slave is optically injected, and specifically for single mode optical injection, the RO frequency can be described as [142]:

$$\omega_R^2 = \frac{G_N}{\tau_p} \left(\frac{E_{0s}^2 - \Delta N \tau_p / \tau_s}{1 + \tau_p G_N \Delta N} \right) \quad (3.11)$$

where E_{0s} is the steady state value for the electric field of the slave laser without optical injection.

tion introduced in Eq. (3.9), and ΔN is given by:

$$\Delta N = -2 \frac{f_d}{G_N} \frac{E_{\text{Inj}}}{E_0} \cos(\phi_L) \quad (3.12)$$

Here, ϕ_L is the locked phase of the slave laser, with $\phi_L = \arctan(\alpha_H)$ in the case of zero detuning. For the optical powers considered here, the RO frequency does not vary significantly from the free running case.

As these preliminary theoretical results indicate that the relaxation oscillations have a strong effect on how well a slave laser can demultiplex an optical comb, the next logical step in this project was to experimentally demonstrate this fact. Sections 3.3 and 3.4 detail the experiment work and results obtained in measuring the SMSR versus comb frequency spacing in two separate ways. The following subsection continues the theoretical investigation into how injecting with an optical comb differs from injecting with just a single frequency, and also comments on what occurs to the slave laser field amplitude, carrier density and phase when the injected comb frequency spacing matches the RO frequency.

3.2.1 Phasor Plots in Optical Comb Injection

Phasor diagrams can be used to show the three-dimensional phase space of Eqns. (3.6), (3.7) and (3.8) [144], [185]. Usually used to indicate asymptotic states, phasor diagrams are a concise way to show the limit cycle of the optically injected laser. This subsection will introduce what we mean by limit cycles, and briefly describe three common limit cycles. Using phasor diagrams, we can then compare how the phase, amplitude and carriers are affected by optical comb injection versus single mode injection, and how the comb spacing affects the damping of the relaxation oscillations in the slave laser.

Figure 3.5 shows three phasor diagrams (and their corresponding optical spectra) for the case of a laser under injection from a single frequency, for three different detunings. The diagrams show how the real E_R and imaginary E_I parts of the electric field vary, relative to the steady state free running values (similarly for the carriers). Each phasor diagram shows the output of the slave laser relative to the master over 50 ns (with $\beta = 0$). In Fig. 3.5(a), the master laser is detuned by -320 MHz from the slave. The phasor diagram shows that the limit cycle of the system is a stationary point, which means that the slave laser has constant intensity, active carriers, and relative phase. In this case, the slave laser is locked, with its phase and frequency matching that of the master.

Figure 3.5(b) shows the phasor diagram at zero detuning for the same optical injected power. Now the limit cycle is seen to oscillate in all three dimensions. This is an example of a limit cycle with bounded phase (i.e, the limit cycle does not orbit around the origin). Extra frequencies appear in the optical spectrum (at multiples m of the relaxation oscillation frequency, $\pm m\omega_r$), as the relaxation oscillations within the slave laser become undamped.

Finally, Fig. 3.5(c) shows a limit cycle with unbounded phase, where the detuning between the master and slave was set to 400 MHz. In this case, the slave laser is not frequency locked to the master, and lases at a frequency slightly shifted from the free running frequency (due to new average carrier density in the slave laser). As can be seen from the projection of the limit cycle onto the plane spanned by E_R and E_I , the limit cycle clearly orbits the origin, with

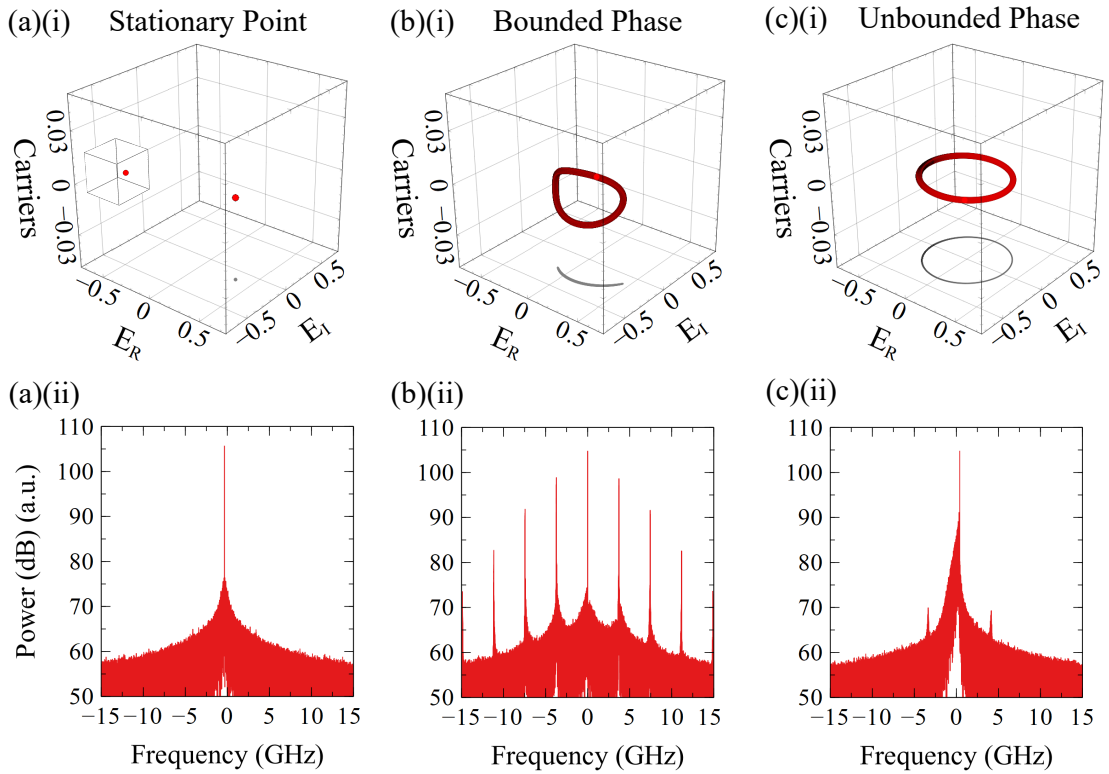


Figure 3.5: (i) Phasor diagrams and (ii) computed optical spectra for single frequency optical injection at different detunings. The optical spectra are plotted relative to the free running frequency of the slave laser. The optically injected power was fixed at $K = 0.0286$ at a slave laser pump of 1.6 times threshold, and the spontaneous emission was set to zero. The results presented are for detunings of (a) -320 MHz, (b) 0 MHz, and (c) 400 MHz. The projection of each limit cycle onto the complex E plane (spanned by E_R and E_I) is plotted in gray in the phasor diagrams. The inset figure in (a)(i) is a zoom on all three axes (Carriers go from -0.003 to 0.001, E_R goes from 0.31 to 0.39, and E_I goes from -0.17 to -0.11).

the slave laser's phase unbounded by the master laser. The optical spectrum now consists of many different frequencies in this case (due to processes referred to as four wave mixing or multiwave mixing [186]–[188]), as the frequency difference between the slave's lasing frequency and the injected frequency causes the slave's optical frequency to be modulated by this difference. Notice also in this case that the relaxation oscillations are less damped than in the stationary point case, appearing at ± 3.75 GHz.

Next, we compare the limit cycles in the single frequency injection case to those when optically injecting with a 10 GHz three line optical comb. In particular, this allows us to see the effect of the unlocked comb lines on how well “bounded” the slave's intensity, phase, and carrier density are under comb injection. In order to make direct comparisons between the single frequency injection cases (Fig. 3.5) and the comb injection cases (Fig. 3.6), the laser parameters and the initialisation of the slave laser was kept identical, however now the master laser signal featured three different frequencies with equivalent optical power as used in Fig. 3.5.

Figure 3.6(a)(i) shows the phasor diagram for a detuning of -320 MHz. In the single frequency injection case, the limit cycle was by definition a stationary point. With comb injection, the unlocked comb lines modulate the slave laser with a frequency corresponding to the comb frequency spacing (this is an inevitability, due to the $\cos(\Delta\omega t)$ and $\sin(\Delta\omega t)$ terms in Eqns. (3.6) and (3.8)). As a result of this modulation, from a strictly mathematical point of view,

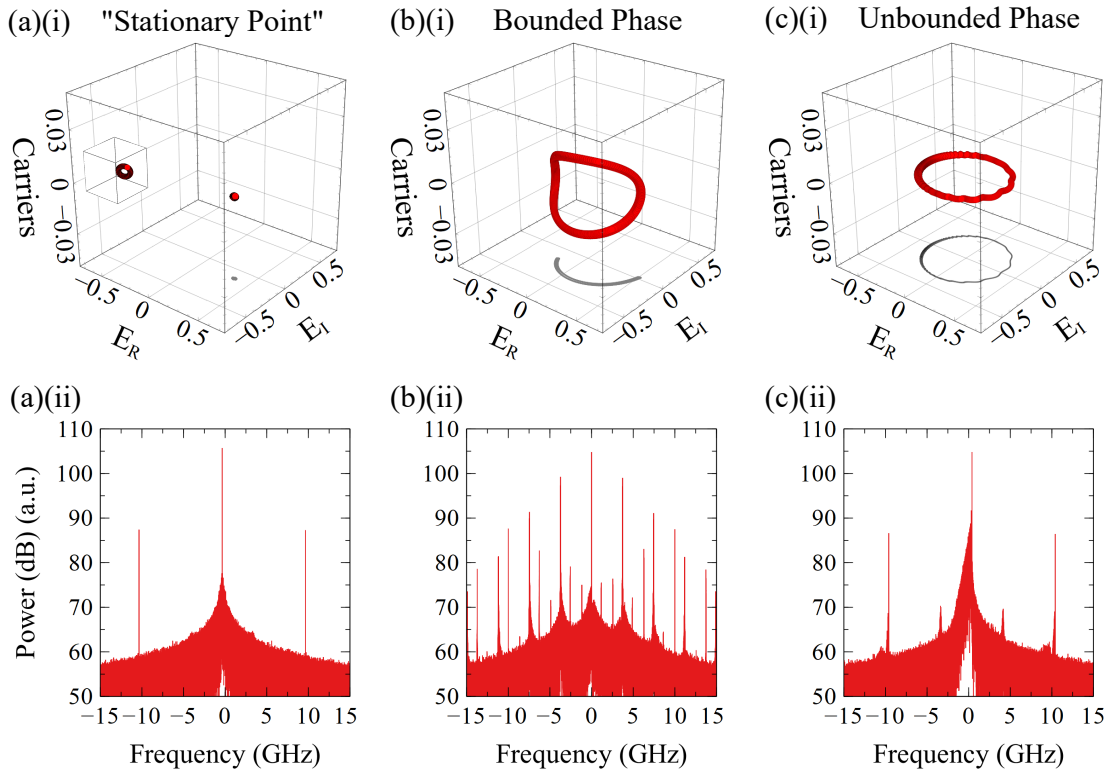


Figure 3.6: (i) Phasor diagrams and (ii) computed optical spectra for comb injection at different detunings. The optical spectra are plotted relative to the free running frequency of the slave laser. Each line in the three line 10 GHz optical comb had a power of $K = 0.0286$. The slave laser was pumped at 1.6 times threshold, and the spontaneous emission was set to zero, allowing a direct comparison between the single frequency injection and optical comb injection case. The diagrams presented are for detunings of (a) -320 MHz, (b) 0 MHz, and (c) 400 MHz. The projection of each limit cycle onto the complex E plane (spanned by E_R and E_I) is plotted in gray. The inset figure in (a)(i) is a zoom on all three axes (Carriers go from -0.003 to 0.001, E_R goes from 0.31 to 0.39, and E_I goes from -0.17 to -0.11).

the slave-master system can never be in a stationary state when the master laser consists of multiple frequencies (hence the quotation marks in the title of Fig. 3.6(a)). Closely comparing Fig. 3.6(a)(i) with Fig. 3.5(a)(i) reveals the projection of the limit cycle is slightly larger in the optical comb case. Of course, the optical spectrum shows all three comb lines present in the spectrum; the centre comb line to which the slave is locked has the largest amplitude, and the two unlocked side modes are significantly suppressed. As the suppression of the unlocked comb lines increases, the limit cycle with comb injection approaches that of the single frequency injection case.

The limit cycle's growth with optical comb injection is more apparent in Fig. 3.6(b)(i). When comparing Fig. 3.6(b)(i) with Fig. 3.5(b)(i), it is clear that E_R , E_I and the carrier density oscillate with a larger amplitude when an optical comb is injected. As with the bounded phase case previously, extra optical frequencies appear in the slave laser's output spectrum. Again, frequencies appear at multiples of the RO frequency, with other weaker frequencies occurring due to four wave mixing between the new RO frequency lines and the unlocked comb lines. As is intuitively clear, regions where the slave laser has undamped ROs need to be avoided when demultiplexing optical combs, as the extra frequencies generated strongly effect the demultiplexing.

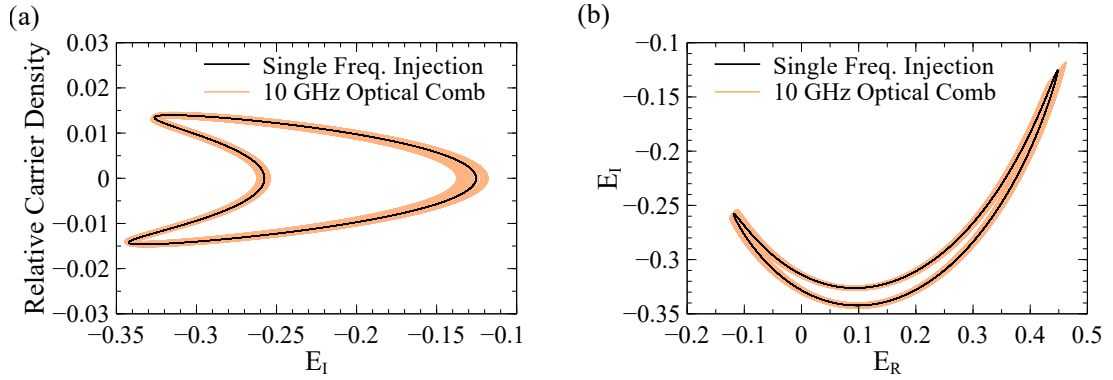


Figure 3.7: Comparison between the bounded phase limit cycles presented in Fig. 3.5(b) and Fig. 3.6(b). This difference is exasperated further when noise is included in the numerical calculations.

Figure 3.7 shows two dimensional comparisons between the single frequency and optical comb bounded phase limit cycles. Figure 3.7 gives a sense of how much more the carrier density and the field's components oscillate. The limit cycle for the case of the optical comb is closely related to the single frequency case, and it is clear the ROs are more weakly damped under injection from the optical comb.

An example of the unbounded phase limit cycle is shown in Fig. 3.6(c)(i), where the slave laser has become unlocked from the centre line of the comb. Again in this case, the limit cycle orbits the origin of the complex E plane. For the parameters chosen, the injected comb was strong enough to cause the carriers to oscillate throughout the limit cycle. The optical spectrum in this case shows many frequencies around the main lasing peak, with four wave mixing occurring around each of the injected comb lines. The unlocked comb lines also contribute to the change in the average carrier density, slightly varying the slave's lasing frequency in this case.

The above results have shown the impact of optically injecting with a 10 GHz comb – as discussed previously (e.g. Fig. 3.4), optically injecting with a comb spacing which matches the RO frequency significantly affects how much the unlocked comb lines are suppressed. As the modulation due to the unlocked comb lines resonates with the natural RO frequency within the slave laser, the ROs become very weakly damped. As an illustration, time traces and a phasor diagram are presented in Fig. 3.8, which show the increase caused in the oscillations when the comb spacing matches the RO frequency. From the time traces in Fig. 3.8(a) and (b), the oscillations in the 10 GHz and 3.75 GHz comb spacings are almost sinusoidal, with the amplitude oscillations an order of magnitude larger in the ω_R case. In Fig. 3.8(c) we see that for a comb spacing of 2 GHz (less than the relaxation oscillation frequency), the limit cycle shrinks in size, approaching the same size as the 10 GHz case. This is as expected from the results presented earlier, as it was shown that the SMSR increases below the RO frequency.

It is possible to experimentally measure the relative phase between a master and slave laser in single frequency optical injection [185], [189], [190]. Using a similar setup as in references [185], [191], it could be of interest to try and measure the relative phase of a demultiplexed line from an injected comb, and experimentally reproduce some of the work presented in this subsection. Due to equipment and time constraints, measuring experimental phasor diagrams was not possible as part of this project.

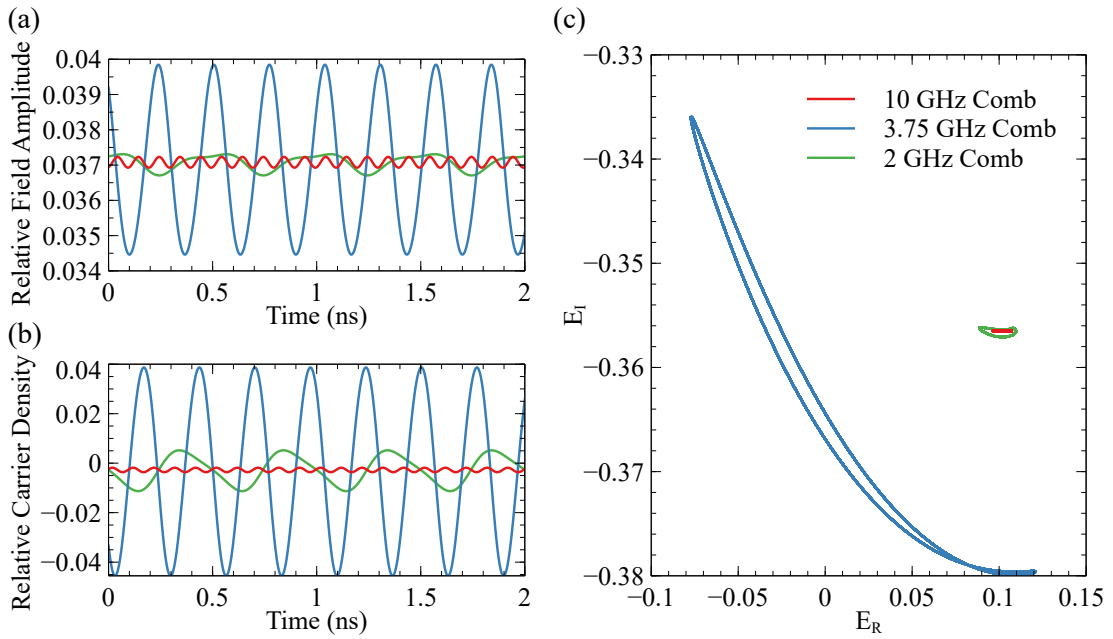


Figure 3.8: Comparison showing how the comb spacing effects the undamping of the relaxation oscillations. In each case, a three line comb with optical power $K = 0.0172$ was injected at zero detuning. The slave laser was pumped at 1.6 times threshold, and the spontaneous emission was set to zero. The results show the slave laser output from the last 2 ns of a 0.15 ms simulation. **(a)** The electric field amplitude from the slave laser, relative to the free running steady state. **(b)** The carrier density, relative to the free running steady state. **(c)** Two dimensional phasor plot, which shows how large the limit cycle grows as the comb spacing approaches the relaxation oscillation frequency ($\omega_r = 3.75$ GHz).

3.3 Probe Signal Method of Measuring Narrowly Spaced Demultiplexed Optical Combs

As discussed in the previous sections, the rate equation model predicts that the performance of these demultiplexers decreases significantly as the frequency spacing of the optical comb approaches the relaxation oscillation frequency. Demonstrating this in an experiment however was difficult, as standard optical spectrum analysers have optical resolutions of 2 GHz. As shown in Fig. 3.9, for optical comb spacings as low as 5 GHz, the power levels of the comb lines which the slave laser is not locked to can become masked by the envelope of the locked comb line. Figure 3.9(a) shows a flat 5 GHz comb measured on the 2 GHz OSA, and for comparison, Fig. 3.9(b) shows the same comb with a lower RF bias, creating a 5 GHz comb with unequal power in the comb lines. Vertical black dotted lines indicate the frequencies of the strongest three lines in the comb. Figure 3.9(b) highlights that the maximum measurable SMSR of a 5 GHz comb is approximately 20 dB, as the side modes in the comb are barely visible in the trace. As the comb spacing decreases, this problem worsens.

Hence, in order to measure these narrowly spaced demultiplexed combs, a separate experimental set-up was created, illustrated in Fig. 3.10(a). The slave laser was a single moded InP device lasing at approximately 1550 nm (as in Appendix A), with a free running SMSR of 40 dB at 90 mA (which was 1.8 times threshold). A circulator was used to collect the light from the slave laser output, which was monitored on an optical spectrum analyser (OSA). As the resolution of the OSA was insufficient to monitor the SMSR of demultiplexed combs with

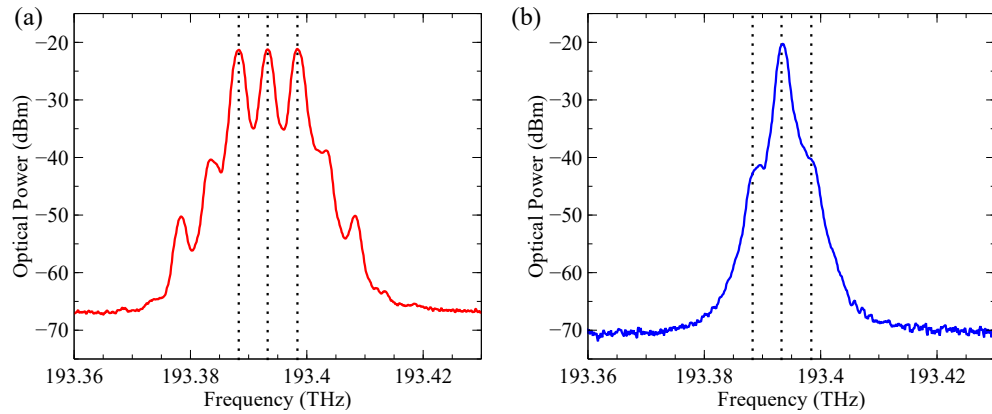


Figure 3.9: Optical spectra from a standard 2 GHz resolution optical spectrum analyser. **(a)** The optical spectrum of a flat 5 GHz optical comb. There is equal power in all three comb lines. Vertical black dotted lines indicate the frequencies of the three main lines in the comb. **(b)** Similar optical spectrum of a 5 GHz optical comb, as an example of how the optical resolution limited the measurement of the SMSR. The RF power of the MZM was lowered from the value used in (a), causing the side comb lines to decrease in power, until they became barely visible. Again, vertical black dotted lines indicate the frequencies of the three main lines in the comb. This example shows that 20 dB SMSR is approximately the maximum SMSR measurable with a 5 GHz comb (or at least on the 2 GHz resolution OSA used). For lower comb spacings, this maximum SMSR decreases further.

spacings below 5 GHz, the beat signal between the unlocked comb lines and a second tunable laser source (TLS) (named the probe TLS) was measured on an electrical spectrum analyser. In this way, the variation in the magnitude of the beat signal was used to monitor the strength of the comb's side modes, as the power of the probe TLS was fixed, and both the photo detector and the ESA had known frequency responses between 1 GHz and 10 GHz. Figure 3.10(b) illustrates how the lasing wavelength of the probe TLS was fixed relative to the comb. The probe TLS was tuned such that, for a comb spacing of Δ , there was a frequency separation of $\Delta/3$ between the unlocked side mode and the probe wavelength.

As an example, an ESA trace of a demultiplexed 6 GHz comb (i.e., $\Delta = 6$) beating with the probe TLS is presented in Fig. 3.11(a). The beat notes at $\Delta/3$ and $2\Delta/3$ are the most pronounced, and a weak signal at 6 GHz can also be seen, which corresponds to the beating between the comb lines. The signals at $\Delta/3$ and $2\Delta/3$ are broad due to a frequency jitter in the probe TLS. The probe TLS used in this case was an ID Photonics CoBrite-DX1, and this frequency jitter is imposed by the manufacturers of the TLS to ensure that the laser's frequency is nominally set around the correct frequency. It was confirmed prior to testing that this is the case using a real time spectrum analyser with a 40 μ s spectrum frame time, and found that clear narrow beat notes could be achieved when beating the demultiplexed comb with several other laser sources around 1550 nm. However, this frequency jitter added an extra uncontrollable element to the measurements, as both the height and position of the beat notes varied with each trace, as shown clearly in Fig. 3.11(b). To average out the variation in magnitude of the beat notes, each ESA trace was recorded 10 times, and the maximum beat note at approximately $\Delta/3$ was then averaged over all traces. The maximum beat note was chosen, as larger beat notes correspond to a worse SMSR, and hence this method should under estimate the change in the SMSR.

The experimental results obtained from the SMSR versus comb spacing experiment are shown in Fig. 3.12. The slave laser was locked to the centre line of the 3 line optical comb, and

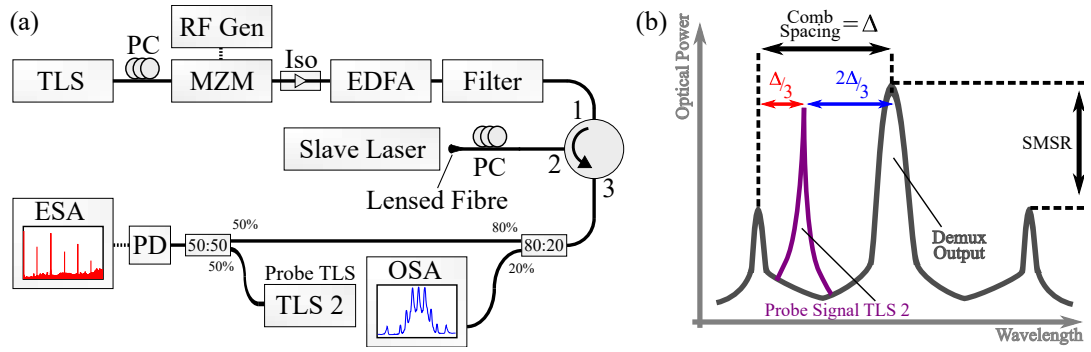


Figure 3.10: (a) The experimental setup used to perform the comb experiments. TLS: Tunable laser source, MZM: Mach zehnder modulator, PC: Polarisation controller, EDFA: Erbium doped fibre amplifier, OSA: Optical spectrum analyser, PD: Photodiode, ESA: Electrical spectrum analyser. The slave laser was a 15 pit device, as described in Appendix A. (b) Illustration showing where the probe wavelength from the second TLS was located relative to the demultiplexed comb. The probe laser could be tuned at each step of the experiment.

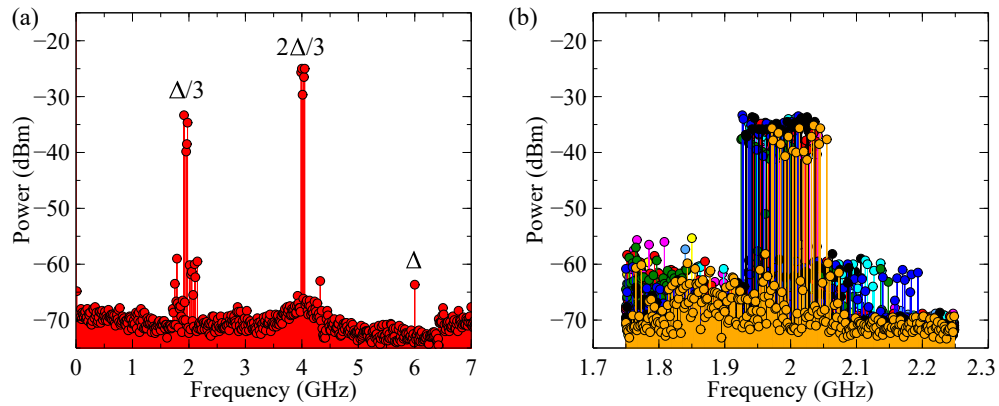


Figure 3.11: Example ESA traces measured while performing the SMSR versus comb spacing experiment. The slave laser was biased at a current of 90 mA throughout, and in this case a 6 GHz comb with an injected power of -8 dBm was used. (a) A wide ESA sweep, showing the beat notes measured at $\Delta/3 = 2$ GHz, $2\Delta/3 = 4$ GHz, and Δ . The beat notes at $\Delta/3$ and $2\Delta/3$ are broad, due to jitter in the probe TLS frequency. (b) Ten separate ESA traces plotted on top of each other. The peak magnitude of each trace was averaged to give the final measured value.

approximately zero detuning was maintained through the experiment. The experimental results (plotted in black on the left vertical axis) show the magnitude of the beat note between the probe TLS and the demultiplexed comb line as the comb spacing was varied. The results show the average beat note obtained over five tests, and the error bars indicate the maximum and minimum beat note strengths measured. Due to the minimum frequency step size of the probe TLS, the comb spacing was varied in steps of 1 GHz. We see the magnitude of the beat note increased significantly around a comb spacing of 5 GHz, and a rise in the beat note between the demultiplexed line and the probing signal indicates that the output SMSR of the device decreased, as the probe TLS had constant power.

These results confirm the early predications made using the rate equation model; for comparison, simulated SMSR results are shown in red, plotted on the right axis in Fig. 3.12. The dotted vertical line indicates the free-running relaxation oscillation (RO) frequency of the slave laser in experiment and theory, which was measured experimentally to be 4.375 GHz at bias of 90 mA. As discussed above in Section 3.2, the dip in the SMSR around the RO frequency is due

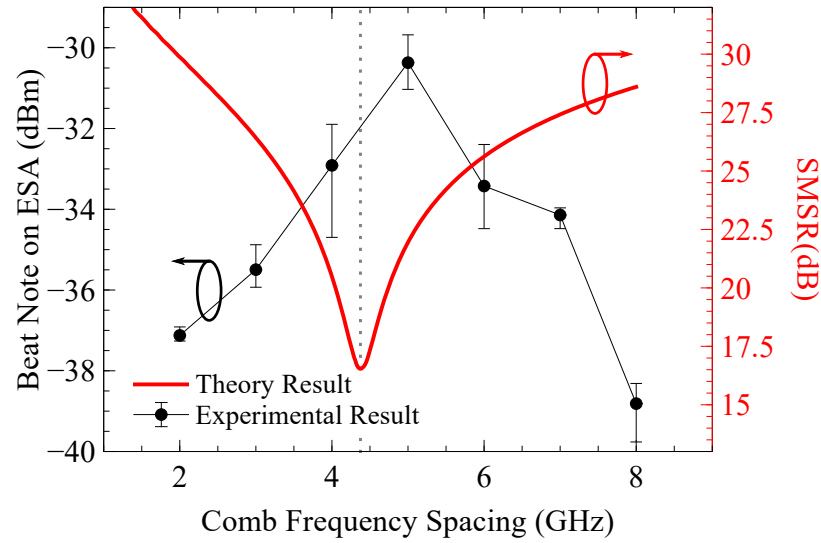


Figure 3.12: Experimental results (left axis) showing the average beat note of the unlocked comb line with the probe TLS versus comb spacing obtained over five experimental runs, with an inject power of -8 dBm. The error bars on the experimental results show the maximum and minimum values obtained over the five experiments performed. On the right axis, simulated SMSR results are presented, for an injected field strength of $K = 0.024$, at 1.8 times threshold.

to modulation of the unlocked comb lines resonating with the natural resonant frequency of the carriers.

Using this method of measuring the SMSR, good agreement between theory and experiment was observed. However, this method of measuring the optical SMSR had several drawbacks. Firstly, we were only able to measured the qualitative change in the SMSR, and hence could not indicate the magnitude of the drop in the SMSR. Additionally, due to the limitations imposed by the probe TLS's frequency step size, the optical comb's spacing could only be varied by 1 GHz. Closely examining what occurred as the comb's frequency spacing matched that of the slave laser's RO frequency was impossible with the set-up presented in this section. For the above reasons, the research group invested in a high resolution optical spectrum analyser, which had an optical resolution of 5 MHz. With such a significant improvement in the optical resolution, the experiment detailed in this chapter was revisited. The following section details the results obtained using the high resolution OSA.

3.4 SMSR Versus Optical Comb Spacing

Due to the reasons outlined in the conclusion of the previous section, a high resolution optical spectrum analyser was purchased in order to directly measure the demultiplexed outputs. The new OSA increased the optical resolution by almost 3 orders of magnitude, from 2 GHz to 5 MHz. Figure 3.13(a) shows the dramatic difference in the resolution obtainable, by comparing the same 5 GHz comb measured on both the high resolution and the standard OSA.

The SMSR versus comb spacing experiment was revisited using the new OSA, with a slightly different experimental set-up, as illustrated in Fig. 3.13(b). A commercial master laser (ID Photonics CoBrite-DX1) was intensity modulated using an Oclaro LiNbO3 Mach-Zehnder modu-

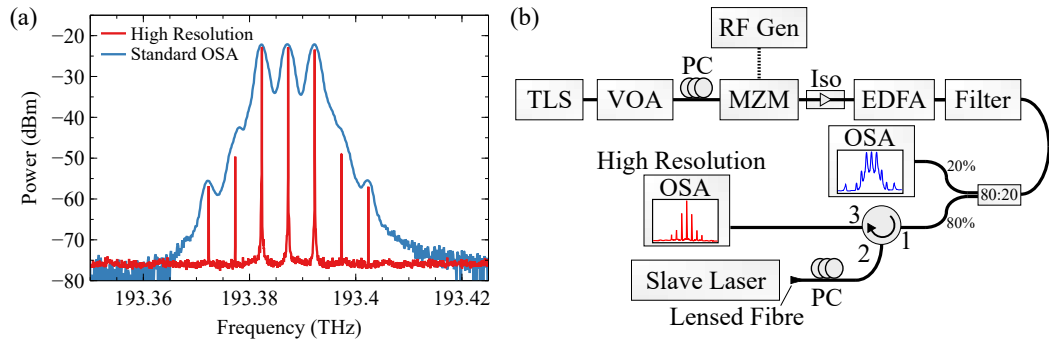


Figure 3.13: (a) Comparison of 5 GHz optical comb spectra, measured on a 2 GHz resolution OSA and a 5 MHz high resolution OSA. (b) Experimental setup used to investigate the SMSR obtainable. TLS: Tunable laser source, VOA: Variable optical attenuator, MZM: Mach zehnder modulator, PC: Polarisation controller, Iso: Optical isolator, EDFA: Erbium doped fibre amplifier, OSA: Optical spectrum analyser.

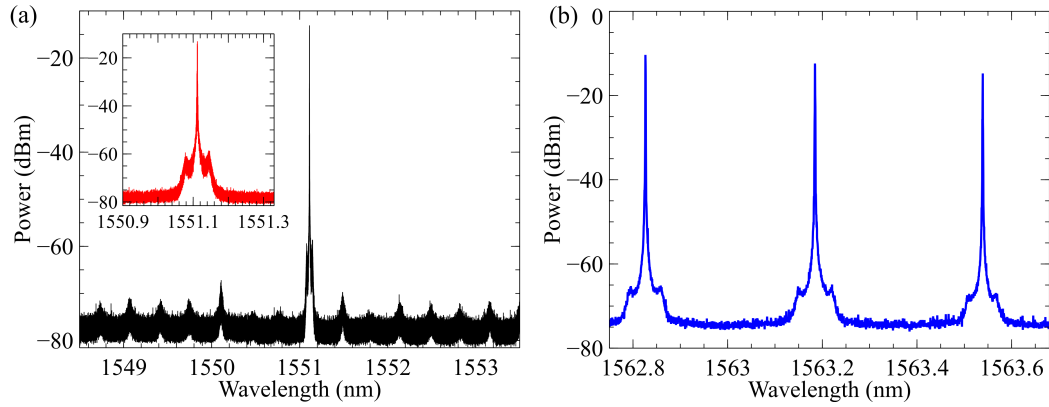


Figure 3.14: Free-running spectra measured using a high resolution optical spectrum analyser. (a) Free running single mode device, at 1.8 times threshold. Inset: Zoom in around the main lasing peak. (b) Free running spectrum of a 1050 μm Fabry-Pérot device at 3.5 times threshold. Only 3 modes in the FP laser spectrum are shown, in order to make the small side peaks on each mode visible.

lator (MZM), to create a 3 line optical comb. The optical comb power injected into the slave laser was controlled using both a variable optical attenuator (VOA) and an erbium doped fibre amplifier (EDFA). An optical filter was used to remove the amplified spontaneous emission introduced by the EDFA. Two optical spectrum analysers (OSAs) were used; the standard 2 GHz resolution OSA (Ando AQ6317B) was used to ensure there was equal power in the 3 lines of the injected optical comb, while the 5 MHz resolution OSA (Apex AP2061A) measured the output SMSR from the slave laser. The slave laser used was an unpackaged single mode laser (a 15 pit device, as described in Appendix A), with a free running SMSR of > 35 dB emitting at 1550 nm, mounted on a brass temperature controller. Optical coupling to the slave laser was achieved using a lensed fibre.

The drop in SMSR at the RO frequency becomes intuitively clear when the free running spectrum of the slave laser's is recorded in high resolution. As shown in Fig. 3.14(a), even with a strongly single mode laser, the modulation caused by the relaxation oscillations adds frequency noise to the optical spectrum of the slave laser. In the inset plot in Fig. 3.14(a), two side peaks at a power level of approximately -60 dBm can be seen on either side of the main lasing mode, at the expected frequency of the ROs. Hence, as the unlocked comb lines approach these side peaks, they sum with the frequency noise created due to the ROs, which causes the

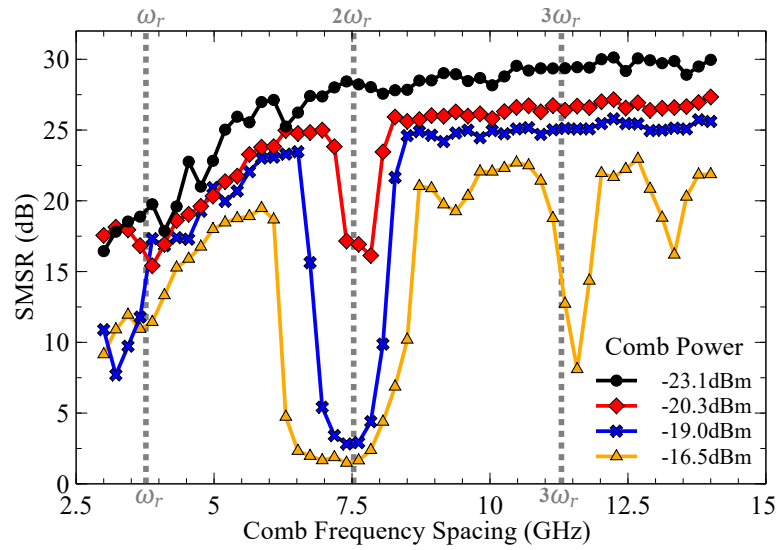


Figure 3.15: Measured SMSR as the frequency spacing of the injected optical comb was varied, for four different optical injection strengths. The slave laser was maintained at current of 80 mA, at which the frequency of it's relaxation oscillations were measured to be 3.765 GHz. The free running power coupled into the lensed fibre from the slave laser was -2 dBm. Each point shows the average of 50 measurements. Vertical gray dotted lines mark the first three multiples of the relaxation oscillation (ω_r , $2\omega_r$, and $3\omega_r$).

SMSR to worsen. These peaks of frequency noise due to the ROs are present around all lasing modes; Figure 3.14(b) shows 3 modes from a FP laser biased at 3.5 times it's threshold. The amount of frequency noise around each longitudinal mode is proportional to the strength of the mode.

Figure 3.15 shows how the measured SMSR varied as the injected optical comb frequency spacing was swept from 14 GHz to 3 GHz, repeating the experiment performed in Section 3.3 with better frequency resolution. The detuning between the slave laser and the centre line of the three line optical comb was approximately zero, and each point shows the average of 50 measurements. Four comb injection strengths are presented; for the lowest injection strength (-23.1 dBm), the SMSR decreases smoothly as the comb spacing was varied from 14 GHz to 3 GHz, dropping 14 dB in total. As shown previously, when the optical comb frequency spacing approaches the frequency of the relaxation oscillations, the SMSR reduces significantly. The relaxation oscillation frequency ω_r of the slave laser was measured to be 3.765 GHz, and the first three multiples of ω_r are marked by grey vertical dotted lines in Fig. 3.15. It is known that optical injection can modify the dampening mechanism of the relaxation oscillations [179], and cause the ROs rise in optical power. The intrinsic modulation due to the relaxation oscillations adds to the frequency noise around each mode within the slave laser, and hence as the unlocked optical comb lines approach the RO frequency, they sum to the already heightened noise floor.

As the optical injection strength is increased in Fig. 3.15, the SMSR can be seen to decrease over all comb spacings. However it was found that the SMSR can also decrease sharply at specific comb spacings. For comb powers of -20.3 dBm (red diamonds) and -19.0 dBm (blue x's), the SMSR drops sharply at 7.5 GHz, as the comb's frequency spacing approaches $2\omega_r$. As the injection strength increases, this dip widens and the SMSR drops to only a few dB. For the highest optical injection strength presented, further decreases in the SMSR are seen,

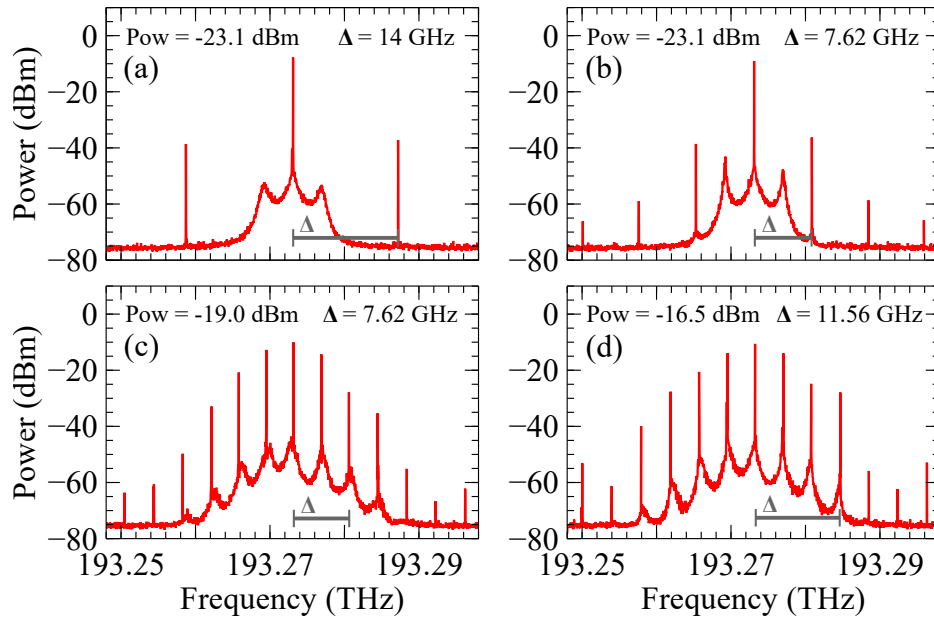


Figure 3.16: Demultiplexed optical spectra, measured using an optical spectrum analyser with 5 MHz resolution. The spectra presented highlight four operating conditions with distinct behaviour. **(a)** Injected power of -23.1 dBm, comb spacing $\Delta = 14$ GHz: Low RO power. **(b)** Injected power of -23.1 dBm, comb spacing $\Delta = 7.62$ GHz: ROs become undamped, rising in power. **(c)** Injected power of -19.0 dBm, comb spacing $\Delta = 7.62$ GHz: ROs frequency lock to $\Delta/2$. **(d)** Injected power of -16.5 dBm, comb spacing $\Delta = 11.56$ GHz: ROs frequency lock to $\Delta/3$.

with another significant decrease occurring as the comb's frequency spacing matches $3\omega_r$, with smaller drops in performance occurring at approximately $\frac{3}{2}\omega_r$ and $\frac{5}{2}\omega_r$.

The cause of these drops in the SMSR at comb spacings of $2\omega_r$ and $3\omega_r$ is shown in Fig. 3.16. Different demultiplexed optical spectra are presented, indicating four different types of behaviour. Figure 3.16(a) shows the slave laser output spectrum as the slave was locked to the centre line of a 14 GHz optical comb, with optical SMSR of 30 dB. The ROs in the slave (located ± 3.675 GHz from the centre line) are 40 dB lower than the lasing peak. As shown in Fig. 3.16(b), the ROs become further undamped when the comb spacing is narrowed to 7.62 GHz. If the optical power is increased even further, the ROs can become excited, rising higher than the sidemodes of the comb and reducing the output SMSR. The excited ROs within the slave laser can even stably frequency lock to half of the optical comb (as shown in Fig. 3.16(c)), which causes the output comb to have half the frequency spacing of the input comb.

As the injected comb's power is increased even further, it has been found that the ROs within the slave laser can frequency lock to the injected optical comb's frequency spacing whenever ω_r matches a multiple the comb's frequency spacing. Demonstrated in Fig. 3.16(d), even while frequency locked to $\frac{1}{3}$ of the optical comb spacing, the excited ROs over take the side modes in the injected optical comb, causing the SMSR to approach zero.

Figure 3.17(a) shows simulated results of the SMSR versus frequency spacing experiment performed in Fig. 3.15. There is good qualitative agreement between theory and experiment; as the experimental results indicated, the SMSR decreases as the injected power is increased. The calculated SMSR declines as the comb spacing was varied from 14 GHz to the relaxation frequency ω_r , however after the reaching the relaxation oscillation frequency, the SMSR can

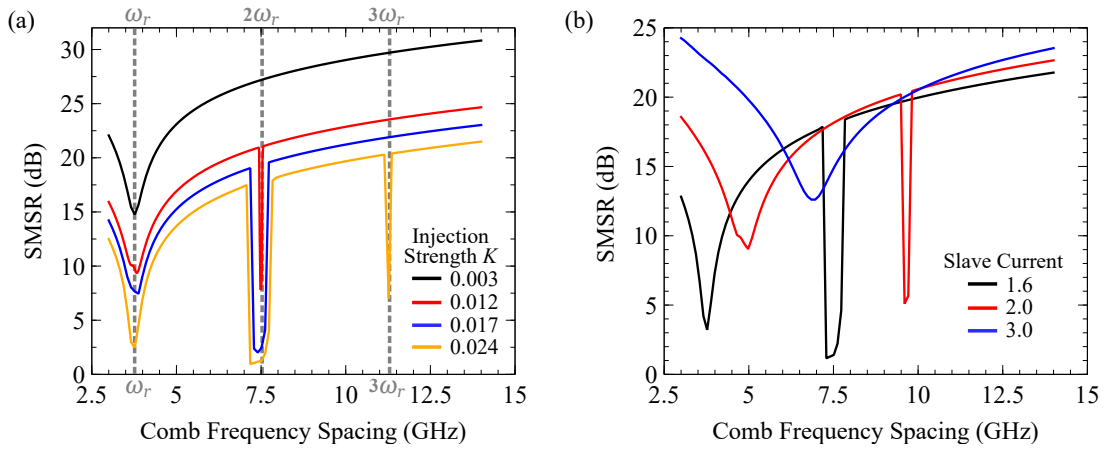


Figure 3.17: (a) Calculated SMSR versus frequency spacing, simulating the experimental results presented in Fig. 3.15. (b) Calculated SMSR versus injected comb frequency spacing for pump currents of 1.6, 2.0 and 3.0 times the free running laser threshold, with an injected comb power of $K = 0.0229$. As the pump current is increased, the relaxation oscillations vary in frequency.

be seen to increase again. This could be due in part to unrealistic modelling of the ROs; the measured device ROs span a wider frequency range than in the calculated results. This is also likely the cause of the discrepancy between the widths of the regions where the ROs become locked, as these are seen to be larger in experiment than in theory. However, good agreement is still seen, as at higher powers the model also predicts drops in the performance at frequency spacings close to ω_r , $2\omega_r$ and $3\omega_r$, as seen in experiment.

The large drops in SMSR at specific comb frequency spacings can be avoided by increasing the slave laser's pump current. Increasing the slave's current increases both the free running RO frequency and the dampening of the ROs. As shown in Fig. 3.17(b), increasing the pump current from 1.6 times threshold to 3.0 times threshold can improve the SMSR at a specific comb spacing, and can even stop the ROs becoming excited and locking to a fraction of the injected comb's frequency spacing. The results from Fig. 3.3(b) can be explained by interpreting Fig. 3.17(b) slightly differently, as the decrease in the SMSR seen with increasing pump current past a certain point in Fig. 3.3(b) is due to the dip in SMSR at the RO frequency moving closer to the comb spacing used. As the bandwidth over which the slave laser remains locked is directly proportional to the ratio of the free-running slave's power to the injected power, increasing the pump current in turn decreases the locking bandwidth. The model also omits any roll off in the laser's gain as the current is increased, and we expect that as laser gain clamps, further increasing the optical pumping will also lead to a degradation in SMSR.

3.5 SMSR Versus Detuning

In the previous section, it was shown that the relaxation oscillations can become excited, and even frequency lock to fractions of the optical comb spacing. The results presented up to this point in this chapter have focused on cases with zero detuning. In the following section, we consider what occurs when the optical comb is detuned from the free running frequency of the slave laser.

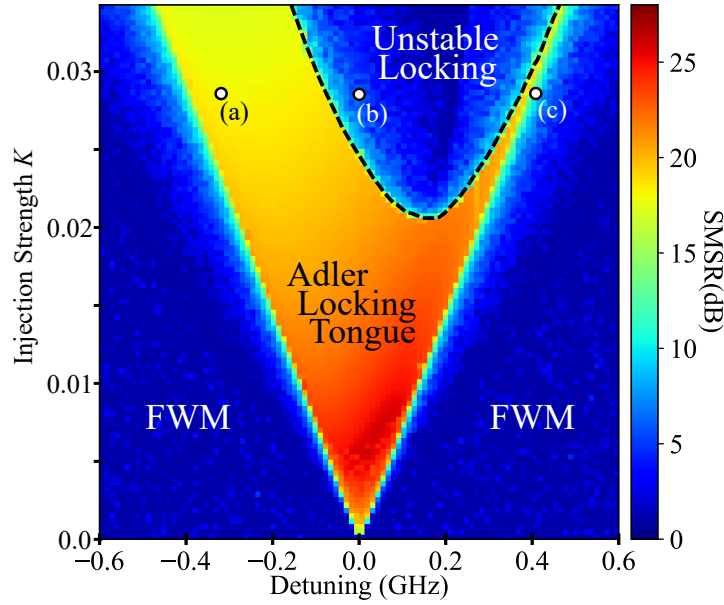


Figure 3.18: Calculated intensity plot showing the slave laser output SMSR, as a function of detuning and optical injection power, for a three line 10 GHz comb. The slave laser was pumped at 1.6 times its threshold. The areas where four wave mixing (FWM), stable locking (within the Adler locking tongue) and unstable locking are marked on the plot. The dashed black line between the boundary of the stable and unstable locking regions marks a Hopf bifurcation line, where the relaxation oscillations become weakly damped, and extra frequencies appear in the optical spectrum. The points marked (a), (b) and (c) coincide with the detuning and power values used in the example phasor diagrams shown in Fig. 3.6.

In order to discuss the behaviour over a wide range of detunings and powers, two dimensional intensity maps were calculated using the model in Section 3.1. These maps will be used throughout this section, as they concisely show the performance of the slave laser as an optical demultiplexer over the whole parameter space. Figure 3.18 shows how the SMSR changes versus detuning and optically injected power, for a 10 GHz optical comb. Our attention is restricted to the Adler locking tongue around the centre comb line - for large comb spacings, the behaviour within each Adler tongue is similar. For low injection strengths and large detunings, the slave laser is unlocked from the comb (marked in the plot as four wave mixing (FWM)). The high SMSR region is where the slave laser is stably locked to the centre line of the comb. The SMSR drops slightly as the optical power is increased, and as expected, the locking bandwidth of the slave laser also increases with stronger injection. A dashed black line indicates where the system undergoes a Hopf bifurcation [132] (where a Hopf bifurcation is a critical point where a system's stability switches and a periodic solution arises). Within the unstable locking region, the ROs become very weakly damped, and extra frequencies appear in the optical spectrum, causing the SMSR to drop to almost zero. The unstable locking region is asymmetric around zero detuning due to the fact that the α parameter has a non-zero value. Within this region, many chaotic bifurcations can occur, particularly at higher injection powers. The points marked (a), (b) and (c) in Fig. 3.18 show the detuning and power values used in the example phasor diagrams shown in Fig. 3.6.

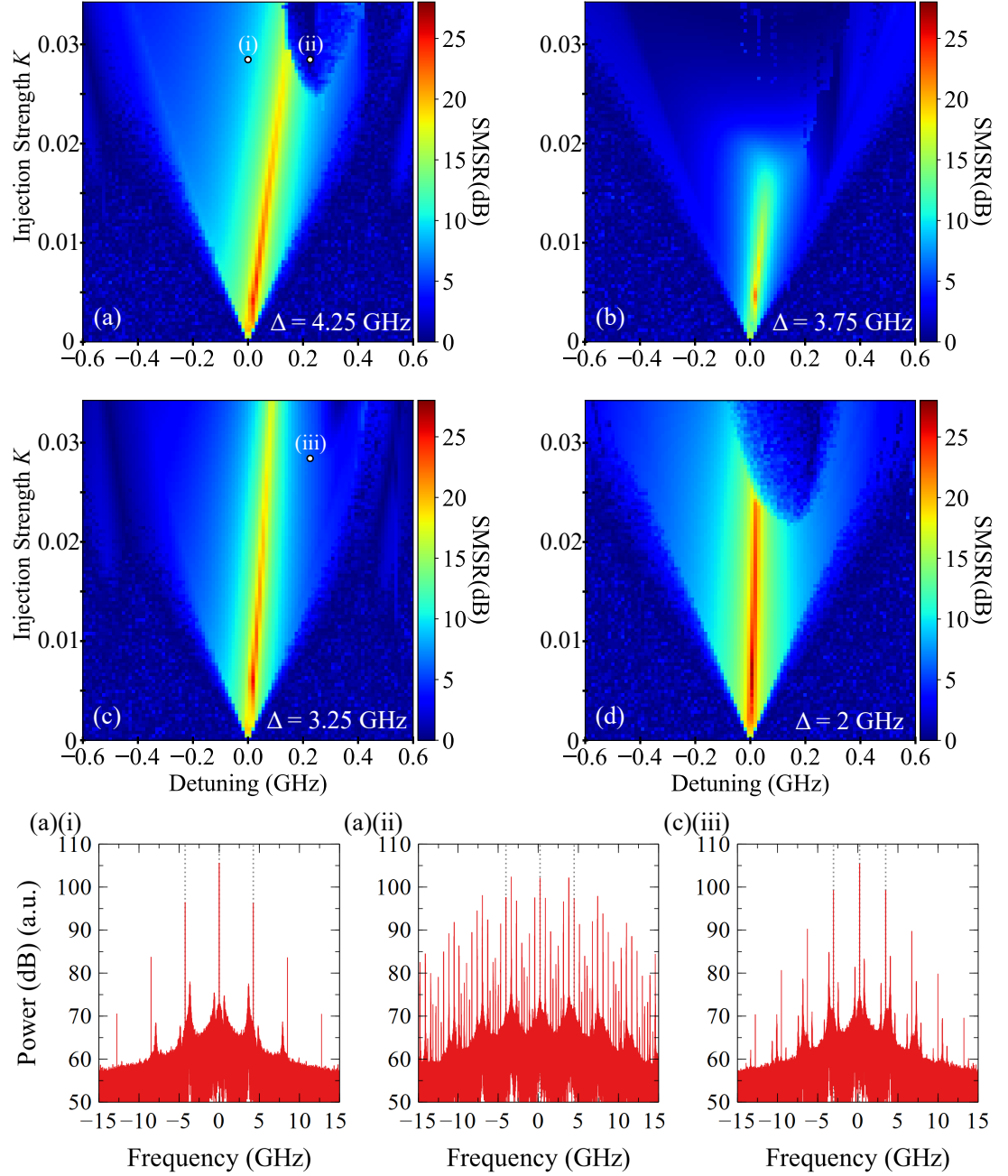


Figure 3.19: Four calculated intensity plots, which show how the SMSR varies around the Adler locking tongue for comb spacings Δ around the relaxation oscillation frequency. The slave laser was driven at 1.6 times threshold. **(a)** $\Delta = 4.25$ GHz, **(b)** $\Delta = 3.75$ GHz (which corresponds approximately to ω_r in this case), **(c)** $\Delta = 3.25$ GHz and **(d)** $\Delta = 2$ GHz. Below the four intensity plots, optical spectra from the slave laser at an injected strength $K = 0.0285$ are shown at detunings of **(a)(i)** 0 MHz and **(a)(ii)** 225 MHz for the $\Delta = 4.25$ GHz case, and in **(c)(iii)** at a detuning of 225 MHz with a comb spacing of 3.25 GHz.

3.5.1 Comb Spacings close to ω_r

We now use these intensity colour plots to examine the dynamics as the comb spacing approaches the critical frequencies ω_r , $2\omega_r$ and $3\omega_r$. Figure 3.19 shows four such intensity maps, for optical comb spacings around ω_r . Figure 3.19(a) presents the case where the comb spacing is 0.5 GHz above the RO frequency. In contrast to the 10 GHz example, there is only a small area with high SMSR (>20 dB). The region of high SMSR starts at zero detuning, and does not grow in size with increased optical injection strength, rather remaining concentrated around a straight line which is orientated toward positive detunings. Most of the locking tongue has very low SMSR, and this SMSR continues to decrease over the whole locking tongue as the comb spacing reaches the RO frequency ω_r . Interestingly, the size of the unstable locking region also shrinks as the comb spacing approaches ω_r , becoming replaced with more stable locking states. Figure 3.19(a)(i) shows the optical spectrum at zero detuning and $K = 0.0286$ injected power, where previously it was shown that for a 10 GHz comb with the same injection strength and detuning the slave laser's output was unstable (for example, Fig. 3.6(b) and Fig. 3.18). The magnitude of the peaks around the ROs in the optical spectrum has risen in comparison with the other stable locking states however. Figure 3.19(a)(ii) shows an example output from the smaller unstable locking region.

When the comb spacing exactly matches the RO frequency (Fig. 3.19(b), $\omega_r \approx \Delta = 3.75$ GHz), the unstable locking region vanishes almost completely within the parameter range chosen. The modulation due to the unlocked optical comb lines resonates with the natural relaxation oscillations, extending the region where the slave laser can stably lock to the comb. This also causes the SMSR to drop to almost zero for higher optical powers, making it difficult to distinguish between the locked and unlocked regions when measuring only the SMSR.

Slightly below the relaxation oscillation frequency (Fig. 3.19(c), $\Delta = 3.25$ GHz), the SMSR within the Adler locking tongue improves, as the slave laser can still stably lock symmetrically around zero detuning. The injected power and detuning used to generate the optical spectrum in Fig. 3.19(c)(iii) is the same as in Fig. 3.19(a)(ii), and yet the spectrum with $\Delta = 3.25$ GHz shows that the ROs are damped more. The combs used to generate these two cases were 500 MHz above and below the RO frequency, yet the behaviour found is significantly different, which shows it's easier to modulate the ROs with lower frequencies than with higher frequencies. The SMSR is also highly sensitive to detuning at low comb spacings, as again the high SMSR region appears around a straight line area. The unstable locking region reappears for comb spacings far below the RO frequency (Fig. 3.19(d), $\Delta = 2$ GHz).

3.5.2 Comb Spacings close to $2\omega_r$

The Adler locking tongue of the comb-slave system undergoes an interesting transformation as the comb's frequency spacing approaches $2\omega_r$. Shown in Fig. 3.20(a), for a comb spacing 200 MHz above $2\omega_r$, the unstable locking region can be seen to have split into two distinct regions. On the negative detuning side, a region where the undamped relaxation oscillations become frequency locked to half of the optical comb spacing appears, and grows in size as the comb spacing approaches $2\omega_r$. The slave laser becomes stably locked to the comb due to the resonance with the relaxation oscillations, which decreases the size of the unstable region. Within this new region where the ROs have become both undamped and frequency locked, the SMSR is significantly reduced.

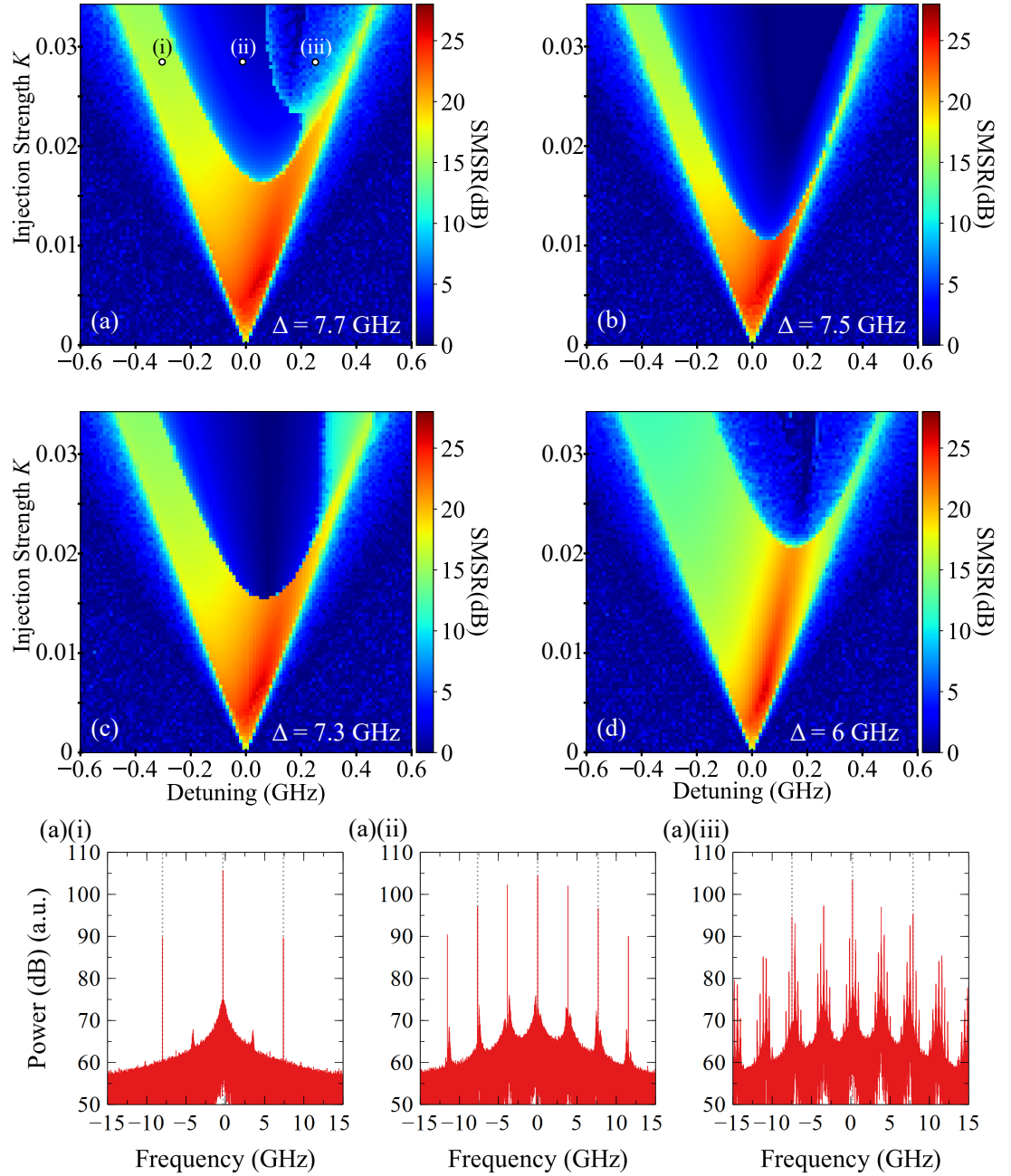


Figure 3.20: Four calculated intensity plots, which show how the SMSR varies around the Adler locking tongue for comb spacings Δ around twice the relaxation oscillation frequency. **(a)** $\Delta = 7.7$ GHz, **(b)** $\Delta = 7.5$ GHz (which corresponds approximately to $2\omega_r$), **(c)** $\Delta = 7.3$ GHz and **(d)** $\Delta = 6$ GHz. Below the four intensity plots, optical spectra from the slave laser are shown for the $\Delta = 7.7$ GHz case, at detunings of: **(a)(i)** -300 MHz, **(a)(ii)** 0 MHz and **(a)(iii)** 220 MHz.

Figures 3.20(a)(i), (ii) and (iii) show output optical spectra at detunings of -300 MHz, 0 MHz, and +220 MHz. In Fig. 3.20(a)(i), the slave laser is stably locked to the centre line of the three line comb. As the detuning is decreased to zero in Fig. 3.20(a)(ii), new frequencies at multiples of the ROs appear, with the slave remaining stably locked to the centre line. In contrast, the optical spectrum in Fig. 3.20(a)(iii) shows further frequencies have been generated, as the slave laser becomes unstably locked.

The new region with RO frequency locking grows until the unstable locking region completely disappears, as in Fig. 3.20(b) (for the parameter ranges tested). For the parameter range presented, almost the full Adler tongue is replaced with low SMSR states due to the undamped and locked ROs. As the comb spacing decreases past $2\omega_r$, the locked RO region shrinks, as the unstable locking region begins to grow again (Fig. 3.20(c)). As might be expected, when the comb spacing is far below $2\omega_r$ (e.g, $\Delta = 6$ GHz, as in Fig. 3.20(d)), the unstable locking region's size in the Adler tongue matches that of cases where the comb spacing is far above $2\omega_r$.

The intensity plots around $2\omega_r$ also show that the high SMSR regions become more sensitive to detuning as the comb spacing shrinks. This is likely as the unlocked comb lines are closer to the frequency noise introduced by the slave ROs.

3.5.3 Comb Spacings close to $3\omega_r$

As indicated previously, higher RO locking harmonics have smaller locking bandwidths. For comb spacings around ω_r , almost the whole Adler locking tongue became a low SMSR region, where the ROs resonated with the modulation due to the unlocked comb lines. At a comb spacing of -500 MHz away from the RO frequency, the unstable locking region within the Adler tongue was stable. For comb spacings around $2\omega_r$, a smaller area of the Adler locking tongue was affected by the resonating ROs. These effects only persist for comb spacings within -350 MHz of $2\omega_r$. When injecting with comb spacings of approximately $3\omega_r$, the locking bandwidth significantly shrinks yet again, where the ROs are only able to lock to one third of the comb spacing within -300 MHz of the $3\omega_r$ comb spacing. Even with a comb spacing 50 MHz above $3\omega_r$ (as shown in Fig. 3.21(a)), no locked RO states appear.

At 11.25 GHz ($\Delta \approx 3\omega_r$, Fig. 3.21(b)), a small region where the ROs frequency lock is visible around the boundary between the high SMSR stable locking region and the unstable locking region. The growth of this locked RO region is not similar to the previous cases – with a comb spacing 150 MHz below $3\omega_r$, the locked RO region no longer borders the stable locking region, but has grown in size (the largest RO locking region no longer happens at three times the free running RO frequency). The optical spectra shown in Figs. 3.21(c)(i), (ii) and (iii) show that at the boundary between the stable and unstable region, the relaxation oscillations are undamped but do not become frequency locked, becoming excited and dominating the SMSR. Figure 3.21(c)(ii), further away from the stable locking region, the ROs become stably frequency locked. At even higher positive detunings, further frequencies appear around the undamped relaxation oscillation peaks in the optical spectrum, as the slave is in again in an unstable bounded phase state. For comb spacings even further below $3\omega_r$ (Fig. 3.21(d)), the locked RO region moves to being predominately in the centre of the unstable locking region, as it begins to shrink.

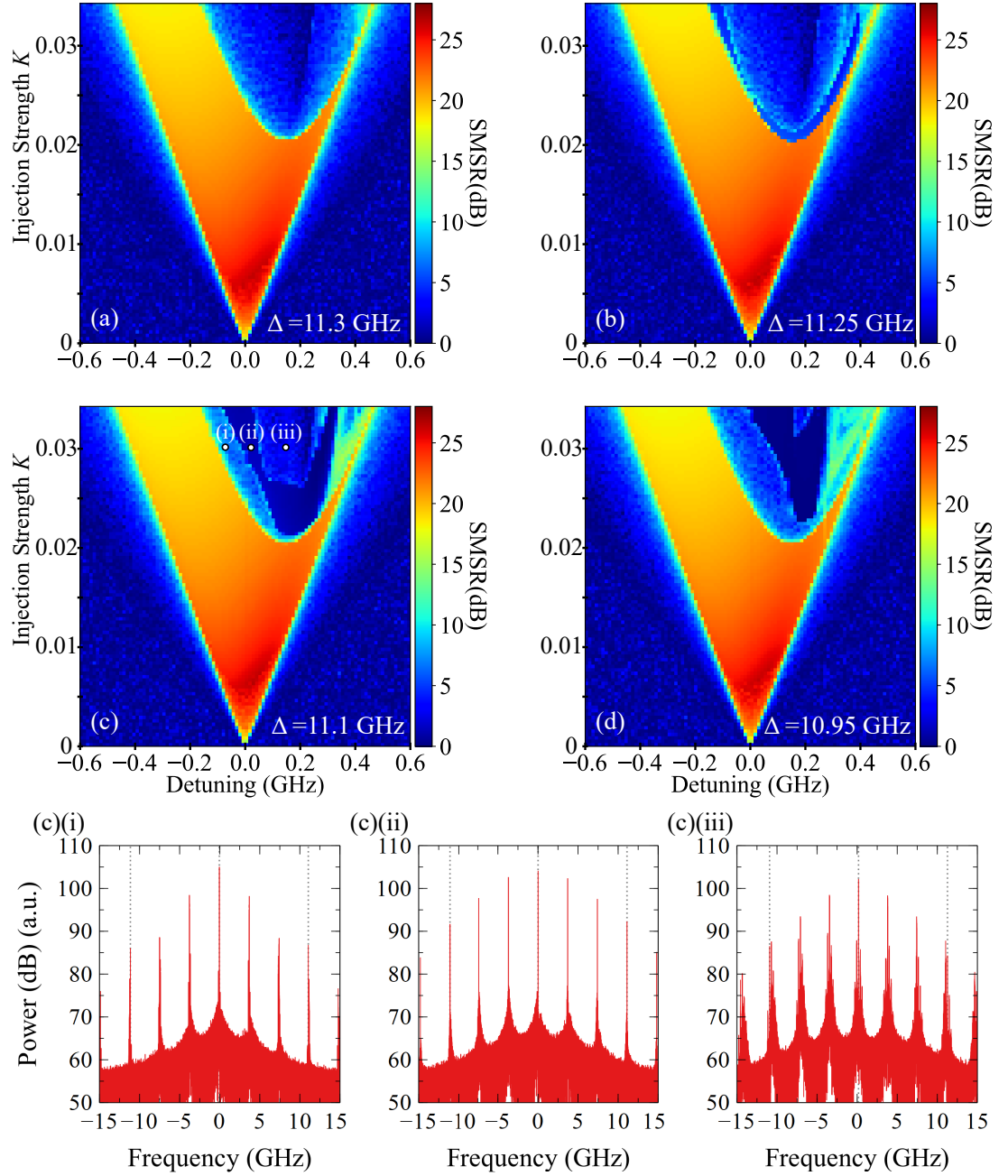


Figure 3.21: Four calculated intensity plots, which show how the SMSR varies around the Adler locking tongue for comb spacings Δ around three times the relaxation oscillation frequency. (a) $\Delta = 11.3$ GHz, (b) $\Delta = 11.25$ GHz (which corresponds approximately to $3\omega_r$), (c) $\Delta = 11.1$ GHz and (d) $\Delta = 10.95$ GHz. Below the four intensity plots, optical spectra from the slave laser are shown for the $\Delta = 11.1$ GHz case, at detunings of: (c)(i) -45 MHz, (c)(ii) 10 MHz and (c)(iii) 170 MHz.

3.6 Chapter Conclusion

In this chapter, a standard single moded rate equation model was introduced, and used to model optical comb injection. The rate equation model has provided some more insight into how semiconductor lasers interact with optical combs, and shown the importance of the slave laser's relaxation oscillations. The effects of single frequency optical injection and optical comb injection on the slave's field, phase and carriers were compared. The model matched experimental results collected, which indicated that there is an optimal current which should be used to pump the slave laser to provide maximum SMSR. Three different asymptotic states were discussed, and in the optical comb case, the comb-slave system will never reach a stationary state. Phasor diagrams were used to show that the unlocked comb lines always modulate the slave laser's field, carriers and phase, and this modulation grows in size when the frequency of the modulation matches the fundamental RO frequency of the slave laser.

It was found that locking to higher, lower or the centre frequency comb line does not affect the demultiplexed SMSR significantly. For comb spacings close to the RO frequency, the SMSR significantly decreased (due to the increase in the modulation effect at the RO frequency). Two different experiments were discussed, where the optical comb spacing was varied, and the SMSR of the demultiplexed signal was measured. Using a high resolution optical spectrum analyser, it was found that the relaxation oscillations within the slave laser can become undamped, and frequency lock to the rational fractions of the optical comb spacing.

The effect of the detuning between the slave laser and the injected comb on the SMSR was also investigated, along with the relative size of the locked RO regions for different comb spacings. The output SMSR becomes more sensitive to detuning as the comb spacing shrinks – however, the model predicted the slave laser locking bandwidth remains constant for all comb spacings over the parameter ranges tested. The relative sizes of the RO locking regions shrinks as the ROs lock to higher harmonics of the comb spacing. At specific comb spacings, the unstable locking region completely vanished over the parameter regions investigated, replaced with a low SMSR region where the undamped ROs frequency lock to the comb.

Chapter 4

Harmonic Locking and the Frequency Locking of Relaxation Oscillations

Following from the results presented in Chapter 3, further investigation into the frequency locking of the undamped relaxation oscillations was performed. The RO locking greatly decreases the SMSR obtainable, however it simultaneously creates a new optical comb with a reduced frequency spacing. Surprisingly, even though optical injection has been a thoroughly researched topic over the last 4 decades, very few studies have reported on the dynamics present when an optical frequency comb is injected into a single mode slave laser (although, two very recent studies (Refs. [149], [150]) show that there is renewed interest in the topic). As optical injection locking has been reasonably recently been proposed as a method of demultiplexing optical combs in optical networks [129], [130], [137], [138], recent literature has been focused on how to optimise the side mode suppression [132], [133], [171] or stability [192] obtainable when injecting optical combs into single mode lasers (including the preceding 2 chapters).

While studying the frequency locking of the relaxation oscillations, another frequency locking mechanism was uncovered - it was found that a slave laser can also stably frequency lock in between the injected optical comb lines. This frequency locking had previously been demonstrated [193], however the underlying mechanism was not understood. In this chapter, it is shown that these frequency locked states (also known as Arnol'd tongues [194]) appear as the slave laser is detuned by a rational fraction of the injected optical comb spacing.

This chapter presents a study of the types of harmonic locking which can occur with optical injection. The chapter is laid out as follows:

- First, Section 4.1 details the experimental set-up, to give context to the results which follow.
- Section 4.2 then presents results from detuning sweeps, as the slave laser's frequency was tuned across the injected comb. Subsection 4.2.1 first presents single frequency de-

tuning sweeps to indicate how the ROs within a slave laser can become undamped due to optical injection, and reveals the well known fact that the undamped ROs can tune as the detuning varies. This is contrasted with the detuning sweeps in Subsections 4.2.2 and 4.2.3, where it is shown that the undamped ROs don't freely tune in frequency when an optical comb is injected. In these subsections, it is pointed out in the experiment results that the lasing frequency of the slave laser can also stably frequency lock in between the injected optical comb lines. Subsection 4.2.4 details a numerical model used to simulate the experiment, and a comparison between the model and experiment is discussed in Subsection 4.2.5.

- The underlying mechanisms behind this frequency locking is then explained in Section 4.3. Firstly, to better understand both types of frequency locking mechanisms observed with comb injection (the RO locking and also the locking of the slave's lasing frequency between the comb lines), a simple non-linear model known as the circle map is introduced in Subsection 4.3.1. The circle map is typically used to demonstrate Arnol'd tongues and harmonic locking, and the well known devil's staircase is also reproduced. In Subsection 4.3.2, a parallel between the circle map and the optical comb injection results is made, and it is shown that a devil's staircase also appears in the slave's lasing frequency. This link between Adler frequency locking and harmonic locking is then discussed further, and it is shown that Arnol'd tongues are present when frequency combs are injected.
- Following this, Section 4.4 studies the effect of the RO frequency and the magnitude of the amplitude-phase coupling α on the size of Arnol'd tongues in parameter space. It is shown that the nonlinearity induced by a large α enables locking of the ROs to higher order resonances of the injected comb, when the laser RO frequency is close to this harmonic comb spacing. This effect is largely suppressed for smaller values of α , with only the second harmonic resonance remaining significant.
- An example of asymmetry in the RO locking around the centre comb line is then present in Section 4.5, and the limits of the harmonic locking mechanism are presented in Section 4.6.

Some of the results presented in this chapter have been published in Optics Express (see Ref. [195]). Another paper has been prepared using more results from this chapter, and is presently available as a pre-print on the arXiv (see Ref. [196] for more details).

4.1 Experimental Set-up

To study the frequency locking of the slave laser's relaxation oscillations (ROs) and lasing frequency under the injection of an optical frequency comb (OFC), a standard injection experimental setup similar to those presented in previous chapters was used, as shown in Fig. 4.1. A commercial ID Photonics CoBrite-DX1 tunable laser source (TLS) was intensity modulated using a LiNbO₃ Mach-Zehnder modulator (MZM) to create a 3 line OFC. The comb's optical power was amplified and controlled using an erbium doped fibre amplifier (EDFA) and variable optical attenuator (VOA) in series. A fixed frequency optical filter with a 50 GHz

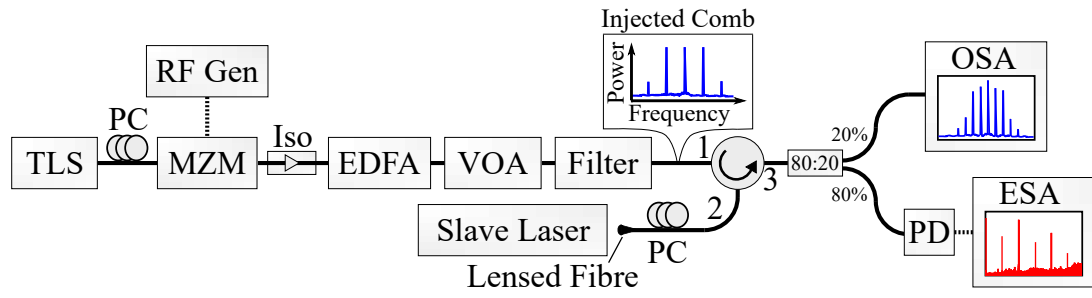


Figure 4.1: Experimental setup for performing optical comb injection. TLS: Tunable laser source, MZM: Mach-Zehnder modulator, PC: Polarisation controller, EDFA: Erbium doped fibre amplifier, VOA: Variable optical attenuator, OSA: Optical spectrum analyser, PD: Photodiode, ESA: Electrical spectrum analyser. The slave laser used was a 15 pit device designed using the inverse scattering method, detailed in Appendix A.

bandwidth at -3 dB removed a significant portion of the amplified spontaneous emission introduced by the EDFA. The slave laser used was an unpackaged single mode AlGaInAs quantum well device emitting at 1550 nm (a 15 pit device, described in full in Appendix A). A lensed fibre was used to optically couple to the device, which is mounted on top of a temperature controlled brass chuck. A circulator was used to optically inject the slave laser, and the light output was monitored on an OSA and ESA simultaneously.

In order to perform the frequency detuning sweeps in the rest of the chapter, the temperature of the slave laser was swept rather than the lasing frequency of the tunable laser. This was due to the fixed centre frequency of the optical filter used; varying the comb's centre frequency would also have resulted in equal power in the optical comb lines. While varying the slave laser's temperature affected the output power of the laser, the temperature ranges used in the experiment were small, and hence the change in optical power was also small.

4.2 Detuning Sweeps

Optical injection detuning sweeps were previously studied in Chapter 2, where the focus of the discussion was on the side mode suppression ratio obtainable as a slave laser was tuned relative to some injected master signal. In this chapter however, detuning sweeps will be used to study different types of dynamics which appear when injecting with optical combs. This relatively long section first details a case with a single frequency injected signal, before continuing with optical comb injection in Subsections 4.2.2 through 4.2.5.

4.2.1 Single Frequency Detuning Sweep

Detuning sweeps of a master-slave system can reveal different regions of behaviour and different types of dynamics. Initially, detuning sweeps with a single injected frequency were studied, and are presented here again to discuss some of the characteristic dynamic behaviour seen in optical injection. The experimental setup used was as in Fig. 4.1, without the MZM, EDFA, VOA or optical filter. The experimental results for one such detuning sweep are shown in Fig. 4.2. Figure 4.2(a) shows a wide range of measured optical frequencies on the OSA. The temperature of the slave laser was used to tune the lasing frequency of the slave ± 20 GHz

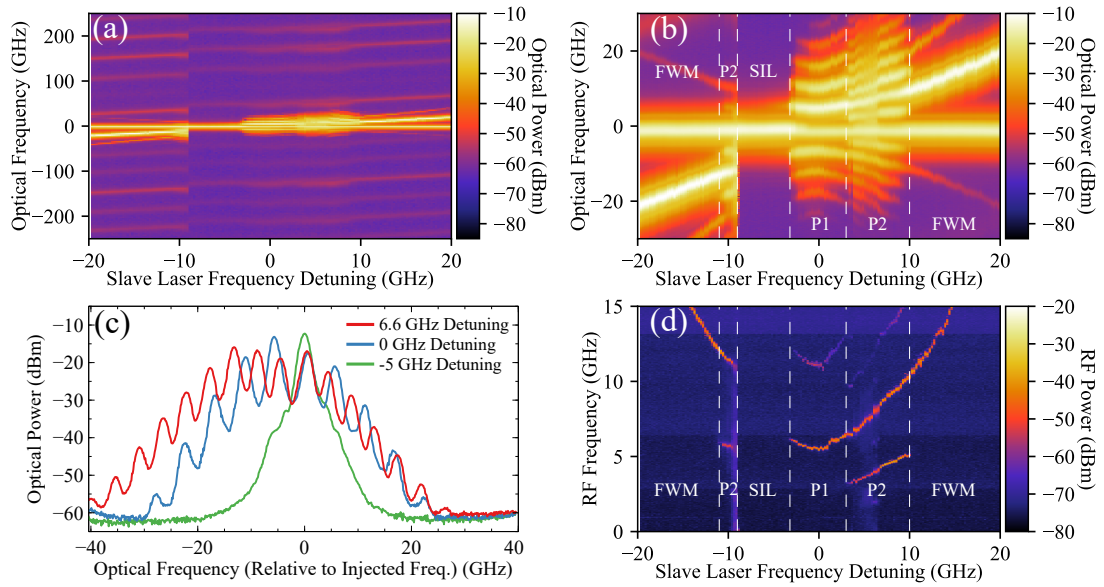


Figure 4.2: Experimental results from a detuning sweep, as a single mode slave laser's frequency was tuned across a single frequency injected signal. The slave laser was initially biased at 1.8 times threshold, with an optical power of -2 dBm. The single frequency source had an optical power of +5 dBm. (a) Intensity plot which shows wide optical spectra, plotted ± 250 GHz around the injected frequency. (b) Intensity plot which shows a close up of the optical spectra centred around the injected frequency. Vertical dotted lines indicate the transitions between different types of dynamics. The acronyms used in the figure stand for four wave mixing (FWM), period 1 (P1), period 2 (P2) and stable injection locking (SIL). (c) Comparison between the optical spectrum as the slave laser is stably locked (at -5 GHz detuning), undergoing period 1 oscillations (at 0 GHz detuning) and undergoing period 2 oscillations (at 6.6 GHz detuning). (d) RF spectra for the same detuning sweep picture in (a) and (b).

from the master signal, and all modes in the slave can be seen to tune at approximately the same rate (this is clear between detuning frequencies of -20 GHz and -11 GHz for example). The temperature was allowed stabilise at each step (by waiting approximately 20 s).

At a detuning of -9 GHz, the slave laser stably locks. The weaker modes in the slave laser can be seen to become more visibly suppressed, and all modes in the slave laser no longer tune with frequency as the temperature was increased further. While the main mode is stably locked to the injected frequency, the frequency of all the modes visible remained constant.

At a detuning of -3 GHz, the slave laser exits the stable locking region. Figure 4.2(b) shows a zoom around the injected frequency, for the same detuning sweep. Vertical dotted lines indicate changes in behaviour visible on the OSA. At large detunings (between -20 GHz and -11 GHz), the slave laser undergoes four wave mixing (FWM), however at -11 GHz, period 2 (P2) oscillations briefly appear in the slave laser's output. Figure 4.2(d) shows the RF spectra recorded on the electronic spectrum analyser (ESA). As the extra frequencies appear in the optical spectrum, we also see an additional frequency appear in the electrical spectrum. As mentioned above, at -9 GHz detuning, the slave laser stably locks to the injected signal. The ESA shows no strong frequencies, and the OSA shows only a single frequency. Following the stable locking region, period 1 oscillations¹ appear for detunings between -3.2 GHz and +3 GHz. Period 1 oscillations occur when the slave's limit cycle is no longer at a stationary

¹In reality, the period 1 oscillations observed in the experimental results presented in Fig. 4.2 are nonlinear period 1 oscillations, as a pure period 1 oscillation would only add a single extra frequency to the slave laser's optical spectrum.

point, and an extra oscillation frequency is added to the slave laser's field and phase [144]. As the detuning continues to grow, the period 1 oscillations undergo period doubling, becoming period 2 oscillations. Notably, while the period 2 oscillations are present, the ESA traces in Fig. 4.2(d) show another lower frequency than the period 1 oscillation frequency. The period 2 region finishes at +10 GHz detuning, as the slave laser tunes away from the injected signal. A line plot shown in Fig. 4.2(c) shows a comparison of the optical spectra when the slave laser is stably locked (at -5 GHz detuning), undergoing period 1 oscillations (at 0 GHz detuning) and undergoing period 2 oscillations (at 6.6 GHz detuning). The pulsed outputs add multiple frequencies to the output spectra. A relatively high optical injection strength was used in Fig. 4.2, and as shown previously in Chapter 3, better SMSRs are achieved at lower optical injection strengths. As a result, lower optical injection strengths were focused on when injecting optical combs, and the optical injection strengths used throughout the rest of the chapter are lower than what was presented in Fig. 4.2.

4.2.2 Frequency comb detuning sweep

Experimental results from a detuning sweep where an optical comb was injected are shown in Fig. 4.3. In this case, the lasing frequency of a single mode slave laser was swept across the 10 GHz optical comb. A wide optical spectrum is shown in Fig. 4.3(a), and unlike in the single frequency case shown in Fig. 4.2, there is very little suppression visible in the slave laser's modes, due to the lower optical power injected. Lowering the optically injected power also causes the locking regions to be significantly shorter. Vertical dotted lines in Fig. 4.3 indicate where the slave laser's frequency matched one of the comb lines, and for low injection strengths, we expect the stable locking region to be centred around 0 detuning. Figure 4.3(b) shows a zoom around the comb's frequencies. In the zoomed image, the slave's frequency can be seen to lock each time the slave's main lasing mode approaches one of the comb lines. As discussed in the previous chapter, the injected comb's strength was strong enough to excite the relaxation oscillations in the slave laser. As the slave positively detunes from the centre of each locking region, additional frequencies (on either side of the comb line which the slave is locked to) become visible.

The ESA spectra from the same detuning sweep are shown in Fig. 4.3(d). As the slave laser tunes from -20 GHz to the first comb line located at -10 GHz, a clear beat note is visible on the ESA. The beat note is steeper than a linear line between the points (-20,10) and (-10, 0), due to non-linear dynamics affecting how the slave laser tunes. The slave laser becomes locked at -11.5 GHz. Even while the slave is stably locked to the comb line, a strong 10 GHz beat note is visible for all detunings, due to the beating between the comb lines. Hence, as the slave stably locks to the lower frequency comb line the ESA still shows the 10 GHz beat note. Midway through the first locking region, the ROs become undamped and lock to a 5 GHz tone, which is visible in the ESA traces. The ROs don't remain locked over the full region where the slave's frequency is locked, and they become unlocked right before the slave becomes unlocked. This is consistent with the model results shown in Fig. 3.20(a) - these experimental detuning sweeps are equivalent to sweeps from negative to positive detuning in the Adler locking tongues shown in Section 3.5. As described during the discussion of Fig. 3.20(a), at negative detunings, the slave laser first stably locks, and as the detuning increases, the ROs become undamped and then frequency lock. Prior to the slave becoming unlocked at positive

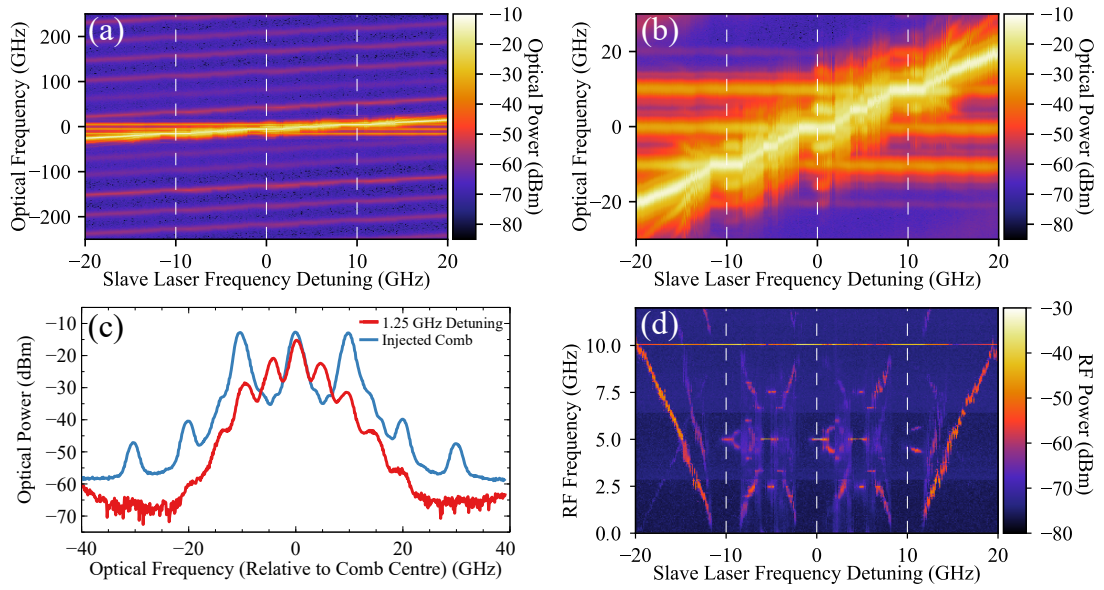


Figure 4.3: Experimental results of a detuning sweep, as a single mode slave laser's frequency was tuned across a three line 10 GHz optical comb. The slave laser was initially biased at 1.8 times threshold, with an optical power of -2 dBm. The optical comb had an injected power of -7 dBm. (a) Intensity plot which shows wide optical spectra, plotted ± 250 GHz around the centre comb line. Vertical dashed white lines indicate where the free-running slave laser's optical frequency coincided with one of the optical comb lines. (b) Intensity plot which shows a close up of the optical spectra centred around the three line optical comb. (c) Comparison between the injected optical comb, and the optical spectrum at a detuning of +1.25 GHz, where the slave laser's ROs have become undamped and frequency locked to half of the optical comb spacing. (d) RF spectra for the same detuning sweep pictured in (a) and (b).

detunings, the ROs become unlocked. Interestingly, Fig. 4.3(d) shows that the ROs become undamped when the slave is locked to the higher frequency comb line, however the ROs don't lock in this case. This shows that there is some asymmetry in the behaviour around the centre line of the comb, due to the laser's α parameter. As shown in Fig. 4.3(c), the output comb from the slave laser has half of the spacing of the input comb, and the new RO peaks are larger than the other comb lines.

As the slave laser tunes between the optical comb lines, rather than a continuous smoothly varying beat note, specific frequencies appear in the ESA traces. In particular, at detunings of ± 5 GHz, the slave laser's optical frequency appears to be locked *inbetween* the comb lines. This was surprising, as upon further investigation, it was found that the slave laser could also lock at detunings which matched rational fractions of the spacing, between the comb lines. Figure 4.4 shows comparisons of different locked states on the ESA for a 10 GHz optical comb with -1.8 dBm injected power. When the slave is unlocked (Fig. 4.4(a)) the beat note between the slave and the comb lines is broad, as the slave and the master aren't coherent with one another. In general, the beat note measured between the comb and the slave is broad if the slave is not locked to the master due to the frequency jitter between the lasers. The 10 GHz beat note is narrow and clear over all traces, as the comb lines beat with one another independent of whether the slave is locked or unlocked to the comb. Figure 4.4(b) shows the ESA spectra when the slave is stably locked to the centre line of the comb. While stably locked, only the beat note from the beating of the unlocked comb lines is visible. As expected, the ROs become undamped and locked at higher detunings, as shown in Fig. 4.4(c). The ESA traces in Figs.

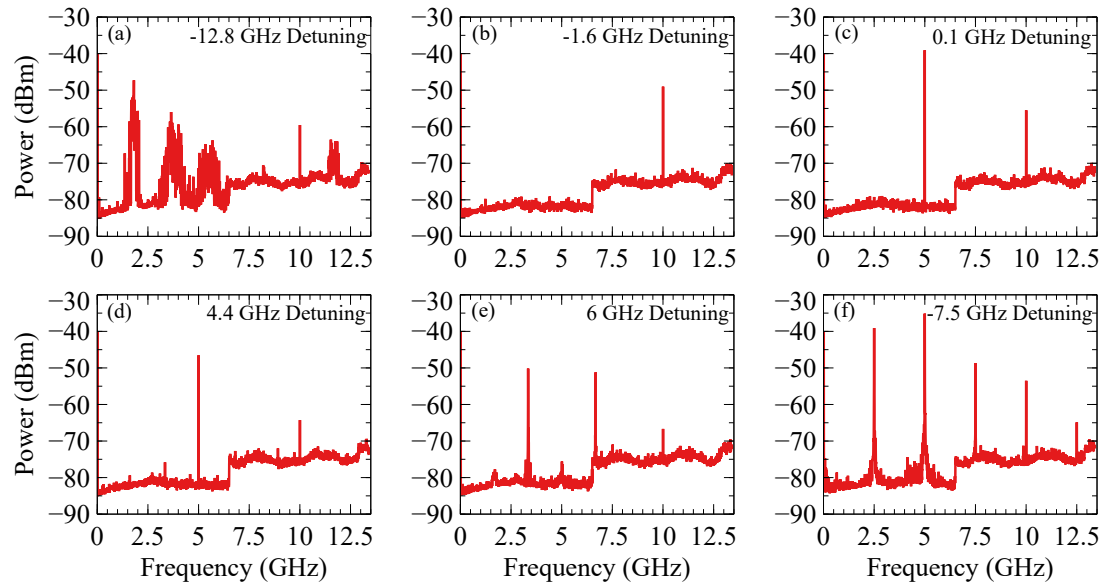


Figure 4.4: Individual ESA traces from a detuning sweep obtained when injecting a three line 10 GHz comb with optical injection strength -1.8 dBm. The slave laser was biased at 1.8 times threshold, and had an output power of -2 dBm. The ESA noise floor has a visible step at 6.5 GHz, which was a limitation of the ESA used. The ESA traces show the measured results when the slave laser was (a) unlocked from the comb, (b) stably locked to the centre comb line, (c) stably locked to the comb line, with the ROs also locked to half the comb spacing, (d) frequency locked half way between the comb lines, (e) frequency locked a third of the way between the comb lines, and (f) frequency locked a quarter of the way between the comb lines.

4.4(d), 4.4(e) and 4.4(f) show the slave laser at detunings in between the main locking regions. At +4.4 GHz detuning, the slave is stably locked to a frequency in between the centre and higher frequency comb lines. Similarly, at +6.6 GHz and -7.5 GHz, the slave's frequency also stably locks to frequencies which were in between the three comb lines. As apparent in Fig. 4.3(d), locking bandwidth of the frequency locked states at detunings of $1/2$, $1/3$, and $1/4$ of the comb spacing decreases as the fraction decreases. It was found that the slave laser could also lock to detunings at multiples of $1/5$ of the comb spacing, however it was difficult to maintain these locked states for long.

These frequency locked states at detunings in between the optical comb lines was previously been reported in [193], where they claim that the frequency locked states arise due to many four-wave mixing tones. The true underlying locking mechanism however will be discussed in detail in Subsection 4.3.2.

4.2.3 Sweeping Direction and Hysteresis

It is well known that optical injection locking can lead to hysteresis and bi-stabilities in a slave laser; since first reported by Otsuka and Kobayashi [197], hysteresis has been found in many different applications of optical injection locking. Examples include hysteresis in the lasing state of 2-state quantum dot lasers [198], to hysteresis in the lasing polarisations of vertical-cavity surface-emitting lasers (VCSELs) [199], [200].

In particular, hysteresis can often be observed in the locking bandwidth of a slave laser. Typically, the locking bandwidth is larger when the master is swept from a positive frequency

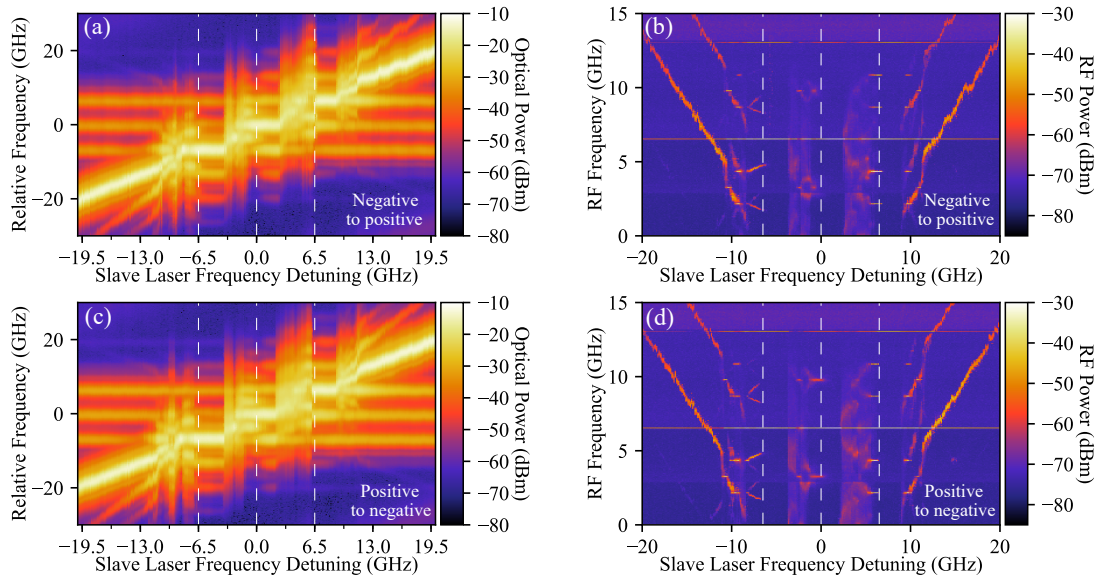


Figure 4.5: Experimental results from two separate detuning sweeps, where a slave laser's frequency was tuned (a), (b) from negative to positive detuning and (c), (d) from positive to negative detuning. The injected comb had a power of -5 dBm in both cases, and a fixed slave laser bias of 90 mA was used, which gave an approximate optical power of -2 dBm. Vertical dashed white lines indicate where the free-running slave laser's optical frequency coincided with one of the optical comb lines.

detuning to a negative frequency detuning, rather than the other way around. This difference in locking bandwidth can be very large in some cases – when comparing the locking bandwidths of VCSELs with strong optical injection, a difference of over 400 GHz was found between positive to negative sweeps versus negative to positive detuning sweeps [201], [202].

The affect of the directionality of the optical comb detuning sweeps was also investigated, in order to determine if there was significant hysteresis in the RO locking or in the locking of the other frequency locked states in the slave laser. Results from two separate 6.5 GHz comb sweeps are shown in Fig. 4.5. In Figs. 4.5(a) and 4.5(b), results from the OSA and ESA are shown as the slave laser was tuned from negative to positive detuning. Results from the corresponding sweep in the opposite direction are shown in Figs. 4.5(c) and 4.5(d). Very similar behaviour is seen in each case, presumably due to the low injection power used in the experiment. In both directions, the slave laser's ROs lock to 1/3 of the optical comb spacing while locked to the higher frequency comb line, while the ROs only become undamped in the other cases. The slave laser's frequency also tunes in a similar manner outside of the Adler-type locking regions in each case.

4.2.4 Modelling Detuning Sweeps

The laser modelling performed in this portion of the thesis was completed in collaboration with Dr. Benjamin Lingnau and Dr. Bryan Kelleher. In order to simulate the optical comb injection experiments described above, we formulated a rate equation equation model [203], modelling the dynamics of the complex electric field inside the cavity, $E(t)$, and the normalised

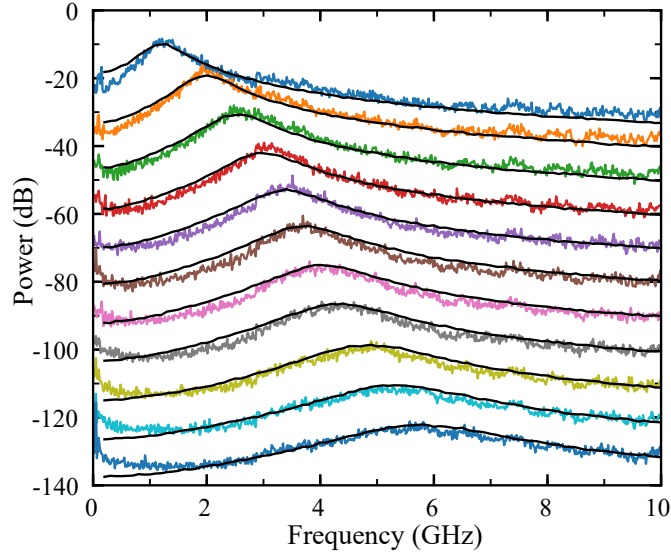


Figure 4.6: Measured free-running ROs of the slave laser from 55 mA to 120 mA, in steps of 5 mA up until 90 mA and steps of 10 mA thereafter, offset vertically from top to bottom by -10 dB for clarity. The laser's threshold was 50mA. Solid black lines indicate simulated results from the model.

gain $N(t)$ (in units of inverse time) due to the active carriers.

$$\frac{d}{dt}E = (1 + i\alpha) \left(\frac{N - N_0}{2} - \kappa \right) E + \frac{\partial E}{\partial t} \Big|_{\text{inj}} + \sqrt{\beta} (\xi'_{sp}(t) + i\xi''_{sp}(t)), \quad (4.1)$$

$$\frac{d}{dt}N = \frac{J - N}{T} - (N - N_0)|E|^2. \quad (4.2)$$

Here, J is the normalised pump current, N_0 is the normalised transparency carrier density (in units of inverse time), T is the carrier lifetime, and α is the amplitude-phase coupling parameter. The optical cavity loss rate is given by 2κ , and we define J_{th} as the threshold pump current. Values for the model were obtained by matching simulation outputs with the measured random intensity noise spectra of a free running laser (as shown in Fig. 4.6).

The optical comb injected into the laser cavity is modelled by an additional driving term:

$$\frac{\partial E}{\partial t} \Big|_{\text{inj}} = K E_0 \left(1 + 2m \cos(\phi_{\text{comb}}) \right) e^{i\phi_{\text{inj}}(t)} - i2\pi\nu_{\text{inj}}E, \quad (4.3)$$

where m is the relative strength of the injected side-modes at frequencies $\nu_{\text{inj}} \pm \Delta_{\text{comb}}$. We neglect comb modes further away from the center mode since, experimentally, their power is well below -30 dB of the three strongest comb modes. The injection strength in this case K is the amplitude ratio of the injected field and the free-running laser emission, with E_0 the free-running intracavity field. The second term in Eq. (4.3) transforms the electric field into the rotating frame of the central comb mode, at a frequency detuning of ν_{inj} with respect to the free-running laser frequency [144].

We model spontaneous emission noise by a stochastic forcing $\sqrt{\beta}(\xi'_{sp}(t) + i\xi''_{sp}(t))$, with the spontaneous emission strength β . Similarly, we implement a timing noise in the optical comb leading to an RF comb linewidth $\Delta\nu_{\text{comb}}$, and a phase noise of the master laser, leading to an

Table 4.1: Simulation parameters used to model the detuning sweeps, unless noted otherwise. Values for the model were obtained by matching simulation outputs with the measured random intensity noise spectra of a free running laser, and the parameters are in line with literature values [144], [203].

Symbol	Value	Meaning
κ	60 ns ⁻¹	Cavity field loss rate
α	3	Linewidth enhancement factor
T	0.22 ns	Carrier lifetime
N_0	100 ns ⁻¹	Normalised transparency carrier density
J_{th}	220 ns ⁻¹	Threshold pump current
Δ_{comb}	10 GHz	Optical comb spacing
β	10 ⁻⁵ ns ⁻¹	Spontaneous emission strength
$\Delta\nu_{comb}$	1 MHz	Optical comb RF linewidth
$\Delta\nu_{inj}$	1 MHz	Master laser linewidth

optical linewidth $\Delta\nu_{inj}$:

$$\frac{\partial\phi_{comb}}{\partial t} = 2\pi\Delta_{comb} + \sqrt{2\pi\Delta\nu_{comb}} \xi_{comb}(t) \quad (4.4)$$

$$\frac{\partial\phi_{inj}}{\partial t} = \sqrt{2\pi\Delta\nu_{inj}} \xi_{inj}(t) \quad (4.5)$$

Here, $\xi_j(t)$ are complex Gaussian white noise source terms, fulfilling the correlation properties $\langle \xi_j(t)\xi_k(t') \rangle = \delta(t - t')\delta_{j,k}$. The parameters used in the simulations are contained in Table 4.1.

4.2.5 Model Comparison with High Resolution Detuning Sweep

A comparison between the model results and experimental data recorded using the high resolution optical spectrum analyser is shown in Fig. 4.7. Very good agreement is seen between the model and experiment. As in the previous subsections, a single mode slave laser's frequency was tuned from -20 GHz to +20 GHz relative to the centre line of a 3 line 10 GHz comb. In Fig. 4.7(a), an intensity plot shows the output optical spectrum of the slave laser. Vertical dashed lines indicate where the frequency of the slave matched that of one of the comb lines. In comparison to the previous detuning sweeps shown (e.g, Fig. 4.3 and Fig. 4.5), the higher resolution provides a better insight into the lasing frequency of the slave and the other frequencies generated. On the left of each of the three dashed lines, the slave laser undergoes standard Adler-type frequency locking, its frequency entrained by the closest optical comb line. For the centre and lower frequency comb lines, the ROs in the slave laser become undamped as the slave is detuned positively from the Adler-type locking region, which is followed by the ROs locking to a 5 GHz frequency. This does not occur in the higher frequency detuning case as there is some asymmetry around zero detuning, due to the α parameter. This is reproduced in the simulated results shown in Fig. 4.7(c). For the higher frequency comb line, the ROs become undamped but do not lock in both cases.

Further detail on the frequencies present in the detuning sweep is visible in the measured and simulated ESA data in Fig. 4.7(b) and 4.7(d). As with the optical spectra, there is strong agreement between the simulated and measured results. As the slave laser undergoes Adler-type locking, the electrical spectrum shows only the strong 10 GHz frequency and its harmonics (not shown). This 10 GHz frequency extends across all detuning values, due to the beating of the injected comb lines. Sub-harmonics at 5 GHz are generated when the ROs become excited,

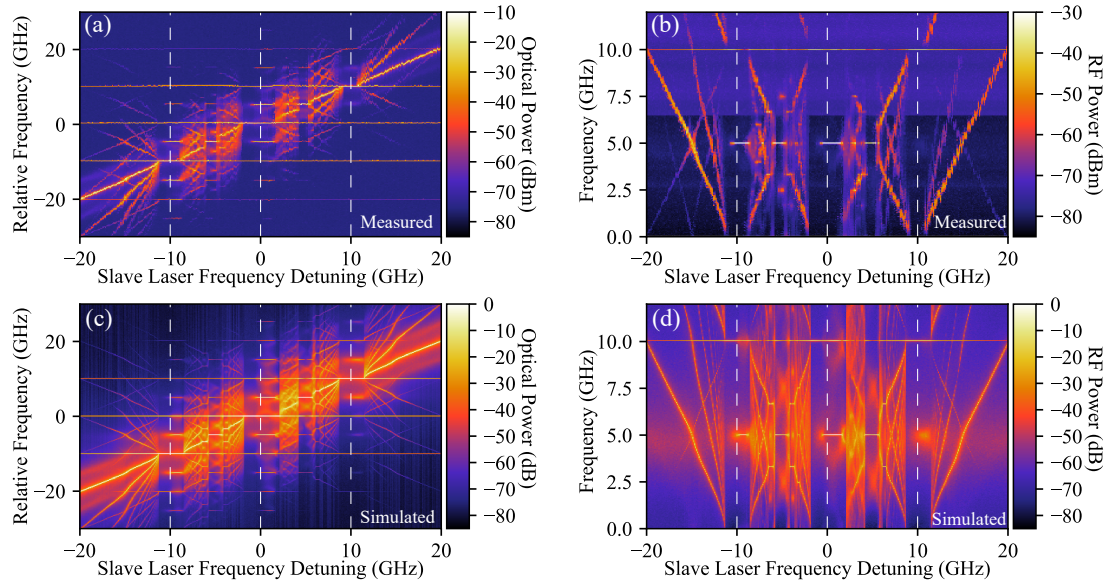


Figure 4.7: Experimental and theoretical results from a frequency detuning sweep (the theoretical modelling was performed by Dr. Benjamin Lingnau). In the experimental results, the slave laser was initially biased at 1.75 times threshold current with free-running power -4.5 dBm, and was injected by 3 line comb of total power -7 dBm, with spacing $\Delta_{\text{comb}} = 10$ GHz. The slave laser's temperature was varied to perform the frequency detuning sweep, and the vertical dashed white lines show where the free-running laser frequency is resonant to one of the optical comb lines. **(a)** Intensity plot of measured optical spectra as the slave laser was tuned across the injected optical comb. The frequency axis has been scaled such that 0 GHz coincides with the centre comb line. **(b)** Electrical power spectrum for the corresponding frequency sweep in (a). **(c)** Intensity plot of simulated optical spectra and **(d)** simulated electrical power spectrum with $K = 0.06$, for the same parameters as in (a) and (b).

and undergo a second frequency locking. The sub-harmonics lock to exactly half the comb spacing, then subsequently unlock and split as the detuning increases, prior to the slave laser becoming unlocked entirely from the comb line.

The high resolution OSA also clearly demonstrates the frequency locking observed as the slave was tuned in between the comb lines. At approximately ± 5 GHz, the slave's frequency can be seen fixed between the comb lines. The model also reproduces this behaviour, and gives further insight into how the slave laser's frequency is tuned between the lines. The ESA intensity plots also show beat notes at 2.5 GHz, 3.3 GHz and 5 GHz (and their higher harmonics) as the slave is tuned between the comb lines. In particular, the locking bandwidth of the 5 GHz resonances (or, the 1 : 2 resonances), located at ± 5 GHz detuning, are the largest (although as will be shown later in Subsection 4.4.1 this is not necessarily always the case).

The agreement seen between theory and experiment reinforces our understanding of how the unlocked comb lines interact with the slave laser. The slave laser clearly locks to (sub-)harmonics of the optical comb's frequency spacing. This is an example of harmonic locking, and while it is well known that harmonic locking appears in many driven oscillator systems, to our knowledge this is the first time harmonic locking has been demonstrated in a laser under optical comb injection. To better understand harmonic locking and how it manifests in a comb-slave system, the following section will first present a standard example of harmonic locking (in a non-linear model known as the circle map). Following this, the link between the circle map and the comb-slave system will be made clear.

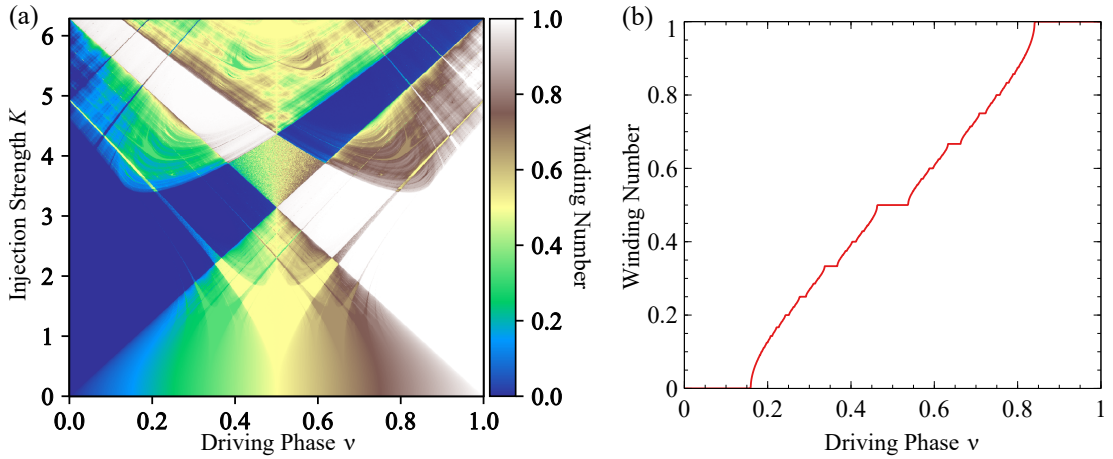


Figure 4.8: (a) Winding number as a function of the driving phase and injection strength for the circle map, for $0 \leq K \leq 2\pi$. (b) Single slice from (a), which shows the complete devil's staircase found in the winding number as the driving phase is swept from 0 to 1, evaluated at $K = 1$.

4.3 Arnol'd Tongues, Harmonic Locking, and the appearance of a Devil's Staircase

The frequency locking of a system to some external driving force is a fundamental phenomenon which occurs across multiple disciplines, from climate studies [204] to electrical circuits [115] to biological synchronisation [205]. Lasers subject to optical injection are a well-studied example [144] of such a system, and semiconductor lasers are a relatively cheap and reliable method of studying interesting dynamics. The following section discusses work which links the harmonic locking seen in the circle map [194], [206], [207] with the classic optical frequency locking observed as a semiconductor laser is injected by a master optical signal.

Subsection 4.3.1 first introduces the circle map, and shows how Arnol'd tongues appear in the circle map's parameter space. Following this, Subsection 4.3.2 links the comb-slave experiments to the experimental results in the previous section, and provides insight into the locking mechanism which causes a devil's staircase to appear in the slave's lasing frequency as it tunes between the comb lines.

4.3.1 The Circle Map

The circle map is a basic non-linear model, which is studied in many nonlinear dynamics textbooks. It can be used to model a periodic system with some pulsed forcing, and applications of the circle map have been found in many applications, including neuronal [208] and biological systems [209], [210].

The discrete circle map can be defined as [211], [212]:

$$\theta_{n+1} = \theta_n + \nu - \frac{K}{2\pi} \sin(2\pi\theta_n). \quad (4.6)$$

Here, K is the coupling strength and ν is driving phase. Often, the right hand side of (4.6) is defined using a modulus, as $\text{mod}(\theta_n + \nu - K \sin \theta_n, 1)$ (or with an equivalent scaling). For

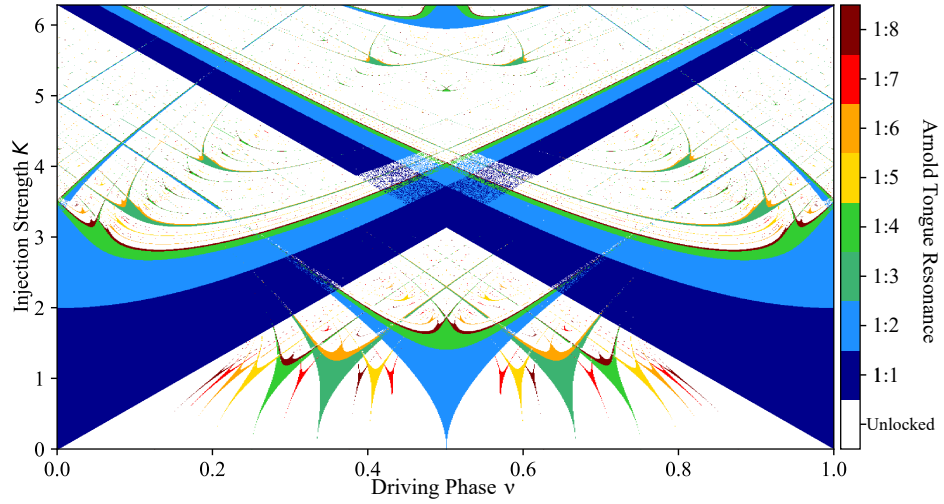


Figure 4.9: Two dimensional map spanning the injection strength K and driving phase ν , showing the Arnol'd tongues which appear, for $0 \leq K \leq 2\pi$. In each Arnol'd tongue, the map is mode locked to a different harmonic. For clarity, only the first 8 resonances are shown.

the case of $K = 0$, the map simply defines a trivial linear rotation at a rate of ν . For $|K| > 0$, the dynamics of the circle map are often characterised using the winding number (or rotation number) ρ defined as:

$$\rho = \lim_{n \rightarrow \infty} \frac{\theta_n - \theta_0}{n}. \quad (4.7)$$

The winding number gives the average phase shift per iteration of the map. A plot of the winding number over the two dimensional space spanned by the driving phase and injection strength is shown in Fig. 4.8(a). At each point in Fig. 4.8(a), the average winding number was averaged over 50 simulations, each case initialised with a random θ_0 . For low injection strength, the winding number tunes almost linearly as the driving phase is varied. However, as K increases, large areas with constant winding number appear. In these regions, θ_n becomes mode locked – this means that future steps in θ_n advance in a multiple of a fixed step size. Transitions to and from these mode locked regions occur through saddle-node bifurcations² [211].

For a fixed value of $|K| > 0$, the mode locked regions form a devil's staircase as the driving phase is altered [213] (the devil's staircase is a function made up of rational numbers which goes from 0 to 1, in which the simplest rational numbers have the largest steps). Shown in Fig. 4.8(b) for $K = 1$, the winding number takes fixed values of $1/2, 1/3, 1/4$, etc., over small bandwidths of the driving phase. In general, if a periodic mode locked state has period q , and during q steps the phase makes p rotations (i.e, $\theta_{n+q} = \theta_n + 2\pi p$), then the winding number $\rho = p/q$. All rational fractions p/q are present in Fig. 4.8(b), however the bandwidth of each winding number p/q is ordered in the same way as the fractions appear in the Farey sequence [214].

Figure 4.9 shows different harmonic mode locked solutions which exist. The first 8 harmonic locked states are plotted, where white regions indicate areas with either higher harmonic dy-

²A saddle node bifurcation is one in which two fixed equilibria collide and disappear.

namics or quasi-periodic dynamics. The vertical tongues extending from low K values³ are called Arnol'd tongues. The symmetry around $\nu = 0.5$ is apparent, and the sizes of the tongues decreases as the sub harmonics decrease (again, as in the Farey sequence). Arnol'd tongues appear in a wide variety of areas, from vibrations in musical instruments [215], [216] to cardiac rhythms [217] to the tidal locking of orbital moons. In the following section, we show that Arnol'd tongues also appear in the lasing frequency of semiconductor lasers when they are optically injected with a frequency comb.

4.3.2 The Devil's Staircase in the Frequency and Amplitude Locking of Nonlinear Oscillators with Continuous Modulated Forcing

Optical injection locking of a semiconductor laser to a master injected signal is an example of synchronisation, and when amplitude oscillations are negligible (i.e, the low injection strength regime), the system is governed by Adler's equation [115]. However, the comb injection results in Subsections 4.2.2 through 4.2.5 cannot be described by Adler's equation alone, as Adler's equation fails to predict the locking of the slave's frequency between the comb lines.

To address this, we start by re-examining Adler's equation:

$$\frac{d}{dt}\phi(t) = -\nu - K \sin(\phi(t)) \quad (4.8)$$

where here ν is the frequency difference between the slave laser and the master laser, and K is the injection strength. Adler's equation describes systems with continuous forcing, however if instead a periodic or modulated forcing is used, of the form $\sum_n \delta(t - nT) \sin(\phi(t))$, Adler's equation reduces to the circle map. This can be noted if you look at Adler's equation evaluated at the time of the n -th forcing:

$$\phi_{n+1} = \phi_n - \tilde{\nu} - K \sin(\phi(t)), \quad (4.9)$$

where $\phi_n = \phi(nT)$ and $\tilde{\nu} = T\nu$. The circle map has a much richer set of dynamics in comparison with Adler's equation, as systems which are described exactly by equation (4.8) can only be either phase locked, or have the phase continuously evolve. As shown in the previous section, the circle map exhibits multiple different phase-locked regions, with Arnol'd tongues appearing at oscillation frequencies corresponding to ratios of the driving frequency T^{-1} . To observe Arnol'd-type locking and dynamics in Adler's equation, we can transform the circle map in equation (4.9) into an ordinary differential equation by expressing the Dirac comb $\sum_n \delta(t - nT) \sin(\phi(t))$ as a Fourier sum:

$$\frac{d}{dt}\phi(t) = -\nu - K \sin(\phi(t)) \times \sum_{n=-\infty}^{\infty} \cos(n\Delta t). \quad (4.10)$$

Here, we define $\Delta = 2\pi/T$. Equation (4.10) only remains continuous for a finite number of Fourier components [218], which in practice is often the case.

The link between Adler's equation and the circle map was noted by Dr. Benjamin Lingnau,

³Using a bifurcation analysis approach, it can be shown that all Arnol'd tongues touch the $K = 0$ axis. With the numerical approach used to calculate the results presented in Fig. 4.9, this was not possible, as the oscillator is very weakly locked close to $K \approx 0$.

and the frequency sweeps discussed in Section 4.2 were used as an exemplary system to study the richer dynamics which occur when a system which is typically described by Adler-type locking is instead driven with periodic forcing. Semiconductor lasers have traditionally been used as a test bed for nonlinear dynamics, as many characteristic nonlinear properties can be reliably reproduced, and laser systems allow for the study of chaos, stochastic resonance effects, and spatio-temporal dynamics, among many other types of dynamics [143]. Hence, to replicate the Fourier sum in Eqn. (4.10) in a semiconductor laser system, we use an optical frequency comb.

A simplified version of the model presented in Section 4.2.4 was used to draw comparison between the standard circle map; while the model in Section 4.2.4 could also have been used to produce similar results, chronologically the model below was used first. A dimensionless rate equation model described the complex field $E(t)$ and the normalised optical gain $N(t)$ as:

$$\frac{d}{dt}E(t) = (1 + i\alpha)N(t)E(t) + \left.\frac{\partial E}{\partial t}\right|_{\text{inj}} + \sqrt{\beta}\xi(t) \quad (4.11)$$

$$T\frac{d}{dt}N(t) = J - N(t) - (N(t) + 1)|E(t)|^2 \quad (4.12)$$

Here, $J = 1.5$ is the normalized pump current, $T = 13.2$ is the relative inversion lifetime, and $\alpha = 3$ is the amplitude-phase coupling parameter. The time t is given in units of the inverse optical cavity lifetime, $\kappa = 60 \text{ ns}^{-1}$. The optical comb injected into the laser cavity is modelled by an additional driving term:

$$\left.\frac{\partial E}{\partial t}\right|_{\text{inj}} = KE_0(1 + 2m\cos(\Delta t)) - i\nu E(t), \quad (4.13)$$

where $m = 1.1$ is the relative strength of the injected side-modes at frequencies $\pm\Delta$. The injection strength K is the amplitude ratio of the injected field and the free-running laser intracavity field E_0 , and the spontaneous emission noise inside the laser cavity by a δ -correlated complex Gaussian white noise source term $\xi(t)$, with a noise strength $\beta = 4 \cdot 10^{-5}$.

Figure 4.10 shows a comparison between the simplified model and experimental results, which are very similar to the experimental and model results shown previously in Fig. 4.7. An optical comb with frequency spacing of 10 GHz was injected into a single mode slave laser, and as previously shown, the slave laser's frequency was tuned ± 20 GHz from the centre line of the comb. The optical spectra in Fig. 4.10(a) show that as the slave laser tunes close to one of the comb lines, the slave laser locks to that comb line. At slightly higher detunings in each case where the slave locks to a comb line, the ROs become undamped, and the ROs can be seen to frequency lock when the slave is locked to the lower frequency and higher frequency line. The simulated optical spectra in Fig. 4.10(b) matches the behaviour seen on the OSA well. Between the comb lines, additional frequency locking occurs. This frequency locking is clearer on the electrical spectrum analyser results shown in Figs. 4.10(c) and 4.10(d). Harmonic locking is visible as the slave laser tunes between the comb lines, and peaks at 5 GHz, 3.33 GHz and 2.5 GHz (and their harmonics) appear between the comb lines.

Using the simplified model presented in this subsection, strong parallels can be drawn between the comb injection experiments and the circle map results in Figs. 4.8 and 4.9. Figure 4.11 shows two dimensional resonance maps, spanned by the detuning between the comb and

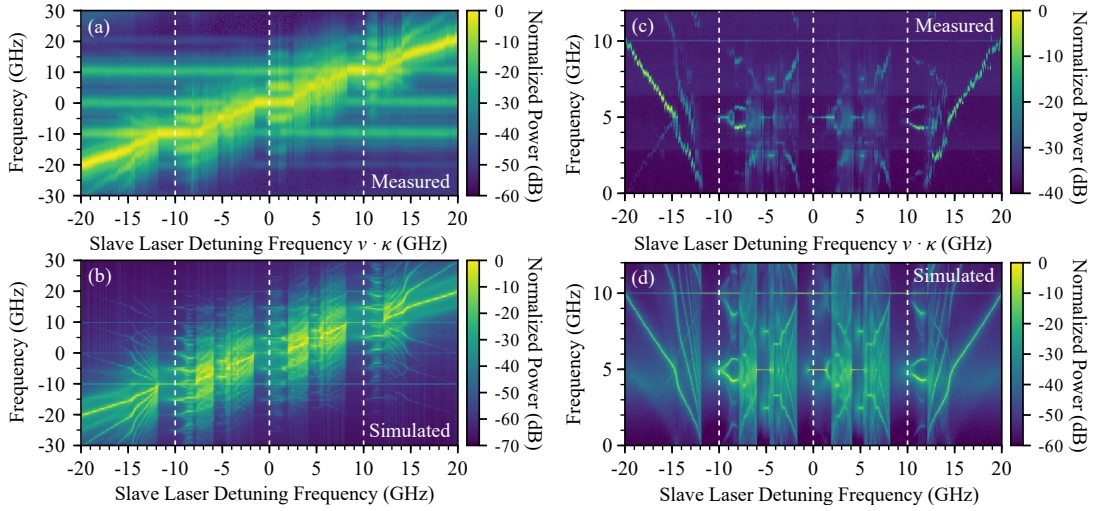


Figure 4.10: (a) Experimental and (b) simulated optical spectra, and the corresponding (c) measured and (d) simulated power spectra of the laser output for a sweep of the relative frequency detuning ν of the slave laser. The simulations were performed by Dr. Benjamin Lingnau. The injected signal consists of three spectral lines with a spacing $\Delta \cdot \kappa = 2\pi \times 10$ GHz. The experiments were performed at a slave laser pump current of 90mA (1.75 times its threshold). The injected optical power is -5 dBm, simulated with $K = 0.06$. The vertical dashed white lines show where the free-running laser frequency is resonant to one of the comb lines.

slave, and optical injection strength. The driving phase in the circle map is analogous to the detuning between the slave and master laser in this system. Figure 4.11(a) shows how many oscillations occur per period over the two dimensional space (where here a single period is considered one full oscillation from the optical comb). The three comb lines injected are centred at detunings of $-1, 0, 1$ in Fig. 4.11(a), and from each a large Adler-type locking tongue visibly grows from low to high injection strength. These are similar to the Adler-type tongues discussed in Subsections 3.5.1 - 3.5.3. For lower injection strengths within these tongues, the slave laser is stably locked to the comb, and the output from the slave laser is some demultiplexed 10 GHz comb. Regions with 2 amplitude oscillations per period have comb spacings of 5 GHz - when the ROs lock within the Adler-type tongues, the ROs lock to half of the comb spacing. The Arnol'd tongues shown in Fig. 4.11 clearly also appear at detunings in between the injected comb lines. Arnol'd locking tongues can be seen with multiple different amplitude oscillations, as the slave laser locks to different harmonic resonances. However, unlike in the circle map case, the resonances aren't symmetric around the mid-point between 1 : 2 resonance.

Figure 4.11(b) shows how the average optical frequency $\langle \nu_{\text{opt}} \rangle := \langle d\phi/dt \rangle$ of the slave laser's output varies over the same parameter space as in Fig. 4.11(a). In essence, the average optical frequency of the slave laser is equivalent to the winding number in the circle map, as can be seen when comparing the winding number results in Section 4.3.1 with Fig. 4.11(b). Within the Adler-type locking tongues, the average output slave laser frequency is exactly the comb line frequency. Arnol'd tongues also appear in the average lasing frequency, and the average lasing frequency locks within multiple resonance tongues in between the comb lines.

The study into periodic forcing in nonlinear oscillators was then extended further, and a Hopf-normal form oscillator was investigated. This type of oscillator describes the dynamics of ev-

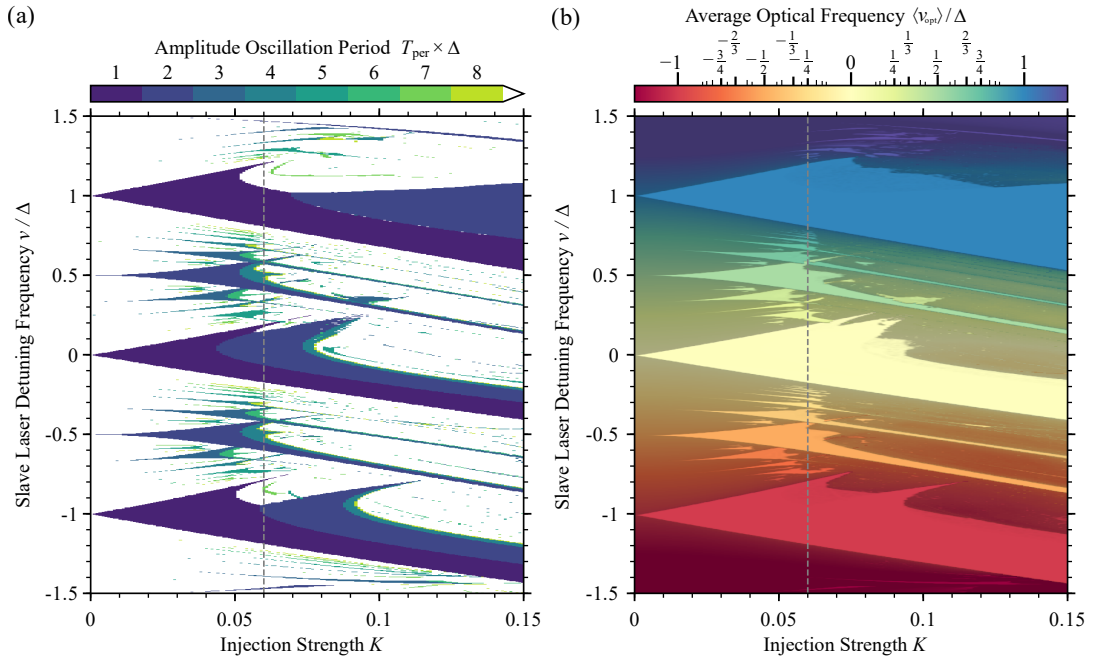


Figure 4.11: Two-dimensional resonance diagrams, showing (a) the period T_{per} of the intensity oscillations, and (b) average optical frequency $\langle \nu_{\text{opt}} \rangle$, in dependence on the injection strength K and the laser detuning ν from the center comb line with respect to the free-running slave laser frequency. Simulated without spontaneous emission noise, $\beta = 0$. The simulations were performed by Dr. Benjamin Lingnau. The plot in (b) highlights areas where the output frequency changes little between neighboring sampling points, i.e., $|\frac{d}{d\nu} \langle \nu_{\text{opt}} \rangle| < 0.05$. The horizontal dashed line denotes the parameter range covered in Figs. 4.10 and 4.12. All frequencies are normalized to the comb spacing Δ .

ery nonlinear oscillator close to a Hopf bifurcation. As Hopf bifurcations are ubiquitous in nonlinear systems, studying the Hopf-normal oscillator extends the relevance and application of these results much further than just a master-slave laser system. Figure 4.12 shows a comparison between results from the Hopf-normal form oscillator, circle map, and a slave laser under optical injected comb. Further information on the details and the parameters used in the simulations of the Hopf-normal form oscillator can be found in [196]. As shown in Fig. 4.8(b), the circle map shows a complete devil's staircase. Note however that the Hopf-normal oscillator also shows a devil's staircase in its average phase velocity $\langle d\phi/dt \rangle$ when forced with periodic forcing. As not all frequencies are present in the Hopf-normal or laser model cases, these devil's staircases are technically referred to as "harmless" staircases [219]. Adler's equation is also solved and plotted in Fig. 4.12 for reference (denoted in the figure as "phase oscillator"), which clearly shows no locking outside of the main resonances around $\nu = 0$ and $\nu = \Delta$.

This frequency locking mechanism is a direct consequence of the amplitude dynamics of the oscillators. Hence, all oscillators forced in this way close to a Hopf bifurcation exhibit a devil's staircase in their average phase frequency.

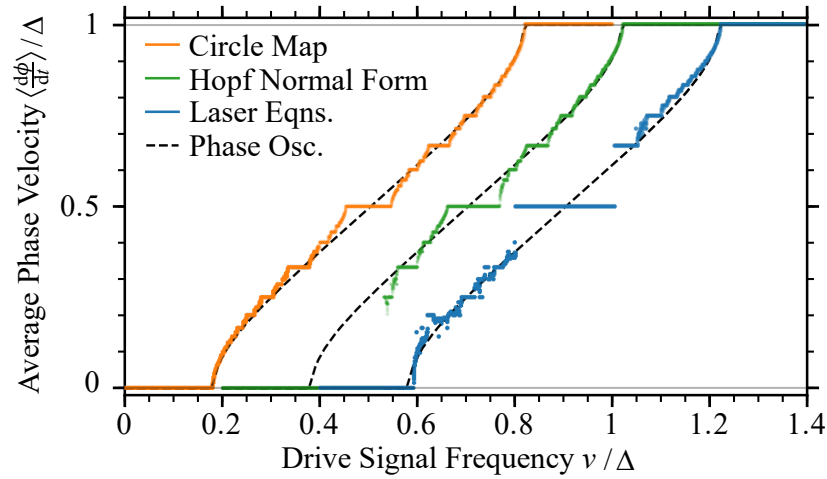


Figure 4.12: Comparison of the locking behaviour of different driven systems, showing the average phase velocity for the circle map (Eq. (4.6), orange, $K = 0.18$), the Hopf normal form (see Ref. [196], green, $K = 0.46$, $\gamma = 1$, $\Delta = 0.5$), and the laser equations (blue, $K = 0.06$, $\beta = 0$). The simulations were performed by Dr. Benjamin Lingnau. The plot shows subsequent curves with an artificial horizontal offset of 0.2 for better readability. The driven phase oscillator (Eq. (4.8), dashed line, $K = 0.18$) is shown as comparison for each model.

4.4 Relative Locking Stability and the Role of Linewidth Enhancement Factor

In the previous section, the mechanism behind the harmonic locking seen in the slave laser's lasing frequency was revealed, and it was shown that there are Arnol'd tongues in the parameter space of the comb-slave system. As there is strong agreement between theory and experiment shown in Sections 4.2.5 and 4.3.2, in this section the theoretical model from Section 4.2.4 is used to further understand how the α parameter affects the size of the locking tongues, and is also used to investigate the stability of the frequency locking and RO locking.

To study the relative range of parameter values that lead to the observed types of locking, two dimensional maps of the parameter space spanned by detuning ν_{inj} and optical injection strength K were calculated and are shown in Fig. 4.13 for a three line optical comb with 10 GHz spacing. In Fig. 4.13(a), the output comb spacing from the slave laser is monitored, for positive detunings only. Large Adler-type locking cones are centred around 0 GHz and 10 GHz detuning, where the slave laser is locked to one of the main comb lines. As the injection strength is increased within these Adler-type locking regions, we see the output comb spacing half in a period-doubling bifurcation, leading to a significantly large area of harmonic locking within the main locking cones. As demonstrated above in Section 3.4, within these regions the slave laser's ROs become undamped and lock to one half of the optical comb's spacing (the ROs lock to the 5 GHz subharmonic as the ROs were approximately 4.375 GHz in this case). The map in Fig. 4.13(a) also shows asymmetry between locking to the centre or higher frequency lines in the comb, as the RO locking occurs at lower injection strengths when the slave is locked to the centre comb line. Interestingly, we see further period doubling at even higher injection strengths in both of the Adler-type locking regions, before the slave unlocks from the injected comb. In order to characterise the stability of each of the locked states, the RF

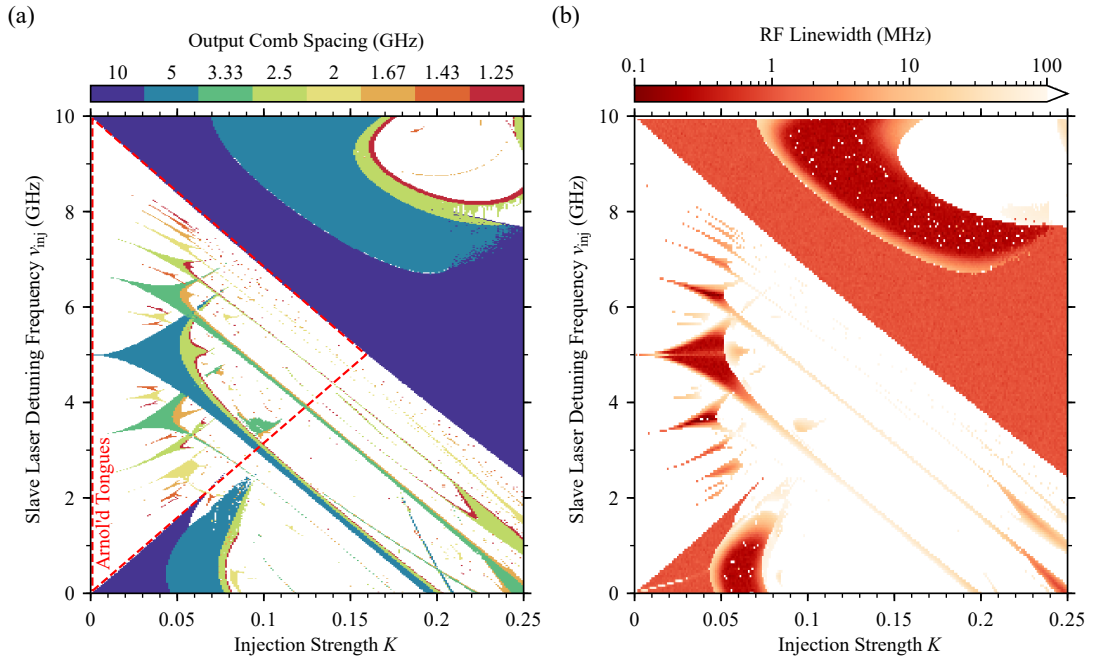


Figure 4.13: Two dimensional maps of the parameter space spanned by detuning and injected power, calculated with $J = 1.82J_{th}$ and $\Delta_{comb} = 10$ GHz. The simulations were performed by Dr. Benjamin Lingnau. **(a)** Map of the output comb frequency spacing. White regions indicate unlocked states. The triangular region enclosed within the dashed lines shows the parameter region used to calculate the relative size of the harmonic locking areas in Fig. 4.14. **(b)** RF linewidth of the dominant harmonic's beat note, over the same parameter space as in (a).

linewidth of the dominant RF peak in each state was calculated over the same parameter space and is presented in Fig. 4.13(b). At low injection strengths, the Adler locking cones around 0 GHz and 10 GHz detuning have RF linewidths close to the simulated comb linewidth of 1 MHz, suggesting these are stable locked states as expected. Within the harmonic RO locking regions of these cones, the RF linewidth decreases further to below 1 MHz, thus improving the comb stability even beyond that of the driving optical comb. This linewidth narrowing is due to the dynamical stability of the induced higher harmonic oscillations. The deterministic dynamics counteracts the effects of noise on the system [220], improving the linewidth. The boundary of the locked RO region is unstable however, as the noise stochastically kicks the injected laser out of the harmonic locking state, leading to a broad RF peak. Higher harmonic locking beyond the secondary period doubling bifurcations at even higher injection strengths can be seen to be highly unstable, with linewidths in excess of 100 MHz, suggesting a clean comb output can be obtained only for harmonic locking ratios that are not too high.

Smaller Arnol'd-type locking tongues can be seen in between the main Adler locking tongues in Fig. 4.13(a). As in the circle map [194], [206], [207], these harmonic locking tongues appear due to a periodic forcing, and in this case they appear due to the periodic forcing of the unlocked comb lines on the slave laser [196]. For low injection strengths, Arnol'd tongues can be seen at detunings corresponding to rational fractions of the optical comb spacing. The 1 : 2 resonance tongue, located at 5 GHz for lower injection powers, is the largest of these Arnol'd tongues, locking the frequency of the slave laser mid-way between the comb lines, causing the output comb spacing of the slave to be 5 GHz. Within this locking tongue, we see some period doubling occur as the injection power is increased. The RF linewidth map in Fig. 4.13(b) sug-

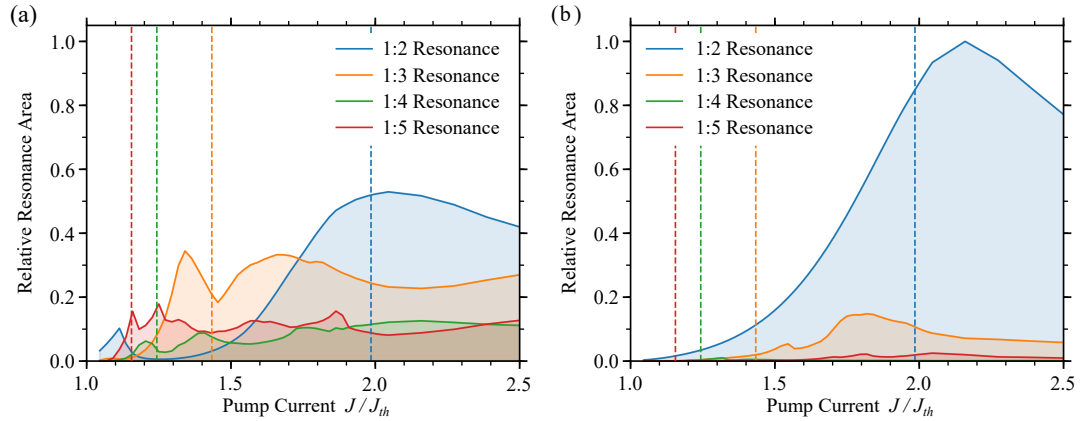


Figure 4.14: Plots showing the relative size of the Arnol'd resonances as a function of slave laser pump current, for (a) $\alpha = 3$, and (b) $\alpha = 0$. The simulations were performed by Dr. Benjamin Lingnau. For each current, a two dimensional map over injection strength and detuning was calculated as in Fig. 4.13 with $\Delta_{comb} = 10$ GHz, and only the area contained in each resonant Arnol'd tongue was counted. The vertical dotted lines indicate the pump currents at which the free-running RO frequency matches that of a resonance. Some of the maps used to calculate the above results are presented in Appendix C.

gests that the centre of the 1 : 2 resonance Arnol'd tongue is stable, with unstable boundaries. As with the Adler-type locking regions, the period doubled states which appear as the injection strength is increased within the 1 : 2 resonance tongue are very unstable. Figure 4.13(a) clearly shows the sizes of the 1 : 3, 1 : 4 and 1 : 5 resonances shrink as the denominator in the rational fraction grows. The corresponding RF linewidth calculation also suggests that these resonances become less stable as the denominator grows.

4.4.1 Relationship Between the Relaxation Oscillations and the Size of Arnol'd Tongues

The free-running frequency of the ROs has to be close to a rational fraction of the comb's frequency spacing, in order for the ROs to lock. The size of the locked RO regions within the Adler-type locking regions in Fig. 4.13 can thus be expected to depend critically on how close the free-running ROs are to a subharmonic of the comb spacing. In the following subsection, we instead investigate the dependence of the Arnol'd regions on the RO frequency of the free-running laser for the 10 GHz injected comb considered in Fig. 4.13. Examples which instead use larger comb spacings are discussed in Section 4.6, where it is shown how the Arnol'd tongues vary and shrink as the optical comb spacing is increased.

Figure 4.14(a) shows a measure of the area of each Arnol'd resonance tongue in the parameter space within the red dashed triangle in Fig. 4.13(a) as a function of the slave pump current, for $\alpha = 3$. For each pump current, a two dimensional map was computed, and the size of each Arnol'd tongue within the area enclosed in the dotted red triangle in Fig. 4.13(a) was counted. Example outputs from the computation are shown in Appendix C. The vertical dotted lines in Fig. 4.14(a) indicate the pump currents at which the free-running RO frequency matches that of a resonance. The results show a strong correlation between the size of the frequency locked resonances and the RO frequency. We find that the 1 : 2 resonance only becomes the largest resonance as the RO frequency approaches half the injected comb spacing. Likewise, as the RO frequency approaches one-third and one-fifth of the comb spacing, the 1 : 3 and

1 : 5 resonances are the largest in the parameter space. The same is not true for the 1 : 4 resonance. Interestingly, in each case, the maximum of the resonance area doesn't correspond exactly with the pump current where the ROs frequency exactly matches the resonance. This could be in part due to variance between the free-running ROs and the ROs in the locked slave laser [179]. The ROs in an injection locked slave laser also vary with optical injection strength and detuning [142], both of which are parameters varied in the two dimensional resonance areas measured. Nevertheless, the theoretical predictions suggest that for a specific harmonic resonance an optimal pump current exists at which that resonance can be produced reliably.

Figure 4.14(b) repeats the calculation of Fig. 4.14(a) with $\alpha = 0$. Example outputs from the computation are shown in Appendix C. It is immediately clear that the magnitude of the amplitude-phase coupling in the slave laser's electric field has a strong impact on the how large the resonance areas are. Interestingly, the 1 : 2 resonance grows in size with decreasing α , with the 1 : 2 resonance remaining dominant for all pump current values in this case. The higher order resonances are severely suppressed in the $\alpha = 0$ case. It is also noteworthy that the correlation between the free-running RO frequency and the peaks of the resonance areas is much weaker in this case, showing that the nonlinearity in the laser response induced by α is a main driving mechanism for the excitation of the higher order resonances.

4.5 Asymmetry of Relaxation Oscillation Locking around the Centre Comb Line

In this section, further results are presented detailing the asymmetry of the RO locking around the optical comb centre. The results which motivate this discussion are shown in Fig. 4.15. Similar to the detuning sweeps presented above, Figs. 4.15(a) and 4.15(b) show measured and simulated ESA spectra as the frequency of a slave laser was tuned ± 14 GHz (from negative to positive) relative to the centre of a 6.5 GHz comb. In this case, an optical comb spacing of 6.5 GHz was chosen to ensure that the free-running ROs of the slave laser approximately matched $\frac{2}{3}$ of the comb spacing.

While locked to the lower frequency comb line, the slave laser ROs become undamped and lock to $\frac{1}{3}$ of the comb spacing. The bandwidth over which the ROs remain locked is narrow, relative to the 10 GHz case shown previously. While the slave is locked to the centre line however, we note that the ROs lock instead to $\frac{1}{2}$ of the comb spacing. This highlights the asymmetry introduced by using a 3 line optical comb – the modulation effect is stronger at zero detuning as the neighbouring comb lines have higher intensity, and as a result the modulation is strong enough to force the ROs to lock to a frequency of 3.25 GHz. For the higher frequency comb line, the ROs become undamped and instead of locking immediately, tune in frequency from 4.8 GHz to 4.33 GHz. The difference between the behaviour of the ROs while locked to the lower frequency and higher comb lines is due to the asymmetry introduced by the amplitude-phase coupling.

Figure 4.15(c) shows a two dimensional map which highlights the output comb spacing, for the parameter space spanned by detuning ν_{inj} and optical injection strength K . The vertical dotted line indicates the injection power used in (b). In this case, we notice that the Arnol'd

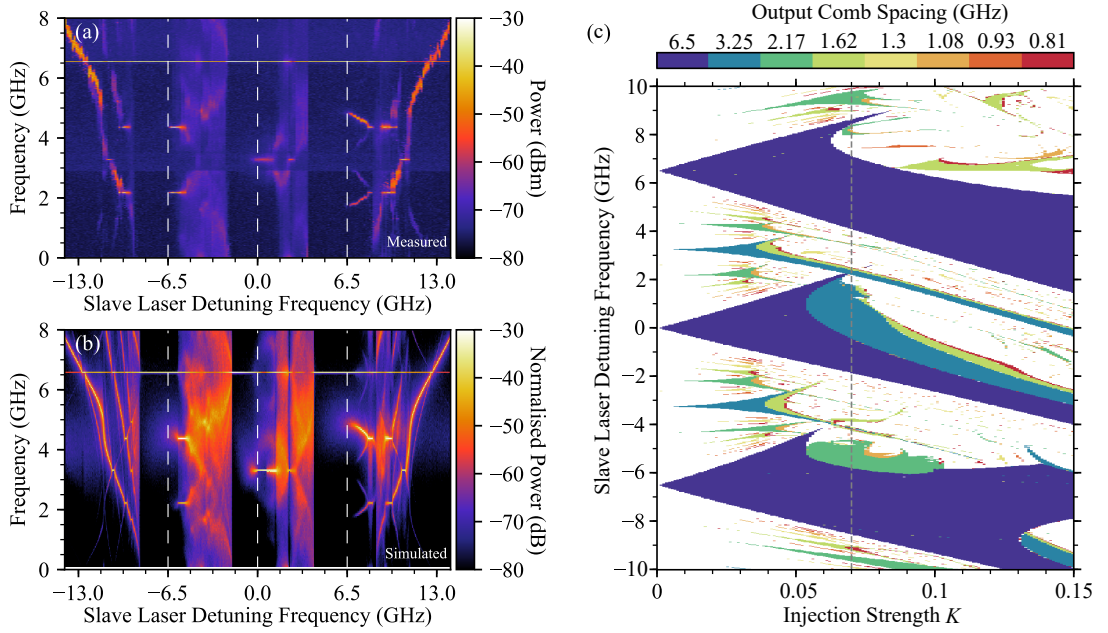


Figure 4.15: (a) Intensity plot showing the electrical spectra measured as the frequency of a single mode slave laser was swept across the injected 6.5 GHz optical comb. The optical comb had a power of -5.0 dBm, and the slave laser was initially biased at 1.75 times threshold current, with -4.4 dBm coupled to the lensed fibre. The vertical dashed white lines show the parameter values where the free-running laser frequency is resonant to one of the optical comb lines. (b) Corresponding simulated experiment for the parameters in (a). (c) Two dimensional map of the parameter space spanned by detuning and injected power, showing the output comb frequency spacing, calculated with $J = 1.75J_{th}$ and $\Delta_{comb} = 6.5$ GHz. The vertical dotted line indicates the injection strength used in (b). White regions indicate unlocked states. The simulations were performed by Dr. Benjamin Lingnau.

tongues are significantly smaller in size than previously seen in the 10 GHz case, due to the narrower spacing of the optical combs. This is reflected in both the experimental and simulated detuning sweeps, as neither have strong locking events as the slave tunes between the comb lines. Likewise, the two dimensional parameter map shows different RO locking behaviour within the three Adler locking cones. The lower frequency Adler cone has a region where the ROs lock to $\frac{1}{3}$ of the optical comb spacing. In the centre Adler cone, the ROs lock instead to $\frac{1}{2}$ of the input comb spacing, and as seen in experiment, the ROs don't lock at all in the higher detuning cone. However, as the number of comb lines increases, the behaviour within the Adler locking cones will only differ for the outer comb lines.

4.6 Large Comb Spacings and the Limits of the Harmonic Locking Mechanism

The results presented up to this point in this chapter have been largely fixated on two separate combs spacings (10 GHz and 6.5 GHz). As a result, the following section investigates what occurs as the comb spacing is increased far beyond 10 GHz, in order to investigate when the Arnol'd tongues disappear. As the spacing between the injected optical comb lines increases, the slave laser's dynamics are less affected by the neighbouring unlocked comb lines. Figure 4.16 presents theoretical results which show how the output comb spacing of the slave laser

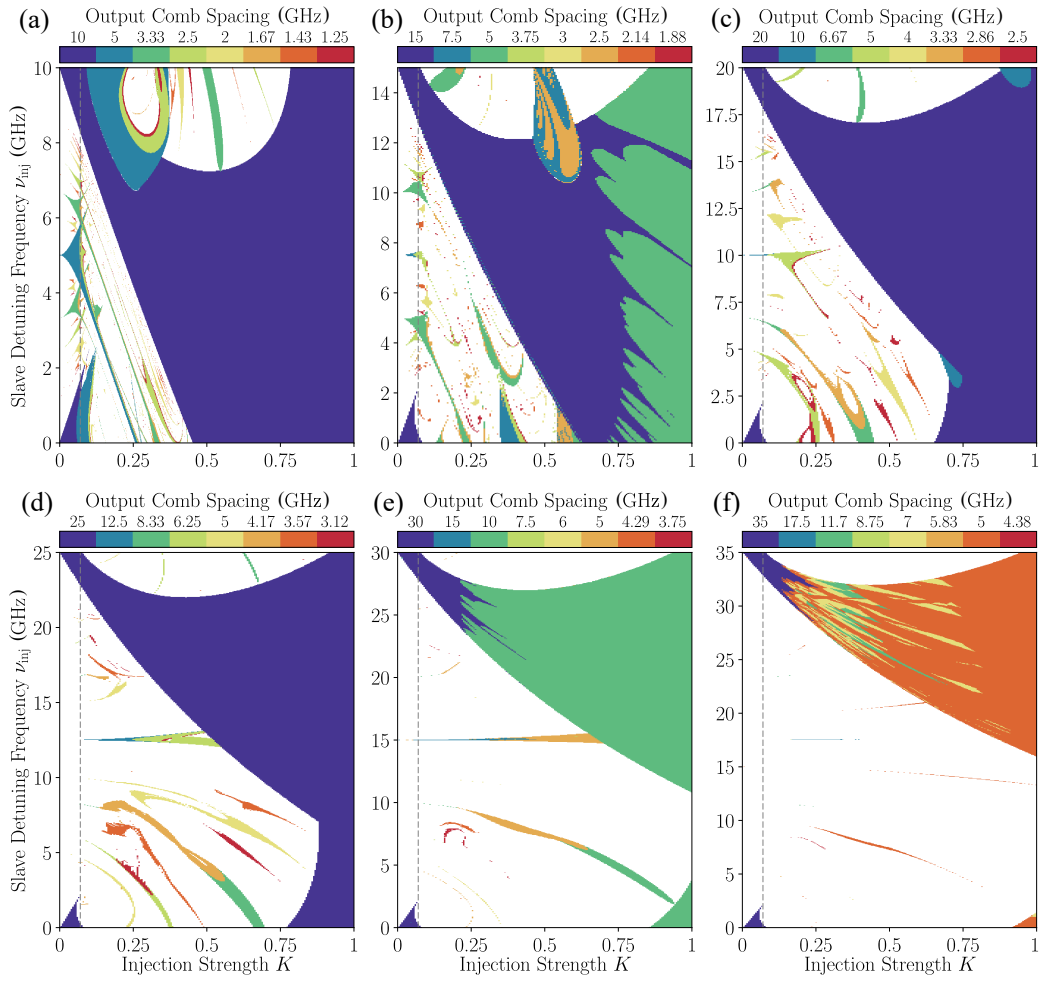


Figure 4.16: Two dimensional maps of the parameter space spanned by detuning and injected power, which show the output frequency spacing of the slave laser, calculated with $J = 1.82J_{th}$ (corresponding to an RO frequency of 4.375 GHz). The comb spacings used were (a) 10 GHz, (b) 15 GHz, (c) 20 GHz, (d) 25 GHz, (e) 30 GHz, and (f) 35 GHz. White regions indicate unlocked states. The simulations were performed by Dr. Benjamin Lingnau.

varies as the injected comb spacing is increased. The vertical dotted lines in Figs. 4.16(a)–4.16(f) show the injection strengths used in the detuning sweeps discussed in Fig. 4.7, and larger injection strengths are presented here to introduce broader regions of interest. As discussed in Section 4.4.1, the frequency of the slave laser’s relaxation oscillations affects the harmonic locking which can occur. Comparing the sizes of the 1 : 2 and 1 : 3 resonances located at detunings between the comb lines in Figs. 4.16(a) and 4.16(b), we find that the 1 : 2 resonance almost disappears as the comb spacing is increased to 15 GHz, whereas the 1 : 3 resonances have almost equivalent size in the both the 10 GHz and 15 GHz cases. The 1 : 3 resonances remain large in the 15 GHz case, as the frequency of the ROs was approximately 5 GHz. Similarly, we find that the 1 : 4 resonance is the most prominent in the 20 GHz case (Fig. 4.16(c)). At a detuning of 10 GHz, a small 1 : 2 resonance can be seen for lower injection strengths, becoming a larger 1 : 4 resonance at higher injection strengths. Again, this occurs as the free running RO frequency is closer to 1 : 4 resonance than the 1 : 2 resonance. For the 25 GHz and 30 GHz cases shown in Figs. 4.16(d) and 4.16(e), the higher harmonics (i.e., 1 : 5, 1 : 6 and 1 : 7 resonances) dominate. Eventually, as the comb spacing is increased further still, the

Arnol'd tongues begin to disappear (Fig. 4.16(f)). The harmonic locking mechanism is thus limited by the RO frequency of the driven laser. The attainable output comb spacing is close to that frequency, and for very large comb spacings the mechanism is greatly suppressed.

The behaviour within the Adler-type locking regions also changes significantly with increased comb spacing. In Fig. 4.16(b), only a small RO locking region is visible at low injection strengths. At higher injection strengths, the ROs in the slave laser strongly lock to smaller fractions of the comb spacing, whenever the slave's ROs are suitably close to a rational fraction of the comb spacing. Interestingly, the RO locking regions are not prevalent in the 20 GHz and 25 GHz cases, yet reappear at high injection strengths for the higher injected comb spacings cases.

4.7 Chapter Conclusion

In the chapter above, further experimental and numerical studies were presented. The discussion in this chapter was focused on two types of frequency locking which occur with optical comb injection, rather than the SMSR obtainable through optical injection. Namely, the frequency locking mechanisms where the locking of the undamped relaxation oscillations, and the Arnol'd type higher order resonance tongues found as the slave laser's frequency lied between the comb lines. In effect, both types of locking can be used to decrease the optical comb spacing of the original injected optical comb. It was shown that relaxation oscillations of the injected laser can lock to harmonics of the injected optical comb, generating extra tones in the optical comb around the slave laser's lasing frequency. The relaxation oscillations can in principle lock to any rational fraction of the input comb's frequency spacing. However, simulations showed that the extent of the locking range in general decreases with the order of the harmonic resonance. Furthermore, through analysing the simulated RF linewidth, it was shown that both Arnol'd frequency locking and the relaxation oscillation locking can be as stable as the standard Adler-type locking, and in some cases reduce the RF linewidth of the produced output comb compared to the injected comb. The effect of the free-running relaxation oscillation frequency on the extent of the Arnol'd resonances in parameter space was also discussed.

The locking range for producing a given harmonic comb can be optimised by tuning the slave laser relaxation oscillation frequency to an optimal value via the pump current, and furthermore, the nonlinearity induced by the α parameter is a driving mechanism for the generation of harmonic locked states in the injected slave laser. The presented locking scenarios can be used to generate optical combs with variable frequency spacing, as well as regenerate noisy frequency combs via the nonlinear interaction within the laser device, producing a comb with narrower RF linewidth.

Chapter 5

Conclusion

The aim of the research in this thesis was to study optical comb injection, both for its technological use as an optical comb demultiplexer, and to further the understanding of the semiconductor laser dynamics which occur when an optical comb is injected into a laser.

It was shown that it is possible to demultiplex narrow optical combs on a photonic integrated circuit. While it was found that there are some drawbacks to using this technique (e.g. the SMSR and locking bandwidth are inversely proportional, and the negative effects introduced by the ROs), it is still possible to monolithically integrate a slave laser on chip to act as a demultiplexer. The results in this thesis map out the favourable operating regions to achieve high SMSR, and further the understanding of optical comb injection.

Further, this thesis results shows that, unsurprisingly, optical comb injection can undamp and excite the relaxation oscillations (ROs) in the slave laser, which in turn ruins the comb demultiplexing. However, it was not known that these undamped ROs can frequency lock to fractions of the comb spacing, which in turn creates a new comb. Hence, optical comb injection could also be used as a method of changing the output optical comb spacing from the input comb spacing.

The following section briefly summarises the main results from each of the results chapters, before possible future work is discussed in Section 5.2.

5.1 Overview of the Results Presented

Chapters 2 and 3 were primarily focused on using optical injection as a method of demultiplexing optical combs. As photonic integration offers many economic advantages (such as reducing cost, device size, energy consumption and device packaging), photonics research has seen increasing investment in reliable photonic integration techniques. Standard integrated optical comb demultiplexers cannot demultiplex narrow optical combs, due to the large device sizes and high resolution fabrication required. As was shown in this thesis, optically injecting a semiconductor with a frequency comb can circumnavigate these restrictions, as optical comb demultiplexing is possible using this technique.

In Chapter 2, optical injection experiments were first introduced. Some of the properties of single frequency optical injection were investigated, such as the amount of mode suppression seen when a slave laser is locked to the injected signal. A numerical model, named the Fabry-Pérot laser model, was developed and initially used to model single frequency optical injection. Optical injection in both Fabry-Pérot and slotted Fabry-Pérot devices was investigated, and good qualitative agreement between the model and experiment was found. The Fabry-Pérot model laser model was then extended to include optical comb injection, and used to model results from a device designed to be a 1×2 optical demultiplexer. Again, good qualitative agreement was found experiment and theory. As the measured side mode suppression ratios (SMSR) at that time had not surpassed 25 dB (with greater than 30 dB ultimately the target), some of the key laser parameters were altered, to try and optimised the output SMSR when demultiplexing a comb.

It was found that increasing the Q factor of devices increases the output SMSR, however this increase occurs nominally at the same rate as it would with a passive device. Fortunately, for a fixed pump rate relative to threshold and a fixed injection ratio, the locking range of the devices appears to tend asymptotically to a fixed value with increasing Q.

While the Fabry-Pérot model was effective at modelling the slotted devices, within the derivation of the model there are several assumptions which limit its usefulness. Firstly, the model assumes that the injected laser is in a steady state, which eliminates any dynamics which can occur due to the optical injection. Secondly, it was assumed that the optically injected field strength was much smaller than the slave lasers field, and hence it is not possible to investigate the high injection limit. For these reasons, a single mode rate equation model was also developed. Rate equations model how the slave laser's field, carriers and phase evolve over time, and allowed an investigation of the dynamics omitted by the Fabry-Pérot model.

In Chapter 3, it was shown that the rate equation model predicted the SMSR obtainable when locking the slave laser to the highest and lowest frequency lines in a comb is nominally the same for large comb frequency spacings, yet this begins to differ at smaller comb frequency spacings. Early results from the rate equation model also predicted that the relaxation oscillations within the slave laser negatively affect the SMSR at low frequency spacings, and these predictions were then confirmed using two separate experiments. The first experiment indirectly measured the magnitude of the demultiplexed comb line, by measuring the beat note between an external laser and the demultiplexed comb line. Results from the experiment validated the model's predictions, however due to equipment limitations, the experiment used large 1 GHz step sizes. When a high resolution optical spectrum analyser became available, the experiment was re-visited, allowing the output SMSR to be directly measured. Using the new optical spectrum analyser, it was found that the relaxation oscillations (ROs) could be undamped and excited using optical comb injection, and that the undamped ROs could be locked to rational fractions of the frequency comb spacing.

The differences between the phasor diagrams of single frequency injection experiments and optical frequency comb injection experiments was also discussed. It was shown that the slave laser's field and phase is modulated slightly when injected with an optical comb, and as a result the laser's limit cycle in phase space can never be at a "stationary point" (by definition). Bounded phase limit cycles can exist with optical comb injection, and a comparison between

the single frequency case and the optical comb case revealed the effects of the modulation of the unlocked comb lines on the limit cycle. The model was then used to map how the SMSR varied over the two dimensional space spanned by the optical injection strength and detuning. Comb spacings which matched multiples of the RO frequency were highlighted and discussed, as it was shown how the regions where the ROs lock to the comb grow and shrink in parameter space. Understanding the relative size of these regions is important, as the output SMSR approaches zero when the ROs become undamped and frequency lock. Both theory and experiment showed that higher injection strengths have lower SMSRs, and so the output SMSR and the locking bandwidth of the slave laser are inversely proportional. Hence, optimal SMSR will always be achieved when the slave laser is very weakly locked to the master.

Chapter 4 then further investigated the dynamics observed. Frequency detuning sweeps were used to show that the injected laser can be stably locked in between the comb's frequency lines, and it was found that a devil's staircase appears in the lasing frequency of the slave laser as it tunes while under injection. This was investigated using a slightly different rate equation model than in Chapter 3, and the results reproduced the experimental observations very well. It became evident that the locking states in between the comb's frequency lines were Arnol'd tongues, and this was confirmed by completing a simple study of the circle map. These results were then completely generalised in a separate study Ref. [196], where it was shown that any non-linear oscillator which is undergoing continuous modulated forcing exhibits a devil's staircase in it's operating frequency.

Two dimensional parameter space maps were used to indicate how stable the different locked states found with optical injection locking are. The simulated RF linewidth fell well below the driving linewidth when the slave laser was either locked in between the comb lines, or when the ROs became locked to a fraction of the comb spacing. Hence, the model suggests that comb linewidths could be improved using optical comb injection. As the output combs are very stable, comb injection could also be used to convert the frequency spacing in an optical comb. Both types of locking (RO locking, and locking between the comb lines) can be used to decrease the optical comb spacing of the original injected optical comb. It was shown that the non-linearity induced by the α parameter has a large effect on the sizes of the different harmonic locking regions, and that by tuning the RO frequency of the slave laser, these harmonic locking regions can grow and shrink in size.

5.2 Future Work

The work in this thesis has contributed towards the realisation of a PIC suitable for optical comb based communication networks. Ideally, an optical comb source capable of producing narrowly spaced comb lines would be integrated with several slave lasers, in order to demultiplex the comb lines. These demultiplexed comb lines could then be modulated and recombined on the same PIC, before being transmitted across a network. Figure 5.1 shows a schematic for such a PIC [221]. Although this device design is highly ambitious, it offers excellent potential as a solution to the approaching bandwidth problem in optical communication networks.

Some of the components required to make such a device have already been developed - in-

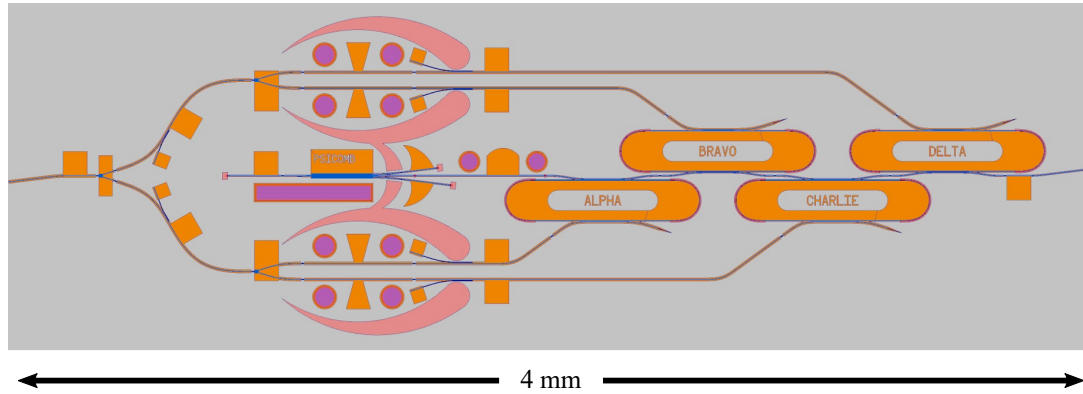


Figure 5.1: Schematic of a photonic integrated circuit (PIC) for the generation of an integrated coherent optical comb transmitter, taken from Ref. [221]. The schematic shows how an optical comb could be generated by injecting a tunable laser signal (labelled PSICOMB, similar to those shown in Ref. [222]) into a gain switch waveguide section, located in the centre-left of the PIC. The optical comb could then be demultiplexed by injection locking each of the ring lasers (labelled ALPHA, BRAVO, CHARLIE, DELTA) to separate line in the comb [223]. The demultiplexed lines can then be modulated, and recombined before being transmitted.

tegrable tunable lasers [222] and optical comb generators [108], [109] have previously been shown. To continue toward making this PIC a reality, the next step would be to optimise the ring lasers to enable high Q cavities. Optically demultiplexing using ring lasers was studied in Ref. [223], and as discussed in Chapter 2, higher Q factors are preferable for high SMSRs. The Q factor of the ring laser can be controlled by the strength of the optical coupling to and from the ring, and an experimental study on the optimal coupling ratio between the rings and the injected comb would reveal how weak the coupling can be before the ring lasers can no longer lock to the comb signal. Weaker coupling would be advantageous as it would improve the SMSR obtainable (as discussed in Chapter 3) while also improving the Q factor of the ring.

This PIC would also require on-chip integrated modulators, and as a result further research to determine the SMSRs required from the demultiplexers to suitably modulate the signal is needed. The speeds of the modulators could also be improved and optimised with future designs. Finally, shrinking the size of the device could be required (for example, shrinking the sizes of the ring lasers used).

This work also revealed that the properties of an injected comb, such as the comb spacing and potentially the comb linewidth, can be altered with optical injection. It would be valuable to experimentally verify that the output optical comb's linewidth can be reduced below the injected comb's linewidth, as this could be of technological interest in the future.

The dynamics which occur with extremely narrow comb spacings were not investigated during the project - it could be of interest to investigate the behaviour of semiconductor lasers when injected with optical comb's with spacings far below the RO frequency. By analogy to other forced non-linear oscillators, it seems likely that the ROs in the injected laser could also be locked to a multiple of the combs frequency spacing when the comb spacing is below the RO frequency.

Finally, further research could be carried out to see if the linewidth and comb spacings of on-chip comb sources can be improved through optical comb injection.

Appendix A

The Inverse Scattering Method for Single Mode Devices

During the introductory chapter of this thesis, the motivation for regrowth-free semiconductor lasers which use standard contact lithography was outlined. The fabrication processes of distributed feedback lasers or distributed Bragg reflector (DBR) lasers can be expensive and time consuming, and as a result, much research has been focused on designing devices and processes which eliminate the need for high precision lithography and epitaxial regrowth.

Slotted Fabry-Pérot lasers [73], [75], [79] are one such example, which use slots etched into the ridge of the waveguide to provide feedback and mode selectivity. Slotted Fabry-Pérot lasers can provide high side-mode suppression ratios (SMSR) and low linewidth, however the slots which provide the wavelength selectivity of the laser are etch depth dependent [79]–[81]. As a result, etch stop layers are required to accurately control the reflectivity of the slots, and the anisotropy of chemical etches [82] can lead to different results across a wafer.

The following Appendix outlines work which was carried out during this project, with the goal of creating strongly single mode devices without using slots in the waveguide. We demonstrate regrowth-free single moded lasers which use etch depth insensitive pits [81] etched into the waveguide of the slave laser. The pits are etched deep into the material, and hence the amount of reflection introduced into the laser cavity does not vary strongly with etch depth, unlike in the case of slots. High SMSR (37 dB) and low linewidth have been previously demonstrated using 30 pits in an integrated DBR like mirror [84]. In the following, single moded lasing is achieved by using pits as local perturbations placed as described by an inverse scattering technique [85]. The inverse scattering technique used has successfully been demonstrated using slots [76] and side wall gratings [86], however in both cases either high resolution e-beam or high reflectance (HR) coatings were applied to the facets of the devices. The design of the devices presented uses Fourier techniques to specify the position each pit should be placed, in order to approximate a target threshold gain function.

The deeply etched waveguide pits, which require no epitaxial regrowth and use standard contact UV lithography, can achieve similar results with higher fabrication tolerances and lower fabrication costs. Each pit is etched down to a depth of 0.8 μm beyond the quantum wells

(QWs) in the centre of the ridge waveguide of the laser, and is circular with a 1 μm diameter. Unlike the reported slotted inverse scattering lasers, the side wall roughness and etch depth of the perturbations used isn't as integral to the device's operation, as the deeply etched pits are used as local perturbations in the laser's waveguide. As a result, devices using pit perturbations have higher device yield than slotted devices, however suffer slightly in performance due to the rudimentary perturbations used, which lead to additional scattering losses. Standard commercial AlInGaAs material grown on a InP substrate was used for the fabrication of the devices, and the details of the epitaxial structure used can be found in Appendix D.

Sections A.1 and A.2 re-derive the method presented in [85], presenting more detail than the published method. Section A.3 describes the method that was used to calculate the perturbation positions required. Finally Section A.4 describes the devices that were designed using this method, with device results presented in Section A.5. Some of the device results presented here were published in IEEE Photonics Journal.

A.1 Derivation of First Order Perturbation to Gain

The inverse scattering method used to achieve single mode lasing was first presented by O'Brien et al. in [224], and was later expanded and described in more detail in [85]. The strength of using the inverse scattering method over a regular periodic grating is the ability to engineer the output spectrum of a semiconductor laser using simple perturbations along the lasers ridge. Single mode, dual mode [76], [225] and optical comb generation [226], [227] have all been modeled using the inverse scattering method. Experimental results for single mode devices have shown SMSRs of up to 50dB, however the fabricated devices used HR coated facets with several etched slots.

When the modeling of the devices was performed, the method used was mostly unchanged from O'Brien's 2011 paper. A full description of the method is presented below, and all the assumptions introduced due to the pit perturbations rather than slots used in [85] and this work are highlighted within the section.

To achieve single mode lasing, the inverse scattering method attempts to lower the threshold gain of a target mode more than the other competing longitudinal Fabry-Pérot modes in the laser cavity. This is achieved by introducing N perturbations into the laser cavity, where each perturbation changes the effective index of the supported optical mode by $\Delta n = n_1 - n_2$, as shown in Fig. A.1(a), where n_1 is the effective refractive index of the waveguide, and n_2 is the effective refractive index of the perturbation section. The method calculates the locations of each perturbation, to minimise the threshold gain of the target mode.

We can describe each section j of the cavity using one dimensional transmission matrices [159]. Similar to Section 2.4, the transmission matrix associated with a small perturbation in index (as shown in Fig. A.1(b)) is given by:

$$F = T_{12}P(\theta_2)T_{23} \quad (\text{A.1})$$

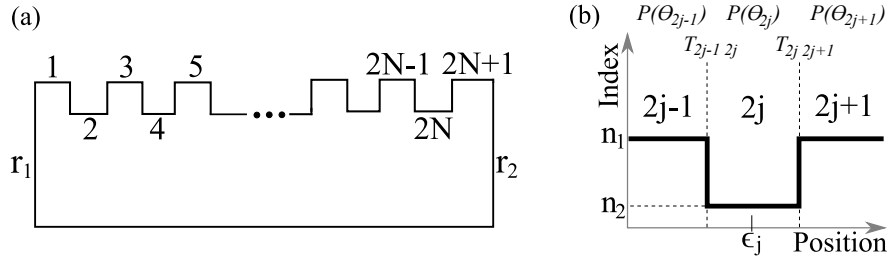


Figure A.1: (a) Illustration of N perturbations introduced to the cavity, creating $2N + 1$ sections. (b) Illustration of a single perturbation, where ϵ_j gives the centre of the perturbation.

where

$$T_{ij} = \frac{1}{t_{ij}} \begin{bmatrix} 1 & -r_{ij} \\ -r_{ji} & r_{ij}r_{ji} + t_{ij}t_{ji} \end{bmatrix} \quad \text{and} \quad P(\theta_k) = \begin{bmatrix} e^{-i\theta_k} & 0 \\ 0 & e^{i\theta_k} \end{bmatrix}. \quad (\text{A.2})$$

The reflection and transmission coefficients r_{ij} and t_{ij} are as previously mentioned in Section 2.4. As $r_{12} = r_{32}$ is true for the perturbations considered here, it can be shown that

$$F_2 = \begin{bmatrix} e^{-i\theta_2} \left(\frac{n_1}{n_2} + \frac{n_2}{n_1} \right) & -\frac{i}{2} \sin(\theta_2) \left(\frac{n_1}{n_2} - \frac{n_2}{n_1} \right) \\ \frac{i}{2} \sin(\theta_2) \left(\frac{n_1}{n_2} - \frac{n_2}{n_1} \right) & e^{i\theta_2} \left(\frac{n_1}{n_2} + \frac{n_2}{n_1} \right) \end{bmatrix} \quad (\text{A.3})$$

Defining $q = \frac{n_1}{n_2}$, this can be written more compactly in terms of the Pauli matrices σ_y and σ_z (as is done in the literature) as

$$F_2 = \begin{bmatrix} e^{-i\theta_2} & 0 \\ 0 & e^{i\theta_2} \end{bmatrix} - q^- \sin(\theta_2) \sigma_y + i(1 - q^+) \sin(\theta_2) \sigma_z, \quad (\text{A.4})$$

where $q^+ = \frac{q+q^{-1}}{2}$ and $q^- = \frac{q-q^{-1}}{2}$. As small perturbations are being considered, we let $n_1 = n$ and $n_2 = n + \Delta n$. Then q^+ and q^- can be approximated using a Taylor expansion to give

$$q^+ = \frac{1}{2} \left(\frac{n}{n + \Delta n} + \frac{n + \Delta n}{n} \right) \approx 1 + \frac{1}{2} \left[\left(\frac{\Delta n}{n} \right)^2 - \dots \right] \quad (\text{A.5})$$

$$q^- = \frac{1}{2} \left(\frac{n}{n + \Delta n} - \frac{n + \Delta n}{n} \right) \approx -\frac{\Delta n}{n} + \frac{1}{2} \left[\left(\frac{\Delta n}{n} \right)^2 - \dots \right] \quad (\text{A.6})$$

Using these approximations in (A.4) gives

$$F_j = P(\theta_j) + \frac{\Delta n}{n} \sin(\theta_j) \sigma_y - \frac{1}{2} \left(\frac{\Delta n}{n} \right)^2 \sin(\theta_j) (\sigma_y + i\sigma_z). \quad (\text{A.7})$$

If there are N total perturbations introduced into a laser cavity, then there are $2N + 1$ sections inside the laser (labelled in Fig. A.1(a)). The matrix F_j relates the input and output fields at each perturbation, as the transmission matrices in section 2.4 did. The total transmission matrix T for the whole cavity with N perturbations is then given by

$$T = P(\theta_1) F_2 P(\theta_3) F_4 \cdots P(\theta_{2N-1}) F_N P(\theta_{2N+1}). \quad (\text{A.8})$$

This expression for T can be expanded using the definitions of $P(\theta_i)$ and F_j , and it can be shown that the general expression for T is given by:

$$T = P \left(\sum_i \theta_i \right) + \left(\frac{\Delta n}{n} \right)^2 \sum_{k>j=1}^N \sin(\theta_{2j}) \sin(\theta_{2k}) P_{0j} [P_{jk}]^{-1} P_{k(N+1)} \quad (\text{A.9})$$

$$+ \left[\frac{\Delta n}{n} - \frac{1}{2} \left(\frac{\Delta n}{n} \right)^2 \right] \sum_{j=1}^N \sin(\theta_{2j}) P_{0j} [P_{j(N+1)}]^{-1} \sigma_y \quad (\text{A.10})$$

$$- \frac{i}{2} \left(\frac{\Delta n}{n} \right)^2 \sum_{j=1}^N \sin(\theta_{2j}) P_{0j} [P_{j(N+1)}]^{-1} \sigma_z, \quad (\text{A.11})$$

where the term

$$P_{jk} = P \left(\sum_{i=2j+1}^{2k-1} \theta_i \right) \quad (\text{A.12})$$

has also been introduced. If there are facets on either side of the laser with reflectivity r_1 and transmission t_1 , then the transfer matrix for the laser is given by:

$$T_{Total} = \frac{1}{t_1} \begin{bmatrix} 1 & -r_1 \\ -r_1 & 1 \end{bmatrix} \begin{bmatrix} T_{11} & T_{12} \\ T_{21} & T_{22} \end{bmatrix} \frac{1}{t_2} \begin{bmatrix} 1 & -r_2 \\ -r_2 & 1 \end{bmatrix} \quad (\text{A.13})$$

Converting T_{Total} to a scattering matrix:

$$S_{Total} = \begin{bmatrix} \frac{T_{21}-T_{11}r_1-T_{22}r_2+T_{21}r_1r_2}{T_{11}-T_{21}r_1-T_{12}r_2+T_{22}r_1r_2} & \frac{\text{Det}[T_{Total}]}{T_{11}-T_{21}r_1-T_{12}r_2+T_{22}r_1r_2} \\ -\frac{t_1t_2}{T_{11}-T_{21}r_1-T_{12}r_2+T_{22}r_1r_2} & \frac{T_{12}-T_{22}r_1-T_{11}r_2+T_{21}r_1r_2}{T_{11}-T_{21}r_1-T_{12}r_2+T_{22}r_1r_2} \end{bmatrix}, \quad (\text{A.14})$$

S_{Total} can now be used to derive the lasing threshold. When

$$T_{11} - T_{21}r_1 - T_{12}r_2 + T_{22}r_1r_2 = 0 \quad (\text{A.15})$$

becomes true, then the expressions in the scattering matrix become large as their denominators go to zero. Hence, (A.15) can be used to find the threshold gain. Using the Pauli matrix definition of T in (A.7), T_{11} , T_{12} , T_{21} and T_{22} can be written as

$$T_{11} = e^{-i \sum_i^{2N+1} \theta_i} \quad (\text{A.16})$$

$$+ \left(\frac{\Delta n}{n} \right)^2 \sum_{k>j=1}^N \sin(\theta_{2j}) \sin(\theta_{2k}) e^{(-\sum_{l=1}^{2j-1} \theta_l + \sum_{l=2j+1}^{2k+1} \theta_l - \sum_{l=2k+1}^{2N+1} \theta_l)} \quad (\text{A.17})$$

$$- \frac{i}{2} \left(\frac{\Delta n}{n} \right)^2 \sum_{j=1}^N \sin(\theta_{2j}) e^{(-\sum_{l=1}^{2j-1} \theta_l + \sum_{l=2j+1}^{2N+1} \theta_l)}, \quad (\text{A.18})$$

$$T_{12} = -i \left[\frac{\Delta n}{n} - \frac{1}{2} \left(\frac{\Delta n}{n} \right)^2 \right] \sum_{j=1}^N \sin(\theta_{2j}) e^{(-\sum_{l=1}^{2j-1} \theta_l + \sum_{l=2j+1}^{2N+1} \theta_l)}, \quad (\text{A.19})$$

$$T_{21} = i \left[\frac{\Delta n}{n} - \frac{1}{2} \left(\frac{\Delta n}{n} \right)^2 \right] \sum_{j=1}^N \sin(\theta_{2j}) e^{(\sum_{l=1}^{2j-1} \theta_l - \sum_{l=2j+1}^{2N+1} \theta_l)}, \quad (\text{A.20})$$

$$T_{22} = e^{-i \sum_{l=1}^{2N+1} \theta_l} \quad (\text{A.21})$$

$$+ \left(\frac{\Delta n}{n} \right)^2 \sum_{k>j=1}^N \sin(\theta_{2j}) \sin(\theta_{2k}) e^{(\sum_{l=1}^{2j-1} \theta_l - \sum_{l=2j+1}^{2k+1} \theta_l + \sum_{l=2k+1}^{2N+1} \theta_l)} \quad (\text{A.22})$$

$$+ \frac{i}{2} \left(\frac{\Delta n}{n} \right)^2 \sum_{j=1}^N \sin(\theta_{2j}) e^{(\sum_{l=1}^{2j-1} \theta_l - \sum_{l=2j+1}^{2N+1} \theta_l)}. \quad (\text{A.23})$$

Plugging in these definitions and diving across by $e^{-i \sum_{l=1}^{2N+1} \theta_l}$ gives:

$$\begin{aligned} 1 = & r_1 r_2 e^{2i \sum_{l=1}^{2N+1} \theta_l} \left(1 + \left(\frac{\Delta n}{n} \right)^2 \sum_{j=1}^N \sin(\theta_{2j}) e^{(\sum_{l=1}^{2j-1} \theta_l - \sum_{l=2j+1}^{2k+1} \theta_l + \sum_{l=2k+1}^{2N+1} \theta_l - \sum_{l=1}^{2N+1} \theta_l)} \right) \\ & - \frac{i}{2} \left(\frac{\Delta n}{n} \right)^2 \sum_{j=1}^N \sin(\theta_{2j}) \left[r_1 e^{(-\sum_{l=1}^{2j-1} \theta_l + \sum_{l=2j+1}^{2N+1} \theta_l + \sum_{l=1}^{2N+1} \theta_l)} \right. \\ & + r_2 e^{i(-\sum_{l=1}^{2j-1} \theta_l + \sum_{l=2j+1}^{2N+1} \theta_l + \sum_{l=1}^{2N+1} \theta_l)} - r_1 r_2 e^{i(\sum_{l=1}^{2j-1} \theta_l - \sum_{l=2j+1}^{2N+1} \theta_l + \sum_{l=1}^{2N+1} \theta_l)} \\ & \left. - e^{i(-\sum_{l=1}^{2j-1} \theta_l + \sum_{l=2j+1}^{2N+1} \theta_l + \sum_{l=1}^{2N+1} \theta_l)} \right] \\ & + i \frac{\Delta n}{n} \sum_{j=1}^N \sin(\theta_{2j}) \left[r_1 e^{i(\sum_{l=1}^{2j-1} \theta_l - \sum_{l=2j+1}^{2N+1} \theta_l + \sum_{l=1}^{2N+1} \theta_l)} \right. \\ & \left. + r_2 e^{i(-\sum_{l=1}^{2j-1} \theta_l + \sum_{l=2j+1}^{2N+1} \theta_l + \sum_{l=1}^{2N+1} \theta_l)} \right] \\ & - \left(\frac{\Delta n}{n} \right)^2 \sum_{k>j=1}^N \sin(\theta_{2j}) \sin(\theta_{2k}) e^{i(-\sum_{l=1}^{2j-1} \theta_l + \sum_{l=2j+1}^{2k+1} \theta_l - \sum_{l=2k+1}^{2N+1} \theta_l + \sum_{l=1}^{2N+1} \theta_l)}. \quad (\text{A.24}) \end{aligned}$$

First, the terms in the exponents can be simplified. The complex exponent in the first term of equation (A.24) can be simplified by introducing new definitions. Let

$$\sum_{l=1}^{2j-1} \theta_l - \sum_{l=2j+1}^{2k+1} \theta_l + \sum_{l=2k+1}^{2N+1} \theta_l - \sum_{l=1}^{2N+1} \theta_l = 2\phi_j^- + 2\phi_k^+ - 2 \sum_{l=1}^{2N+1} \theta_l = e^{-2i\phi_{jk}}. \quad (\text{A.25})$$

Here, ϕ_j^- is the total complex phase contribution to the field due to it traversing from the left facet to the perturbation at position $2j$. Similarly ϕ_k^+ is the phase due to traversing the distance to the right facet. The formal definitions are:

$$\phi_j^- = \frac{\theta_{2j}}{2} + \sum_{l=1}^{2j-1} \theta_l, \quad (\text{A.26})$$

$$\phi_k^+ = \frac{\theta_{2k}}{2} + \sum_{l=2k+1}^{2N+1} \theta_l. \quad (\text{A.27})$$

The phase between two sections j and k is then given by

$$\phi_{jk} = \sum_{l=1}^{2N+1} \theta_l - \phi_j^- - \phi_k^+. \quad (\text{A.28})$$

Using ϕ_j^- , ϕ_k^+ and ϕ_{jk} in equation (A.24) leaves:

$$\begin{aligned} 1 = & r_1 r_2 e^{2i \sum_{l=1}^{2N+1} \theta_l} \left(1 + \left(\frac{\Delta n}{n} \right)^2 \sum_{j=1}^N \sin(\theta_{2j}) e^{-2i\phi_{jk}} \right) \\ & - \frac{i}{2} \left(\frac{\Delta n}{n} \right)^2 \sum_{j=1}^N \sin(\theta_{2j}) \left[r_1 e^{2i\phi_j^-} + r_2 e^{2i\phi_j^+} - r_1 r_2 e^{2i\phi_j^-} - e^{2i\phi_j^+} \right] \\ & + i \frac{\Delta n}{n} \sum_{j=1}^N \sin(\theta_{2j}) \left[r_1 e^{2i\phi_j^-} + r_2 e^{2i\phi_j^+} \right] - \left(\frac{\Delta n}{n} \right)^2 \sum_{k>j=1}^N \sin(\theta_{2j}) \sin(\theta_{2k}) e^{2i\phi_{jk}}. \end{aligned} \quad (\text{A.29})$$

As in [85], we will only consider the terms up to first order in Δn , and also include the second order terms in Δn that arise from the coupling between pairs of features (j, k) . Hence, retaining these terms the lasing condition becomes

$$\begin{aligned} 1 = & r_1 r_2 e^{2i \sum_{l=1}^{2N+1} \theta_l} \left(1 + \left(\frac{\Delta n}{n} \right)^2 \sum_{j=1}^N \sin(\theta_{2j}) e^{-2i\phi_{jk}} \right) \\ & + i \frac{\Delta n}{n} \sum_{j=1}^N \sin(\theta_{2j}) \left[r_1 e^{2i\phi_j^-} + r_2 e^{2i\phi_j^+} \right] - \left(\frac{\Delta n}{n} \right)^2 \sum_{k>j=1}^N \sin(\theta_{2j}) \sin(\theta_{2k}) e^{2i\phi_{jk}}. \end{aligned} \quad (\text{A.30})$$

In order to derive the first order and second order contributions to the threshold gain of the laser due to Δn , it is useful first to derive the threshold gain assuming no perturbations exist (or alternatively, when $\Delta n = 0$). In this case, the lasing condition simplifies to

$$1 = r_1 r_2 e^{2i \sum \theta} = r_1 r_2 e^{2i \sum \theta'} e^{-2 \sum \theta''}, \quad (\text{A.31})$$

where θ' and θ'' are the real and imaginary parts of the phase respectively. Looking at the magnitude of (A.31) gives

$$\begin{aligned} \left| \frac{1}{r_1 r_2} \right| &= \left| e^{-2 \sum \theta''} \right|, \\ -2 \sum \theta'' &= \ln \frac{1}{|r_1 r_2|}. \end{aligned} \quad (\text{A.32})$$

From textbook definitions of gain (see Coldren and Corzine [159] for example), we know that the zeroth order gain $\gamma^{(0)}$ must be

$$\gamma^{(0)} = \frac{1}{L_c} \ln \frac{1}{|r_1 r_2|}, \quad (\text{A.33})$$

where L_c is the length of the cavity. Hence, comparing this with (A.32) implies that $\sum \theta'' =$

$-\frac{1}{2}\gamma L_c$. In general, considering more than just the zeroth order, we have

$$\sum \theta'' = -\frac{1}{2} \left(\gamma_m^{(0)} + \frac{\Delta n}{n} \gamma_m^{(1)} + \left(\frac{\Delta n}{n} \right)^2 \gamma_m^{(2)} + \dots \right) L_c, \quad (\text{A.34})$$

where the subscript m has been added to allow the gain to be different for each mode supported by the laser cavity.

The goal now is to derive the expression for the threshold gain in higher orders of Δn . To date, only first order corrections to the threshold gain have been considered. Eliminating second order terms in (A.30), and expanding ϕ_j^- and ϕ_k^+ into real and imaginary parts (as was done with θ), we have that the lasing condition up to first order is given by:

$$1 = r_1 r_2 e^{2i \sum (\theta' + i\theta'')} + i \frac{\Delta n}{n} \sum_{j=1}^N \sin(\theta_{2j}) \left[r_1 e^{2i(\phi_j^{-'} + i\phi_j^{-''})} + r_2 e^{2i(\phi_j^{+'} + i\phi_j^{+''})} \right]. \quad (\text{A.35})$$

To match the notation in [85], we will now define the position of each perturbation as a fraction of the position along the cavity. Let $-\frac{1}{2} < \epsilon_j < \frac{1}{2}$ be the position of the center of the j -th perturbation. Then it follows that

$$\phi_j^{-''} = \left(\epsilon_j + \frac{1}{2} \right) \sum \theta'', \quad (\text{A.36})$$

$$\phi_j^{+''} = \left(\frac{1}{2} - \epsilon_j \right) \sum \theta''. \quad (\text{A.37})$$

Using ϕ_j^- and ϕ_j^+ in terms of ϵ_j and also equation (A.34) in (A.35) gives:

$$\begin{aligned} 1 = & r_1 r_2 e^{2i \sum (\theta')} e^{\gamma_m^{(0)} L_c} e^{\left(\frac{\Delta n}{n} \gamma_m^{(1)} + \left(\frac{\Delta n}{n} \right)^2 \gamma_m^{(2)} + \dots \right) L_c} \\ & + i \frac{\Delta n}{n} \sum_{j=1}^N \sin(\theta_{2j}) \left[r_1 e^{2i\phi_j^{-'}} e^{\epsilon_j \gamma_m^{(0)} L_c} e^{\epsilon_j \left(\frac{\Delta n}{n} \gamma_m^{(1)} + \left(\frac{\Delta n}{n} \right)^2 \gamma_m^{(2)} + \dots \right) L_c} e^{\frac{\gamma_m^{(0)} L_c}{2}} \right. \\ & \left. + r_2 e^{2i\phi_j^{+'}} e^{-\epsilon_j \gamma_m^{(0)} L_c} e^{\epsilon_j \left(\frac{\Delta n}{n} \gamma_m^{(1)} + \left(\frac{\Delta n}{n} \right)^2 \gamma_m^{(2)} + \dots \right) L_c} e^{\frac{\gamma_m^{(0)} L_c}{2}} \right]. \end{aligned} \quad (\text{A.38})$$

Taylor expanding the exponential with $\gamma_m^{(1)}$, we find that

$$e^{\epsilon_j \left(\frac{\Delta n}{n} \gamma_m^{(1)} + \left(\frac{\Delta n}{n} \right)^2 \gamma_m^{(2)} + \dots \right) L_c} \approx 1 + \epsilon_j \frac{\Delta n}{n} \gamma_m^{(1)} L_c + \left(\frac{\Delta n}{n} \right)^2 \gamma_m^{(2)} L_c + \dots \quad (\text{A.39})$$

Also we have that $e^{\frac{\gamma_m^{(0)} L_c}{2}} = \frac{1}{\sqrt{|r_1 r_2|}}$, and hence

$$\begin{aligned} 1 = & r_1 r_2 e^{2i \sum (\theta')} e^{\gamma_m^{(0)} L_c} \left(1 + \epsilon_j \frac{\Delta n}{n} \gamma_m^{(1)} L_c + \left(\frac{\Delta n}{n} \right)^2 \gamma_m^{(2)} L_c + \dots \right) \\ & + i \frac{\Delta n}{n} \frac{1}{\sqrt{|r_1 r_2|}} \sum_{j=1}^N \sin(\theta_{2j}) \left(1 + \epsilon_j \frac{\Delta n}{n} \gamma_m^{(1)} L_c + \left(\frac{\Delta n}{n} \right)^2 \gamma_m^{(2)} L_c + \dots \right) \\ & \times \left[r_1 e^{2i\phi_j^{-'}} e^{\epsilon_j \gamma_m^{(0)} L_c} + r_2 e^{2i\phi_j^{+'}} e^{-\epsilon_j \gamma_m^{(0)} L_c} \right]. \end{aligned} \quad (\text{A.40})$$

Only keeping the terms with $\frac{\Delta n}{n}$, we have:

$$e^{2i\sum\theta'}\gamma_m^{(1)} = -i\frac{1}{\sqrt{|r_1r_2|}}\sum_{j=1}^N\sin(\theta_{2j})\left[r_1e^{2i\phi_j^{-'}}e^{\epsilon_j\gamma_m^{(0)}L_c} + r_2e^{2i\phi_j^{+'}}e^{-\epsilon_j\gamma_m^{(0)}L_c}\right]. \quad (\text{A.41})$$

At each mode m , assuming that the perturbations Δn have negligible effect on the cavity mode wavelengths, we have that $\sum\theta' = 2m\pi$ (as otherwise the light in mode m would not constructively interfere within the cavity). Hence, the LHS of (A.41) must be real. This implies the RHS of (A.41) is also real, which gives:

$$\gamma_m^{(1)} = \frac{1}{\sqrt{|r_1r_2|}}\sum_{j=1}^N\sin(\theta_{2j})\left[r_1\sin\left(2\phi_j^{-'}\right)e^{\epsilon_j\gamma_m^{(0)}L_c} + r_2\sin\left(2\phi_j^{+'}\right)e^{-\epsilon_j\gamma_m^{(0)}L_c}\right]. \quad (\text{A.42})$$

Hence, up to first order perturbations in Δn , we can describe the gain of each mode in the cavity by including the above expression. The following sections now describe how we can use equation (A.42) to our advantage, and manipulate the threshold gain of a particular mode using an inverse Fourier transform technique.

A.2 Solving the Inverse Problem

The goal of the previous section was to find how the introduction of N perturbations of magnitude Δn effected the threshold of the modes in a laser cavity. This section will outline how (A.42) can be used to determine the positions required to make a single moded device. Specifically, the positions of ϵ_j must be determined using (A.42) to modify the threshold gain of the modes in the cavity, to favour one mode over all others.

We'll start by writing each mode m in terms of the target mode m_0 . If $m = m_0 + \Delta m$, and we assume that there are no phase changes due to the facets, then $\phi_j^{\pm'}$ can be expanded to give:

$$\phi_j^{\pm'} = \sum_i\theta'_i - \phi_j^{-'} = \left(1 - \left(\epsilon_j + \frac{1}{2}\right)\right)\sum_i\theta'_i = \left(\frac{1}{2} - \epsilon_j\right)m\pi \quad (\text{A.43})$$

as each mode's total optical path length must resonate within the cavity in order for the mode to constructively interfere. Hence $\sin\left(2\phi_j^{\pm'}\right)$ becomes:

$$\sin\left(2\phi_j^{\pm'}\right) = \mp\cos(m\pi)\sin(2\epsilon_jm\pi). \quad (\text{A.44})$$

As a result it follows that $\sin\left(2\phi_j^{-'}\right) = -\sin\left(2\phi_j^{+'}\right)$. We can now re-write (A.42) as

$$\gamma_m^{(1)} = \frac{1}{\sqrt{|r_1r_2|}}\sum_{j=1}^N\sin(\theta_{2j})\left[r_1e^{\epsilon_j\gamma_m^{(0)}L_c} - r_2e^{-\epsilon_j\gamma_m^{(0)}L_c}\right]\cos(m\pi)\sin(2\epsilon_jm\pi). \quad (\text{A.45})$$

As we're trying to optimise the positions ϵ_j of the perturbations to create a single moded laser, only the terms containing ϵ_j in (A.45) can be altered. The $\sin(2\epsilon_jm\pi)$ term can be used to maximise the modulation of the threshold gain envelope, as will be seen later. All that remains

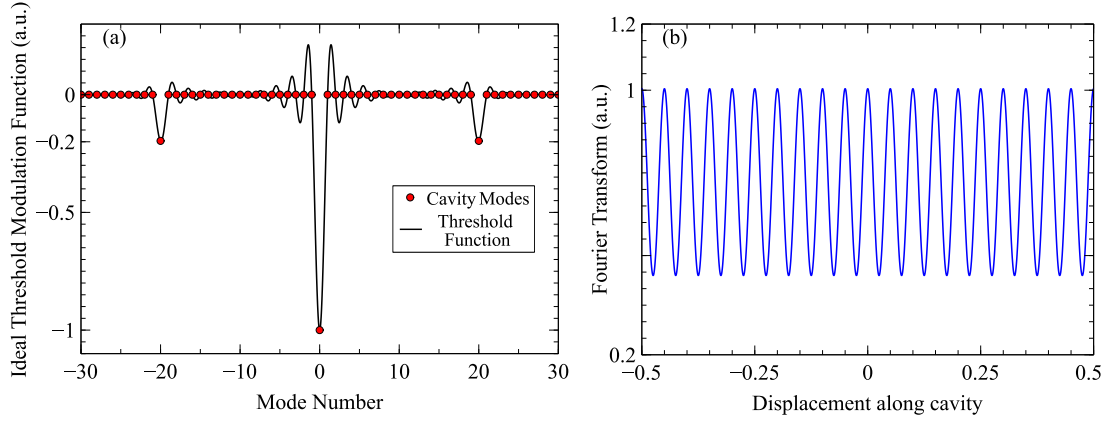


Figure A.2: (a) Ideal threshold modulation function, as given by Eq. (A.47) for $a = 20$ and $\tau = 0.036$. The red points give the value at each of the cavity modes. (b) Fourier transform of the ideal threshold modulation function shown in (a).

to be optimised are the terms with $e^{\pm \epsilon_j \gamma_m^{(0)} L_c}$. Let the function $f(\epsilon_j)$ be defined as:

$$f(\epsilon_j) = r_1 e^{\epsilon_j \gamma_m^{(0)} L_c} - r_2 e^{-\epsilon_j \gamma_m^{(0)} L_c}. \quad (\text{A.46})$$

The positions of ϵ_j should be chosen such that $f(\epsilon_j)$ maximises the change in the threshold gain at $\Delta m = 0$, and has zero change in threshold for all other modes $m \neq m_0$. So, in wavenumber space, an ideal threshold modulation envelope would be

$$-\text{sinc}(\Delta m) = -\frac{\sin(\Delta m \pi)}{\Delta m \pi} \approx -e^{-\pi \tau^2 \Delta m^2} \sum_{n=-\infty}^{\infty} \text{sinc}(\Delta m - na). \quad (\text{A.47})$$

The $-\text{sinc}(\Delta m \pi)$ function has value -1 at the target mode m_0 , and is 0 for every other mode $m \neq m_0$, as shown in Fig. A.2(a). The variables τ and a have been introduced to include the finite gain bandwidth of semiconductor lasers, and the spacing a of cavity modes. The Fourier transform of this threshold gain function can be approximated discretely as an infinite sum of Gaussians of the form:

$$\Gamma_n(\epsilon) = e^{-\frac{\pi \left(\epsilon - \frac{n}{a}\right)^2}{\tau^2}}, \quad (\text{A.48})$$

which is plotted in Fig. A.2(b).

The first approximation for the positions of the perturbations is then determined by computing the integral of $f(\epsilon_j)^{-1}$ and the transform of our target threshold modulation function $\text{sinc}(\Delta m \pi)$ over the interval where we wish to place the perturbations. Each perturbation j is placed by solving

$$A \sum_n \int_{\epsilon_{min}}^{\epsilon_j} [f(x)]^{-1} \Gamma_n(x) dx = j - \frac{1}{2} \quad (\text{A.49})$$

for ϵ_j . Here, ϵ_{min} is a lower bound for the possible positions that the perturbations can take, and A is a normalisation constant, described in the next section.

Once the first approximation for the positions ϵ_j have been determined, the perturbations

must then be repositioned to maximise the $\sin(2\phi_j^{\pm'})$ terms in (A.42), and then repositioned again to take the other perturbations in the cavity into account. The method used for solving for these positions is presented in the following section.

A.3 Method for Computing Perturbation Positions

The positions ϵ_j need to be determined using (A.49). First, the normalisation constant A needs to be determined. To do this, we will consider the left hand side (i.e, $\epsilon_j < 0$) and the right hand side (i.e, $\epsilon_j > 0$) separately, as there may be a different numbers of perturbations on each side. A is proportional to the number of perturbations introduced, and is given by:

$$A = \frac{N + \frac{1}{2}}{\int_{\epsilon_{min}}^{\epsilon_{max}} \sum_n f(x) \Gamma_n(x) dx} \quad (\text{A.50})$$

where ϵ_{max} and ϵ_{min} are the upper and lower bound values that ϵ_j can take. In general, $\epsilon_{max} = \pm 0.5$ depending on which side is being calculated, however ϵ_{min} can be chosen to suit the size of the perturbations in use.

Using the value of A , ϵ_j can now be calculated using (A.49). This first estimate of ϵ_j can be improved by optimising each ϵ_j such that $\sin(2\epsilon_j m \pi) = \pm 1$, depending on the sign of ϵ_j . This is due to the $\cos(m\pi) \sin(2\epsilon_j m \pi)$ term that is in (A.45). Although this shift in position is small in magnitude, it has a large effect on the threshold gain.

The final adjustment necessary is to adjust the position of each ϵ_j to take into account the other perturbations in the cavity. Equation (A.49) does not take into account that there may already be other perturbations in the cavity, and hence every ϵ_j must be shifted relative to one of the facets. Hence, to take the phase of the perturbations to the left of position ϵ_j into account, each ϵ_j must be shifted by:

$$\Delta\epsilon_j = \frac{\beta \Delta n (1 + N_j^- - 2N_j^- \epsilon_j)}{2(n + N_j^- \beta \Delta n)}, \quad (\text{A.51})$$

where β is the ratio of the perturbation width relative to the cavity length, and N_j^- is the number of perturbations to the left of position j . Figure A.3 shows the grating positions calculated for 60 perturbations with $\tau = 0.036$, $a = 20$, and perturbation width $w = 0.121 \mu\text{m}$. The density of perturbations is larger near the center of the device. There are no perturbations between -0.0125 and 0.0125 , as this was the value of ϵ_{min} .

Figure A.4 shows the threshold gain obtained from the grating in Fig. A.3, assuming that the total length of the device was $400 \mu\text{m}$. The target mode was at 1550 nm , which corresponds to $m_0 = 1652$. The threshold gain for the target mode was reduced by approximately 0.8 cm^{-1} , which should be sufficient for single mode operation. The dotted line in black in Fig. A.4 shows the threshold gain $\gamma_m^{(0)}$, which would be the threshold gain prior to the introduction of any of the perturbations.

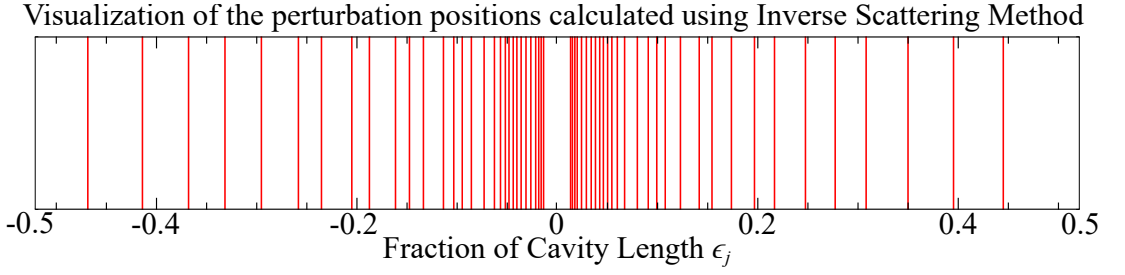


Figure A.3: Plot of the perturbation positions required to make a single moded device with lasing wavelength at $1.55 \mu\text{m}$. The positions were calculated assuming $N = 60$, $n = 3.2$, $\Delta n = 0.005$, and with a perturbation width of $w = 0.121 \mu\text{m}$.

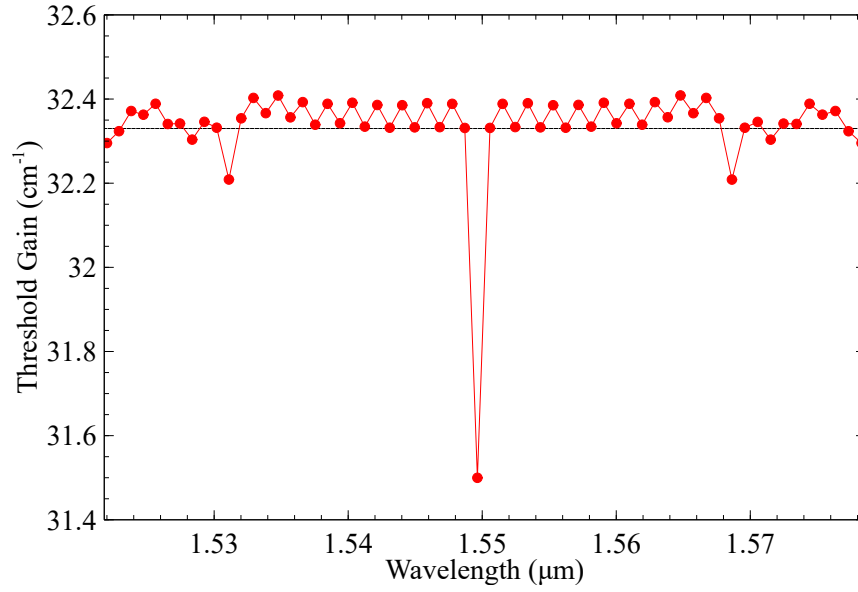


Figure A.4: Plot of the threshold gain from the grating in Fig. A.3. The black dashed line indicates the threshold gain value $\gamma_m^{(0)}$ without the introduction of any of the perturbations.

A.4 Designing Etched Facet Devices

To be useful as an integrated laser on a photonic integrated circuit however, any device designed by the inverse scattering method would need to operate without a cleaved facet. Integrated mirrors such as etched facets or MMI loops have different reflection values, which need to be taken into account in the inverse scattering method. The center of the perturbations needs to shift when the reflections on either side of the cavity centre are unequal. The new center of the perturbations is given by:

$$\text{Perturbation Center} = \frac{-\log[r_1/r_2]}{2 \log[1/r_1 r_2]} \quad (\text{A.52})$$

Unfortunately, in reality each perturbation introduced into the cavity also introduces further optical loss. Real devices cannot feature 60 perturbations (unless those perturbations have extremely low loss), and hence the example results shown in Figs. A.3 and A.4 are not feasible. To investigate how many pit perturbations were required to achieve single mode, devices with varying numbers of pit perturbations were designed.

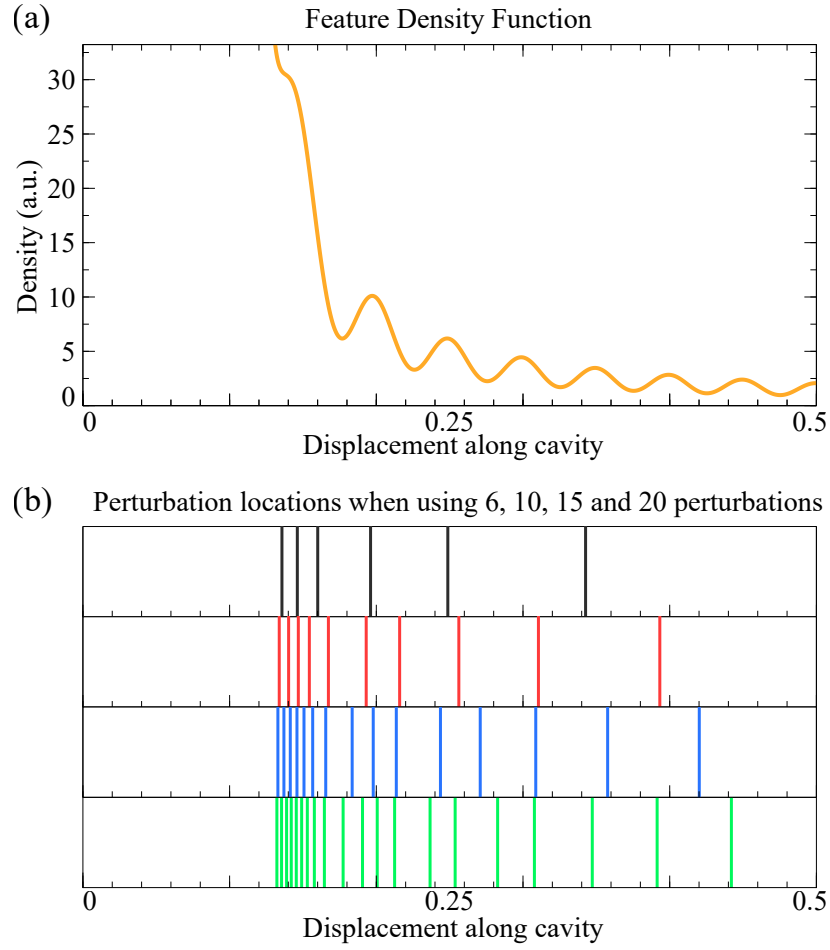


Figure A.5: (a) Feature density function for the etched facet side of the device only, for a 1 mm long laser cavity, with $a = 20$, $\tau = 0.036$, $\Delta n = 0.0075$, and $w = 1 \mu\text{m}$. The x-axis is scaled so that 0.0 is the physical centre of the cavity, and +0.5 is right facet. The grating centre was at a displacement of 0.118267 along the cavity, due to the mismatched reflections of the cleaved and etched facets. (b) Illustration of the perturbation positions found using the inverse scattering method when 6, 10, 15 and 20 perturbations are used.

As knowing the exact optical path length between perturbations and the facets is pivotal in the above, metal covered deep etched facets (defined by the same lithography step which created the perturbations) were used on one side of the device to accurately control the relative distance of each perturbation to this etched facet. The other facet was an un-coated cleaved facet, which had a positional tolerance of $\pm 10 \mu\text{m}$. The metal covered deep etched facet's reflection was estimated to be 45%, compared with the uncoated facet's reflection of 27.5%. Due to this mismatch in the reflective strengths of the facets, the centre of the feature density function shifts. Figure A.5(a) shows the feature density function (which is the product of $\Gamma_n(\epsilon)$ and $f(\epsilon)^{-1}$) for the actual parameters used when fabricating the pit devices. The feature density function gives a sense of where the features should be position along the cavity.

As only the etched facet's location could be accurately controlled, single sided gratings were designed. Figure A.5(b) shows the perturbation locations for 6, 10, 15 and 20 pit devices, for $\epsilon_{min} = 0.0125$, with $\Delta n = 0.0075$. As the number of perturbations is increased, notably more are located close to the zero of the $f(x)$ function. The wavelength control and selectivity should also increase with more perturbations. There are two main limits however to the number of

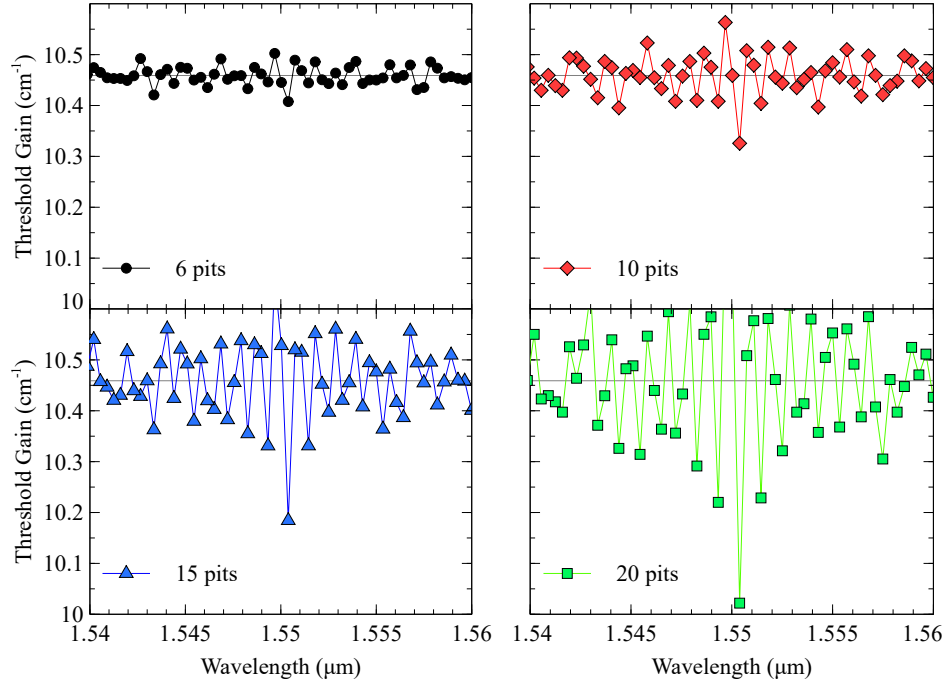


Figure A.6: Calculated threshold gain versus wavelength for the gratings shown in Fig. A.5(b). The solid horizontal line in each plot is the calculated unperturbed threshold gain of the laser cavity, i.e., $\gamma_m^{(0)} = 10.46 \text{ cm}^{-1}$.

perturbations which can be introduced: the loss per pit, and the physical size of the pits.

The corresponding threshold gains calculated for the gratings in Fig. A.5(b) are plotted in Fig. A.6. As the number of perturbations is increased in the model, the threshold of the target mode significantly decreases – however, the loss per pit is not included in these calculations. As a result, indefinitely increasing the number of pits does not increase the SMSR or output lasing power of the targeted mode.

A.5 Device Results

The devices were fabricated on standard commercial material with 5 $\text{Al}_{0.24}\text{GaIn}_{0.71}\text{As}$ QWs grown on InP. The details of thicknesses and the structure of the epitaxial layers of the material can be found Appendix D. The fabrication process used only two etch depths in order to reduce the time and cost involved.

Each patterning step of the fabrication of the devices used contact photo lithography to define the areas for deposition/etching of the devices. In brief, the fabrication process of the devices was as follows; first, plasma-enhanced chemical vapor deposition (PECVD) of silicon oxide was deposited over all the devices. Photo resist (PR) was evenly spun onto the wafer, developed to define the ridge waveguides, and then the developed PR was removed. The exposed silicon oxide was removed, leaving silicon oxide lines only where the ridge waveguides should be. PECVD of silicon nitride was then performed, to protect areas of the wafer from the following etch step. PR was again used to define the deep etch regions, and after

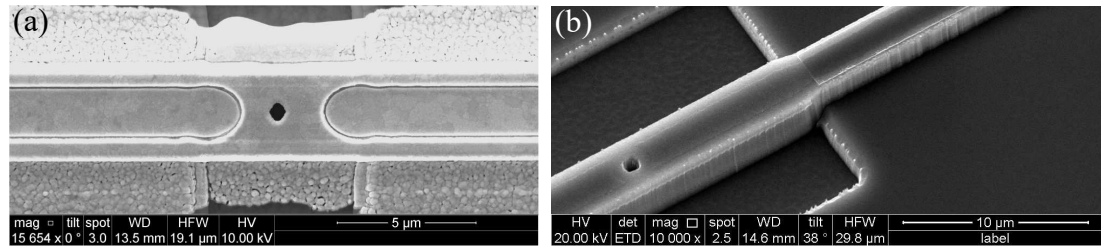


Figure A.7: (a) Scanning electron microscope image of one of the pits used as perturbations in the waveguide. (b) View of the sidewall of a test device after the second etch step in the process, showing the two different etch depths used in fabrication, with a pit perturbation visible in the bottom left of the image.

the developed PR was removed, the areas which required a deep etch (including the metal covered etched facets and the pits) were etched to a depth of $1\ \mu\text{m}$ by using an inductively coupled plasma (ICP) etcher. The silicon nitride was then removed, the ridge waveguide was defined and protected as in the previous steps, and a further $1.8\ \mu\text{m}$ of material was etched. This process leaves the ridge waveguide's height at $1.8\ \mu\text{m}$, while leaving the areas of the pits and the metal covered etched facets a depth of $2.8\ \mu\text{m}$ below the top of the ridge.

The fabrication process was then completed by depositing oxide over the whole device, leaving oxide openings only along the ridge, and evaporating a $400\ \text{nm}$ thick mix of titanium and gold onto the devices for the electrical contact. The substrate was also thinned, and titanium and gold was also evaporated onto back of the thinned substrate for better contact. Scanning electron microscope (SEM) images of a pit can be seen in Fig. A.7(a), and a side view of the two etch depths can be seen in Fig. A.7(b). Further SEM images of the devices, including images of the metal covered etched facets, are included in Appendix B.

The devices were tested by mounting each un-packaged chip on a temperature controlled brass chuck. Light from the un-coated cleaved facet of the devices was collected using a lensed fibre. A comparison between the optical spectrum of a Fabry-Pérot laser and a device with 15 pits is shown in Fig. A.9(a). The total length of both devices was $1\ \text{mm}$, and both were pumped with $140\ \text{mA}$. The spectral effect of placing the pits as described by the inverse scattering method can be clearly seen, as strong single mode lasing is apparent upon the introduction of the pits.

To determine the optimal number of pits required for single mode lasing, the number of pits in a $1\ \text{mm}$ cavity was varied. Figures A.9(b) and (c) show example IV and LI curves from devices with 6, 10, 15 and 20 pits. Each pit perturbations adds scattering losses to the laser cavity, and as a result the device thresholds increase from $37\ \text{mA}$ at 6 pits to $53\ \text{mA}$ at 20 pits. However, increasing the number of perturbations in the cavity also increases the wavelength selectivity and single mode behaviour of the device.

The optical spectra from the same devices are shown in Fig. A.10. All devices lased close to the target wavelength of $1550\ \text{nm}$, however the SMSR varies slightly between devices. A summary of the SMSRs and the lasing wavelengths obtained as the number of pits was varied is plotted in Fig. A.11(a). The lasing wavelength of the 6 and 8 pit devices aren't adequately close to the target wavelength, as neither had a sufficient number of perturbations to control the spectral characteristics of the device. However in the case of the 10, 12 and 15 pit devices, the lasing wavelengths of the devices at 20°C were within $0.35\ \text{nm}$ of the target wavelength. As the

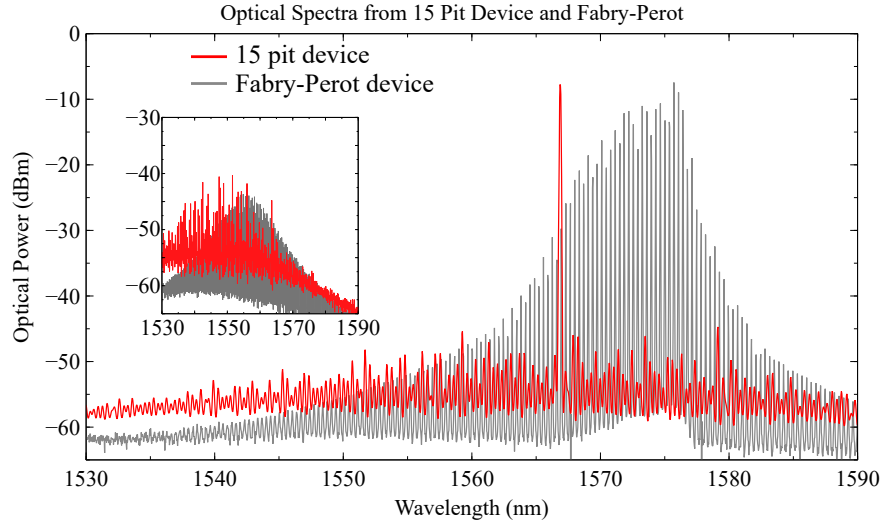


Figure A.8: Comparison between the spectra of a FP cavity and a 15 pit device at 140 mA, at 20°C. Both devices were 1 mm long, with one cleaved facet and one metal covered etched facet. Inset: Optical spectrum from the same two devices just below threshold. (30 mA for the FP device, and 47 mA for the 15 pit device).

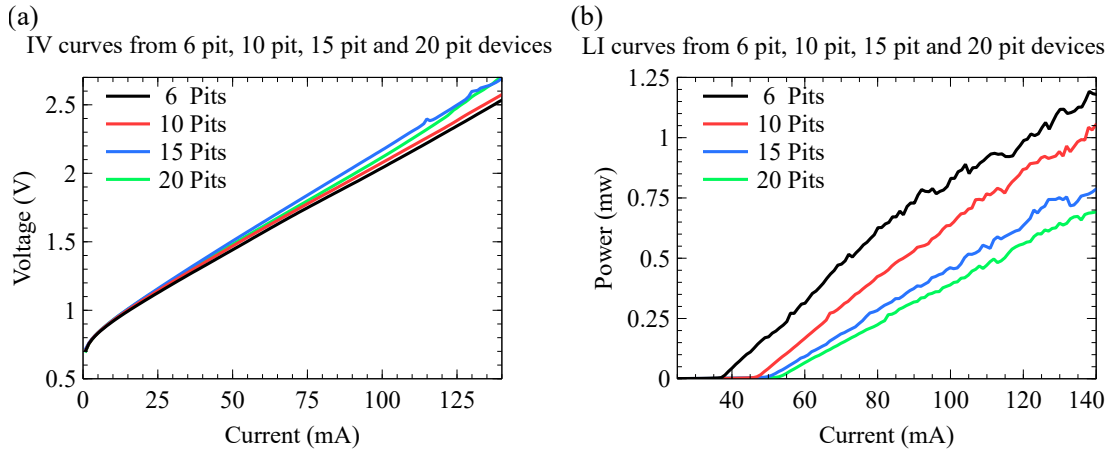


Figure A.9: (a) A plot of voltage versus current for 1 mm long devices with 6, 10, 15 and 20 pits. **(b)** LI curves for the devices plotted in (b). The thresholds of the devices were 37 mA, 46 mA, 49 mA, and 53 mA respectively. The kinks in the curves are due to vibrations in the optical fibre used to collect the light.

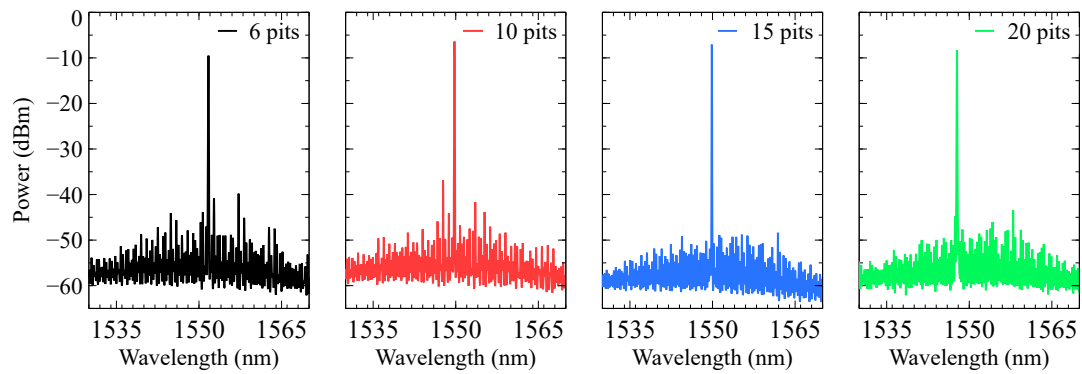


Figure A.10: Optical spectra from the fabricated devices, for the gratings shown in Fig. A.5(b), at injected currents of 1.5 times threshold at 20°C.

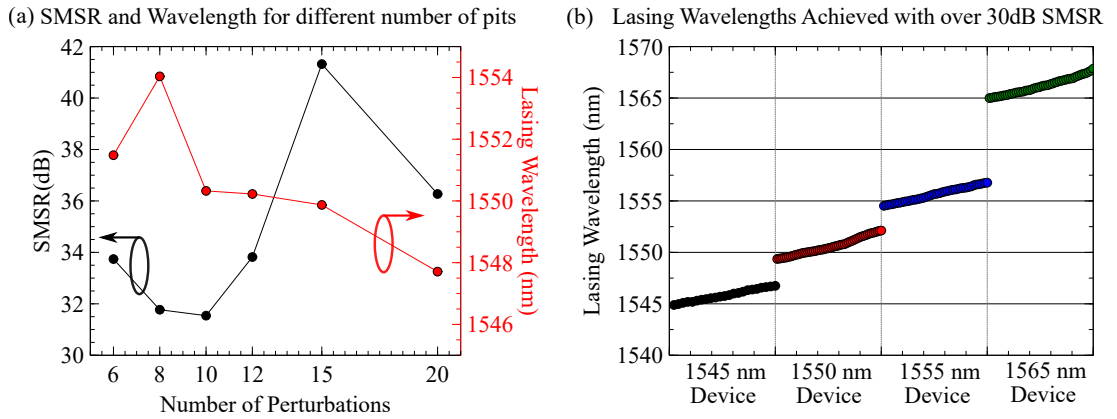


Figure A.11: (a) Comparison between the lasing SMSR and the lasing wavelength of devices as the number of pits was altered, at 20°C. (b) Lasing wavelengths with over 30 dB SMSR from a set of devices designed to lase at 1545 nm, 1550 nm, 1555 nm, and 1565 nm.

number of pits were increased further to 20, the wavelength accuracy of the design process was lost again. This can be explained as the increase in the number of pits can perturb the Fabry-Pérot modes of the 1 mm cavity away from their natural wavelengths, and the calculations assume that $N\Delta n/n \ll 1$. The model could be improved by taking into account the shift in the Fabry-Pérot mode positions, as well as taking into account second order perturbations [85].

Although the locations of the perturbations were fixed relative to the etched facet, the location of the cleaved facet on the uncoated hand side of the devices had a tolerance of approximately $\pm 10 \mu\text{m}$. This error in the location of the cleaved facet affects more severely devices with fewer perturbations, as the threshold gain modulation isn't as strong in these cases.

Devices with 15 pits were fabricated to target wavelengths around the material peak gain, to demonstrate the wavelength accuracy of the technique. Devices with target wavelengths of 1545 nm, 1550 nm, 1555 nm, and 1565 nm were designed and fabricated, and the lasing wavelengths achieved are shown in Fig. A.11(b). The laser's wavelengths were tuned using both current (from 70 mA to 180 mA) and temperature (from 15°C to 28°C), and continuous tuning of 2 nm was achieved in all cases. These shifts observed in lasing wavelengths are due to the change in optical path lengths of the laser cavities, including the thermal expansion of the cavities and the slight variation in the refractive index of the material with temperature.

A.6 Conclusions

In the above Appendix, the inverse scattering method for designing single moded lasers was described. The method uses the introduction of N perturbations to produce a single moded laser, and a step by step discussion of how compute the positions of the perturbations was presented above. These devices were used throughout this thesis, primarily as during the device's development, an abundance of suitably strongly single mode devices were fabricated. In future, this method could potentially be used to design devices which don't require cleaved facets, in order to make the devices fully integrable.

Appendix B

Scanning Electron Microscope Images of Device Sections

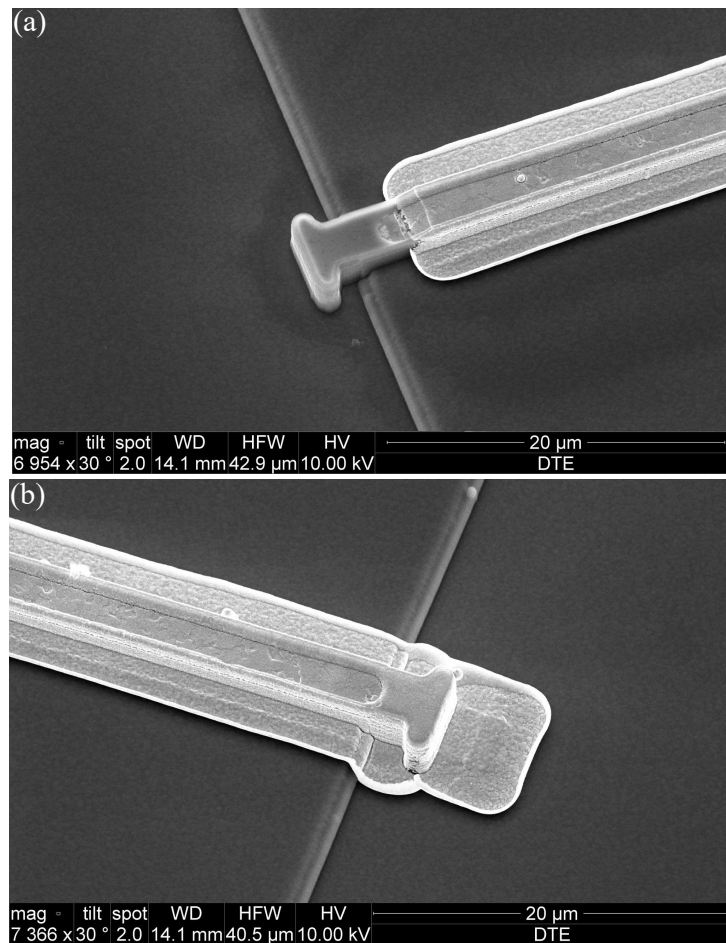


Figure B.1: Scanning electron microscope images of (a) an etched facet and (b) a metal covered etched facet used in device designs. The metal covered etched facet gives stronger reflection than the non-coated version. The stub shape at the end of the waveguide ensures the facet face is flat.

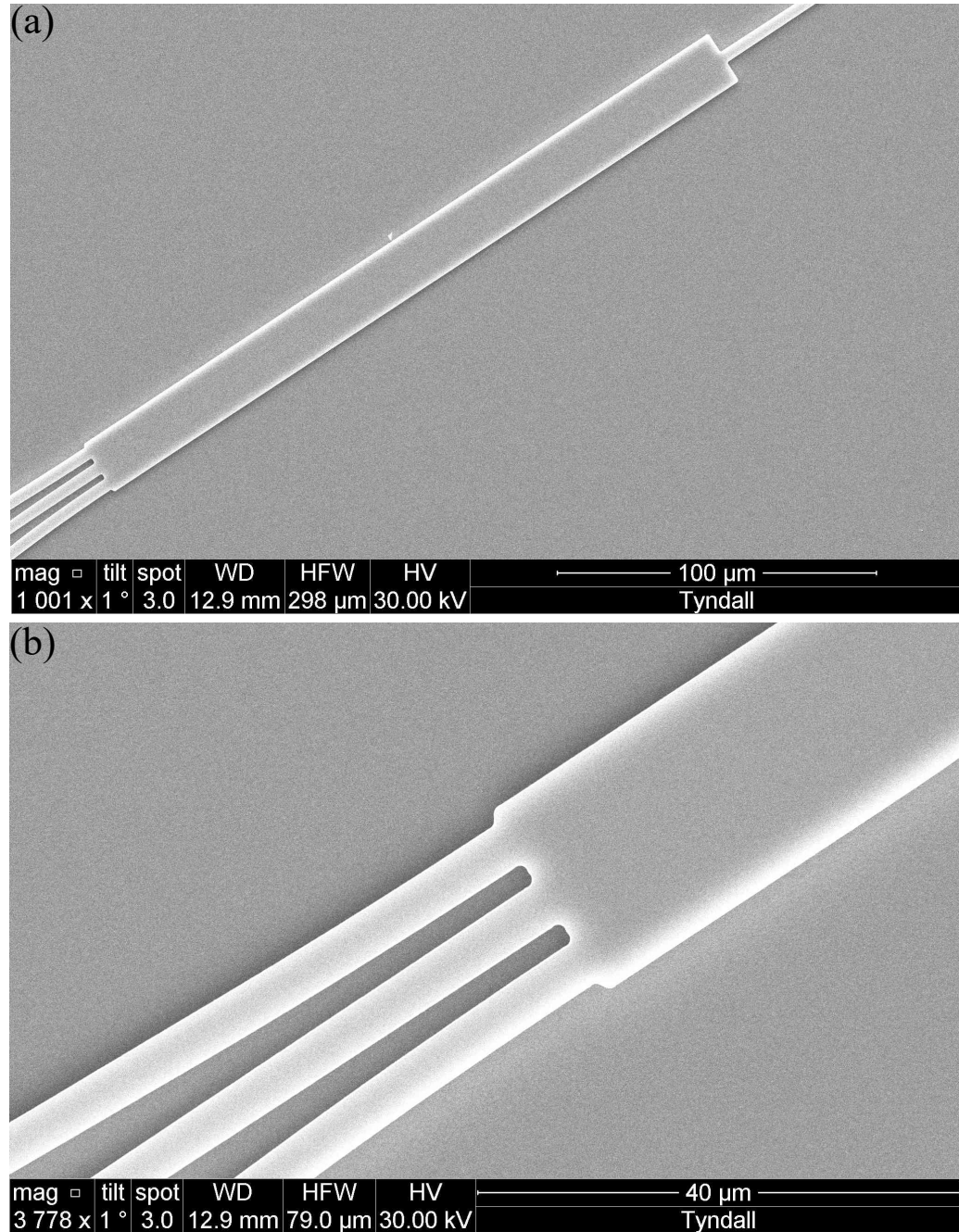


Figure B.2: (a) Scanning electron microscope image of a 1×3 multimode interferometer (MMI). (b) A close up of the output waveguides from the MMI in (a). The corners of the MMI would ideally be square, however due to the finite resolution of the lithography process, the corners are slightly rounded.

B. SCANNING ELECTRON MICROSCOPE IMAGES OF
DEVICE SECTIONS

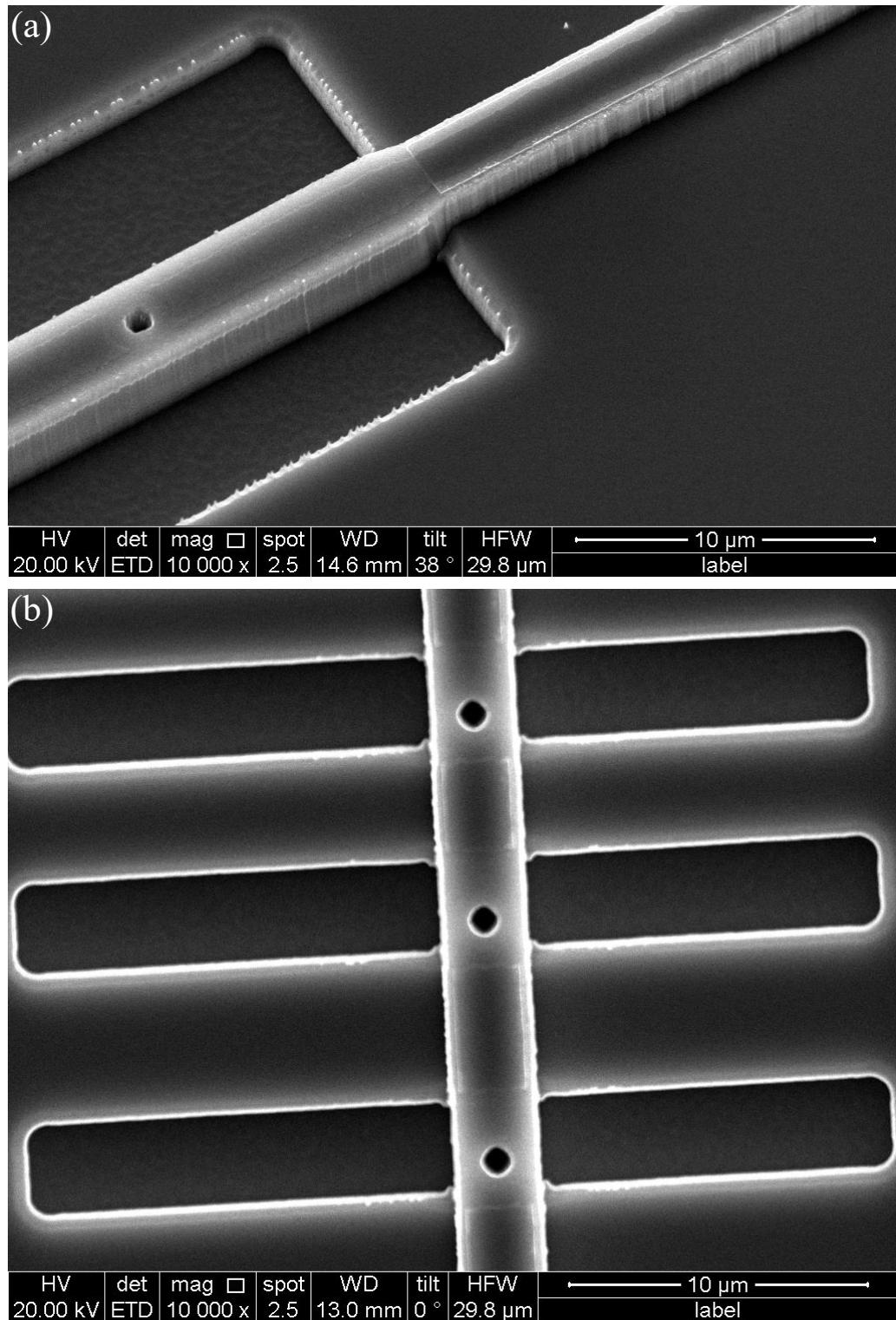


Figure B.3: Scanning electron microscope images of pit perturbations. **(a)** Side view of a pit perturbation etched into the centre of a waveguide, which shows the height difference between the deep etched and shallow etched regions. **(b)** A series of pit perturbations etched in an inverse scattering device. The pits are align to the waveguide, and hence inaccuracies in the location of the deep etches are only significant if they completely miss the deep etched region.

Appendix C

Growth of Arnol'd Tongues with Pump Current for $\alpha = 0$ and $\alpha = 3$

$\alpha = 0$

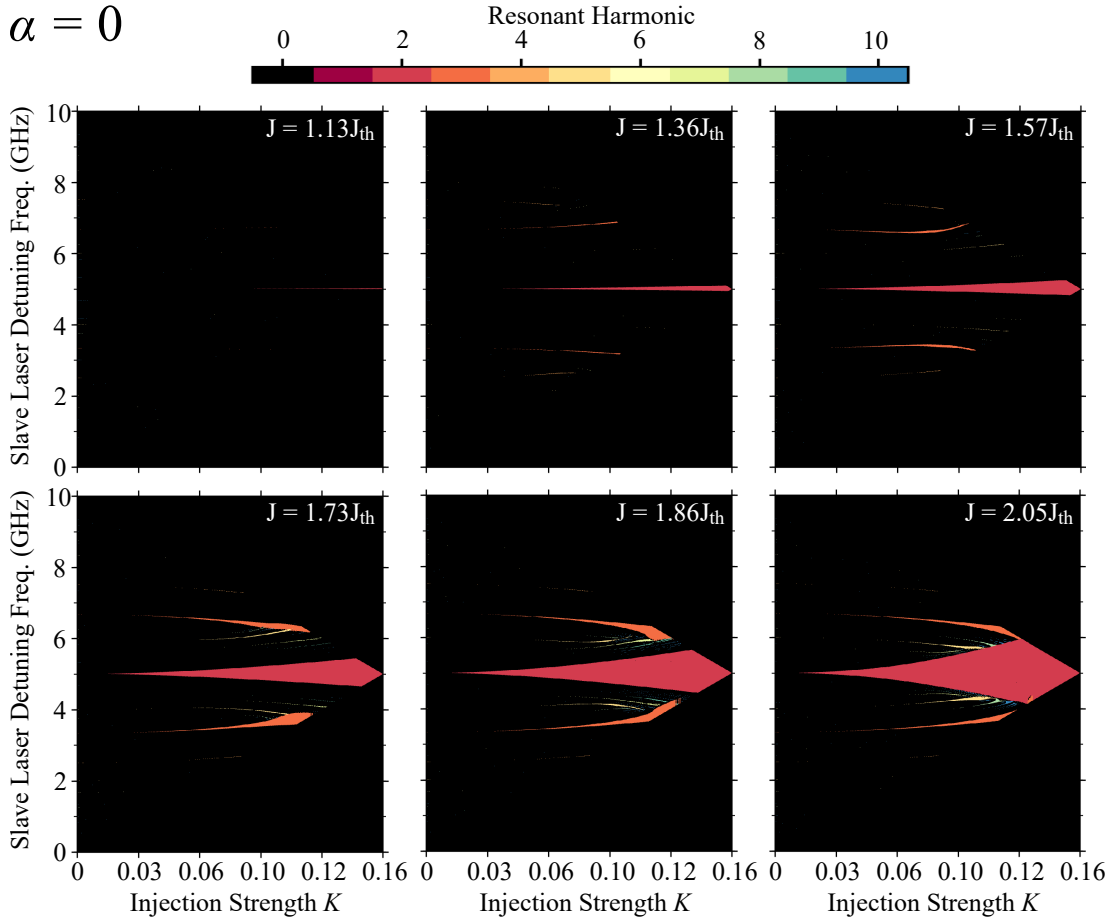


Figure C.1: Two dimensional maps of the slave laser behaviour while under injection of a 10 GHz optical comb, for the case of $\alpha = 0$. The 6 plots shown at different pump currents were taken from the calculations used to plot Fig. 4.14(b).

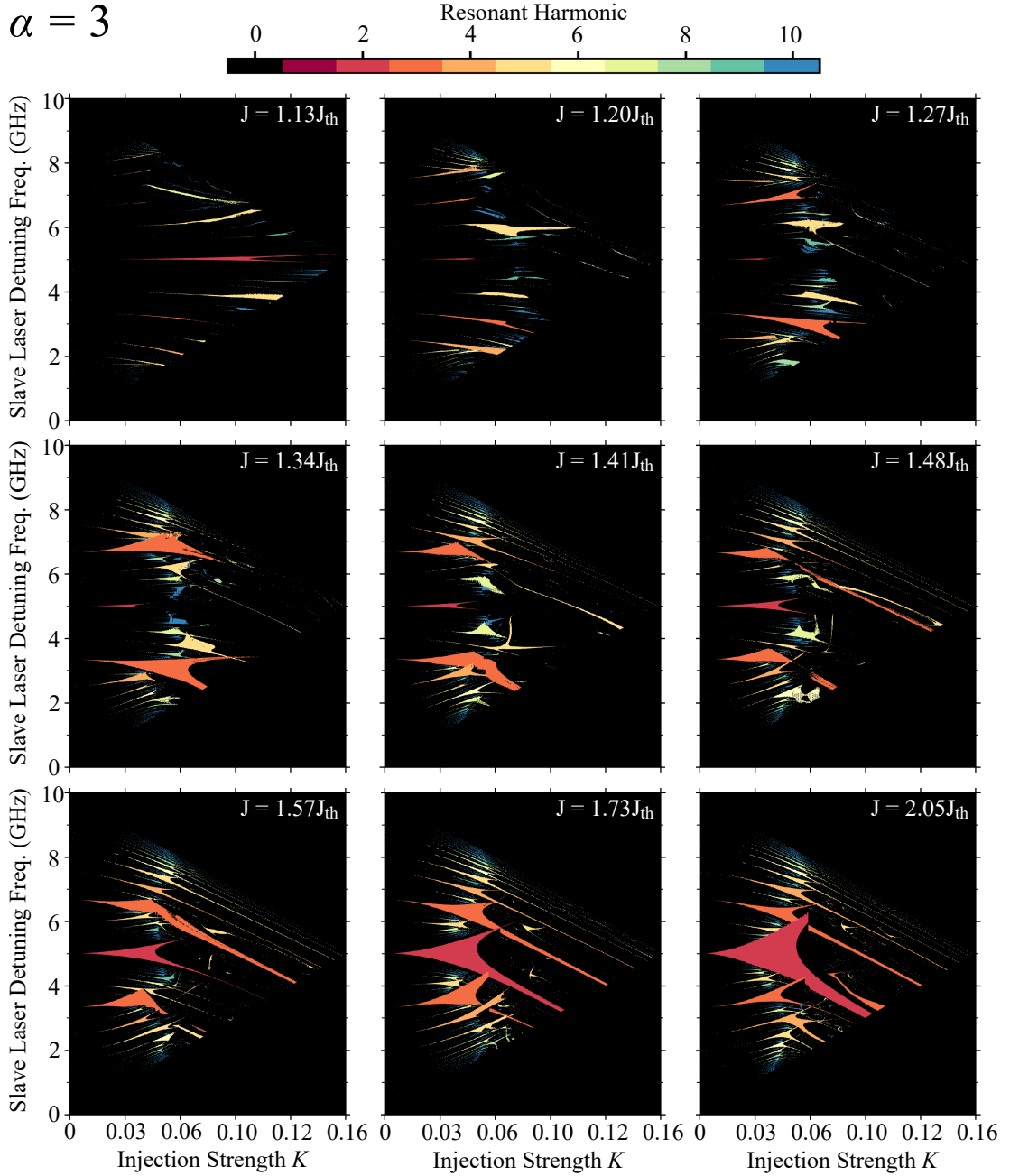


Figure C.2: Two dimensional maps of the slave laser behaviour while under injection of a 10 GHz optical comb, for the case of $\alpha = 3$. The 9 plots shown at different pump currents were taken from the calculations used to plot Fig. 4.14(a).

Appendix D

Material and Substrate Information

The epitaxial layers of the material and the substrate used for the fabrication of the devices is provided below. A brief description of the fabrication process used is given in Section A.5, and further details can be found in [221], [223].

Table D.1: Epitaxial structure of the material. A right arrow (\rightarrow) indicates a gradient in composition, from lower layer numbers to higher layer numbers.

Layer No.	Material	Composition		Strain (%)	Thickness (μm) ($\pm 10\%$)
		x	y		
16	GaIn(x)As	0.53			0.200
15	GaIn(x)As(y)P	0.71	0.62		0.050
14	InP				0.100
13					1.500
12	GaIn(x)As(y)P	0.85	0.33		0.020
11	InP				0.050
10	[Al(x)Ga]In(y)As	0.90	0.53		0.060
9		0.72 \rightarrow 0.90			0.060
8		0.44	0.49	-0.3	0.010
7 \times 5		0.24	0.71	+1.2	0.006
6 \times 5		0.44	0.49	-0.3	0.010
5		0.90 \rightarrow 0.72	0.53		0.060
4		0.90			0.060
3		0.86 \rightarrow 0.92			0.010
2	InP				0.500
1					0.300

Table D.2: Doping information for the layers contained in Table D.1.

Layer No.	Material	C-V doping level (cm^{-3}) ($\pm 30\%$)	Dopant	Type
16	GaIn(x)As	$> 1.5 \times 10^{19}$	Zn	P
15	GaIn(x)As(y)P	$> 3.0 \times 10^{18}$		
14	InP	$> 1.5 \times 10^{18}$		
13		1.0×10^{18}		
12	GaIn(x)As(y)P			
11	InP	7.0×10^{17}		
10	[Al(x)Ga]In(y)As	4.0×10^{17}		
9				
8				
7×5				
6×5				
5				
4		1.0×10^{18}	Si	N
3				
2				
1	InP	3.0×10^{18}		

Table D.3: Epitaxial structure of the substrate on which the material in Table D.1 was grown on.

Substrate Details - 2" InP:S			
Orientation (100) \pm 0.5	Thickness (μm) 350 ± 20	Material InP:S	Carrier Concentration (cm^{-3}) $(1 \rightarrow 8) \times 10^{18}$
Flat Specification EJ	EPD (cm^2) <1000	Finish P/P	

Appendix E

Runge-Kutta Formula

The Euler method of for numerically predicting future time steps in a first order ordinary differential equation (ODE) y is given by:

$$y_{t+\Delta t} = y_t + \Delta t f(t, y_t) \quad (\text{E.1})$$

where here, Δt is the time step used, and $f(t, y)$ is the time derivative of the function $y(t)$. This method is also the simplest Runge-Kutta method to implement, and is not recommended for serious numerical work, as the method is not accurate when compared to other methods with equivalent step sizes (as it has errors of order $O(\Delta t^2)$), and is also not suitably stable.

The Euler method lacks accuracy as it relies only on information from the time step t to predict the value at $t + 1$, which is an asymmetric approximation (illustrated in Fig. E.1(a)). Higher orders of the Runge-Kutta method are superior, as they use trial steps across the interval to compute the actual value over the whole time step. This symmetrization cancels out higher order error terms, resulting in errors of order $O(\Delta t^5)$ in the fourth order Runge-Kutta method. The fourth order Runge-Kutta method (sometimes abbreviated to RK4) is the most widespread implementation of Runge-Kutta solvers, and written in the same form as above is given as:

$$k_1 = \Delta t f(t, y_t) \quad (\text{E.2})$$

$$k_2 = \Delta t f\left(t + \frac{\Delta t}{2}, y_t + \frac{k_1}{2}\right) \quad (\text{E.3})$$

$$k_3 = \Delta t f\left(t + \frac{\Delta t}{2}, y_t + \frac{k_2}{2}\right) \quad (\text{E.4})$$

$$k_4 = \Delta t f(t + \Delta t, y_t + k_3) \quad (\text{E.5})$$

$$y_{t+\Delta t} = y_t + \frac{k_1}{6} + \frac{k_2}{3} + \frac{k_3}{3} + \frac{k_4}{6} \quad (\text{E.6})$$

Hence, for each time step of Δt , there are four evaluations at times between t and $t + \Delta t$, as illustrated in Fig. E.1(b). However, in order for the method to be accurate, a sufficiently small time step Δt is still required. The following section details the investigation into how a suitable time step was chosen when modelling the rate equations for optical comb injection.

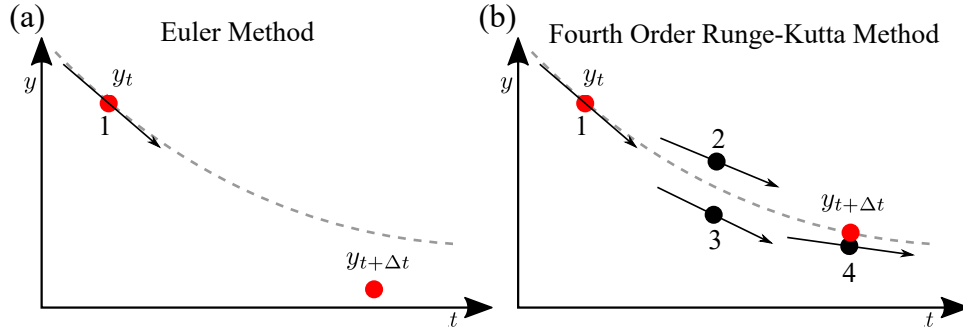


Figure E.1: (a) Illustration of how the Euler method integrates an ordinary differential equation (ODE). The derivative at the starting point of each interval is used to extrapolate the function value at time $t + \Delta t$. (b) Illustration of how the fourth order Runge-Kutta method integrates an ODE. For each step, four evaluations are made; once at the starting point, twice at trial midpoints, and once at a trial endpoint. Using the trial points and the initial point, the function is evaluated at time $t + \Delta t$.

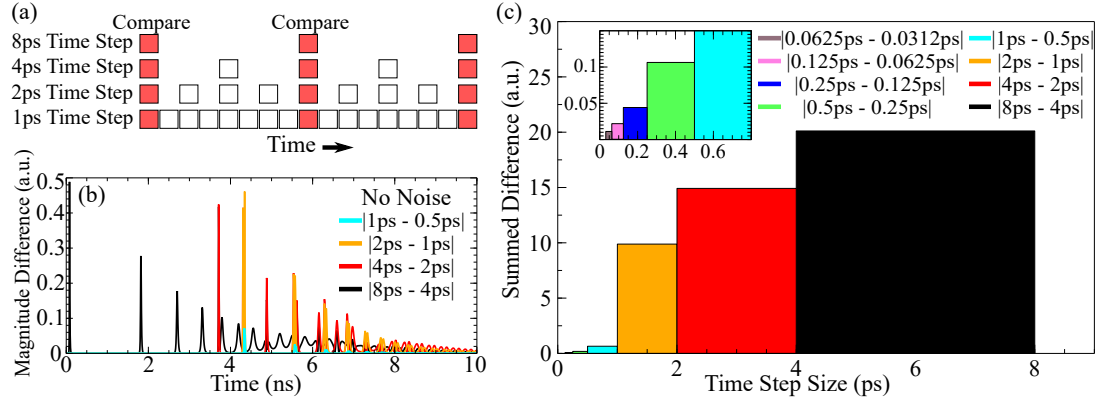


Figure E.2: (a) Illustration showing how the simulation time steps were compared. (b) Time traces which indicate the magnitude of the difference between simulations which used different time steps (as highlighted in red in (a)), over the first 10 ns. The data shows how that for very coarse time steps, the Runge-Kutta method does not accurately predict the behaviour of the slave laser. (c) Total magnitude difference summed over all comparison times for 50 ns simulations, with no noise in the rate equations.

E.1 Varying the Time Steps used in Rate Equation Models

To analyse the relation between the time step used and the accuracy of the Runge-Kutta method, simulation outputs were compared at set times during simulations with equivalent initial conditions (as shown in Fig. E.2(a)). The model and parameters used can be found in Section 3.1, and the RK4 method was used to simulate the field, phase and carriers of the slave laser.

Figure E.2(b) shows the differences in the laser's field observed when using large time steps. Each curve represented the difference between two free-running simulations. The simulations used no spontaneous emission to avoid any contribution due to random noise, and instead were all initialised in the same way. The Runge-Kutta method doesn't accurately model the relaxation oscillations until a sufficiently small time step is used. Even more indicative are the compiled results shown in Fig. E.2(c), which plot the sum of the magnitude difference at each time step, over 50 ns simulations. It is immediately clear that there is still large disagreement between the simulations with 2 ps time steps and the simulations with 1 ps time steps, and hence, for noiseless simulations time steps below 1 ps are preferable. A drawback of us-

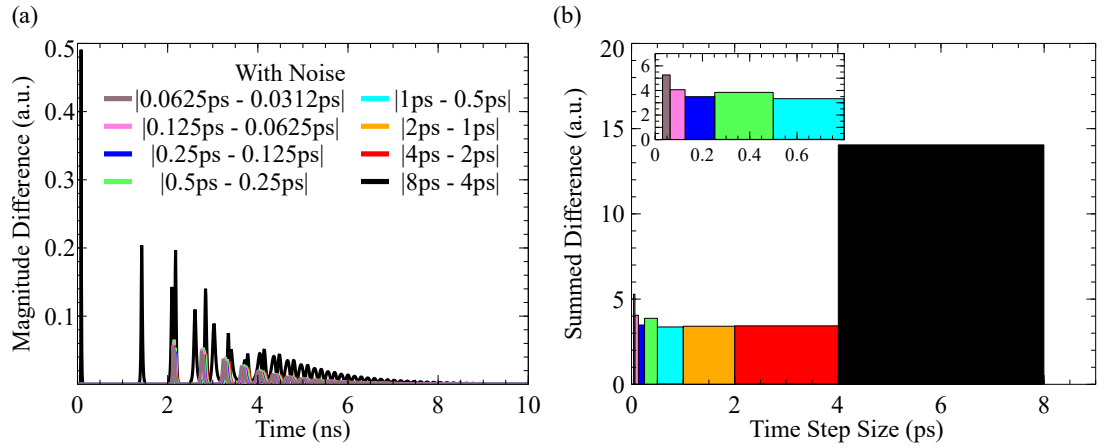


Figure E.3: (a) Time traces which indicate the magnitude of the difference between simulations which used different time steps (as highlighted in red in Fig. E.2(a)), over the first 10 ns. The data shows how that for very coarse time steps, the Runge-Kutta method does not accurately predict the behaviour of the slave laser. (b) Total magnitude difference summed over all comparison times for 50 ns simulations.

ing smaller time steps, is that they increase the length of time required to perform the same frequency range in simulations.

When noise is introduced into the simulations, the results appear to depend less on the time steps used. Figure E.3(a) shows the differences between the output time traces of simulations using different consecutive time steps, similar to Fig. E.2(b), however including noise. The simulations were all initialised in the same way, but the randomly generated noise added at each time step varied from run to run. It's clear that the ringing due to the relaxation oscillations dampens quicker when noise is included. The difference between the 8 ps and 4 ps traces is large, whereas the results for all smaller times steps seem to agree (at least qualitatively over the first 10 ns). While this suggests that adding noise to the simulations allows larger time steps to achieve greater accuracy, the insight gained from the noiseless simulations indicates that shorter time steps (≈ 1 ps) should still likely be used.

Finally, Fig. E.3(b) shows the summed results from the different simulations when noise was included. In these cases, optical comb injection occurred midway through the 50 ns simulation. Unlike in the noiseless case, there is little change below 8 ps, as shorter time steps disagree with one another quite significantly. This is likely due to the noise in the system, however it is important to note that each case was compared at exactly the same points in time.

The above calculations were also carried out for the simulated laser's phase and active carriers, and similar results were found in each case.

Bibliography

- [1] United Nations Human Rights Council, "The promotion, protection and enjoyment of human rights on the Internet," vol. A/HRC/32/L, 2016. [Online]. Available: https://www.article19.org/data/files/Internet_Statement_Adopted.pdf.
- [2] Statista, "Data volume of global consumer internet traffic from 2017 to 2022, by subsegment," 2019. [Online]. Available: <https://www.statista.com/>.
- [3] Nielsen Norman Group, "Nielsen's Law of Internet Bandwidth," [Online]. Available: <https://www.nngroup.com/articles/law-of-bandwidth/>.
- [4] Fang-Shang Chen, "Modulators for optical communications," *Proceedings of the IEEE*, vol. 58, no. 10, pp. 1440–1457, 1970, ISSN: 0018-9219. DOI: 10.1109/PROC.1970.7970. [Online]. Available: <http://ieeexplore.ieee.org/document/1449900/>.
- [5] U. Koren, T. L. Koch, H. Presting, and B. I. Miller, "InGaAs/InP multiple quantum well waveguide phase modulator," *Applied Physics Letters*, vol. 50, no. 7, pp. 368–370, 1987, ISSN: 0003-6951. DOI: 10.1063/1.98201. [Online]. Available: <http://aip.scitation.org/doi/10.1063/1.98201>.
- [6] P. J. Winzer, "High-Spectral-Efficiency Optical Modulation Formats," *Journal of Light-wave Technology*, vol. 30, no. 24, pp. 3824–3835, 2012, ISSN: 0733-8724. DOI: 10.1109/JLT.2012.2212180. [Online]. Available: <http://ieeexplore.ieee.org/document/6280581/>.
- [7] C. Brackett, "Dense wavelength division multiplexing networks: principles and applications," *IEEE Journal on Selected Areas in Communications*, vol. 8, no. 6, pp. 948–964, 1990, ISSN: 07338716. DOI: 10.1109/49.57798. [Online]. Available: <http://ieeexplore.ieee.org/document/57798/>.
- [8] A. Ellis and F. Gunning, "Spectral density enhancement using coherent WDM," *IEEE Photonics Technology Letters*, vol. 17, no. 2, pp. 504–506, 2005, ISSN: 1041-1135. DOI: 10.1109/LPT.2004.839393. [Online]. Available: <http://ieeexplore.ieee.org/document/1386363/>.
- [9] D. J. Richardson, "Filling the Light Pipe," *Science*, vol. 330, no. 6002, 2010.
- [10] C. E. Shannon, "A Mathematical Theory of Communication," *Bell System Technical Journal*, vol. 27, no. 3, pp. 379–423, 1948, ISSN: 00058580. DOI: 10.1002/j.1538-7305.1948.tb01338.x. [Online]. Available: <http://ieeexplore.ieee.org/lpdocs/epic03/wrapper.htm?arnumber=6773024>.
- [11] G. Keiser, *Optical fiber communications*. McGraw-Hill Companies, 2011, p. 654, ISBN: 9780073380711.
- [12] J. M. Jacobs, "The Impact of Hydrogen on Optical Fibers," *Corning White Paper*, 2004.

- [13] G. P. Agrawal, *Fiber-optic communication systems*. Wiley, 2010, p. 603, ISBN: 9780470505113. [Online]. Available: <https://www.wiley.com/en-us/Fiber+Optic+Communication+Systems%2C+4th+Edition-p-9780470505113>.
- [14] R. Mears, L. Reekie, I. Jauncey, and D. Payne, "Low-noise erbium-doped fibre amplifier operating at $1.54\mu\text{m}$," *Electronics Letters*, vol. 23, no. 19, p. 1026, 1987, ISSN: 00135194. DOI: 10.1049/el:19870719. [Online]. Available: https://digital-library.theiet.org/content/journals/10.1049/el_19870719.
- [15] M. N. Petrovich, F. Poletti, J. P. Wooller, A. M. Heidt, N. K. Baddela, Z. Li, D. R. Gray, R. Slavík, F. Parmigiani, N. V. Wheeler, J. R. Hayes, E. Numkam, L. Gruner-Nielsen, B. Pálsdóttir, R. Phelan, B. Kelly, M. Becker, N. MacSuibhne, J. Zhao, F. G. Gunning, A. D. Ellis, P. Petropoulos, S. U. Alam, and D. J. Richardson, "First Demonstration of $2\mu\text{m}$ Data Transmission in a Low-Loss Hollow Core Photonic Bandgap Fiber," in *European Conference and Exhibition on Optical Communication*, Washington, D.C.: OSA, 2012, Th.3.A.5, ISBN: 978-1-55752-950-3. DOI: 10.1364/ECEOC.2012.Th.3.A.5. [Online]. Available: <https://www.osapublishing.org/abstract.cfm?URI=ECEOC-2012-Th.3.A.5>.
- [16] J. Zhang, Y. Zhao, X. Yu, J. Zhang, M. Song, Y. Ji, and B. Mukherjee, "Energy-Efficient Traffic Grooming in Sliceable-Transponder-Equipped IP-Over-Elastic Optical Networks [Invited]," *Journal of Optical Communications and Networking*, vol. 7, no. 1, A142, 2015, ISSN: 1943-0620. DOI: 10.1364/JOCN.7.00A142. [Online]. Available: <https://www.osapublishing.org/abstract.cfm?URI=jocn-7-1-A142>.
- [17] N. Kavanagh, K. Shortiss, H. Zhang, M. Sadiq, K. Thomas, A. Gocalinska, Y. Zhao, E. Pelucchi, P. O'Brien, F. Peters, B. Corbett, and F. Gunning, "Impact of DWDM at 50GHz spacing in the $2\mu\text{m}$ waveband," in *2016 Conference on Lasers and Electro-Optics, CLEO 2016*, 2016, ISBN: 9781943580118.
- [18] F. C. Garcia Gunning, N. Kavanagh, E. Russell, R. Sheehan, J. O'Callaghan, and B. Corbett, "Key enabling technologies for optical communications at 2000nm," *Applied Optics*, vol. 57, no. 22, E64, 2018, ISSN: 1559-128X. DOI: 10.1364/AO.57.000E64. [Online]. Available: <https://www.osapublishing.org/abstract.cfm?URI=ao-57-22-E64>.
- [19] P. J. Roberts, F. Couny, H. Sabert, B. J. Mangan, D. P. Williams, L. Farr, M. W. Mason, A. Tomlinson, T. A. Birks, J. C. Knight, and P. St. J. Russell, "Ultimate low loss of hollow-core photonic crystal fibres," *Optics Express*, vol. 13, no. 1, p. 236, 2005, ISSN: 1094-4087. DOI: 10.1364/OPEX.13.000236. [Online]. Available: <https://www.osapublishing.org/oe/abstract.cfm?uri=oe-13-1-236>.
- [20] Z. Li, A. M. Heidt, J. M. O. Daniel, Y. Jung, S. U. Alam, and D. J. Richardson, "Thulium-doped fiber amplifier for optical communications at $2\mu\text{m}$," *Optics Express*, vol. 21, no. 8, p. 9289, 2013, ISSN: 1094-4087. DOI: 10.1364/OE.21.009289. [Online]. Available: <https://www.osapublishing.org/oe/abstract.cfm?uri=oe-21-8-9289>.
- [21] E. Russell, F. Gunning, K. Shortiss, and N. Kavanagh, "Development of thulium-doped fibre amplifiers for the $2\mu\text{m}$ waveband," in *Fiber Lasers and Glass Photonics: Materials through Applications*, S. Taccheo, M. Ferrari, and J. I. Mackenzie, Eds., vol. 10683, SPIE, 2018, p. 97, ISBN: 9781510618923. DOI: 10.1117/12.2306462. [Online]. Available: <https://www.spiedigitallibrary.org/conference-proceedings->

- of - spie / 10683 / 2306462 / Development - of - thulium - doped - fibre - amplifiers - for - the - 2um - waveband / 10.1117/12.2306462.full.
- [22] V. Ataie, E. Temprana, L. Liu, E. Myslivets, B. P.-P. Kuo, N. Alic, and S. Radic, "Flex-grid Compatible Ultra Wide Frequency Comb Source for 31.8 Tb/s Coherent Transmission of 1520 UDWDM Channels," in *Optical Fiber Communication Conference: Postdeadline Papers*, Washington, D.C.: OSA, 2014, Th5B.7, ISBN: 978-1-55752-994-7. DOI: 10.1364/OFC.2014.Th5B.7. [Online]. Available: <https://www.osapublishing.org/abstract.cfm?URI=OFC-2014-Th5B.7>.
 - [23] P. M. Anandarajah, M. Deseada Gutierrez Pascual, S. O'Duill, J. Bradell, F. Smyth, and P. Landais, "Integrated frequency combs for flexible optical networks," in *2017 Photonics North (PN)*, IEEE, 2017, pp. 1–1, ISBN: 978-1-5386-2192-9. DOI: 10.1109/PN.2017.8090555. [Online]. Available: <http://ieeexplore.ieee.org/document/8090555/>.
 - [24] M. Mazur, A. Lorences-Riesgo, J. Schroder, P. A. Andrekson, and M. Karlsson, "10 Tb/s PM-64QAM Self-Homodyne Comb-Based Superchannel Transmission With 4% Shared Pilot Tone Overhead," *Journal of Lightwave Technology*, vol. 36, no. 16, pp. 3176–3184, 2018, ISSN: 0733-8724. DOI: 10.1109/JLT.2018.2820166. [Online]. Available: <https://ieeexplore.ieee.org/document/8327487/>.
 - [25] V. Torres-Company, J. Schröder, A. Fülöp, M. Mazur, L. Lundberg, Ó. B. Helgason, M. Karlsson, and P. A. Andrekson, "Laser Frequency Combs for Coherent Optical Communications," *J. Lightwave Technol.*, vol. 37, no. 7, pp. 1663–1670, 2019. [Online]. Available: <http://jlt.osa.org/abstract.cfm?URI=jlt-37-7-1663>.
 - [26] S. Chandrasekhar, L. Xiang, B. Zhu, and D. W. Peckham, "Transmission of a 1.2-Tb/s 24-carrier no-guard-interval coherent OFDM superchannel over 7200-km of ultra-large-area fiber," in *35th European Conference on Optical Communication*, 2009.
 - [27] D. J. Blumenthal, "Integrated combs drive extreme data rates," *Nature Photonics*, vol. 12, no. 8, pp. 447–450, 2018, ISSN: 1749-4885. DOI: 10.1038/s41566-018-0222-4. [Online]. Available: <http://www.nature.com/articles/s41566-018-0222-4>.
 - [28] L. Lundberg, M. Karlsson, A. Lorences-Riesgo, M. Mazur, V. Torres-Company, J. Schröder, P. Andrekson, L. Lundberg, M. Karlsson, A. Lorences-Riesgo, M. Mazur, V. Torres-Company, J. Schröder, and P. A. Andrekson, "Frequency Comb-Based WDM Transmission Systems Enabling Joint Signal Processing," *Applied Sciences*, vol. 8, no. 5, p. 718, 2018, ISSN: 2076-3417. DOI: 10.3390/app8050718. [Online]. Available: <http://www.mdpi.com/2076-3417/8/5/718>.
 - [29] C. Liu, J. Pan, T. Detwiler, A. Stark, Y.-T. Hsueh, G.-K. Chang, and S. E. Ralph, "Joint digital signal processing for superchannel coherent optical communication systems," *Optics Express*, vol. 21, no. 7, p. 8342, 2013, ISSN: 1094-4087. DOI: 10.1364/OE.21.008342. [Online]. Available: <https://www.osapublishing.org/oe/abstract.cfm?uri=oe-21-7-8342>.
 - [30] I. Tomkos, S. Azodolmolky, J. Sole-Pareta, D. Careglio, and E. Palkopoulou, "A tutorial on the flexible optical networking paradigm: State of the art, trends, and research challenges," *Proceedings of the IEEE*, vol. 102, no. 9, pp. 1317–1337, 2014, ISSN: 0018-9219. DOI: 10.1109/JPROC.2014.2324652. [Online]. Available: <http://ieeexplore.ieee.org/document/6824237/>.

- [31] G. Zhang, M. De Leenheer, A. Morea, and B. Mukherjee, "A Survey on OFDM-Based Elastic Core Optical Networking," *IEEE Communications Surveys & Tutorials*, vol. 15, no. 1, pp. 65–87, 2013, ISSN: 1553-877X. DOI: 10.1109/SURV.2012.010912.00123. [Online]. Available: <http://ieeexplore.ieee.org/document/6148192/>.
- [32] L. Lundberg, M. Mazur, A. Mirani, B. Foo, J. Schröder, V. Torres-Company, M. Karlsson, and P. A. Andrekson, "Phase-coherent lightwave communications with frequency combs," *Nature Communications*, vol. 11, no. 1, p. 201, 2020, ISSN: 2041-1723. DOI: 10.1038/s41467-019-14010-7. [Online]. Available: <http://www.nature.com/articles/s41467-019-14010-7>.
- [33] M. D. G. Pascual, R. Zhou, F. Smyth, P. M. Anandarajah, and L. P. Barry, "Software reconfigurable highly flexible gain switched optical frequency comb source," *Optics Express*, vol. 23, no. 18, p. 23 225, 2015, ISSN: 1094-4087. DOI: 10.1364/OE.23.023225. [Online]. Available: <https://www.osapublishing.org/abstract.cfm?URI=oe-23-18-23225>.
- [34] T. Zami, "Co-Optimizing Allocation of Nyquist Superchannels and Physical Impairments Aware Placement of Regenerators in Elastic WDM Networks," *Journal of Lightwave Technology*, Vol. 32, Issue 16, pp. 2830-2840, vol. 32, no. 16, pp. 2830–2840, 2014. [Online]. Available: <https://www.osapublishing.org/jlt/abstract.cfm?uri=jlt-32-16-2830>.
- [35] M. Klinkowski, M. Ruiz, L. Velasco, D. Careglio, V. Lopez, and J. Comellas, "Elastic Spectrum Allocation for Time-Varying Traffic in FlexGrid Optical Networks," *IEEE Journal on Selected Areas in Communications*, vol. 31, no. 1, pp. 26–38, 2013, ISSN: 0733-8716. DOI: 10.1109/JSAC.2013.130104. [Online]. Available: <http://ieeexplore.ieee.org/document/6381741/>.
- [36] T. H. Maiman, "Stimulated Optical Radiation in Ruby," *Nature*, vol. 187, no. 4736, pp. 493–494, 1960, ISSN: 0028-0836. DOI: 10.1038/187493a0. [Online]. Available: <http://www.nature.com/articles/187493a0>.
- [37] A. Yariv and J. Gordon, "The laser," *Proceedings of the IEEE*, vol. 51, no. 1, pp. 4–29, 1963, ISSN: 0018-9219. DOI: 10.1109/PROC.1963.1654. [Online]. Available: <http://ieeexplore.ieee.org/document/1443584/>.
- [38] G. P. Agrawal and N. K. Dutta, *Long wavelength semiconductor lasers*. Van Nostrand Reinhold, Jan. 1986, ISBN: 9789401169967.
- [39] E. Kapon, *Semiconductor lasers. Volume 1, Fundamentals*. Academic Press, 1999, ISBN: 9780123976307.
- [40] Z. Wang, Y. Ning, Y. Zhang, J. Shi, X. Zhang, L. Zhang, W. Wang, D. Liu, Y. Hu, H. Cong, L. Qin, Y. Liu, and L. Wang, "High power and good beam quality of two-dimensional VCSEL array with integrated GaAs microlens array," *Optics Express*, vol. 18, no. 23, p. 23 900, 2010, ISSN: 1094-4087. DOI: 10.1364/OE.18.023900. [Online]. Available: <https://www.osapublishing.org/oe/abstract.cfm?uri=oe-18-23-23900>.
- [41] E. Watanabe and K. Kodate, "Multi-light source compact optical parallel correlator (MLCOPaC) for facial recognition using VCSEL array," G. C. Righini and A. Consortini, Eds., vol. 4829, International Society for Optics and Photonics, 2003, p. 208. DOI: 10.1117/12.523842. [Online]. Available: <http://proceedings.spiedigitallibrary.org/proceeding.aspx?doi=10.1117/12.523842>.

- [42] Y. N. Srikant, "Classics," *Resonance*, vol. 17, no. 11, pp. 1100–1115, 2012, ISSN: 0971-8044. DOI: 10.1007/s12045-012-0124-6. [Online]. Available: <http://link.springer.com/10.1007/s12045-012-0124-6>.
- [43] SMART Photonics, "Multi Project Wafers (MPW)," [Online]. Available: <https://smartphotonics.nl/our-offering/mpw/>.
- [44] K. Kato and Y. Tohmori, "PLC hybrid integration technology and its application to photonic components," *IEEE Journal of Selected Topics in Quantum Electronics*, vol. 6, no. 1, pp. 4–13, 2000, ISSN: 1077-260X. DOI: 10.1109/2944.826866. [Online]. Available: <http://ieeexplore.ieee.org/document/826866/>.
- [45] D. Thomson, A. Zilkie, J. E. Bowers, T. Komljenovic, G. T. Reed, L. Vivien, D. Marris-Morini, E. Cassan, L. Viot, J.-M. Fédéli, J.-M. Hartmann, J. H. Schmid, D.-X. Xu, F. Boeuf, P. O'Brien, G. Z. Mashanovich, and M. Nedeljkovic, "Roadmap on silicon photonics," *Journal of Optics*, vol. 18, no. 7, p. 073003, 2016, ISSN: 2040-8978. DOI: 10.1088/2040-8978/18/7/073003. [Online]. Available: <http://stacks.iop.org/2040-8978/18/i=7/a=073003?key=crossref.4a5bbda045e84b8801eba3e3605b6fb2>.
- [46] M. J. R. Heck, J. F. Bauters, M. L. Davenport, J. K. Doylend, S. Jain, G. Kurczveil, S. Srinivasan, Y. Tang, and J. E. Bowers, "Hybrid Silicon Photonic Integrated Circuit Technology," *IEEE Journal of Selected Topics in Quantum Electronics*, vol. 19, no. 4, pp. 6100117–6100117, 2013, ISSN: 1077-260X. DOI: 10.1109/JSTQE.2012.2235413. [Online]. Available: <http://ieeexplore.ieee.org/document/6387568/>.
- [47] M. A. Foster, A. C. Turner, J. E. Sharping, B. S. Schmidt, M. Lipson, and A. L. Gaeta, "Broad-band optical parametric gain on a silicon photonic chip," *Nature*, vol. 441, no. 7096, pp. 960–963, 2006, ISSN: 0028-0836. DOI: 10.1038/nature04932. [Online]. Available: <http://www.nature.com/articles/nature04932>.
- [48] M. Tran, D. Huang, T. Komljenovic, J. Peters, A. Malik, and J. Bowers, "Ultra-Low-Loss Silicon Waveguides for Heterogeneously Integrated Silicon/III-V Photonics," *Applied Sciences*, vol. 8, no. 7, p. 1139, 2018, ISSN: 2076-3417. DOI: 10.3390/app8071139. [Online]. Available: <http://www.mdpi.com/2076-3417/8/7/1139>.
- [49] M. Wale and C. Edge, "Self-aligned flip-chip assembly of photonic devices with electrical and optical connections," *IEEE Transactions on Components, Hybrids, and Manufacturing Technology*, vol. 13, no. 4, pp. 780–786, 1990, ISSN: 01486411. DOI: 10.1109/33.62593. [Online]. Available: <http://ieeexplore.ieee.org/document/62593/>.
- [50] A. Moscoso-Martir, F. Merget, J. Mueller, J. Hauck, S. Romero-Garcia, B. Shen, F. Lelarge, R. Brenot, A. Garreau, E. Mentovich, A. Sandomirsky, A. Badihi, D. E. Rasmussen, R. Setter, and J. Witzens, "Hybrid silicon photonics flip-chip laser integration with vertical self-alignment," in *2017 Conference on Lasers and Electro-Optics Pacific Rim (CLEO-PR)*, IEEE, 2017, pp. 1–4, ISBN: 978-1-5090-6290-4. DOI: 10.1109/CLEOPR.2017.8118971. [Online]. Available: <http://ieeexplore.ieee.org/document/8118971/>.
- [51] B. Corbett, R. Loi, J. O'Callaghan, and G. Roelkens, "Transfer Printing for Silicon Photonics," *Semiconductors and Semimetals*, vol. 99, pp. 43–70, 2018, ISSN: 0080-8784. DOI: 10.1016/BS.SEMSEM.2018.08.001. [Online]. Available: <https://www.sciencedirect.com/science/article/pii/S0080878418300231>.

- [52] R. Loi and Ruggero, "Heterogeneous integration of InP etched facet lasers to silicon photonics by micro transfer printing," PhD thesis, 2019. [Online]. Available: <https://cora.ucc.ie/handle/10468/8562>.
- [53] J. Zhang, B. Haq, J. O'Callaghan, A. Gocalinska, E. Pelucchi, A. J. Trindade, B. Corbett, G. Morthier, and G. Roelkens, "Transfer-printing-based integration of a III-V-on-silicon distributed feedback laser," *Optics Express*, vol. 26, no. 7, p. 8821, 2018, ISSN: 1094-4087. DOI: 10.1364/OE.26.008821. [Online]. Available: <https://www.osapublishing.org/abstract.cfm?URI=oe-26-7-8821>.
- [54] G. Roelkens, J. Van Campenhout, J. Brouckaert, D. Van Thourhout, R. Baets, P. R. Romeo, P. Regreny, A. Kazmierczak, C. Seassal, X. Letartre, G. Hollinger, J. Fedeli, L. Di Cioccio, and C. Lagahe-Blanchard, "III-V/Si photonics by die-to-wafer bonding," *Materials Today*, vol. 10, no. 7-8, pp. 36–43, 2007, ISSN: 1369-7021. DOI: 10.1016/S1369-7021(07)70178-5. [Online]. Available: <https://www.sciencedirect.com/science/article/pii/S1369702107701785>.
- [55] L. Megalini, B. Bonef, B. C. Cabinian, H. Zhao, A. Taylor, J. S. Speck, J. E. Bowers, and J. Klamkin, "1550-nm InGaAsP multi-quantum-well structures selectively grown on v-groove-patterned SOI substrates," *Applied Physics Letters*, vol. 111, no. 3, p. 032105, 2017, ISSN: 0003-6951. DOI: 10.1063/1.4994318. [Online]. Available: <http://aip.scitation.org/doi/10.1063/1.4994318>.
- [56] M. Liao, S. Chen, S. Huo, S. Chen, J. Wu, M. Tang, K. Kennedy, W. Li, S. Kumar, M. Martin, T. Baron, C. Jin, I. Ross, A. Seeds, and H. Liu, "Monolithically Integrated Electrically Pumped Continuous-Wave III-V Quantum Dot Light Sources on Silicon," *IEEE Journal of Selected Topics in Quantum Electronics*, vol. 23, no. 6, pp. 1–10, 2017, ISSN: 1077-260X. DOI: 10.1109/JSTQE.2017.2693025. [Online]. Available: <https://ieeexplore.ieee.org/document/7898434/>.
- [57] A. Y. Liu, J. Peters, X. Huang, D. Jung, J. Norman, M. L. Lee, A. C. Gossard, and J. E. Bowers, "Electrically pumped continuous-wave 1.3 μm quantum-dot lasers epitaxially grown on on-axis (001) GaP/Si," *Optics Letters*, vol. 42, no. 2, p. 338, 2017, ISSN: 0146-9592. DOI: 10.1364/OL.42.000338. [Online]. Available: <https://www.osapublishing.org/abstract.cfm?URI=ol-42-2-338>.
- [58] C. R. Doerr, L. Chen, Y.-K. Chen, and L. L. Buhl, "Wide Bandwidth Silicon Nitride Grating Coupler," *IEEE Photonics Technology Letters*, vol. 22, no. 19, pp. 1461–1463, 2010, ISSN: 1041-1135. DOI: 10.1109/LPT.2010.2062497. [Online]. Available: <http://ieeexplore.ieee.org/document/5535118/>.
- [59] L. A. Coldren, S. C. Nicholes, L. Johansson, S. Ristic, R. S. Guzzon, E. J. Norberg, and U. Krishnamachari, "High Performance InP-Based Photonic ICs – A Tutorial," *Journal of Lightwave Technology*, vol. 29, no. 4, pp. 554–570, 2011, ISSN: 0733-8724. DOI: 10.1109/JLT.2010.2100807. [Online]. Available: <http://ieeexplore.ieee.org/document/5680569/>.
- [60] S. Nicholes, M. Masanovic, B. Jevremovic, E. Lively, L. Coldren, and D. Blumenthal, "An 8 x 8 InP Monolithic Tunable Optical Router (MOTOR) Packet Forwarding Chip," *Journal of Lightwave Technology*, vol. 28, no. 4, pp. 641–650, 2010, ISSN: 0733-8724. DOI: 10.1109/JLT.2009.2030145. [Online]. Available: <http://ieeexplore.ieee.org/document/5204280/>.

- [61] M. Funabashi, H. Nasu, T. Mukaihara, T. Kimoto, T. Shinagawa, T. Kise, K. Takaki, T. Takagi, M. Oike, T. Nomura, and A. Kasukawa, "Recent Advances in DFB Lasers for Ultradense WDM Applications," *IEEE Journal of Selected Topics in Quantum Electronics*, vol. 10, no. 2, pp. 312–320, 2004, ISSN: 1077-260X. DOI: 10.1109/JSTQE.2004.826576. [Online]. Available: <http://ieeexplore.ieee.org/document/1303579/>.
- [62] H. Kawanishi, Y. Yamauchi, N. Mineo, Y. Shibuya, H. Mural, K. Yamada, and H. Wada, "EAM-integrated DFB laser modules with more than 40-GHz bandwidth," *IEEE Photonics Technology Letters*, vol. 13, no. 9, pp. 954–956, 2001, ISSN: 1041-1135. DOI: 10.1109/68.942658. [Online]. Available: <http://ieeexplore.ieee.org/document/942658/>.
- [63] M. Aoki, H. Sano, M. Suzuki, M. Takahashi, K. Uomi, and A. Takai, "Novel structure MQW electroabsorption modulator/DFB-laser integrated device fabricated by selective area MOCVD growth," *Electronics Letters*, vol. 27, no. 23, p. 2138, 1991, ISSN: 00135194. DOI: 10.1049/el:19911324. [Online]. Available: https://digital-library.theiet.org/content/journals/10.1049/el_19911324.
- [64] R. Martin, S. Forouhar, S. Keo, R. Lang, R. Hunsperger, R. Tiberio, and P. Chapman, "CW performance of an InGaAs-GaAs-AlGaAs laterally-coupled distributed feedback (LC-DFB) ridge laser diode," *IEEE Photonics Technology Letters*, vol. 7, no. 3, pp. 244–246, 1995, ISSN: 1041-1135. DOI: 10.1109/68.372734. [Online]. Available: <http://ieeexplore.ieee.org/document/372734/>.
- [65] V. Tolstikhin, "Distributed feedback lasers for regrowth-free multi-guide vertical integration in InP," in *2010 IEEE Photonic Society's 23rd Annual Meeting*, IEEE, 2010, pp. 521–522, ISBN: 978-1-4244-5368-9. DOI: 10.1109/PHOTONICS.2010.5698990. [Online]. Available: <http://ieeexplore.ieee.org/document/5698990/>.
- [66] R. Lammert, J. Hughes, S. Roh, M. Osowski, A. Jones, and J. Coleman, "Low-threshold narrow-linewidth InGaAs-GaAs ridge-waveguide DBR lasers with first-order surface gratings," *IEEE Photonics Technology Letters*, vol. 9, no. 2, pp. 149–151, 1997, ISSN: 1041-1135. DOI: 10.1109/68.553068. [Online]. Available: <http://ieeexplore.ieee.org/document/553068/>.
- [67] H. Zhao, S. Pinna, F. Sang, B. Song, S. T. Suran Brunelli, L. A. Coldren, and J. Klamkin, "High-Power Indium Phosphide Photonic Integrated Circuits," *IEEE Journal of Selected Topics in Quantum Electronics*, vol. 25, no. 6, pp. 1–10, 2019, ISSN: 1077-260X. DOI: 10.1109/JSTQE.2019.2908788. [Online]. Available: <https://ieeexplore.ieee.org/document/8680753/>.
- [68] N. Holonyak, "Impurity-induced layer disordering of quantum-well heterostructures: discovery and prospects," *IEEE Journal of Selected Topics in Quantum Electronics*, vol. 4, no. 4, pp. 584–594, 1998, ISSN: 1077260X. DOI: 10.1109/2944.720468. [Online]. Available: <http://ieeexplore.ieee.org/document/720468/>.
- [69] S. Charbonneau, E. Koteles, P. Poole, J. He, G. Aers, J. Haysom, M. Buchanan, Y. Feng, A. Delage, F. Yang, M. Davies, R. Goldberg, P. Piva, and I. Mitchell, "Photonic integrated circuits fabricated using ion implantation," *IEEE Journal of Selected Topics in Quantum Electronics*, vol. 4, no. 4, pp. 772–793, 1998, ISSN: 1077260X. DOI: 10.1109/2944.720491. [Online]. Available: <http://ieeexplore.ieee.org/document/720491/>.

- [70] Sang Kee Si, Deok Ho Yeo, Hyung Hun Yoon, and Sung June Kim, "Area selectivity of InGaAsP-InP multiquantum-well intermixing by impurity-free vacancy diffusion," *IEEE Journal of Selected Topics in Quantum Electronics*, vol. 4, no. 4, pp. 619–623, 1998, ISSN: 1077260X. DOI: 10.1109/2944.720471. [Online]. Available: <http://ieeexplore.ieee.org/document/720471/>.
- [71] L. Hou and J. H. Marsh, "Photonic Integrated Circuits Based on Quantum well Intermixing Techniques," *Procedia Engineering*, vol. 140, pp. 107–114, 2016, ISSN: 1877-7058. DOI: 10.1016/J.PROENG.2015.10.152. [Online]. Available: <https://www.sciencedirect.com/science/article/pii/S1877705815036425>.
- [72] M. Schell, *Photonic Integration for Communication and Sensing - Economic Success and Failure*, Zurich, 2018.
- [73] B. Corbett and D. McDonald, "Single longitudinal mode ridge waveguide 1.3 μm Fabry-Perot laser by modal perturbation," *Electronics Letters*, vol. 31, no. 25, pp. 2181–2182, 1995, ISSN: 0013-5194. DOI: 10.1049/el:19951487. [Online]. Available: http://digital-library.theiet.org/content/journals/10.1049/el_19951487.
- [74] S. K. Mondal, B. Roycroft, P. Lambkin, F. Peters, B. Corbett, P. Townsend, and A. Ellis, "A Multiwavelength Low-Power Wavelength-Locked Slotted Fabry-Pérot Laser Source for WDM Applications," *IEEE Photonics Technology Letters*, vol. 19, no. 10, pp. 744–746, 2007, ISSN: 1041-1135. DOI: 10.1109/LPT.2007.895888. [Online]. Available: <http://ieeexplore.ieee.org/document/4156232/>.
- [75] D. Byrne, J. Engelstaedter, Wei-Hua Guo, Qiao Yin Lu, B. Corbett, B. Roycroft, J. O'Callaghan, F. Peters, and J. Donegan, "Discretely Tunable Semiconductor Lasers Suitable for Photonic Integration," *IEEE Journal of Selected Topics in Quantum Electronics*, vol. 15, no. 3, pp. 482–487, 2009, ISSN: 1077-260X. DOI: 10.1109/JSTQE.2009.2016981. [Online]. Available: <http://ieeexplore.ieee.org/document/4926148/>.
- [76] S. O'Brien, F. Smyth, K. Shi, J. O'Carroll, P. M. Anandarajah, D. Bitauld, S. Osborne, R. Phelan, B. Kelly, J. O'Gorman, F. H. Peters, B. Roycroft, B. Corbett, and L. P. Barry, "Design, Characterization, and Applications of Index-Patterned Fabry-Pérot Lasers," *IEEE Journal of Selected Topics in Quantum Electronics*, vol. 17, no. 6, pp. 1621–1631, 2011, ISSN: 1077-260X. DOI: 10.1109/JSTQE.2011.2118192. [Online]. Available: <http://ieeexplore.ieee.org/document/5755170/>.
- [77] Qiaoyin Lu, Wei-Hua Guo, D. Byrne, and J. F. Donegan, "Design of Slotted Single-Mode Lasers Suitable for Photonic Integration," *IEEE Photonics Technology Letters*, vol. 22, no. 11, pp. 787–789, 2010, ISSN: 1041-1135. DOI: 10.1109/LPT.2010.2045888. [Online]. Available: <http://ieeexplore.ieee.org/document/5437332/>.
- [78] K. Shi, F. Smyth, D. Reid, B. Roycroft, B. Corbett, F. Peters, and L. Barry, "Characterization of a tunable three-section slotted Fabry-Perot laser for advanced modulation format optical transmission," *Optics Communications*, vol. 284, no. 6, pp. 1616–1621, 2011, ISSN: 0030-4018. DOI: 10.1016/J.OPTCOM.2010.11.022. [Online]. Available: <https://www.sciencedirect.com/science/article/pii/S0030401810012356>.
- [79] R. Phelan, W.-H. Guo, Q. Lu, D. Byrne, B. Roycroft, P. Lambkin, B. Corbett, F. Smyth, L. P. Barry, B. Kelly, J. O'Gorman, and J. F. Donegan, "A Novel Two-Section Tunable

- Discrete Mode Fabry-Pérot Laser Exhibiting Nanosecond Wavelength Switching," *IEEE Journal of Quantum Electronics*, vol. 44, no. 4, pp. 331–337, 2008, ISSN: 0018-9197. DOI: 10.1109/JQE.2007.914219. [Online]. Available: <http://ieeexplore.ieee.org/document/4456801/>.
- [80] Q. Y. Lu, W. H. Guo, R. Phelan, D. Byrne, J. F. Donegan, P. Lambkin, and B. Corbett, "Analysis of Slot Characteristics in Slotted Single-Mode Semiconductor Lasers Using the 2-D Scattering Matrix Method," *IEEE Photonics Technology Letters*, vol. 18, no. 24, pp. 2605–2607, 2006, ISSN: 1041-1135. DOI: 10.1109/LPT.2006.887328. [Online]. Available: <http://ieeexplore.ieee.org/document/4026621/>.
- [81] M. Dernaika, N. Kelly, L. Caro, K. Shortiss, and F. Peters, "Regrowth-free single-mode semiconductor laser suitable for monolithic integration based on pits mirror," *Optical Engineering*, vol. 56, no. 8, 2017, ISSN: 15602303. DOI: 10.1117/1.OE.56.8.086107.
- [82] J. J. Kelly and H. G. Philipsen, "Anisotropy in the wet-etching of semiconductors," *Current Opinion in Solid State and Materials Science*, vol. 9, no. 1-2, pp. 84–90, 2005, ISSN: 1359-0286. DOI: 10.1016/J.COSSMS.2006.04.003. [Online]. Available: <https://www.sciencedirect.com/science/article/pii/S1359028606000283#fig2>.
- [83] M. Dernaika, L. Caro, N. P. Kelly, and F. H. Peters, "Single facet semiconductor laser with deep etched V-notch reflectors integrated with an active multimode interference reflector," *Journal of Modern Optics*, vol. 64, no. 19, pp. 1941–1946, 2017, ISSN: 0950-0340. DOI: 10.1080/09500340.2017.1327621. [Online]. Available: <https://www.tandfonline.com/doi/full/10.1080/09500340.2017.1327621>.
- [84] M. Dernaika, L. Caro, N. P. Kelly, J. K. Alexander, F. Dubois, P. E. Morrissey, and F. H. Peters, "Deeply Etched Inner-Cavity Pit Reflector," *IEEE Photonics Journal*, vol. 9, no. 1, pp. 1–8, 2017, ISSN: 1943-0655. DOI: 10.1109/JPHOT.2017.2656252. [Online]. Available: <http://ieeexplore.ieee.org/document/7828054/>.
- [85] S. O'Brien, A. Amann, R. Fehse, S. Osborne, E. P. O'Reilly, and J. M. Rondinelli, "Spectral manipulation in Fabry-Perot lasers: perturbative inverse scattering approach," *Journal of the Optical Society of America B*, vol. 23, no. 6, p. 1046, 2006, ISSN: 0740-3224. DOI: 10.1364/JOSAB.23.001046. [Online]. Available: <https://www.osapublishing.org/abstract.cfm?URI=josab-23-6-1046>.
- [86] G. Adolfsson, J. Bengtsson, Å. Haglund, B. Nilsson, and A. Larsson, "Realization of spectrally engineered semiconductor Fabry-Perot lasers with narrow geometrical tolerances," *Journal of Applied Physics*, vol. 109, no. 9, p. 093112, 2011, ISSN: 0021-8979. DOI: 10.1063/1.3587359. [Online]. Available: <http://aip.scitation.org/doi/10.1063/1.3587359>.
- [87] K. Shortiss, M. Dernaika, L. Caro, M. Seifikar, and F. H. Peters, "Inverse Scattering Method Design of Regrowth-Free Single-Mode Semiconductor Lasers Using Pit Perturbations for Monolithic Integration," *IEEE Photonics Journal*, vol. 10, no. 5, pp. 1–10, 2018, ISSN: 1943-0655. DOI: 10.1109/JPHOT.2018.2873048. [Online]. Available: <https://ieeexplore.ieee.org/document/8477050/>.
- [88] T. Fortier and E. Baumann, "20 years of developments in optical frequency comb technology and applications," *Communications Physics*, vol. 2, no. 1, p. 153, 2019, ISSN: 2399-3650. DOI: 10.1038/s42005-019-0249-y. [Online]. Available: <http://www.nature.com/articles/s42005-019-0249-y>.

- [89] E. Baumann, F. R. Giorgetta, J. W. Nicholson, W. C. Swann, I. Coddington, and N. R. Newbury, "High-performance, vibration-immune, fiber-laser frequency comb," *Optics Letters*, vol. 34, no. 5, p. 638, 2009, ISSN: 0146-9592. DOI: 10.1364/OL.34.000638. [Online]. Available: <https://www.osapublishing.org/abstract.cfm?URI=ol-34-5-638>.
- [90] P. Del'Haye, A. Schliesser, O. Arcizet, T. Wilken, R. Holzwarth, and T. J. Kippenberg, "Optical frequency comb generation from a monolithic microresonator," *Nature*, vol. 450, no. 7173, pp. 1214–1217, 2007, ISSN: 0028-0836. DOI: 10.1038/nature06401. [Online]. Available: <http://www.nature.com/articles/nature06401>.
- [91] E. Oelker, R. B. Hutson, C. J. Kennedy, L. Sonderhouse, T. Bothwell, A. Goban, D. Kedar, C. Sanner, J. M. Robinson, G. E. Marti, D. G. Matei, T. Legero, M. Giunta, R. Holzwarth, F. Riehle, U. Sterr, and J. Ye, "Demonstration of 4.8×10^{-17} stability at 1 s for two independent optical clocks," *Nature Photonics*, vol. 13, no. 10, pp. 714–719, 2019, ISSN: 1749-4885. DOI: 10.1038/s41566-019-0493-4. [Online]. Available: <http://www.nature.com/articles/s41566-019-0493-4>.
- [92] C. W. Chou, D. B. Hume, T. Rosenband, and D. J. Wineland, "Optical clocks and relativity," *Science (New York, N.Y.)*, vol. 329, no. 5999, pp. 1630–3, 2010, ISSN: 1095-9203. DOI: 10.1126/science.1192720. [Online]. Available: <http://www.ncbi.nlm.nih.gov/pubmed/20929843>.
- [93] NIST, *Getting Better All the Time: JILA Strontium Atomic Clock Sets New Records — NIST*. [Online]. Available: <https://www.nist.gov/news-events/news/2015/04/getting-better-all-time-jila-strontium-atomic-clock-sets-new-records> (visited on 10/17/2019).
- [94] T. Udem, R. Holzwarth, and T. W. Hänsch, "Optical frequency metrology," *Nature*, vol. 416, no. 6877, pp. 233–237, 2002, ISSN: 0028-0836. DOI: 10.1038/416233a. [Online]. Available: <http://www.nature.com/articles/416233a>.
- [95] E. Cartlidge, "With better atomic clocks, scientists prepare to redefine the second," *Science*, 2018, ISSN: 0036-8075. DOI: 10.1126/science.aat4586. [Online]. Available: <http://www.sciencemag.org/news/2018/03/better-atomic-clocks-scientists-prepare-redefine-second>.
- [96] N. Picqué and T. W. Hänsch, "Frequency comb spectroscopy," *Nature Photonics*, vol. 13, no. 3, pp. 146–157, 2019, ISSN: 1749-4885. DOI: 10.1038/s41566-018-0347-5. [Online]. Available: <http://www.nature.com/articles/s41566-018-0347-5>.
- [97] N. R. Newbury, "Searching for applications with a fine-tooth comb," *Nature Photonics*, vol. 5, no. 4, pp. 186–188, 2011, ISSN: 1749-4885. DOI: 10.1038/nphoton.2011.38. [Online]. Available: <http://www.nature.com/articles/nphoton.2011.38>.
- [98] C.-B. Huang, Z. Jiang, D. Leaird, J. Caraquiten, and A. Weiner, "Spectral line-by-line shaping for optical and microwave arbitrary waveform generations," *Laser & Photonics Review*, vol. 2, no. 4, pp. 227–248, 2008, ISSN: 18638880. DOI: 10.1002/lpor.200810001. [Online]. Available: <http://doi.wiley.com/10.1002/lpor.200810001>.
- [99] S. T. Cundiff and A. M. Weiner, "Optical arbitrary waveform generation," *Nature Photonics*, vol. 4, no. 11, pp. 760–766, 2010, ISSN: 1749-4885. DOI: 10.1038/nphoton.2010.196. [Online]. Available: <http://www.nature.com/articles/nphoton.2010.196>.

- [100] M. L. Davenport, S. Liu, and J. E. Bowers, "Integrated heterogeneous silicon/III-V mode-locked lasers," *Photonics Research*, vol. 6, no. 5, p. 468, 2018, ISSN: 2327-9125. DOI: 10.1364/PRJ.6.000468. [Online]. Available: <https://www.osapublishing.org/abstract.cfm?URI=prj-6-5-468>.
- [101] A. Pasquazi, M. Peccianti, L. Razzari, D. J. Moss, S. Coen, M. Erkintalo, Y. K. Chembo, T. Hansson, S. Wabnitz, P. Del'Haye, X. Xue, A. M. Weiner, and R. Morandotti, "Microcombs: A novel generation of optical sources," *Physics Reports*, vol. 729, pp. 1–81, 2018, ISSN: 0370-1573. DOI: 10.1016/J.PHYSREP.2017.08.004. [Online]. Available: <https://www.sciencedirect.com/science/article/pii/S0370157317303253>.
- [102] A. Fülöp, M. Mazur, A. Lorences-Riesgo, T. A. Eriksson, P.-H. Wang, Y. Xuan, D. E. Leaird, M. Qi, P. A. Andrekson, A. M. Weiner, and V. Torres-Company, "Long-haul coherent communications using microresonator-based frequency combs," *Optics Express*, vol. 25, no. 22, p. 26 678, 2017, ISSN: 1094-4087. DOI: 10.1364/OE.25.026678. [Online]. Available: <https://www.osapublishing.org/abstract.cfm?URI=oe-25-22-26678>.
- [103] P. Marin-Palomo, J. N. Kemal, M. Karpov, A. Kordts, J. Pfeifle, M. H. P. Pfeiffer, P. Trocha, S. Wolf, V. Brasch, M. H. Anderson, R. Rosenberger, K. Vijayan, W. Freude, T. J. Kippenberg, and C. Koos, "Microresonator-based solitons for massively parallel coherent optical communications," *Nature*, vol. 546, no. 7657, pp. 274–279, 2017, ISSN: 0028-0836. DOI: 10.1038/nature22387. [Online]. Available: <http://www.nature.com/articles/nature22387>.
- [104] D. K. Armani, T. J. Kippenberg, S. M. Spillane, and K. J. Vahala, "Ultra-high-Q toroid microcavity on a chip," *Nature*, vol. 421, no. 6926, pp. 925–928, 2003, ISSN: 0028-0836. DOI: 10.1038/nature01371. [Online]. Available: <http://www.nature.com/articles/nature01371>.
- [105] P. M. Anandarajah, R. Maher, Y. Q. Xu, S. Latkowski, J. O'Carroll, S. G. Murdoch, R. Phelan, J. O'Gorman, and L. P. Barry, "Generation of Coherent Multicarrier Signals by Gain Switching of Discrete Mode Lasers," *IEEE Photonics Journal*, vol. 3, no. 1, pp. 112–122, 2011, ISSN: 1943-0655. DOI: 10.1109/JPHOT.2011.2105861. [Online]. Available: <http://ieeexplore.ieee.org/document/5686909/>.
- [106] K. Y. Lau, "Gain switching of semiconductor injection lasers," *Applied Physics Letters*, vol. 52, no. 4, pp. 257–259, 1988, ISSN: 0003-6951. DOI: 10.1063/1.99486. [Online]. Available: <http://aip.scitation.org/doi/10.1063/1.99486>.
- [107] S. Tarucha and K. Otsuka, "Response of semiconductor laser to deep sinusoidal injection current modulation," *IEEE Journal of Quantum Electronics*, vol. 17, no. 5, pp. 810–816, 1981, ISSN: 0018-9197. DOI: 10.1109/JQE.1981.1071186. [Online]. Available: <http://ieeexplore.ieee.org/document/1071186/>.
- [108] J. K. Alexander, P. E. Morrissey, H. Yang, M. Yang, P. J. Marraccini, B. Corbett, and F. H. Peters, "Monolithically integrated low linewidth comb source using gain switched slotted Fabry-Perot lasers," *Optics Express*, vol. 24, no. 8, p. 7960, 2016, ISSN: 1094-4087. DOI: 10.1364/OE.24.007960. [Online]. Available: <https://www.osapublishing.org/abstract.cfm?URI=oe-24-8-7960>.

- [109] J. K. Alexander, "Low-linewidth optical comb sources based on gain-switched lasers," PhD thesis, 2017. [Online]. Available: <https://cora.ucc.ie/handle/10468/5467>.
- [110] M. D. Gutierrez Pascual, "Development and investigation of optical frequency combs for photonic communication systems," PhD thesis, Dublin City University, 2017.
- [111] M. D. Gutierrez Pascual, V. Vujicic, J. Braddell, F. Smyth, P. M. Anandarajah, and L. P. Barry, "InP photonic integrated externally injected gain switched optical frequency comb," *Optics Letters*, vol. 42, no. 3, p. 555, 2017, ISSN: 0146-9592. DOI: 10.1364/OL.42.000555. [Online]. Available: <https://www.osapublishing.org/abstract.cfm?URI=ol-42-3-555>.
- [112] H. Ito, H. Yokoyama, S. Murata, and H. Inaba, "Picosecond optical pulse generation from an r.f. modulated AlGaAs d.h. diode laser," *Electronics Letters*, vol. 15, no. 23, p. 738, 1979, ISSN: 00135194. DOI: 10.1049/el:19790528. [Online]. Available: https://digital-library.theiet.org/content/journals/10.1049/el_19790528.
- [113] C. Huyghens, "Ouevres Completes de Christian Huyghens," *The Netherlands: Societe Hollandaise des Sciences*, vol. 5, p. 243, 1893.
- [114] C. A. Czeisler, J. F. Duffy, T. L. Shanahan, E. N. Brown, J. F. Mitchell, D. W. Rimmer, J. M. Ronda, E. J. Silva, J. S. Allan, J. S. Emens, D. J. Dijk, and R. E. Kronauer, "Stability, Precision, and Near-24-Hour Period of the Human Circadian Pacemaker," *Science*, vol. 284, no. 5423, pp. 2177–2181, 1999, ISSN: 00368075. DOI: 10.1126/science.284.5423.2177. [Online]. Available: <http://www.ncbi.nlm.nih.gov/pubmed/10381883> <http://www.sciencemag.org/cgi/doi/10.1126/science.284.5423.2177>.
- [115] R. Adler, "A Study of Locking Phenomena in Oscillators," *Proceedings of the IRE*, vol. 34, no. 6, pp. 351–357, 1946, ISSN: 0096-8390. DOI: 10.1109/JRPROC.1946.229930. [Online]. Available: <http://ieeexplore.ieee.org/document/1697085/>.
- [116] T. Erneux and P. Glorieux, *Laser dynamics*. Cambridge University Press, 2010, ISBN: 9780511776908.
- [117] D. Ziemann, R. Aust, B. Lingnau, E. Schöll, and K. Lüdge, "Optical injection enables coherence resonance in quantum-dot lasers," *EPL (Europhysics Letters)*, vol. 103, no. 1, p. 14002, 2013, ISSN: 0295-5075. DOI: 10.1209/0295-5075/103/14002. [Online]. Available: <http://stacks.iop.org/0295-5075/103/i=1/a=14002?key=crossref.24e27114a40a838247075b8a4878d770>.
- [118] J. Thévenin, M. Romanelli, M. Vallet, M. Brunel, and T. Erneux, "Resonance Assisted Synchronization of Coupled Oscillators: Frequency Locking without Phase Locking," *Physical Review Letters*, vol. 107, no. 10, p. 104101, 2011, ISSN: 0031-9007. DOI: 10.1103/PhysRevLett.107.104101. [Online]. Available: <https://link.aps.org/doi/10.1103/PhysRevLett.107.104101>.
- [119] T. Simpson and J. Liu, "Enhanced modulation bandwidth in injection-locked semiconductor lasers," *IEEE Photonics Technology Letters*, vol. 9, no. 10, pp. 1322–1324, 1997, ISSN: 1041-1135. DOI: 10.1109/68.623250. [Online]. Available: <http://ieeexplore.ieee.org/document/623250/>.
- [120] E. K. Lau, L. J. Wong, X. Zhao, Y.-K. Chen, C. J. Chang-Hasnain, and M. C. Wu, "Bandwidth Enhancement by Master Modulation of Optical Injection-Locked Lasers," *Journal of Lightwave Technology*, vol. 26, no. 15, pp. 2584–2593, 2008, ISSN: 0733-8724. DOI:

- 10.1109/JLT.2008.927192. [Online]. Available: <http://ieeexplore.ieee.org/document/4652285/>.
- [121] R. Wyatt, D. Smith, and K. Cameron, "Megahertz linewidth from a 1.5 μm semiconductor laser with HeNe laser injection," *Electronics Letters*, vol. 18, no. 7, p. 292, 1982, ISSN: 00135194. DOI: 10.1049/el:19820199. [Online]. Available: https://digital-library.theiet.org/content/journals/10.1049/el_19820199.
- [122] W. W. Chow, "Phase locking of lasers by an injected signal," *Optics Letters*, vol. 7, no. 9, p. 417, 1982, ISSN: 0146-9592. DOI: 10.1364/OL.7.000417. [Online]. Available: <https://www.osapublishing.org/abstract.cfm?URI=ol-7-9-417>.
- [123] T. Habruseva, G. Huyet, and S. P. Hegarty, "Dynamics of Quantum-Dot Mode-Locked Lasers With Optical Injection," *IEEE Journal of Selected Topics in Quantum Electronics*, vol. 17, no. 5, pp. 1272–1279, 2011, ISSN: 1077-260X. DOI: 10.1109/JSTQE.2011.2123875. [Online]. Available: <http://ieeexplore.ieee.org/document/5749681/>.
- [124] S. P. Ó Dúill, P. M. Anandarajah, R. Zhou, and L. P. Barry, "Numerical investigation into the injection-locking phenomena of gain switched lasers for optical frequency comb generation," *Applied Physics Letters*, vol. 106, no. 21, p. 211 105, 2015, ISSN: 0003-6951. DOI: 10.1063/1.4921852. [Online]. Available: <http://aip.scitation.org/doi/10.1063/1.4921852>.
- [125] J. K. Alexander, P. E. Morrissey, L. Caro, M. Dernaika, N. P. Kelly, and F. H. Peters, "On-Chip Investigation of Phase Noise in Monolithically Integrated Gain-Switched Lasers," *IEEE Photonics Technology Letters*, vol. 29, no. 9, pp. 731–734, 2017, ISSN: 1041-1135. DOI: 10.1109/LPT.2017.2682560. [Online]. Available: <http://ieeexplore.ieee.org/document/7879169/>.
- [126] K. Balakier, M. J. Fice, F. van Dijk, G. Kervella, G. Carpintero, A. J. Seeds, and C. C. Renaud, "Optical injection locking of monolithically integrated photonic source for generation of high purity signals above 100 GHz," *Optics Express*, vol. 22, no. 24, p. 29 404, 2014, ISSN: 1094-4087. DOI: 10.1364/OE.22.029404. [Online]. Available: <https://www.osapublishing.org/oe/abstract.cfm?uri=oe-22-24-29404>.
- [127] C. Gordón, F. V. Dijk, G. Kervella, G. Carpintero, M. Chitoui, and R. C. Guzmán, "Photonic Integrated Circuits for Radio-Frequency Signal Generation," *Journal of Lightwave Technology*, Vol. 34, Issue 2, pp. 508–515, vol. 34, no. 2, pp. 508–515, 2016. [Online]. Available: <https://www.osapublishing.org/jlt/abstract.cfm?uri=jlt-34-2-508>.
- [128] W. E. Cotter, D. Goulding, B. Roycroft, J. O'Callaghan, B. Corbett, and F. H. Peters, "Investigation of active filter using injection-locked slotted Fabry-Perot semiconductor laser," *Applied Optics*, vol. 51, no. 30, p. 7357, 2012, ISSN: 0003-6935. DOI: 10.1364/AO.51.007357. [Online]. Available: <https://www.osapublishing.org/abstract.cfm?URI=ao-51-30-7357>.
- [129] M. D. Gutierrez, J. Braddell, F. Smyth, and L. P. Barry, "Monolithically integrated 1x4 comb de-multiplexer based on injection locking," in *European Conf. Integrated Optics*, 2016, pp. 1–2.
- [130] W. Cotter, P. E. Morrissey, H. Yang, J. O'Callaghan, B. Roycroft, B. Corbett, and F. H. Peters, "Integrated demultiplexing and amplification of coherent optical combs," *Optics Express*, vol. 27, no. 11, p. 16 012, 2019, ISSN: 1094-4087. DOI: 10.1364/OE.27.016012.

- [Online]. Available: <https://www.osapublishing.org/abstract.cfm?URI=oe-27-11-16012>.
- [131] P. D. Lakshmijayasimha, E. P. Martin, S. P. Ó Duill, P. Landais, P. M. Anandarajah, and A. Kaszubowska-Anandarajah, "Performance of an injection-locked active demultiplexer for FSR-tunable optical frequency combs," in *Conference on Lasers and Electro-Optics*, Washington, D.C.: OSA, 2019, STu4N.5, ISBN: 978-1-943580-57-6. DOI: 10.1364/CLEO_SI.2019.STu4N.5. [Online]. Available: https://www.osapublishing.org/abstract.cfm?URI=CLEO_SI-2019-STu4N.5.
 - [132] A. Gavrielides, "Comb Injection and Sidebands Suppression," *IEEE Journal of Quantum Electronics*, vol. 50, no. 5, pp. 364–371, 2014, ISSN: 0018-9197. DOI: 10.1109/JQE.2014.2309532. [Online]. Available: <http://ieeexplore.ieee.org/document/6762828/>.
 - [133] S. P. Ó Duill, P. M. Anandarajah, F. Smyth, L. P. Barry, A. J. Seeds, S. V. Chernikov, M. J. Guy, J. R. Taylor, and A. S. Siddiqui, "Injection-locking criteria for simultaneously locking single-mode lasers to optical frequency combs from gain-switched lasers," in *IEEE J. Quantum Electron*, B. Witzigmann, M. Osinski, and Y. Arakawa, Eds., vol. 18, International Society for Optics and Photonics, 2017, 100980H. DOI: 10.1117/12.2249769. [Online]. Available: <http://proceedings.spiedigitallibrary.org/proceeding.aspx?doi=10.1117/12.2249769>.
 - [134] D. J. Richardson, D. S. Wu, G. Marra, and R. Slavík, "Direct Selection and Amplification of Individual Narrowly Spaced Optical Comb Modes Via Injection Locking: Design and Characterization," *Journal of Lightwave Technology*, Vol. 31, Issue 14, pp. 2287–2295, vol. 31, no. 14, pp. 2287–2295, 2013. [Online]. Available: <https://www.osapublishing.org/jlt/abstract.cfm?uri=jlt-31-14-2287#>.
 - [135] D. S. Wu, D. J. Richardson, and R. Slavík, "Selective amplification of frequency comb modes via optical injection locking of a semiconductor laser: influence of adjacent unlocked comb modes," in *Proc. SPIE 8781, Integrated Optics: Physics and Simulations*, 2013, 87810J. DOI: 10.1117/12.2017371. [Online]. Available: <http://proceedings.spiedigitallibrary.org/proceeding.aspx?doi=10.1117/12.2017371>.
 - [136] M. S. Pramod, T. Yang, K. Pandey, M. Giudici, and D. Wilkowski, "Selective injection locking of a multi-mode semiconductor laser to a multi-frequency reference beam," *The European Physical Journal D*, vol. 68, no. 7, p. 186, 2014, ISSN: 1434-6060. DOI: 10.1140/epjd/e2014-40732-4. [Online]. Available: <http://link.springer.com/10.1140/epjd/e2014-40732-4>.
 - [137] A. C. Bordonalli, M. J. Fice, and A. J. Seeds, "Optical injection locking to optical frequency combs for superchannel coherent detection," *Optics Express*, vol. 23, no. 2, p. 1547, 2015, ISSN: 1094-4087. DOI: 10.1364/OE.23.001547. [Online]. Available: <https://www.osapublishing.org/abstract.cfm?URI=oe-23-2-1547>.
 - [138] R. Zhou, T. Shao, M. D. Gutierrez Pascual, F. Smyth, and L. P. Barry, "Injection Locked Wavelength De-Multiplexer for Optical Comb-Based Nyquist WDM System," *IEEE Photonics Technology Letters*, vol. 27, no. 24, pp. 2595–2598, 2015, ISSN: 1041-1135. DOI: 10.1109/LPT.2015.2478791. [Online]. Available: <http://ieeexplore.ieee.org/document/7268864/>.
 - [139] R. Zhou, M. D. Gutierrez Pascual, P. M. Anandarajah, T. Shao, F. Smyth, and L. P. Barry, "Flexible wavelength de-multiplexer for elastic optical networking," *Optics Let-*

- ters, vol. 41, no. 10, p. 2241, 2016, ISSN: 0146-9592. DOI: 10.1364/OL.41.002241. [Online]. Available: <https://www.osapublishing.org/abstract.cfm?URI=ol-41-10-2241>.
- [140] R. Lang, "Injection locking properties of a semiconductor laser," *IEEE Journal of Quantum Electronics*, vol. 18, no. 6, pp. 976–983, 1982, ISSN: 0018-9197. DOI: 10.1109/JQE.1982.1071632. [Online]. Available: <http://ieeexplore.ieee.org/document/1071632/>.
- [141] C. Henry, N. Olsson, and N. Dutta, "Locking range and stability of injection locked 1.54 μm InGaAsP semiconductor lasers," *IEEE Journal of Quantum Electronics*, vol. 21, no. 8, pp. 1152–1156, 1985, ISSN: 0018-9197. DOI: 10.1109/JQE.1985.1072787. [Online]. Available: <http://ieeexplore.ieee.org/document/1072787/>.
- [142] F. Mogensen, H. Olesen, and G. Jacobsen, "Locking conditions and stability properties for a semiconductor laser with external light injection," *IEEE Journal of Quantum Electronics*, vol. 21, no. 7, pp. 784–793, 1985, ISSN: 0018-9197. DOI: 10.1109/JQE.1985.1072760. [Online]. Available: <http://ieeexplore.ieee.org/document/1072760/>.
- [143] M. C. Soriano, J. García-Ojalvo, C. R. Mirasso, and I. Fischer, "Complex photonics: Dynamics and applications of delay-coupled semiconductor lasers," *Reviews of Modern Physics*, vol. 85, no. 1, pp. 421–470, 2013, ISSN: 0034-6861. DOI: 10.1103/RevModPhys.85.421. [Online]. Available: <https://link.aps.org/doi/10.1103/RevModPhys.85.421>.
- [144] S. Wieczorek, B. Krauskopf, T. Simpson, and D. Lenstra, "The dynamical complexity of optically injected semiconductor lasers," *Physics Reports*, vol. 416, no. 1-2, pp. 1–128, 2005, ISSN: 0370-1573. DOI: 10.1016/J.PHYSREP.2005.06.003. [Online]. Available: <https://www.sciencedirect.com/science/article/pii/S0370157305002656>.
- [145] S. Wieczorek, T. B. Simpson, B. Krauskopf, and D. Lenstra, "Bifurcation transitions in an optically injected diode laser: theory and experiment," *Optics Communications*, vol. 215, no. 1-3, pp. 125–134, 2003, ISSN: 0030-4018. DOI: 10.1016/S0030-4018(02)02191-0. [Online]. Available: <https://www.sciencedirect.com/science/article/abs/pii/S0030401802021910?via%3Dihub>.
- [146] T. Simpson, "Mapping the nonlinear dynamics of a distributed feedback semiconductor laser subject to external optical injection," *Optics Communications*, vol. 215, no. 1-3, pp. 135–151, 2003, ISSN: 0030-4018. DOI: 10.1016/S0030-4018(02)02192-2. [Online]. Available: <https://www.sciencedirect.com/science/article/pii/S0030401802021922>.
- [147] N. Al-Hosiny, I. Henning, and M. Adams, "Secondary locking regions in laser diode subject to optical injection from two lasers," *Electronics Letters*, vol. 42, no. 13, p. 759, 2006, ISSN: 00135194. DOI: 10.1049/el:20061128. [Online]. Available: https://digital-library.theiet.org/content/journals/10.1049/el_20061128.
- [148] Yu-Shan Juan and Fan-Yi Lin, "Photonic Generation of Broadly Tunable Microwave Signals Utilizing a Dual-Beam Optically Injected Semiconductor Laser," *IEEE Photonics Journal*, vol. 3, no. 4, pp. 644–650, 2011, ISSN: 1943-0655. DOI: 10.1109/JPHOT.

- 2011.2158413. [Online]. Available: <http://ieeexplore.ieee.org/document/5783879/>.
- [149] R. Desmet and M. Virte, "Laser diodes with modulated optical injection: towards a simple signal processing unit?" *Journal of Physics: Photonics*, vol. 2, no. 2, p. 025 002, 2020, ISSN: 2515-7647. DOI: 10.1088/2515-7647/ab7081. [Online]. Available: <https://iopscience.iop.org/article/10.1088/2515-7647/ab7081>.
 - [150] Y. Doumbia, T. Malica, D. Wolfersberger, K. Panajotov, and M. Sciamanna, "Optical injection dynamics of frequency combs," *Optics Letters*, vol. 45, no. 2, p. 435, 2020, ISSN: 0146-9592. DOI: 10.1364/OL.381039. [Online]. Available: <https://www.osapublishing.org/abstract.cfm?URI=ol-45-2-435>.
 - [151] P. Studenkov, M. Gokhale, W. Lin, I. Glesk, P. Prucnal, and S. Forrest, "Monolithic integration of an all-optical Mach-Zehnder demultiplexer using an asymmetric twin-waveguide structure," *IEEE Photonics Technology Letters*, vol. 13, no. 6, pp. 600–602, 2001, ISSN: 1041-1135. DOI: 10.1109/68.924035. [Online]. Available: <http://ieeexplore.ieee.org/document/924035/>.
 - [152] S.-H. Jeong and Y. Tanaka, "Silicon-wire optical demultiplexers based on multistage delayed Mach-Zehnder interferometers for higher production yield," *Applied Optics*, vol. 57, no. 22, p. 6474, 2018, ISSN: 1559-128X. DOI: 10.1364/AO.57.006474. [Online]. Available: <https://www.osapublishing.org/abstract.cfm?URI=ao-57-22-6474>.
 - [153] Jian-Jun He, B. Lamontagne, A. Delage, L. Erickson, M. Davies, and E. Koteles, "Monolithic integrated wavelength demultiplexer based on a waveguide Rowland circle grating in InGaAsP/InP," *Journal of Lightwave Technology*, vol. 16, no. 4, pp. 631–638, 1998, ISSN: 07338724. DOI: 10.1109/50.664075. [Online]. Available: <http://ieeexplore.ieee.org/document/664075/>.
 - [154] D. Melati, P. G. Verly, A. Del  ge, S. Wang, J. Lapointe, P. Cheben, J. H. Schmid, S. Janz, and D.-X. Xu, "Compact and Low Crosstalk Echelle Grating Demultiplexer on Silicon-On-Insulator Technology," *Electronics*, vol. 8, no. 6, p. 687, 2019, ISSN: 2079-9292. DOI: 10.3390/electronics8060687. [Online]. Available: <https://www.mdpi.com/2079-9292/8/6/687>.
 - [155] M. Smit, "New focusing and dispersive planar component based on an optical phased array," *Electronics Letters*, vol. 24, no. 7, p. 385, 1988, ISSN: 00135194. DOI: 10.1049/el:19880260. [Online]. Available: https://digital-library.theiet.org/content/journals/10.1049/el_19880260.
 - [156] H. Takahashi, S. Suzuki, K. Kato, and I. Nishi, "Arrayed-waveguide grating for wavelength division multi/demultiplexer with nanometre resolution," *Electronics Letters*, vol. 26, no. 2, p. 87, 1990, ISSN: 00135194. DOI: 10.1049/el:19900058. [Online]. Available: https://digital-library.theiet.org/content/journals/10.1049/el_19900058.
 - [157] C. Dragone, "An N*N optical multiplexer using a planar arrangement of two star couplers," *IEEE Photonics Technology Letters*, vol. 3, no. 9, pp. 812–815, 1991, ISSN: 1041-1135. DOI: 10.1109/68.84502. [Online]. Available: <http://ieeexplore.ieee.org/document/84502/>.
 - [158] M. Smit and C. Van Dam, "PHASAR-based WDM-devices: Principles, design and applications," *IEEE Journal of Selected Topics in Quantum Electronics*, vol. 2, no. 2, pp. 236–

- 250, 1996, ISSN: 1077260X. DOI: 10.1109/2944.577370. [Online]. Available: <http://ieeexplore.ieee.org/document/577370/>.
- [159] L. A. Coldren, S. W. Corzine, and M. Mashanovitch, *Diode lasers and photonic integrated circuits*. Wiley, 2012, p. 709, ISBN: 0470484128.
- [160] T. Goh, S. Suzuki, and A. Sugita, "Estimation of waveguide phase error in silica-based waveguides," *Journal of Lightwave Technology*, vol. 15, no. 11, pp. 2107–2113, 1997, ISSN: 07338724. DOI: 10.1109/50.641530. [Online]. Available: <http://ieeexplore.ieee.org/document/641530/>.
- [161] K. Shang, S. Pathak, C. Qin, and S. J. B. Yoo, "Low-Loss Compact Silicon Nitride Arrayed Waveguide Gratings for Photonic Integrated Circuits," *IEEE Photonics Journal*, vol. 9, no. 5, pp. 1–5, 2017, ISSN: 1943-0655. DOI: 10.1109/JPHOT.2017.2751003. [Online]. Available: <http://ieeexplore.ieee.org/document/8030983/>.
- [162] F. Soares, Wei Jiang, Sang-Woo Seo, Jong Hwa Baek, R. Broeke, Jing Cao, F. Olsson, S. Lourdudoss, and S. Yoo, "20 GHz channel spacing InP-based arrayed waveguide grating," in *33rd European Conference and Exhibition on Optical Communication - ECOC 2007*, vol. 2007, IEE, 2007, pp. 254–254, ISBN: 978-3-8007-3042-1. DOI: 10.1049/ic:20070118. [Online]. Available: https://digital-library.theiet.org/content/conferences/10.1049/ic_20070118.
- [163] K. Takada, M. Abe, T. Shibata, and K. Okamoto, "1-GHz-spaced 16-channel arrayed-waveguide grating for a wavelength reference standard in DWDM network systems," *Journal of Lightwave Technology*, vol. 20, no. 5, pp. 850–853, 2002, ISSN: 0733-8724. DOI: 10.1109/JLT.2002.1007939. [Online]. Available: <http://ieeexplore.ieee.org/document/1007939/>.
- [164] M. Gehl, D. Trotter, A. Starbuck, A. Pomerene, A. L. Lentine, and C. DeRose, "Active phase correction of high resolution silicon photonic arrayed waveguide gratings," *Optics Express*, vol. 25, no. 6, p. 6320, 2017, ISSN: 1094-4087. DOI: 10.1364/OE.25.006320. [Online]. Available: <https://www.osapublishing.org/abstract.cfm?URI=oe-25-6-6320>.
- [165] J. Baek, F. Soares, S. Seo, W. Jiang, N. Fontaine, R. Broeke, J. Cao, F. Olsson, S. Lourdudoss, and S. Yoo, "10-GHz and 20-GHz Channel Spacing High-Resolution AWGs on InP," *IEEE Photonics Technology Letters*, vol. 21, no. 5, pp. 298–300, 2009, ISSN: 1041-1135. DOI: 10.1109/LPT.2008.2008205. [Online]. Available: <http://ieeexplore.ieee.org/document/4663491/>.
- [166] F. M. Soares, N. K. Fontaine, R. P. Scott, J. H. Baek, X. Zhou, T. Su, S. Cheung, Y. Wang, C. Junesand, S. Lourdudoss, K. Y. Liou, R. A. Hamm, W. Wang, B. Patel, L. A. Gruezke, W. T. Tsang, J. P. Heritage, and S. J. B. Yoo, "Monolithic InP 100-Channel \times 10-GHz Device for Optical Arbitrary Waveform Generation," *IEEE Photonics Journal*, vol. 3, no. 6, pp. 975–985, 2011, ISSN: 1943-0655. DOI: 10.1109/JPHOT.2011.2170558. [Online]. Available: <http://ieeexplore.ieee.org/document/6032697/>.
- [167] W. Jiang, K. Okamoto, F. M. Soares, F. Olsson, S. Lourdudoss, and S. J. Yoo, "5 GHz Channel Spacing InP-Based 32-Channel Arrayed-Waveguide Grating," in *Optical Fiber Communication Conference and National Fiber Optic Engineers Conference*, Washington, D.C.: OSA, 2009, OWO2, ISBN: 978-1-55752-865-0. DOI: 10.1364/OFC.2009.OWO2. [Online]. Available: <https://www.osapublishing.org/abstract.cfm?uri=OFC-2009-OWO2>.

- [168] W. E. Cotter, "Photonic integrated circuit for the manipulation of coherent optical combs," PhD thesis, 2014. [Online]. Available: <https://cora.ucc.ie/handle/10468/1913>.
- [169] K. Cooney and F. H. Peters, "Analysis of multimode interferometers," *Optics Express*, vol. 24, no. 20, p. 22 481, 2016, ISSN: 1094-4087. DOI: 10.1364/OE.24.022481. [Online]. Available: <https://www.osapublishing.org/abstract.cfm?URI=oe-24-20-22481>.
- [170] N. P. Kelly, M. Dernaika, L. Caro, P. E. Morrissey, and F. H. Peters, "Monolithic Integration of Photonic Devices for Use in a Regrowth-Free CoWDM Transmitter," *IEEE Photonics Technology Letters*, vol. 29, no. 12, pp. 941–944, 2017, ISSN: 1041-1135. DOI: 10.1109/LPT.2017.2693318. [Online]. Available: <http://ieeexplore.ieee.org/document/7919190/>.
- [171] K. Shortiss, M. Shayesteh, W. Cotter, A. H. Perrott, M. Dernaika, and F. H. Peters, "Mode Suppression in Injection Locked Multi-Mode and Single-Mode Lasers for Optical Demultiplexing," *Photonics*, vol. 6, no. 1, p. 27, 2019, ISSN: 2304-6732. DOI: 10.3390/photonics6010027. [Online]. Available: <https://www.mdpi.com/2304-6732/6/1/27>.
- [172] A. Hurtado, I. Henning, and M. Adams, "Polarisation effects on injection locking bandwidth of 1550 nm VCSEL," *Electronics Letters*, vol. 45, no. 17, p. 886, 2009, ISSN: 00135194. DOI: 10.1049/el.2009.0411. [Online]. Available: <http://digital-library.theiet.org/content/journals/10.1049/el.2009.0411>.
- [173] D. T. Cassidy, "Comparison of rate-equation and Fabry-Perot approaches to modeling a diode laser," *Applied Optics*, vol. 22, no. 21, p. 3321, 1983, ISSN: 0003-6935. DOI: 10.1364/AO.22.003321. [Online]. Available: <https://www.osapublishing.org/abstract.cfm?URI=ao-22-21-3321>.
- [174] E. I. Gordon, "Optical Maser Oscillators and Noise," *Bell Syst. Tech. J.*, vol. 43, p. 507, 1964.
- [175] F. H. Peters and D. T. Cassidy, "Model of the spectral output of gain-guided and index-guided semiconductor diode lasers," *Journal of the Optical Society of America B*, vol. 8, no. 1, p. 99, 1991, ISSN: 0740-3224. DOI: 10.1364/JOSAB.8.000099. [Online]. Available: <https://www.osapublishing.org/abstract.cfm?URI=josab-8-1-99>.
- [176] D. T. Cassidy, "Technique for measurement of the gain spectra of semiconductor diode lasers," *Journal of Applied Physics*, vol. 56, no. 11, pp. 3096–3099, 1984, ISSN: 0021-8979. DOI: 10.1063/1.333867. [Online]. Available: <http://aip.scitation.org/doi/10.1063/1.333867>.
- [177] M. M. Ibrahim and M. Ibrahim, "A comparison between rate-equation and Fabry-Perot amplifier models of injection locked laser diodes," *Optics & Laser Technology*, vol. 28, no. 1, pp. 39–42, 1996, ISSN: 0030-3992. DOI: 10.1016/0030-3992(95)00042-9. [Online]. Available: <https://www.sciencedirect.com/science/article/pii/0030399295000429>.
- [178] A. E. Siegman, *Lasers*. University Science Books, 1986, p. 1283, ISBN: 0935702113. [Online]. Available: https://books.google.ie/books/about/Lasers.html?id=1BZVwUZLTkAC&redir_esc=y.
- [179] I. Petitbon, P. Gallion, G. Debarge, and C. Chabran, "Locking bandwidth and relaxation oscillations of an injection-locked semiconductor laser," *IEEE Journal of Quantum*

- Electronics*, vol. 24, no. 2, pp. 148–154, 1988, ISSN: 0018-9197. DOI: 10.1109/3.108. [Online]. Available: <http://ieeexplore.ieee.org/document/108/>.
- [180] B. W. Hakki and T. L. Paoli, “Gain spectra in GaAs double-heterostructure injection lasers,” *Journal of Applied Physics*, vol. 46, no. 3, pp. 1299–1306, 1975. DOI: 10.1063/1.321696. [Online]. Available: <http://aip.scitation.org/doi/10.1063/1.321696>.
- [181] E. Hecht, *Optics*. Addison-Wesley, 2002, p. 698, ISBN: 9780805385663.
- [182] K. Shortiss, M. Dernaika, M. Shayesteh, and F. H. Peters, “The Effect of Relaxation Oscillations in Integrated Optical Comb Demultiplexers based on Injection Locking,” *IEEE Journal of Quantum Electronics*, pp. 1–1, 2019, ISSN: 0018-9197. DOI: 10.1109/JQE.2019.2942053. [Online]. Available: <https://ieeexplore.ieee.org/document/8844062/>.
- [183] W. H. Press, W. T. Vetterling, S. A. Teukolsky, and B. P. Flannery, *Numerical recipes in C++ : the art of scientific computing*. Cambridge University Press, 2002, p. 1002, ISBN: 0521750334. [Online]. Available: <https://dl.acm.org/citation.cfm?id=506164>.
- [184] L. F. Shampine and H. A. Watts, “The art of writing a Runge-Kutta code. II,” *Applied Mathematics and Computation*, vol. 5, no. 2, pp. 93–121, 1979, ISSN: 0096-3003. DOI: 10.1016/0096-3003(79)90001-8. [Online]. Available: <https://www.sciencedirect.com/science/article/abs/pii/0096300379900018>.
- [185] B. Kelleher, D. Goulding, B. Baselga Pascual, S. P. Hegarty, and G. Huyet, “Phasor plots in optical injection experiments,” *The European Physical Journal D*, vol. 58, no. 2, pp. 175–179, 2010, ISSN: 1434-6060. DOI: 10.1140/epjd/e2010-00063-2. [Online]. Available: <http://www.springerlink.com/index/10.1140/epjd/e2010-00063-2>.
- [186] D. Lenstra, G. H. van Tartwijk, W. A. van der Graaf, and P. C. De Jagher, “Multiwave-mixing dynamics in a diode laser,” in *Chaos in Optics*, R. Roy, Ed., vol. 2039, International Society for Optics and Photonics, 1993, pp. 11–22. DOI: 10.1117/12.164762. [Online]. Available: <http://proceedings.spiedigitallibrary.org/proceeding.aspx?articleid=938586>.
- [187] G. H. M. van Tartwijk and D. Lenstra, “Semiconductor lasers with optical injection and feedback,” *Quantum and Semiclassical Optics: Journal of the European Optical Society Part B*, vol. 7, no. 2, pp. 87–143, 1995, ISSN: 1355-5111. DOI: 10.1088/1355-5111/7/2/003. [Online]. Available: <http://stacks.iop.org/1355-5111/7/i=2/a=003?key=crossref.91ba292925cfd64e1bacc312af262acd>.
- [188] J.-W. Wu and Y. H. Won, “Nearly Degenerate Four-Wave Mixing in Single-Mode Fabry-Pérot Laser Diode Subject to Single Beam Optical Injection,” *IEEE Photonics Journal*, vol. 9, no. 1, pp. 1–14, 2017, ISSN: 1943-0655. DOI: 10.1109/JPHOT.2016.2636744. [Online]. Available: <http://ieeexplore.ieee.org/document/7776788/>.
- [189] B. Kelleher, D. Goulding, S. P. Hegarty, G. Huyet, E. A. Viktorov, and T. Erneux, “Optically Injected Single-Mode Quantum Dot Lasers,” in *Quantum Dot Devices*, New York, NY: Springer New York, 2012, pp. 1–22. DOI: 10.1007/978-1-4614-3570-9_1. [Online]. Available: http://link.springer.com/10.1007/978-1-4614-3570-9_1.

- [190] F. Gustave, L. Columbo, G. Tissoni, M. Brambilla, F. Prati, B. Kelleher, B. Tykalewicz, and S. Barland, "Dissipative Phase Solitons in Semiconductor Lasers," *Physical Review Letters*, vol. 115, no. 4, p. 043 902, 2015, ISSN: 0031-9007. DOI: 10.1103/PhysRevLett.115.043902. [Online]. Available: <https://link.aps.org/doi/10.1103/PhysRevLett.115.043902>.
- [191] M. Dillane, J. Robertson, M. Peters, A. Hurtado, and B. Kelleher, "Neuromorphic dynamics with optically injected quantum dot lasers," *The European Physical Journal B*, vol. 92, no. 9, p. 197, 2019, ISSN: 1434-6028. DOI: 10.1140/epjb/e2019-90733-6. [Online]. Available: <http://link.springer.com/10.1140/epjb/e2019-90733-6>.
- [192] D. S. Wu, R. Slavík, G. Marra, and D. J. Richardson, "Phase Noise and Jitter Characterization of Pulses Generated by Optical Injection Locking to an Optical Frequency Comb," in *Frontiers in Optics 2012/Laser Science XXVIII*, Washington, D.C.: OSA, 2012, FW2A.3, ISBN: 978-1-55752-956-5. DOI: 10.1364/FIO.2012.FW2A.3. [Online]. Available: <https://www.osapublishing.org/abstract.cfm?uri=FiO-2012-FW2A.3>.
- [193] A. S. Tistomo and S. Gee, "Laser frequency fixation by multimode optical injection locking," *Optics Express*, vol. 19, no. 2, p. 1081, 2011, ISSN: 1094-4087. DOI: 10.1364/OE.19.001081. [Online]. Available: <https://www.osapublishing.org/oe/abstract.cfm?uri=oe-19-2-1081>.
- [194] V. I. Arnol'd, "Small denominators. I. Mapping of the circumference onto itself," *AMS Transl., Ser. 2*, vol. 46, pp. 213-284, 1965.
- [195] K. Shortiss, B. Lingnau, F. Dubois, B. Kelleher, and F. H. Peters, "Harmonic frequency locking and tuning of comb frequency spacing through optical injection," *Optics Express*, vol. 27, no. 25, p. 36 976, 2019, ISSN: 1094-4087. DOI: 10.1364/OE.27.036976. [Online]. Available: <https://www.osapublishing.org/abstract.cfm?URI=oe-27-25-36976>.
- [196] B. Lingnau, K. Shortiss, F. Dubois, B. Kelleher, and F. H. Peters, "The Devil's Staircase in the Frequency and Amplitude Locking of Nonlinear Oscillators with Continuous Periodic Forcing," 2019. arXiv: 1905.01122. [Online]. Available: <http://arxiv.org/abs/1905.01122>.
- [197] K. Otsuka and S. Kobayashi, "Optical bistability and nonlinear resonance in a resonant-type semiconductor laser amplifier," *Electronics Letters*, vol. 19, no. 7, p. 262, 1983, ISSN: 00135194. DOI: 10.1049/el:19830181. [Online]. Available: https://digital-library.theiet.org/content/journals/10.1049/el_19830181.
- [198] B. Tykalewicz, D. Goulding, S. P. Hegarty, G. Huyet, I. Dubinkin, N. Fedorov, T. Erneux, E. A. Viktorov, and B. Kelleher, "Optically induced hysteresis in a two-state quantum dot laser," *Optics Letters*, vol. 41, no. 5, p. 1034, 2016, ISSN: 0146-9592. DOI: 10.1364/OL.41.001034. [Online]. Available: <https://www.osapublishing.org/abstract.cfm?URI=ol-41-5-1034>.
- [199] A. Hurtado, A. Quirce, A. Valle, L. Pesquera, and M. J. Adams, "Power and wavelength polarization bistability with very wide hysteresis cycles in a 1550nm-VCSEL subject to orthogonal optical injection," *Optics Express*, vol. 17, no. 26, p. 23 637, 2009, ISSN: 1094-4087. DOI: 10.1364/OE.17.023637. [Online]. Available: <https://www.osapublishing.org/oe/abstract.cfm?uri=oe-17-26-23637>.

- [200] M. F. Salvade, C. Masoller, and M. S. Torre, "Polarization Switching and Hysteresis in Vertical-Cavity Surface-Emitting Lasers Subject to Orthogonal Optical Injection," *IEEE Journal of Quantum Electronics*, vol. 50, no. 10, pp. 848–853, 2014, ISSN: 0018-9197. DOI: 10.1109/JQE.2014.2352032. [Online]. Available: <http://ieeexplore.ieee.org/document/6883196/>.
- [201] P. Guo, W. Yang, D. Parekh, C. J. Chang-Hasnain, A. Xu, and Z. Chen, "Experimental and theoretical study of wide hysteresis cycles in 1550 nm VCSELs under optical injection," *Optics Express*, vol. 21, no. 3, p. 3125, 2013, ISSN: 1094-4087. DOI: 10.1364/OE.21.003125. [Online]. Available: <https://www.osapublishing.org/oe/abstract.cfm?uri=oe-21-3-3125>.
- [202] A. A. Qader, Y. Hong, and K. Alan Shore, "Ultra-wide hysteresis frequency bistability in vertical cavity surface emitting lasers subject to orthogonal optical injection," *Applied Physics Letters*, vol. 103, no. 2, p. 021108, 2013, ISSN: 0003-6951. DOI: 10.1063/1.4813492. [Online]. Available: <http://aip.scitation.org/doi/10.1063/1.4813492>.
- [203] J. Ohtsubo, *Semiconductor lasers: stability, instability and chaos*. Springer, 2013, ISBN: 9783642301476.
- [204] M. Crucifix, "Oscillators and relaxation phenomena in Pleistocene climate theory," *Philosophical Transactions of the Royal Society A: Mathematical, Physical and Engineering Sciences*, vol. 370, no. 1962, pp. 1140–1165, 2012, ISSN: 1364-503X. DOI: 10.1098/rsta.2011.0315. [Online]. Available: <https://royalsocietypublishing.org/doi/10.1098/rsta.2011.0315>.
- [205] S. H. Strogatz and I. Stewart, "Coupled Oscillators and Biological Synchronization on JSTOR," *Scientific American*, vol. 269, no. 6, pp. 102–109, 1993.
- [206] M. Brøns, P. Gross, and K. Bar-Eli, "Circle Maps and the Devil's Staircase in a Periodically Perturbed Oregonator," *International Journal of Bifurcation and Chaos*, vol. 07, no. 11, pp. 2621–2628, 1997, ISSN: 0218-1274. DOI: 10.1142/S0218127497001783. [Online]. Available: <http://www.worldscientific.com/doi/abs/10.1142/S0218127497001783>.
- [207] R. E. Ecke, J. D. Farmer, and D. K. Umberger, "Scaling of the Arnold tongues," *Nonlinearity*, vol. 2, no. 2, pp. 175–196, 1989, ISSN: 0951-7715. DOI: 10.1088/0951-7715/2/2/001. [Online]. Available: <http://stacks.iop.org/0951-7715/2/i=2/a=001?key=crossref.d3882881308b4b6aa485de4758fa18ef>.
- [208] S. Coombes and P. C. Bressloff, "Mode locking and Arnold tongues in integrate-and-fire neural oscillators," *Physical Review E*, vol. 60, no. 2, pp. 2086–2096, 1999, ISSN: 1063-651X. DOI: 10.1103/PhysRevE.60.2086. [Online]. Available: <https://link.aps.org/doi/10.1103/PhysRevE.60.2086>.
- [209] R. E. Mirollo and S. H. Strogatz, "Synchronization of Pulse-Coupled Biological Oscillators," *SIAM Journal on Applied Mathematics*, vol. 50, no. 6, pp. 1645–1662, 1990, ISSN: 0036-1399. DOI: 10.1137/0150098. [Online]. Available: <http://epubs.siam.org/doi/10.1137/0150098>.
- [210] F. C. Hoppensteadt and J. P. Keener, "Phase locking of biological clocks," *Journal of Mathematical Biology*, vol. 15, no. 3, pp. 339–349, 1982, ISSN: 0303-6812. DOI: 10.1007/BF00275692. [Online]. Available: <http://link.springer.com/10.1007/BF00275692>.

- [211] A. Pikovsky, M. Rosenblum, and J. J. Kurths, *Synchronization : a universal concept in nonlinear sciences*. Cambridge University Press, 2003, p. 411, ISBN: 9780521533522. [Online]. Available: <https://www.cambridge.org/ie/academic/subjects/physics/nonlinear-science-and-fluid-dynamics/synchronization-universal-concept-nonlinear-sciences?format=PB&isbn=9780521533522>.
- [212] D. D. Nolte, *Introduction to modern dynamics : chaos, networks, space and time*. Oxford University Press, 2014, p. 432, ISBN: 9780199657049.
- [213] M. H. Jensen, P. Bak, and T. Bohr, "Complete Devil's Staircase, Fractal Dimension, and Universality of Mode-Locking Structure in the Circle Map," *Physical Review Letters*, vol. 50, no. 21, pp. 1637–1639, 1983, ISSN: 0031-9007. DOI: 10.1103/PhysRevLett.50.1637. [Online]. Available: <https://link.aps.org/doi/10.1103/PhysRevLett.50.1637>.
- [214] G. H. Hardy, E. M. Wright, D. R. Heath-Brown, and J. H. Silverman, *An introduction to the theory of numbers*. Oxford University Press, 2008, p. 621, ISBN: 9780199219858. [Online]. Available: <https://global.oup.com/academic/product/an-introduction-to-the-theory-of-numbers-9780199219858?cc=ie&lang=en&>.
- [215] J. Sawicki, M. Abel, and E. Schöll, "Synchronization of organ pipes," *The European Physical Journal B*, vol. 91, no. 2, p. 24, 2018, ISSN: 1434-6028. DOI: 10.1140/epjb/e2017-80485-8. [Online]. Available: <http://link.springer.com/10.1140/epjb/e2017-80485-8>.
- [216] G. Pareyon, "Tuning Systems Nested Within the Arnold Tongues: Musicological and Structural Interpretations," in 2017, pp. 221–230. DOI: 10.1007/978-3-319-47337-6_23. [Online]. Available: http://link.springer.com/10.1007/978-3-319-47337-6_23.
- [217] L. Glass, "Cardiac arrhythmias and circle maps – A classical problem," *Chaos: An Interdisciplinary Journal of Nonlinear Science*, vol. 1, no. 1, pp. 13–19, 1991, ISSN: 1054-1500. DOI: 10.1063/1.165810. [Online]. Available: <http://aip.scitation.org/doi/10.1063/1.165810>.
- [218] J. R. Engelbrecht and R. Mirollo, "Structure of Long-Term Average Frequencies for Kuramoto Oscillator Systems," *Physical Review Letters*, vol. 109, no. 3, p. 034 103, 2012, ISSN: 0031-9007. DOI: 10.1103/PhysRevLett.109.034103. [Online]. Available: <https://link.aps.org/doi/10.1103/PhysRevLett.109.034103>.
- [219] P. Bak, "Commensurate phases, incommensurate phases and the devil's staircase," *Reports on Progress in Physics*, vol. 45, no. 6, pp. 587–629, 1982, ISSN: 0034-4885. DOI: 10.1088/0034-4885/45/6/001. [Online]. Available: <http://stacks.iop.org/0034-4885/45/i=6/a=001?key=crossref.8e3767f22c464cc50350520fbc89f951>.
- [220] C. W. Gardiner, *Stochastic methods : a handbook for the natural and social sciences*. Springer, 2009, p. 447, ISBN: 9783540707127.
- [221] L. Caro, "Design and fabrication of single-mode tunable lasers for regrowth-free monolithically integrated photonic circuits," PhD thesis, 2019. [Online]. Available: <https://cora.ucc.ie/handle/10468/7824>.

- [222] L. Caro, N. P. Kelly, M. Dernaika, M. Shayesteh, P. E. Morrissey, J. K. Alexander, and F. H. Peters, "A facetless regrowth-free single mode laser based on MMI couplers," *Optics & Laser Technology*, vol. 94, pp. 159–164, 2017, ISSN: 0030-3992. DOI: 10.1016/J.OPTLASTEC.2017.03.029. [Online]. Available: <https://www.sciencedirect.com/science/article/pii/S0030399217300257>.
- [223] M. Dernaika, "Monolithically integrated coherent comb de-multiplexer using facetless semiconductor ring lasers," PhD thesis, 2019. [Online]. Available: <https://cora.ucc.ie/handle/10468/8602>.
- [224] S. O'Brien and E. P. O'Reilly, "Theory of improved spectral purity in index patterned Fabry-Pérot lasers," *Applied Physics Letters*, vol. 86, no. 20, p. 201 101, 2005, ISSN: 0003-6951. DOI: 10.1063/1.1919389. [Online]. Available: <http://aip.scitation.org/doi/10.1063/1.1919389>.
- [225] G. Adolfsson, J. Bengtsson, and A. Larsson, "Spectral engineering of semiconductor Fabry-Perot laser cavities in the weakly and strongly perturbed regimes," *Journal of the Optical Society of America B*, vol. 27, no. 1, p. 118, 2010, ISSN: 0740-3224. DOI: 10.1364/JOSAB.27.000118. [Online]. Available: <https://www.osapublishing.org/abstract.cfm?URI=josab-27-1-118>.
- [226] D. Bitauld, S. Osborne, and S. O'Brien, "Design of waveguide-integrated semiconductor laser sources for optical frequency comb generation," *Optics Letters*, vol. 36, no. 15, p. 2985, 2011, ISSN: 0146-9592. DOI: 10.1364/OL.36.002985. [Online]. Available: <https://www.osapublishing.org/abstract.cfm?URI=ol-36-15-2985>.
- [227] S. O'Brien, S. Osborne, D. Bitauld, and A. Amann, "Design and applications of discrete mode Fabry-Perot diode lasers," *Photonics and Nanostructures - Fundamentals and Applications*, vol. 8, no. 4, pp. 218–227, 2010, ISSN: 1569-4410. DOI: 10.1016/J.PHOTONICS.2010.04.013. [Online]. Available: <https://www.sciencedirect.com/science/article/pii/S1569441010000490?via%3Dihub>.